Spatio-temporal organization and regulation of enzymes involved in siderophore biosynthesis in Pseudomonas

Hanna Manko

Université de Strasbourg

École doctorale des sciences de la vie et de la santé

Thèse

présentée pour l'obtention du grade de :

Docteur de l'université de Strasbourg

Discipline : Biophysique

par

Hanna Manko

soutenue le : 28/09/2022

Organisation spatio-temporelle et régulation des enzymes impliquées dans la biosynthèse d'un sidérophore chez *Pseudomonas*

Laboratoire de bioimagerie et pathologies - UMR 7021 CNRS

Membres du jury :

Dr Cécile Morlot	Rapportrice externe, Chercheuse CNRS, Université de Grenoble
Dr Laurent Cognet	Rapporteur externe, Directeur de recherche CNRS, Université de Bordeaux
Dr Myriam Seemann	Examinatrice interne, Directeur de recherche CNRS, Université de Strasbourg
Dr Julien Godet	Directeur de thèse, Maîtres de confŕences, Université de Strasbourg

Somewhere, something incredible is waiting to be known.

- Carl Sagan

Table des matières

Acknowledgements

Finally I came to this point, when my thesis manuscript is ready and my three year of work are almost complete. These years were full of everything new to me. This was my first experience of living alone so far from my hometown, of real lab work, of writing the scientific manuscripts, doing microscopy, my first code in Python etc. Covid19 confinement was one of the craziest things.

Now, by looking back I can say that I am really happy to spend my last four years here.

It is been a long way now from the start of my studies in Ukraine. I am really grateful to my mother for always supporting me and my desire to become a physicist. I would also like to thank Yves Mély for the opportunity to continue my Master's 2 studies at the University of Strasbourg and to perform my master internship in the Laboratory of Bioimaging and Pathologies. I am grateful to Yves for all the help in my preparation to the concours of école doctorale whereafter I've got my PhD funding.

But, most of all I would like to thank my supervisor, Julien Godet, for teaching, guiding, motivating and being the greatest example for me. Julien is one of the brightest minds I have ever met and one of the best teachers. I am very happy to have this opportunity to work with him.

I thank Dmytro Danylchuk for advising, helping, and motivating me.

I am grateful to Dr. Pascal Didier, Dr. Frederic Przybilla, Dr. Manuel Boutant, Dr. Nicholas Humbert, Dr. Halina Anton and Dr. Ludovic Richert for advising and helping during my work.

I would like to thank my colleagues Srijayee, Mary, Soumajit, Dmytro, Olha, Deep, Aqib, Nina, Kyong, Caterina, Alex, Viola, Albane and others for the good time I spent in the lab. My thanks to Marlyse Wernert and Ingrid Barthel for providing the infrastructure and help.

Thank you all!

- Hanna

Overview

Various microorganism adaptation mechanisms include the biosynthesis of secondary metabolites. Secondary metabolites usually results from the activation of specific metabolic pathways dedicated to their production. Bacteria have evolved complex pathways, with multiple proteins and advanced biosynthesis strategies, including the synthesis of peptides independently from the ribosomal machinery. Such synthesis mechanisms allow to provide much wider functional diversity of metabolites.

Understanding the spatial and temporal organization of the enzymes and proteins involved in the synthesis of secondary metabolites is challenging but exciting. Many questions regarding these organizations at the sub-cellular level may be addressed by super-resolution (SR) microscopy techniques. Further developments of these techniques should enable new opportunities for their exploration. In particular, imaging and tracking multiple target simultaneously and directly in bacterial cells can be a game changer.

In this thesis manuscript, we will focus on the organization of Non Ribosomal peptide synthetase involved in the pyoverdine pathway in *Pseudomonas aeruginsa*.

In the first section we applied several SR methods such as sptPALM, single- and two-color DNA-PAINT in order to obtain the information about NRPSs mobility, localization and colocalization. Further, the FLIM-FRET experiments were performed allowing to confirm the interaction of some proteins. The obtained data allows to suggest that four NRPSs involved in pyoverdine biosynthesis may form a very dynamic complexes in the regions near the bacteria cell membrane.

We also dedicated significant efforts to advance single molecule localization microscopy (SMLM) approaches. In this manuscript, we introduce SMLM approaches and their latest developments including spectrally-resolved SMLM (srSMLM). We reviewed the state of art in srSMLM. We also introduced basics of deep learning to better understand the work we have done to enhance srSMLM with deep learning. Our improvements are exciting and subsequent experiments could include the utilization of spectrally-resolved (sr) microscopy technique to provide the capability to follow the diffusion and localize multiple enzymes at the same time in cells provided that the performance can be improved. Furthermore, we propose the application of spectral phasor in order to consider full spectra information and consequently enhance the analysis of spectrally-

resolved microscopy data.

Finally , this manuscript includes some preliminary experiments on a related but slightly different project performed in order to investigate the effect of carbapenems (Meropenem) on the bacteria cell and the mechanism of *P.aeruginosa* tolerance to this antibiotic.

Introduction

1.1 Super-resolution fluorescence microscopy

1.1.1 Fluorescence

Fluorescence is the phenomena of emission of light from molecules that have been transitioned to singlet exited states. The transition to exited states can be induced by absorption of a photon with energy $h\nu_a$ corresponding to a gap between singlet ground state (S_0) and exited states (S_1, S_2) (Figure 1.1.1).

This process is followed by fast non-radiative internal conversions to the lowest singlet excited state (S_1) from which radiative or non-radiative transitions to ground state can occur (Figure 1.1.1). The time a molecule spends in the exited state is called fluorescence lifetime (typical values are about few nanoseconds). The energy of absorption is typically higher than that of emission ($h\nu_a > h\nu_F$) resulting in a longer emission wavelength as compared to the absorption wavelength (Figure 1.1.1). This difference between absorbed and emitted wavelengths is called Stokes shift and was named after G. Stokes who first observed this effect experimentally [1].

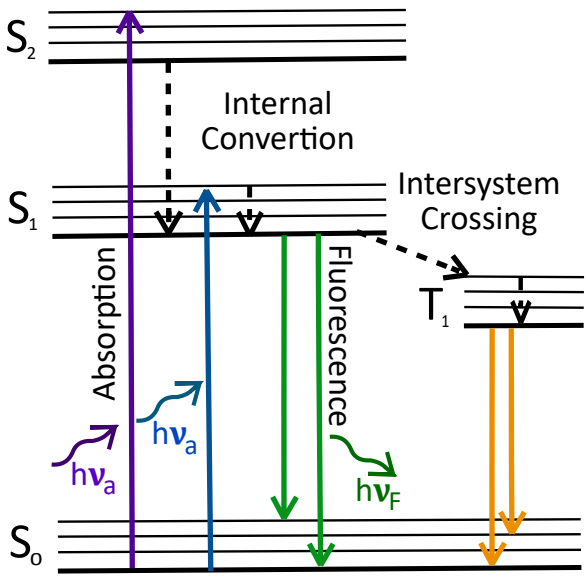

Figure 1.1.1 – Jablonski diagram

There are other ways to depopulate the exited states. It includes Förster resonance energy transfer (FRET) in which the energy can be transferred from a "donor" to an "acceptor" molecule.

FRET is a non-radiative dipole-dipole coupling that can occur under some situations as the efficiency of the transfer depends on the spectral overlaps between the emission spectra of the donor and absorption spectra of the acceptor, angle between the dipoles but also strongly on the distance between them. As FRET is depopulating the excited state of a donor, it is associated to a shortening of its fluorescence lifetime.

Under its continuous excitation, a fluorophore can randomly switch between ON (bright) and OFF (dark) states - a phenomenon called blinking. This effect can be explained by certain probability of fluorescent molecule not to come back to singlet ground state but transit to triplet state T_1. The lifetime of the triplet state is much longer(μs) due to forbidden transition between triplet and ground states. In this state the molecule do not emit any photons so that it is switched temporarly to a "off" state. Once the molecule returns to the ground state it can be excited again and emit photons[1, 2].

Finally, a molecule can go through a finite number of excitation-emission cycles before it undergo irreversible chemical reactions in the fluorophore, turning it permanently unable to fluoresce (photobleaching). The number of photons a single molecule can emit is therefore limited (typically $10^4 - 10^5$ for eGFP for example, or $10^5 - 10^6$ for most organic fluorophores)

Fluorescence became an important tool in biochemistry and biophysics due to its specificity, versatility and high speed but also because it is non (or low) perturbating nor destructive. It is broadly used to study live organisms at cellular and molecular levels. Various targets as proteins, nucleic acids, lipids can be labelled with fluorophores which include organic dyes (NileRed, AlexaFluor, fluorescein and BODIPY), fusion fluorescent proteins (GFP, YFP, RFP) or fluorescent particles as quantum dots.

1.1.2 Fluorescence microscopy

Principle

In fluorescence microscopy, the labeled specimen is illuminated by a light of specific wavelength. The illumination of the sample and the collection of emitted light is usually done by the same objective. As the excited fluorophores emit light with longer wavelengths due to the Stokes shift, the fluorescence emitted light can be separated from the excitation light with a dichroic filter. The illumination with a parallel beam of light passed directly upwards through the sample is called epi-illumination (Figure 1.1.2, A). Epi-illumination can be used for widefield imaging. It maximizes the amount of illumination but also lead to high out-of-focus background signal, sometimes reducing the contrast. Alternative illumination or fluorescence collection modes are available such as confocal or TIRF illumination. In confocal microscopes the observation volume

can be reduced by focusing the excitation beam on small part of the sample by the objective and by introducing the pinhole in the detection path (Figure 1.1.2, B). The resulting microscopy images are created either by scanning over the specimen or by using a spinning disk [3]. In case of scanning the temporal resolution is limited by its rate.

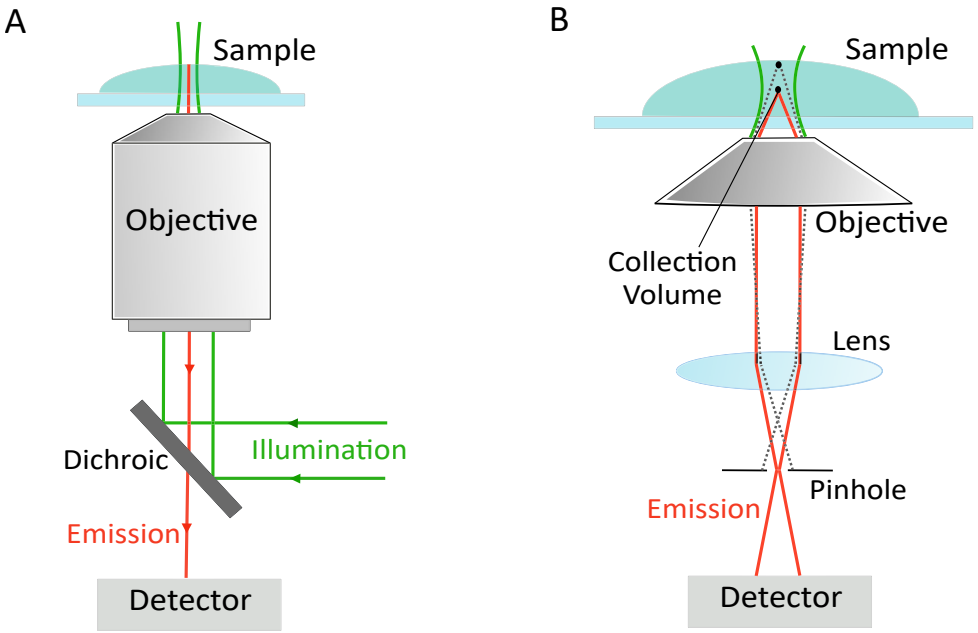

Figure 1.1.2 – **A.** Epi-fluorescence setup **B.** Confocal setup

The observed volume can be restricted more by limiting the excitation volume using another mode of illumination called Total Internal Reflection Fluorescence (TIRF) (Figure 1.1.3). When a beam of light reaches the sample which refractive index is lower than that of the coverslip and if the angle of incidence exceeds the critical angle (the value is around 60°), the beam is totally internally reflected and the intensity of the transmitted light drops to 0 - but an electromagnetic field, also known as an evanescent wave, is generated at the solid-liquid interface with the same frequency as the excitation light. Then a very small volume of the sample near the coverslip (∼150 - 200 nm in depth) is illuminated with the evanescent wave. Due to the restriction in the illumination of the sample, the background is substantially decreased. There is virtually no out-of-focus fluorescence collected (which decrease blurring effects) and the sample is exposed to significantly smaller amount of light which limits phototoxicity. Using appropriate objectives (with high NA aperture), one can easily switch between standard widefield fluorescence and TIRF just by changing the off-axis position of the beam focus at the objective's back focal plane.

Nevertheless, as for epi or confocal microscopes, the resolution of TIRF microscopy is limited by the diffraction limit.

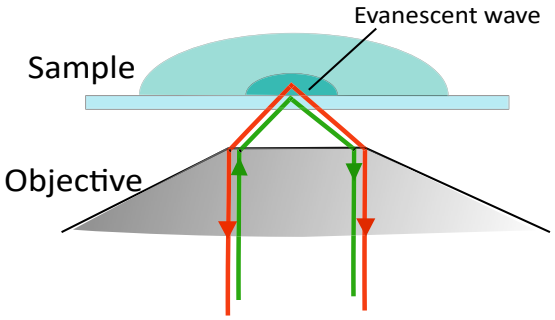

Figure 1.1.3 – Total Internal Reflection Fluorescence microscopy principle

Diffraction Limit

The resolution of an optical system is defined by the minimal distance between two emitters at which they can still be distinguished.

When the light coming from a point object passes through a circular aperture diffraction will occur. Therefore the image of the object will have the shape of the diffraction pattern. This pattern, also called point spread function (PSF) of the imaging system, contains a bright central spot, known as Airy disc, surrounded by circular diffraction orders. The diameter of Airy disc determines the minimal size of the image of the point object. Consequently, if two emitters are located on the distance smaller than this diameter they will appear as one single blurry spot on the image (Figure 1.1.4). Ernst Abbe defined this distance as the diffraction limit. He proposed that the diffraction limit is proportional to the wavelength of light divided by the numerical aperture (NA) of the objective lens[4] (equation 1.1).

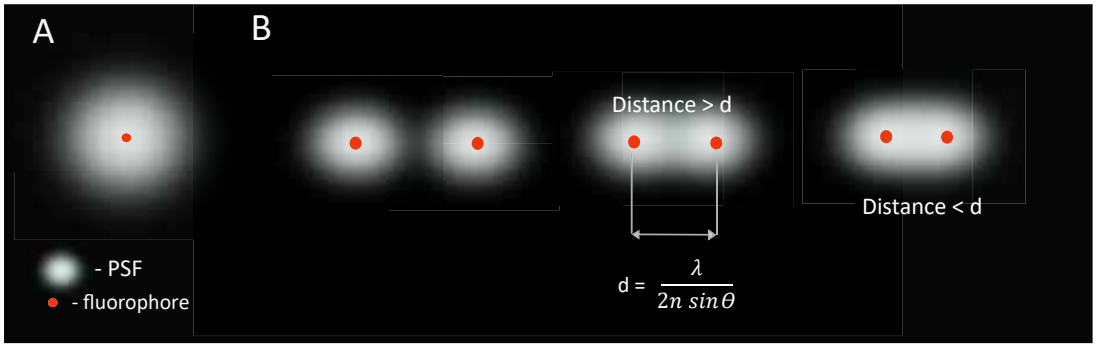

Figure 1.1.4 – A. Fluorophore compared to PSF spot size. **B**. Two fluorophores located at different distance.

$$d = \frac{\lambda}{2n \cdot sin\theta} = \frac{\lambda}{2NA} \tag{1.1}$$

If we consider an illumination wavelength of 500 nm and a NA of 1, the diffraction limit is ~250 nm. For modern optics NA can reach about 1.4 -1.5 allowing to get minimum resolvable distance

of ∼180 nm. This resolution is sufficient to visualize most of cells structures but objects such as viruses, proteins or small molecules have sizes clearly below this value.

1.1.3 Super-resolution microscopy techniques

There are several approaches to overcome the Abbe's diffraction limit. These approaches can be divided into two main categories. In the first broad category the super resolution is achieved by using patterned illumination or differential modulation of fluorescent emission of molecules.

In one of the first presented technique higher resolution can be achieved by illuminating the sample with focused excitation beam combined with a donut-shaped beam, also called the stimulated-emission-depletion (STED) beam, which stimulates emission of the fluorophores at the outer regions (Figure 1.1.5). This technique results in effective fluorophore emission only in the central region of the donut shaped beam[5]. Instead of stimulated emission, the fluorophores on the outer regions can be stitched to non-emissive state by other mechanism, such as photoswitching (in RESOLFT technique [6]). Since the illuminated region is very small, scanning across the sample is required in order to obtain super resolved image.

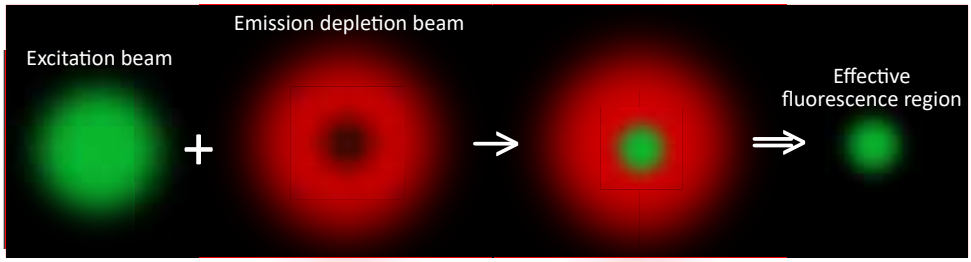

Figure 1.1.5 – Prinsiple of STED super-resolution microscopy

Alternatively, in order to increase image resolution various illumination patterns can be used. In structured illumination microscopy (SIM) technique the sample is illuminated with a number of standing waves with different orientations or phases [7]. The resolution can be further improved in saturated SIM technique by saturating the ground state (S_0) using intense illumination [8].

The lateral resolution achieved with these techniques is ∼30-80 nm, and the axial resolution is in the order of 100 nm[9].

The second broad category includes all the single molecule localization microscopy (SMLM) techniques. These methods are based on imaging individual fluorophores at different time points. Each frame is then processed in order to localize the position of each fluorescent molecule (Figure 1.1.6, A). The precise coordinates of each isolated emitter can be determined by localizing the

center of its PSF. This can be done by fitting the intensity profile of single emitter image (Figure 1.1.6, B). The precise coordinates of fluorophore positions can be determined if their PSFs do not overlap. Further all the determined localizations are concatenated to reconstruct a super-resolution image.

The stochastic activation of a tiny fraction of fluorophores per single frame can be achieved in different ways. The STORM technique is originally based on switching between fluorescent and dark state of Cy5 dye using two fluorophores and two lasers. The recovery rate of the dye into the fluorescent state depends on the distance to second dye, Cy3 [10]. Later, it has been shown that photoswitching can be achieved without an activator fluorophore by imaging sample immobilized on the microscope slide in the aqueous buffer in direct STORM (dSTORM) technique [11]. For this technique photoswitchable organic dyes are required. In PALM technique the photoactivatable fluorescent protein are used in order to achieve stochastic blinking [12].

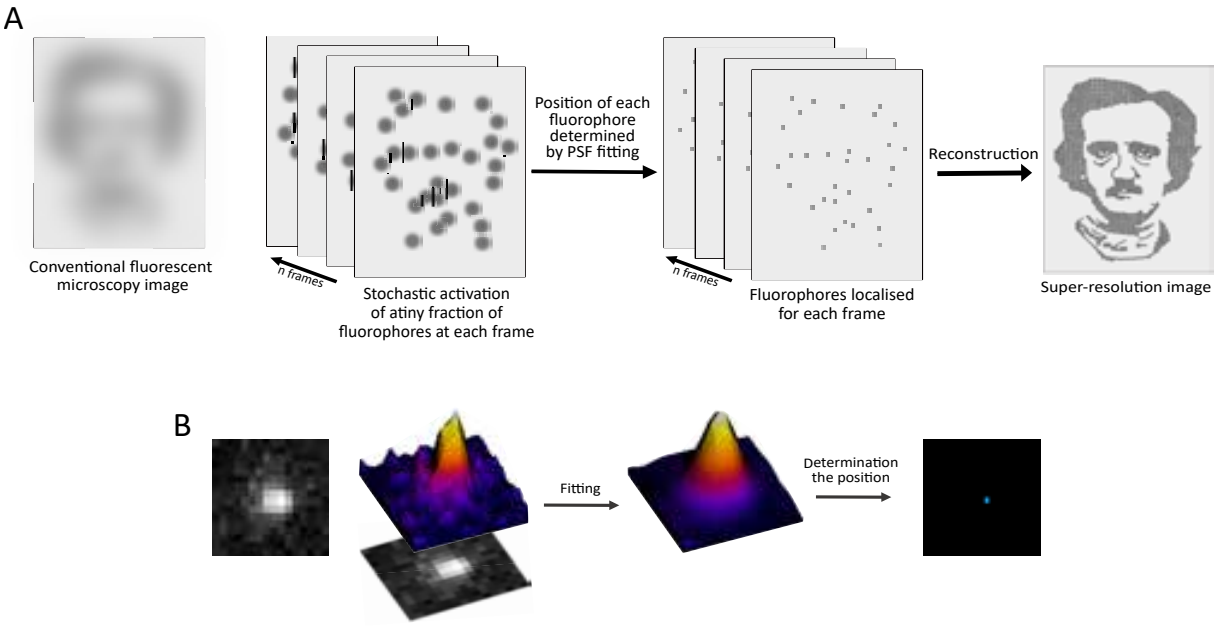

Figure 1.1.6 – Principle of SMLM super-resolution microscopy. A. The fine structures are indistinguishable on the diffraction limited image obtained via conventional microscopy. The resolution can be improved by activating small amount of fluorophores so their PSFs are not overlapping. Therefore, the coordinates of each fluorescent molecule can be precisely determined by its PSF spot fitting. The super-resolution image is reconstructed by combining all the coordinates. **B**. The procedure to determine precise localization of the fluorescent molecule.

Alternatively, stochastic turn-on process can be created by using fluorescent probes present in solution able to turn on their fluorescence once bound transiently to the object. In this technique, called Point accumulation for imaging in nanoscale topography (PAINT), the blinking rate can be controlled easily by regulating the concentration of probes in solution. PAINT was amongst the first reported SMLM technique [13]. In PAINT, the binding between the fluorescent

molecules and the target is mainly governed by diffusion but also by hydrophobic or electrostatic interactions making it difficult to image specific biomolecules. High specificity to the target molecule was achieved in uPAINT [14] and more recently in DNA-PAINT [15] technique. This technique combines the advantages of PAINT and immuno-labeling. The target-specific antibody is conjugated to single DNA docking strand while the complementary imager strand is conjugated to the fluorophore which diffuses in the solution (Figure 1.1.7). SMLM techniques permit to achieve resolutions of 10-30 nm[16].

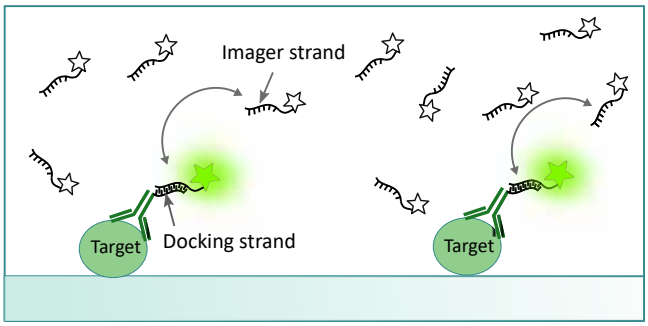

Figure 1.1.7 – DNA-PAINT principle

Recently, a technique combining patterned illumination and SMLM techniques resulted in a new concept called MINimal photon FLUXes (MINFLUX)[17, 18, 19]. In this technique the localization of the molecule is defined by intensity zero instead of maximum. The excitation beam is shaped in such a way so that intensity in the central part is equal to zero. The position of the emitting molecule is then found by performing probing steps. The resulting fluorescence of the molecule is stepwise reduced by approaching the zero intensity centre of the beam to the true molecule position (Figure 1.1.8). This approach strongly reduces the number of photons required to localize molecules and MINFLUX is able to achieve impressive 1-3 nanometer precision. MINFLUX technique is highly suitable for fast single molecule tracking allowing to achieve remarkable spatial and temporal resolution. Indeed, the resolution of MINIFLUX can be as good as few nm, corresponding to sizes of most proteins in cells. Microscopy is then approaching molecular microscopy.

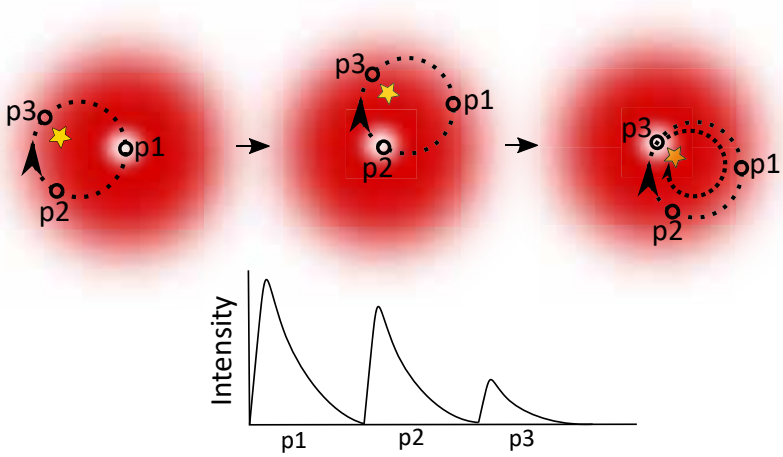

Figure 1.1.8 – MINFLUX microscopy principle. The laser beam with intensity zero in the central part is used to find the position of the molecule by performing probing steps. The central part of the beam is approaching the true molecule position by finding the emission intensity minimum.

Detection

The super-resolution microscopy techniques allow to obtain remarkable resolution. Nevertheless, the best performance can only be achieved by optimal combination of all the setup parts including the use of properly chosen detectors.

In the field of microscopical imaging the signal is typically detected by CCD (Charge-Coupled Device) or CMOS (Complementary Metal-Oxide Semiconductor) sensors. The performance of the microscope setup depends on several parameters of the chosen detection unit. One of the most important parameters is the resolution, which depends mostly on the objective and the detector.

In general, there are two main parameters, which affect the resolution of a given setup : the sensor pixel size in the detector and the total magnification. A decrease in pixel size and an increase in total magnification lead to better resolution, however, the best resolution can be achieved only by matching the magnification of the objective and the pixel size of the detector. According to a so-called Nyquist criterion, the size of a single pixel should be twice as small as the desired maximum resolution in order to be able to distinguish the adjacent features on an image. For instance, in order to achieve the maximum possible resolution (corresponding to a diffraction limit), a conventional setup featuring a 60x magnification should have a pixel size not more than 6.5 μm.

Another factor is the signal-to-noise ratio (SNR). Generally, there is an offset between the detector sensitivity and the noise level. In case of lower illumination intensities, lower imaging frame duration and/or less bright fluorophores the relatively low emission signal demands an increase in detector sensitivity, which in turn leads to increased background noise. SNR is of particular importance in advanced imaging techniques, such as super-resolution microscopy.

1.1.4 3D imaging in super-resolution microscopy

Conventional super-resolution microscopy allows to obtain super-resolved images in 2D. Several 3D imaging techniques in SR fluorescence microscopy were developed. One of the widely used techniques is based on astigmatism. To introduce astigmatism into the microscopical image, a cylindrical lens can be inserted into the light path before the detector (Figure 1.1.9, A). Thus the PSF retains the round shape when the emitter is located precisely in the imaging plane, but becomes characteristically elongated when the fluorophore is either above or below the plane. Using the distortion pattern it becomes possible to decipher the z-position for a given localization and ultimately create a 3D image (Figure 1.1.9, D)) [20]. Another approach used to create a 3D SR image is biplane imaging. In this technique the emission is split in two using a 50 :50 beam splitter leading to acquisition of two separate images on the camera sensor with two different

focus positions (Figure 1.1.9, C)). Biplane is obtained by adding an additional lens is inserted into one of the channel in order to create a shift between the focus planes. The differences in PSF shapes on the two images are later used to determine the precise z-positions, needed to reconstruct a 3D image (Figure 1.1.9, D)). [21]. Double helix PSF is another additional method to build 3D images. In this method, z position is determined by angular orientation between two lobes created using reflective spatial light modulator (Figure 1.1.9, B,D)) [22] or using a phase mask in the Fourier plane of the microscope [23]. The z-position is calibrated as a function of the angular rotation of the two lobe of the PSF with the advantage that molecules away from the focal plane do not appear quite blurry (unlike biplane or astigmatism), while the position of the molecule is determined as the mid-distance between the two lobes (therefore losing a bit of (x-y) precision).

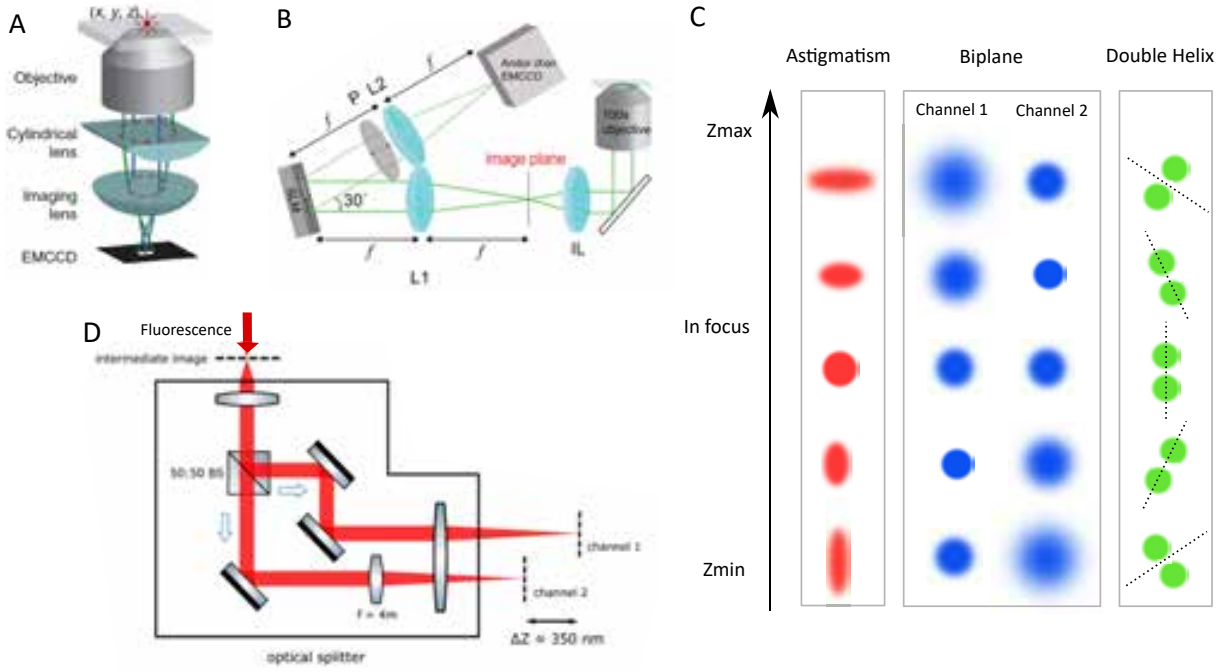

Figure 1.1.9 – **A**. Schematic setup of a 3D SMLM with astigmatic lens. **B**. Schematic setup of a 3D SMLM with double helix PSF. **C**. Schematic setup of a 3D SMLM with biplane. **D**. Retrieving z positions from the modified PSF.

1.1.5 Single molecule tracking

The information about the motion of biomolecules within live cells can help to understand fundamental molecular processes. Single-molecule tracking (SMT) or single-particle tracking (SPT) techniques allowed to follow the movement of molecules of interest and record their trajecto-

ries. TIRF-, HILO[24]- or light sheet microscopy[25]- based SMT can be used to investigate the processes on the cellular membrane or deeper inside the cells. Single-molecule trajectories are extracted using frame-by-frame video analysis by identifying the same molecule in each frame and connecting the corresponding particles positions in subsequent frames (Figure 1.1.10, A) [26].

In the case of low molecule densities the trajectory formation task can be reduced to simple problem of linking to the nearest neighbor in the subsequent frames [27]. The systems with higher molecule densities impose more challenges on the proper trajectory formation, such as particle merging and splitting, motion heterogeneity, and temporal disappearance. To overcome these challenges more sophisticated approaches were employed. These include multiple-hypothesis tracking [28], improvements of this method[29] and Global Nearest Neighbour [30].

In order to quantitatively describe the motion of the molecules the diffusion coefficients need to be determined from the obtained trajectories. The investigation of the biological samples via single molecule tracking microscopy requires robust analysis methods which are able to provide correct interpretation of the obtained tracks.

A typical way to obtain the diffusion coefficients is to plot the mean-square displacement (MSD) which is the measure of particle deviation over time. MSD is calculated for all the positions in the track over multiples of the smallest interval Δt, 2Δt, 3Δt etc. The diffusion coefficient can be obtained by calculating the slope of MSD over Δt plot (Figure 1.1.10, B). In MSD analysis the diffusion coefficients obtained for each trajectory individually are then averaged. However, such averaging can possibly lead to an inability to distinguish different diffusion regimen in the mixture. Moreover, this type of analysis becomes inaccurate in the case of short trajectories.

An alternative way to analyze the particle trajectories is to use jump-distance (JD) analysis [31, 32, 33, 34]. This approach allows to analyze all particle displacements of all the trajectories. The diffusion coefficients can be obtained by plotting the distribution of all the calculated jump distances (the distance on which an individual particle was displaced within a fixed time interval Δt) and subsequently fitting by theoretically derived probability distribution (Figure 1.1.10,C) [34]

$$p(r^2, \Delta t)dr^2 = \frac{1}{4D\Delta t} exp(-\frac{r^2}{4D\Delta t})dr^2 \tag{1.2}$$

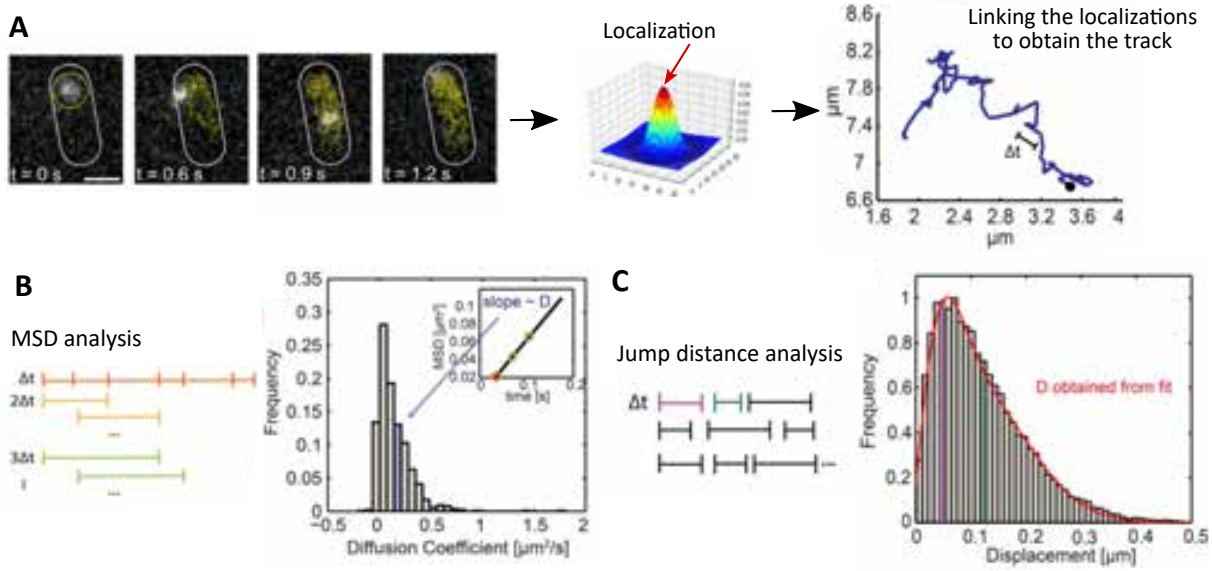

Figure 1.1.10 – A. In the single molecule tracking experiments the motion of fluorescent molecule is recorded. After the determination of the molecule position and linking the localizations in each consecutive frame the track can be formed. Diffusion coefficients can be calculated with two different approaches. **B**. MSD analysis calculation principle **C**. Jump distance analysis calculation principle (Image modified from[34])

In JD analysis different probability distributions of the jumps will correspond to various diffusive populations. The diffusion coefficients of several populations can be derived by extending the expression analytically used to fit the distribution of the jumps :

$$p(r^2, \Delta t)dr^2 = \sum_{j=1}^{m} \frac{f_j}{4D_j\Delta t} exp(-\frac{r^2}{4D_j\Delta t})dr^2, \tag{1.3}$$

where D_j corresponds to a respective diffusion coefficient of particles in a given mobility mode j and f_j corresponds to the fraction of the total amount of particles in this mobility mode.

In case of JD analysis the information about the single trajectory is lost but the diffusion coefficient is obtained for an ensemble of trajectories in the same mobility mode allowing to distinguish between several diffusive species.

1.1.6 Spectrally-resolved super-resolution microscopy

Super-resolution microscopy techniques have achieved remarkable spatial resolution. However, these techniques are almost limited to extracting spatial information and spectral information could only be recorded when having different color channels. To overcome this limit several SMLM based techniques were reported allowing to simultaneously record spatial and spectral information from individual fluorescent molecules [35, 36, 37, 38].

Principle

In spectrally-resolved SMLM (srSMLM) techniques an additional dispersive element is introduced into the light path in order to capture spectral information. Thus the stochastic emission from each fluorescent molecule is divided into two parts forming the two corresponding images. In the spatial part, no dispersion is imposed to the fluorescence emission and the signal can be used to determine the coordinates of the fluorophore with sub-diffraction resolution - identical to conventional SMLM techniques. In the spectral part photons are passing through the dispersive element which leads to a wavelength-dependent change in the angle of light propagation. The true emission wavelength of a specific localization is then determined using the distance between the corresponding peaks in spatial and the position of spectral parts in the image(Figure 1.1.11)).

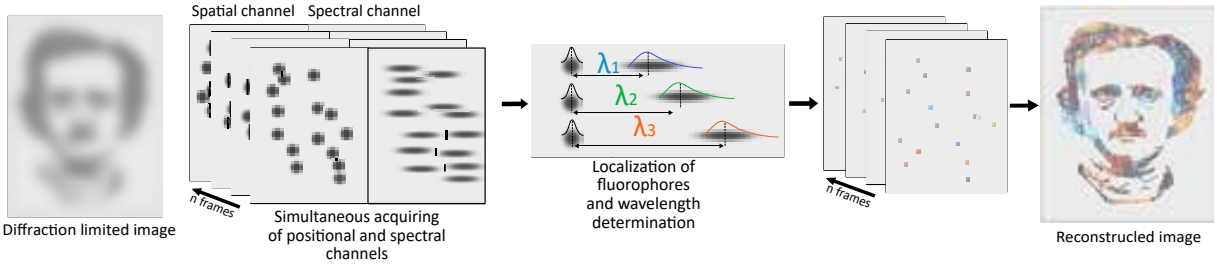

Figure 1.1.11 – Principle of srSMLM super-resolution microscopy.

There are two main configuration for srSMLM that differ in the dispersive element used, either prism or diffraction grating. In the setups using refraction prisms the emission from the sample is first separated into two optical paths. This can be achieved in dual objective systems[35, 39] where the emission from the sample is simultaneously recorded by two opposing objectives. The light collected by the first objective passes through the refraction prism creating a spectral image and the light collected by the second objective is used to create a spatial image. Dual objective systems provide high light collection efficiency but limit the choice of sample types and increase the configuration complexity [35].

Another approach to achieve light separation is to introduce a beam splitter with a desired positional :spectral splitting ratio of 50 :50[37, 40, 41] or 30 :70[42]. Since the two separate light paths are created the first one is used in order to create the positional image while in the second path the light is dispersed by the prism creating a spectral image (Figure 1.1.12). The refraction prisms are mostly used for applications requiring low spectral precision due to their relatively low dispersion. Furthermore, additional calibration may be required in order to correct for the nonlinear spectral dispersion of prisms. The optical losses in the configuration with a prism may occur at the surface of reflection mirrors, beam splitter and the prism but the transmission efficiency of prism is usually high.

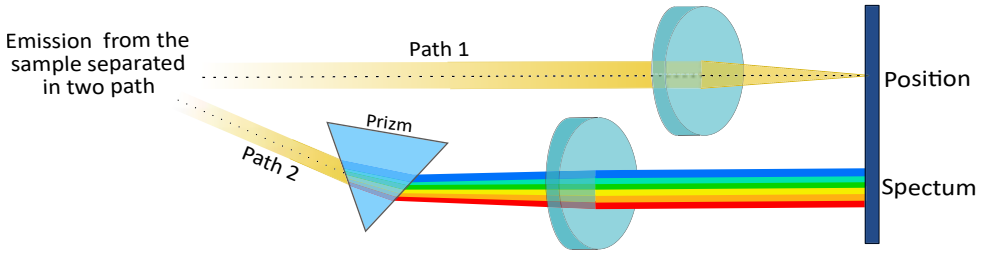

Figure 1.1.12 – Prinsiple of srSMLM super-resolution microscopy using a dispersive prism.

In contrast to the refraction prisms, the use of transmission diffraction gratings does not require beam splitting. Typically, blazed transmission diffraction gratings are used in this type of configurations. Therefore the emission from the sample can be collected in the 0^{th} and the 1^{st} diffraction orders [36, 43, 44, 45, 46] (Figure 1.1.13, A) for the spatial and spectral image, respectively (Figure 1.1.13, B). The use of gratings allows to strongly simplify the setup and to avoid additional sophisticated alignment. Moreover, diffraction gratings provide a wider spectral dispersion with good linear properties. The dispersion properties can be further adjusted by choosing the proper gratings with appropriate number of lines per millimeter. Nevertheless, wavelength dependent efficiency and high dispersion may lead to reduced SNR and consequently lower spectral precision. Additionally, gratings dispersion also occurs in small proportion in higher orders (2nd, 3rd, ...) and symmetrical orders (-1,-2,...). Since these orders are not collected, a small amount of light coming from the emitters is lost.

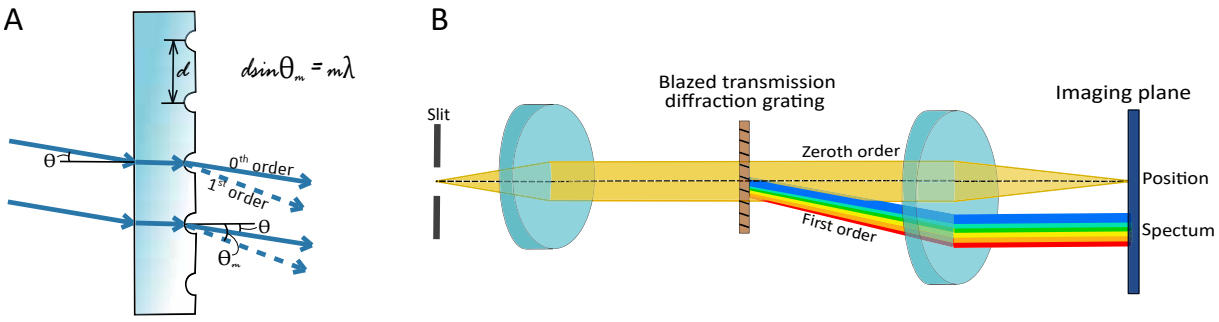

Figure 1.1.13 – Principle of srSMLM super-resolution microscopy using a blazed diffraction grating.

Applications

Multi-colour imaging. SMLM can be used for multi-colour imaging but require the use of fluorophores with well distinguishable excitation and emission peaks. The choice of fluorescent molecules is strongly limited due to strict requirements as high brightness, photo stability, spectral range and biocompability. This limited selection makes almost impossible to achieve full spectral separation of more than two fluorophores because of spectral cross-talk. Even for two colors, most of the time, the spectral filtering is reducing significantly the signal intensity of one

or both fluorophores based on filter choice and trade-offs made in term of laser excitation.

In srSMLM techniques spectral cross-talk is not an issue because wavelength can be determined precisely for each spectral peak allowing to achieve the cross-talk values smaller then 2% while imaging different fuorophores with spectral separation of 10 nm. Theoretically it is possible to simultaneously image up to 15-20 different emissive species with emission peaks separated by ∼20 nm [37]. Furthermore, srSMLM can be used in order to perform multi-colour single molecule tracking allowing to achieve ∼10nm spectral resolution and ∼20 ms time resolution [42]. Such abilities of srSMLM can provide high potential for investigation of complex biological processes.

Polarity sensing. An extra information can be obtained by using probes that can specifically target cellular organelles and biomolecules or probes displaying emission spectra variation due to their interactions, conformational variations or in response to environmental properties such as viscosity, polarity or molecular order [47]. One of the solvatochromic probes that can be used in srSMLM technique is Nile Red. This dye was used to investigate hydrophobicity of mammalian cell plasma membrane [36], cholesterol levels in organelle or plasma membranes [40] and to study surface hydrophobicity of protein aggregates[36, 43].

Single molecule spectroscopy. The capability of srSMLM to distinguish minor differences in the emission spectra was used to identify individual molecules [38]. Furthermore, srSMLM was used to distinguish the *cis-trans* isomers of spyropyran molecule, which cannot be done using conventional spectroscopy methods [39]. The same difficulties are arising while studying the conformational changes of biomolecules like BODIPY chromophore [48].

Limitations

There are several major trade-offs for srSMLM, and the first one is photon collection efficiency vs the simplicity of microscopy setup. In most variants of a single-objective setup configurations only a fraction of collected fluorescence emission is used for each of the two channels, which increases the number of frames needed to reconstruct an image, thus increasing the total acquisition time. Moreover, in order to obtain enough signal in each channel the fluorophores are required to possess sufficient photon count and photostability. On the contrary, a dual objective setup allows to increase greatly the number of the collected photons, as the two objectives are able to collect the signal needed for the spacial and the spectral channel independently. However, this enhanced light collection comes at a price of a more sophisticated setup and limitations concerning the possible sample types. Spatial precision vs the spectral precision is another trade-off for srSMLM. Obviously, each of the two parameters will depend on the corresponding fraction of light collected after the emission separation in setups using prisms or gratings. The precision in both channels also depends on the background noise level. Moreover, the signal in the spectral part is more spread than in spatial one, which leads to lower SNR and limited ability to determine the spectral parameters for all the detected localizations. Additional error may be also introduced due to spectral calibration procedure leading to a sub-pixel spectral shift. In

general, the optimal imaging conditions can be varied in a rather broad range and should be optimized depending on the sample, peculiarities of data analysis and the desired outcome.

As a newly developed method, srSMLM improvements are regularly proposed in the literature. At the end of the 'Introduction' chapter we will present the draft of a review manuscript in which we discuss the trends and the most significant latest improvement proposed these last years in srSMLM (because this review will includes two articles which are expected to be published soon : spectral Phasor and srUnet, it is not submitted at the moment).

1.2 NRPSs in *Pseudomonas aeruginosa* pyoverdine pathway

1.2.1 Nonribosomal peptides

Proteins and peptides are key components of life. Proteins are polymers formed by one or more polypeptide chains. Each of these chains consists of a sequence of amino acid residues linked together by peptide bonds. Proteins are almost exclusively produced by a dedicated cellular machinery : the ribosomes. To assemble proteins, ribosomes bind to messenger RNAs and use the mRNA sequences to determine the correct sequence of amino acids to insert into the nascent protein. Amino acids are selected and transported to the ribosome by transfer RNA (tRNA) molecules, which enter the ribosome and bind to the messenger RNA chain via an anti-codon stem loop. For each coding triplet (codon) in the messenger RNA, there is a (almost if we condider wobble base pairs) unique transfer RNA that must have an exact match with the anticodon, and which carries the correct amino acid for incorporation into a growing polypeptide chain. Once the protein is produced, it can then fold to produce a functional three-dimensional structure.

While more than 500 naturally occurring amino acids are known to constitute monomer units of peptides, only 22 amino acids are naturally incorporated into proteins. They are called proteinogenic or natural amino acids. 20 out these 22 are encoded by the universal genetic code (standard or canonical amino acids). Therefore, proteins resulting from the ribosomal machinerie are composed almost exclusively from proteinogenic AA, even if some non-proteinogenic amino acids can be found in proteins resulting from post-translational modifications. On the oposite, a huge variety of building blocks is found in NRPs[49]. Aside from the 22 proteinogenic amino acids, many non-proteinogenic amino acids are found in NRPs which includes notably hydroxy - AA (alpha or beta), methyl -AA (including aminoisobutyric acid) or N-based side-chain aminoacids (like ornithine) [50].

With the exception of achiral glycine, natural amino acids have L configurations. They are the only ones found in proteins during translation in the ribosome. Amino acid residues D are exceptionally present in some proteins. On the oposite, AA with D configurations are regularly found in NRPs. This specifity led to the discovery of NRPS. Indeed, in the early 1960s, short after the ribosomal code had been deciphered, researchers investigating how certain cyclic peptides containing D-amino acids were synthesized showed that the cell-based biosynthesis of tyrocidine was not affected by ribosome inhibitors such as aureomycin (chlorotetracyclin). This discovery led

them to propose a distinct mechanism from ribosomal protein synthesis for producing peptides with D-AA.

This diversity of AA and AA configurations allow the assembly of complex natural products with extensively modified peptide structures. The diversity of non-ribosomal peptides is due to the combination of the ability to incorporate an expanded range of monomers compared to ribosomal peptide biosynthesis but also with extensive modifications of the peptide both during and after chain assembly [51].

Nonribosomal peptides are amongst the most widespread and structurally diverse secondary metabolites in nature. They are usually produced by microorganisms like bacteria and fungi. Many microorganisms rely on nonribosomal synthesis to produce diverse natural products, some of which are related to cellular growth, signaling, nutrient acquisition, quorum sensing and virulence [52, 49]. The broad variety of building blocks used by NRPS allows synthesizing numerous secondary metabolites with wide range of structural and functional diversity, including toxins, pigments, surfactants, phytotoxins, virulence factors, siderophores or molecules with antibacterial activities. NRPs are therefore a unique source of bioactive molecules that can be exploited for therapeutic applications. The usefulness and potential of NRPs as drugs is already demonstrated by nearly 30 NRP core marketed drugs (NRPs or semisynthetically modified NRPs) that contribute to billions of sales in the chemical and pharmaceutical industry. Among them, we can find drugs with antibacterial (penicillin, vancomycin, daptomycin), antitumor (bleomycin), antifungal and immunosuppressant (cyclosporin) activity[50] (Figure 1.2.1) to cite few.

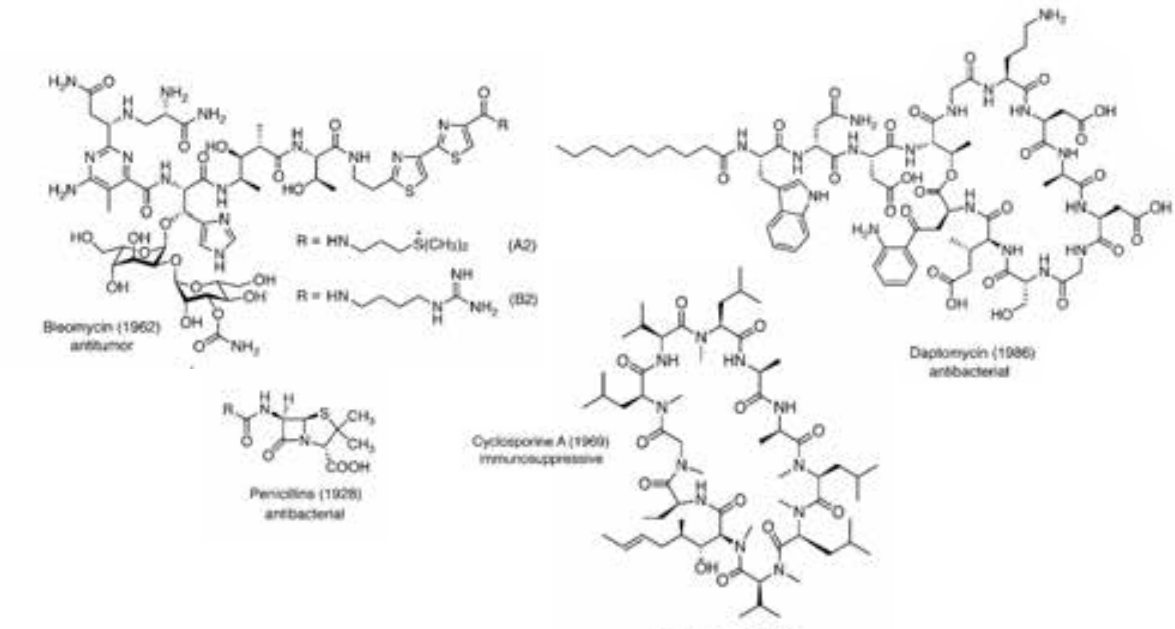

Figure 1.2.1 – Examples of clinically approved peptides synthesized by NRPS or semisynthetic (such as Penicilin) [50]

The NRPs are generally small in size, with linear or cyclic structures. Nonribosomal peptides

are often dimers or trimers of identical sequences chained together or cyclized, or even branched. They often carry modifications like N-methyl and N-formyl groups, or are glycosylated, acylated, halogenated, or hydroxylated. Cyclization of amino acids against the peptide "backbone" is often performed to give protection against proteases. The largest known nonribosomal peptide (NRP) which consist of 25 amino acids is syringopeptin which is phytotoxin produced by *Pseudomonas syringae* [53]. The biosynthesis of this molecule involve the action of three NRPSs.

1.2.2 NonRibosomal Peptide Synthetases

NRPs are synthesized by nonribosomal peptide synthetases (NRPSs). NRSPs are large enzymes with high molecular weights with modules specific for the metabolite they synthesized.

Modular structures and domains

NRPS are generally multimodular proteins, wherein each module is responsible for the activation and coupling of a single amino acid to a growing peptide chain. The number of modules and their domain organization controls the structures of the peptide and usually corresponds to the sequence of amino acids in the peptide. According to this principle (collinearity rule), the biosynthesis of a heptapeptide requires seven such modules.

A minimal module consists of three domains : a condensation (C) domain, an adenylation (A) domain, and a carrier protein [CP] domain, which is often termed a thiolation (T) or peptidyl-carrier protein (PCP) (Figure 1.2.2). These domains harbor the different catalytic centers required for peptide synthesis :

— the adenylation (A) domain for selection, activation, and loading of the amino acid.
The initial step of NRP synthesis is the selection and activation of amino acid substrates. Activation is carried out by the formation of an amino acyl adenylate intermediate through the consumption of ATP and Mg. These functions are fulfilled by the A domain (ca. 60 kDa). The A domains are organised into two subdomains : the central N-terminal domain of about 50 kDa (Acore) and the C-terminal subdomain of about 10 kDa (Asub), which are flexibly connected by a hinge region of about five residues. The specific binding of an amino acid and Mg ATP occurs within the Acore domain close to the Acore–Asub interface. The activated amino acid is then undergoing thiolation.

— the thiolation (T) domain, also referred to as peptidyl carrier protein (PCP) domain
The activated molecule is transferred to the PCP domain where it is covalently binds via thioester linkage to the thiol group of the 4'-phosphopantetheine (Ppant). The holo-T domain with its Ppant extension (about 18 Å) can be considered as the flexible robotic arm of the NRPS assembly line that sequesters and covalently transfers the amino acyl-/peptidyl-thioester intermediates to all catalytic centers [54]. This conformational

flexibility is an essential requirement for the communication and choreography of NRPS domains. The T domain (ca. 10 kDa) adopts a four-helix bundle [55]. The questions of how NRPSs control substrate trafficking with productive directionality is not fully understood. It possibly results from a combination of competitive binding, conformational selection, and synchronized domain movements that may guide substrate migration and catalytic turnover.

— the condensation (C) domain, where coupling to the upstream nascent peptide chain is established

The tethered amino acid is then shuttled to the condensation domain. The C domain (approximately 50 kDa) catalyzes the central coupling reaction of the amino acyl or peptidyl intermediate arising from module n-1 to the α-amino group of the building block attached to module n. The C domain is a V-shaped pseudodimer of an N-terminal (CNTD) and a C-terminal subdomain (CCTD)[56]. The donor and acceptor Ppant arms must enter from opposite sides to reach the conserved active site motif (HHxxxDG). [57]. The mechanism of the C domains is still under debate, since the catalytic impact of the His residue varies markedly for different C domains. Comparison of all currently available C domain structures indicates that there are opening and closing dynamics between the CNTD and the CCTD [58, 59, 56, 60, 61]. C can act as a second proofreading to minimize the error rate - that would help because it becomes more complicated to control the sequence of a growing peptide chain. C domains have major interaction with the intramodule A and T domains as well as the donor T domain of the upstream module. The C domain is also involved in epimerization,[62] cyclization,[63] β-lactam formation, or recruitment[64] of auxiliary enzymes to generate structural homologues with diverse NRPS-relevant functions.

Once NRP synthesis is completed, the termination module the thioesterase (TE) domain (ca. 30 kDa) catalyzes the release of the completed peptide from the NRPS by hydrolysis or aminolysis (in both cases, it liberates a linear peptide). TE domain may also act as cyclases to form a cyclic compound. Once released the peptide can be further modified by additional enzymes. Such modifications are is often essential for molecule bioactivity [65] but can also include minor changes in already functional product. The diversity of the NRPs is also resulting from the various modifications performed by the tailoring domains such as cyclization (Cy), oxidation (Ox), epimerase (E), ketoacyl reductase (KR) and methyltranferase (M) [50, 66].

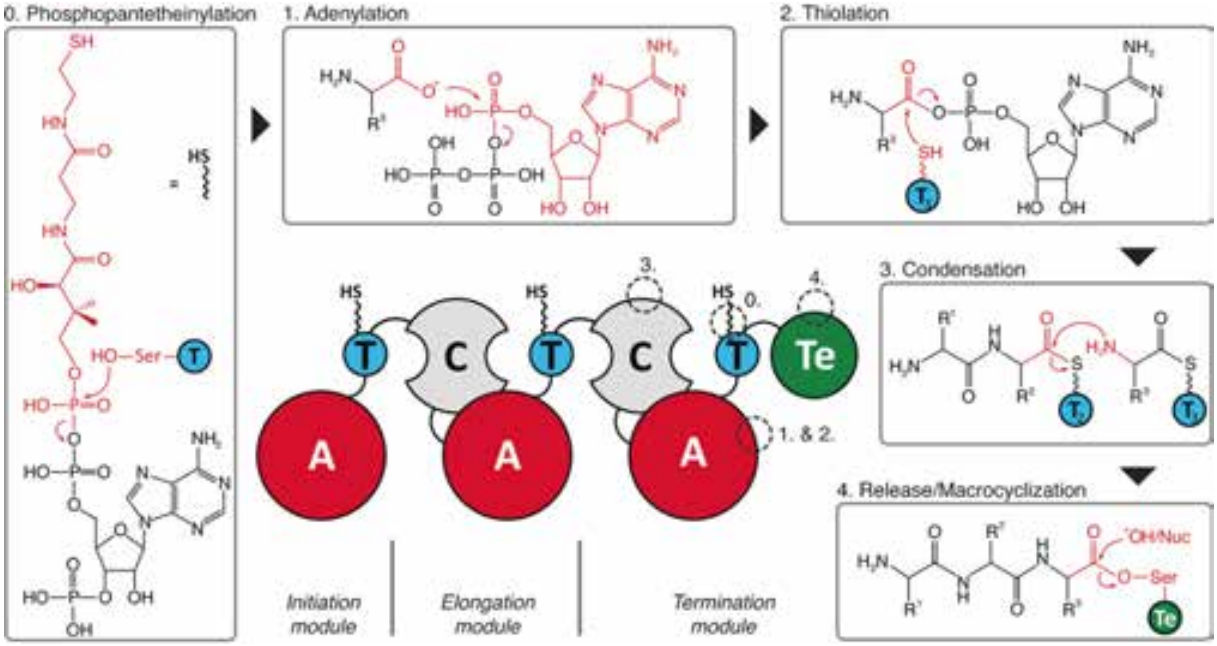

Figure 1.2.2 – Domain arrangement of bacterial NRPSs and their catalyzed reactions.

Worth to notice that unlike to typical modules of the NRPSs the first module is characterized by the absence of C domain.

At the moment, we have a limited understanding of the dynamic regulating the synthesis steps in between the different domains in a module.

Mode of synthesis

The biosynthesis of NRPs can occur in different modes which were classified in three categories.

In the linear mode (Type A) each amino acid is incorporated by a specific NRPS module so that the number of modules is equal to the number of amino acids in the final molecule. The assembly of monomers is done in order of activation, so that a synthetase with "n" modules will assemble a peptide with "n" amino acids. Cyclosporin A, the ACV tripeptide precursor of penicillin and cephalosporin [67] surfactin [68], or vancomycin (Figure 1.2.3, Type A) are synthesized in a linear fashion.

During the iterative mechanism (Type B) the modules can participate several times in the incorporation of amino acids usually resulting in the molecular symmetry of the product. It leads to the formation of a peptide containing repeating units whose number will be greater than the number of modules in the NRPS (Figure 1.2.3, Tybe B). Gramicidin S synthetases [69], enterobactin synthetases [70] and Enniatin synthetases (Figure 1.2.3, Type B) works with iterative mechanism.

In the third, nonlinear mode (Type C) the same domain of the module can be used several times and the arrangement of modules does not correspond to the sequence of amino acids in the synthesized molecule [50, 66]. Type C is characterized by a different arrangement of domains compared to the classical arrangement (C-A-T), or an incorporation of small molecules from another synthetic pathway. Unlike linear biosynthesis, this pathway can lead to internal cyclizations or branching in the final peptide [71]. The most common example of a molecule synthesized by this pathway is vibriobactin [72] (Figure 1.2.3, Type C).

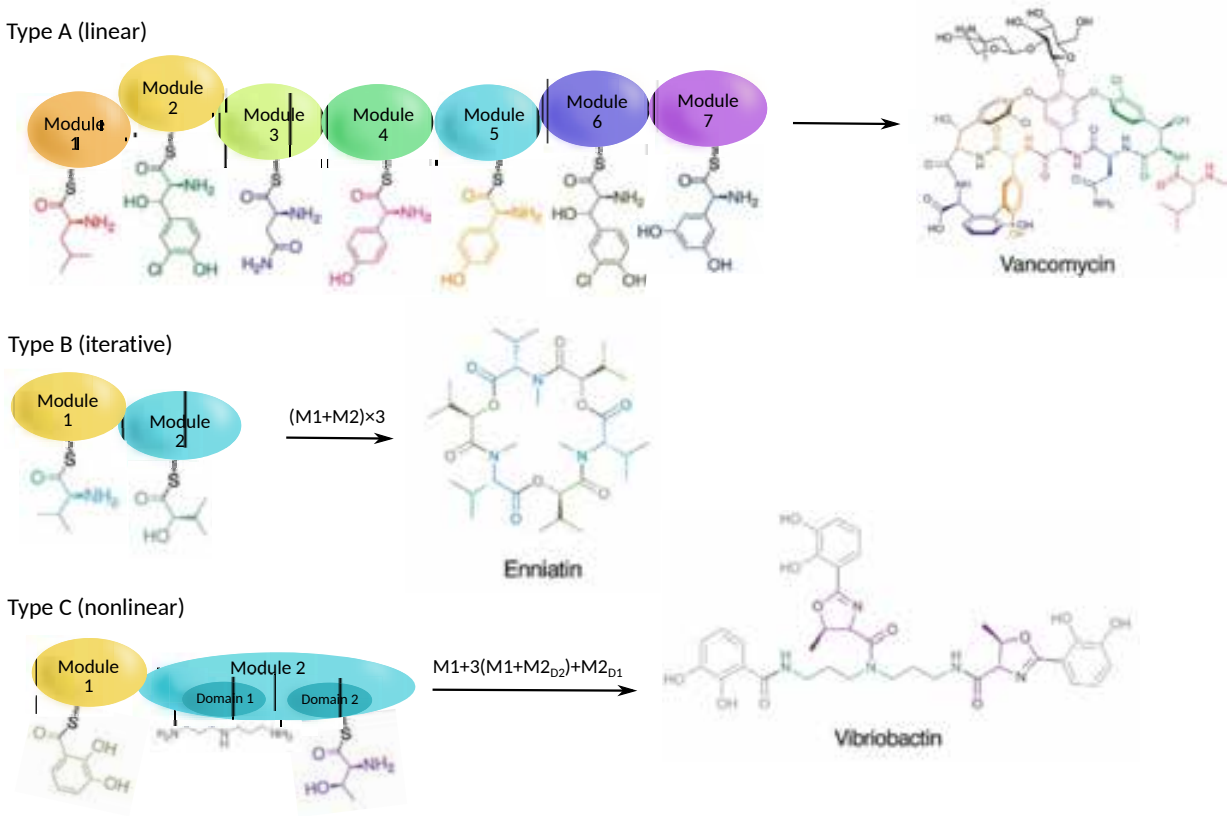

Figure 1.2.3 – Nonribosomal peptides assembling strategies.

To make the view more complex, about 10% percent of bacterial NRPS are not laid out as a single large modular protein, but are produced by separate enzymes [73]. Therefore, in addition to module to module exchange within a single NRPS, the growing AA chains has then to be transferred in between different NRPS. The dynamics and the regulation of the complete "NRPS assembly line" (the sequence of NRPS modules that together assemble a core NRP) is poorly described. A better understanding of the dynamic processes taking place during the NRPs biosynthesis could rationalize the use of NRPS pathways for the production of desired peptides.

Gene clusters

In bacteria, NRPSs coding genes are found within discrete localized sections of microbial genomes in large biosynthetic gene clusters [74, 75] (BGCs). Moreover, NRPs are not directly encoded in the genome, but are rather produced by metabolic pathways encoded by BGCs. Genome mining methods have been developed for predicting the possible NRP sequences from their BGC sequences [76, 77], and vice versa. In additions to that, bioinformatic analysis has also identified conserved signature motifs of the A-domain, useful in genome mining approaches and in the identification of cryptic or silent BGCs [78, 79, 80]. These works led to the conclusion that NRP chemical diversity is much higher than previously estimated [81] and that many more NRPs are still to be discovered.

Interestingly, many chromosomally adjacent genes coding for enzymes producing non-proteinogenic amino-acids are also found in these BGCs and are physically clustered with NRPSs genes. This suggest that since BCG are likely to be expressed and regulate as a whole, all the proteins encoded by the BCGs are then concomitantly expressed - a necessity for complexes to form - or even a way to regulate the presence or absence of complexes

We will now focus on the NRPs found in Pseudomonas.

1.2.3 *Pseudomonas aeruginosa*

Pseudomonas aeruginosa are rod-shaped Gram-negative bacteria which act as an opportunistic human pathogen. These bacteria commonly cause hospital-acquired pneumonia in immunocompromized patients particularly with cystic fibrosis and cancer [82]. *P. aeruginosa* typically infects airway, urinary tract, wounds and also may cause blood infections and may cause chronic infections which can not be treated with traditional antibiotic therapy. Because of their intrinsic resistance to several antibiotics, the treatment of these infections usually includes the combination of several antibiotics. Furthermore, these bacteria demonstrate the ability to develop specific antibiotics resistance after unsuccessful treatment.

P. aeruginosa are capable of producing several toxins such as exotoxin A, which inactivates the elongation factor 2 leading to the inability of cells to synthesize proteins and resulting in cell death [83] and ExoU which causes damage to cell the membrane leading to lysis [84]. Moreover, it was showed that one of the siderophores (pyoverdine) produced by *P. aeruginosa* may function as a toxin while removing iron from the mitochondria [85].

The standard laboratory strain of *P. aeruginosa* - PaO1 - was one of the largest bacterial genome sequenced in the early 2000s with 6.3 million base pairs [86]. Moreover, this genome contains the highest proportion of regulatory genes ~ 500 and about 370 genes involved in bacterial virulence providing high adaptational capabilities.

P. aeruginosa is able to colonize various environments (Figure 1.2.4) thanks to its metabolic biosynthesis diversity, its high resistance to antibiotics and to the number of virulence factors which this bacteria is able to produce.

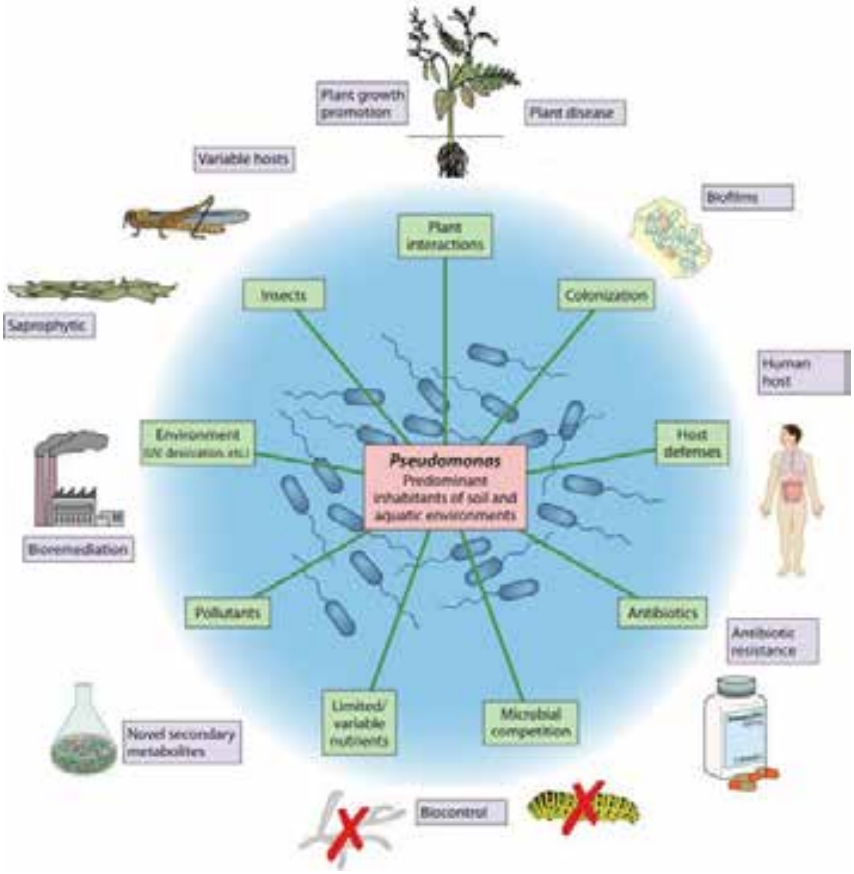

Figure 1.2.4 – Pseudomonas ecological niches (modified from [87])

Pseudomonas NRPs and NRPSs

Pseudomonas species are able to produce a variety of NRPs including virulence factors, toxins and effector molecules.

Various *Pseudomonas* were found to express several NRPs exhibiting antifungal activity such as nunapeptin and nunamycin allowing them to affect the growth and health of plants. The biosynthesis of nunapeptin and nunamycin is catalyzed by three NRPS in collinear manner and other three which does not respect the collinearity rule, respectively [88].

Pseudomonas syringae and other closely related pathovars can also produce a peptide molecule, called tabtoxin. A hydrolytic product of tabtoxin, tabtoxinine-β-lactame, can cause chlorosis in plant cells by inhibiting the plant Glutamate synthetase [89].

Another effector molecule, which can be secreted by the strains of *Pseudomonas syringae pv. syringae (Pss)*, is a product of a mixed non-ribosomal peptide/polyketide synthetase, called syringolin A (SylA). This molecule is capable of irreversibly inhibiting all three catalytic activities of eukaryotic proteasomes throught a covalent binding to their catalytic subunits. [90]

Bacterial cyclodipeptides (CDPs) are the NRPs which influence quorum-sensing of bacteria and play a role in root architecture remodelling in plants.[91]. The CDP production in *P. aeruginosa* depends on the functional multi-modular-NRPS. There are several well characterized NRPs of *P. aeruginosa*, including AMB (L-2-methoxy-trans-3-butenoic acid) which has been shown to inhibit the growth of eukaryotic and bacterial cells. Production of AMB requires a five-gene cluster encoding a putative LysE-type transporter (AmbA), two non-ribosomal peptide synthetases (AmbB and AmbE), and two iron(II)/α-ketoglutarate-dependent oxygenases (AmbC and AmbD). [92]. Under the action of AmbC, AmbD, and tailoring domains of AmbE, L-Glu is converted in AMB.

Another class of molecules, produced in various *Aeruginosa* cells are siderophores. NPSs-produced siderophores include pyoverdine and pyocheline molecules. The pyoverdine biosynthesis pathway involves an action of four NRPSs [93], being one of the biggest NRPS systems in bacteria.

Siderophores

Siderophores are an important family of iron chelating agents that play a key role in bacterial iron homeostasis [93]. Siderophores are produced and secreted by bacteria or fungi under conditions where iron is not widely available. Indeed, although iron is one of the most abundant elements on earth, it is not readily available. In most aerobic environments, (soil, sea, ...) iron exists in its ferric state (Fe^{3+}) , which tends to form insoluble rust-like solids [94]. Similarly, in mammals, almost all iron is bound to proteins such as haemoglobin, transferrin, lactoferrin and ferritin, with very low free concentration of about 10^{-24} mol L^{-1}. As a consequence, during infection, there is a great evolutionary pressures on pathogenic bacteria that compete for iron [93].

Siderophores generally have a molecular weight between 200 and 2000 Da. They are characterized by a very high affinity for ferric iron (Fe^{3+}) [95]. The major groups of siderophores include catecholates (phenolates), hydroxamates and carboxylates (e.g. derivatives of citric acid). Citric acid can also act as a siderophore [96].

Along with their secretion, bacteria express transporters on their cell surface able to uptake these molecules complexed to iron [97, 98, 99]. Siderohores belongs to the large family of virulence factors as they are helpful for infection.

In bacteria, the main representative siderophores are enterobactin (*E. coli*), salmochelin (*Salmonella*) or pyoverdine (*P.aeruginosa*).

Pyoverdine (PVD) molecule comprises of 11 amino acids and is able to chelate ferric iron with an affinity of 10^{32} M^{-1}. PVD is produced in conditions when iron deficiency greatly increases and it appears to be a primary siderophore that plays significant role in infection process.

Pyocheline molecule is smaller (3 amino acids) and exhibits smaller affinity to iron(10^{18} M^{-1})[100]. This kind of siderophores, which are expressed when the access to iron is not highly limited, are considered as 'backup' systems, also called 'secondary siderophores'[101].

1.2.4 Pyoverdine pathway

The biosynthetic pathways of PVDI and PCH produced by *P. aeruginosa* have been extensively investigated (see [93] and references herein).

PVD is produced in conditions when iron is deficient and it appears to be a primary siderophore that plays significant role in infection process.

P. aeruginosa strains can produce four specific pyoverdines - PVDI, PVDII, PVDIII and PVDIV, which possess different peptide chain. For each of these molecules these is a corresponding transporter expressed on the outer membrane - FpvAI, FpvAII, FpvAIII and FpvAIV. In case of PVDI, produced by *P. aeruginosa* PaO1 strain (Figure 1.2.5), the biosynthesis steps were widely investigated and all the enzymes involved were characterized.

The PVDI precursor is assembled in the cytoplasm by four NRPSs : four-modular PvdL and PvdI and two-modular PvdJ and PvdD (Figure 1.2.5, 1.2.6) [93]. Each module performs an activation of one specific amino acid and incorporates it into the precursor peptide chain, thus forming a backbone of 11 amino acids (Figure 1.2.6). This intermediate molecule is transferred from PvdL to PvdI, then to PvdJ and finally to PvdD. In addition, the biosynthesis of PVD precursor involves three smaller enzymes - PvdA, PvdF and PvdH, which are responsible for generation of the two non-peptidogenic amino acids present in the PVD molecule.

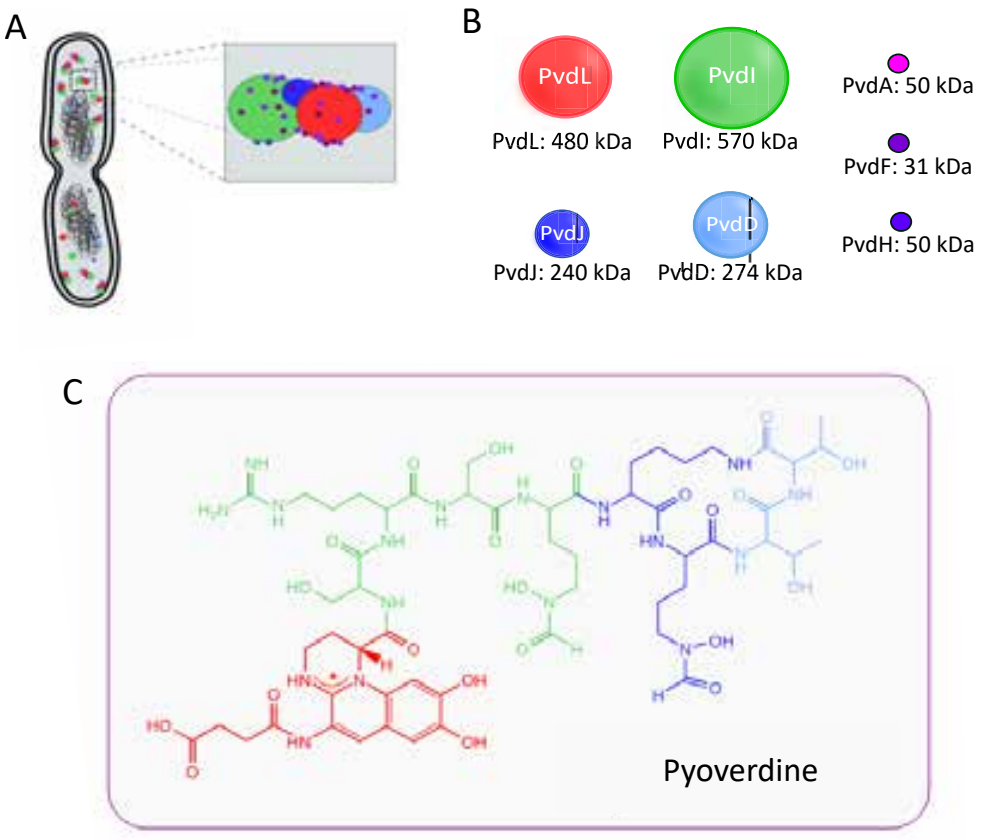

Figure 1.2.5 – **A**. Hypothetic organisation of NRPS involved in pyoverdine pathway of *P. aeruginosa*. **B**. Enzymes involved cytoplasmic in PVDI precursor synthesis. **C**. The structure of PVDI molecule (color code corresponds to NRPS enzyme responsible for the synthesis of this part)

At the first stage of biosynthesis the first module of PvdL introduces a myristic or a myristoleic acid chain, which is supposed to keep the PVD precursor at the inner membrane during its assembly [102]. M2 and M3 modules of PvdL bind L-Glu and L-Tyr is isomerized to D-Tyr. The M4 module adds an unusual amino acid, L-Dab, provided by PvdH.

The second NRPS involved in the synthesis is PvdI. Its first three modules add $_D$-Ser, $_L$-Arg, $_D$-Ser amino acids, respectively. The fourth module is responsible for incorporation of a second unusual amino acid, $_L$-fOHOrn synthesised by PvdA and PvdF. Next, PvdJ M1 module adds $_L$-Lys followed by the addition of a second $_L$-fOHOrn by M2 module.

At last, PvdD incorporates two $_L$-Thr in the sequence. M2 module also catalyzes the hydrolysis of PVD precursor from the NRPS together with the cyclization of the sequence.

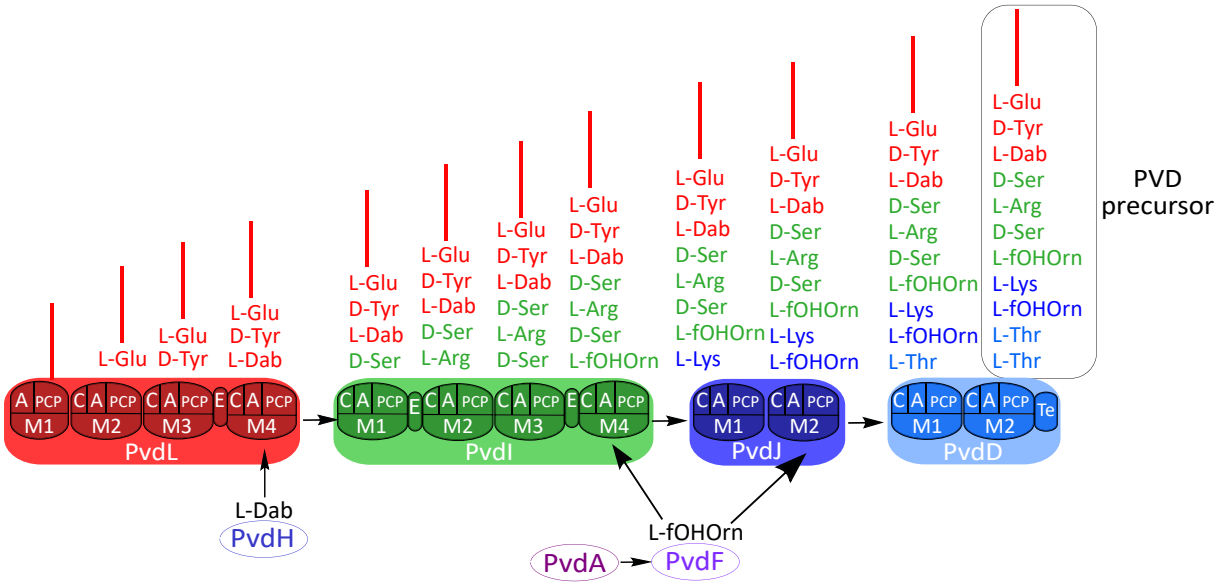

Figure 1.2.6 – Assembly of PVD precursor in the cytoplasm. It is synthesized by four NRPS (PvdL PvdI, PvdJ and PvdD). Each enzyme is composed of modules (M) which in turn are composed of different domains including adenylation (A), condensation (C), peptidyl carrier protein (PCP), epimerization (E) and thioesterase (Te). Each module incorporates one specific amino acid into precursor peptide chain

This 11 AA peptide sequence is a precursor of the maturated PVD. This peptide is transported to the periplasm by the inner membrane transporter, PvdE[103]. In the cytoplasm, the non-fluorescent PVDI precursor is modified by five small enzymes (PvdQ, PvdP, PvdO, PvdN and PtaA)[93]. PvdQ is responsible for removing the myristic or myristoleic acid. PvdP and PvdO are known to play the central role in fluorophore formation from $_L$-Dab and $_D$-Tyr[104, 105]. The last modifications are done by PvdN and PtaA leading to different isoforms of PVD that are not essential for pyoverdine function.

After the periplasmic maturation, PVDI is finally secreted into the extracellular environment by the efflux pump PvdRT-OmpQ[106] (Figure 1.2.7).

In the extracellular environment, and even in the presence of very low concentrations of iron, pyoverdines are able to chelate Fe^{3+} to form ferri-pyoverdine. The Fe-PVD complex can be recognized and internalized by the outer membrane receptor, FpvA. This uptake process is energized by the TonB periplasmic protein[107]. Once in the periplasm the Fe^{3+} is reduced to Fe^{2+}[104] - by a network of five interacting proteins composed of two inner-membrane proteins, FpvG (iron reductase) and FpvH (unknown function), and three periplasmic proteins, FpvJ (unknown function), FpvF (periplasmic PVDI-binding protein), and FpvC (iron periplasmic-binding protein)[108] - to release Fe and recycling the free pyoverdine. Finally, Fe is transported by FpvE into cytoplasm (Figure 1.2.7).

Together, there are more than 20 proteins expressed in the pyoverdine pathway. Due to the high

number of proteins involved, and to minimize the cost, all these proteins have to be regulated to control their concomitant expression.

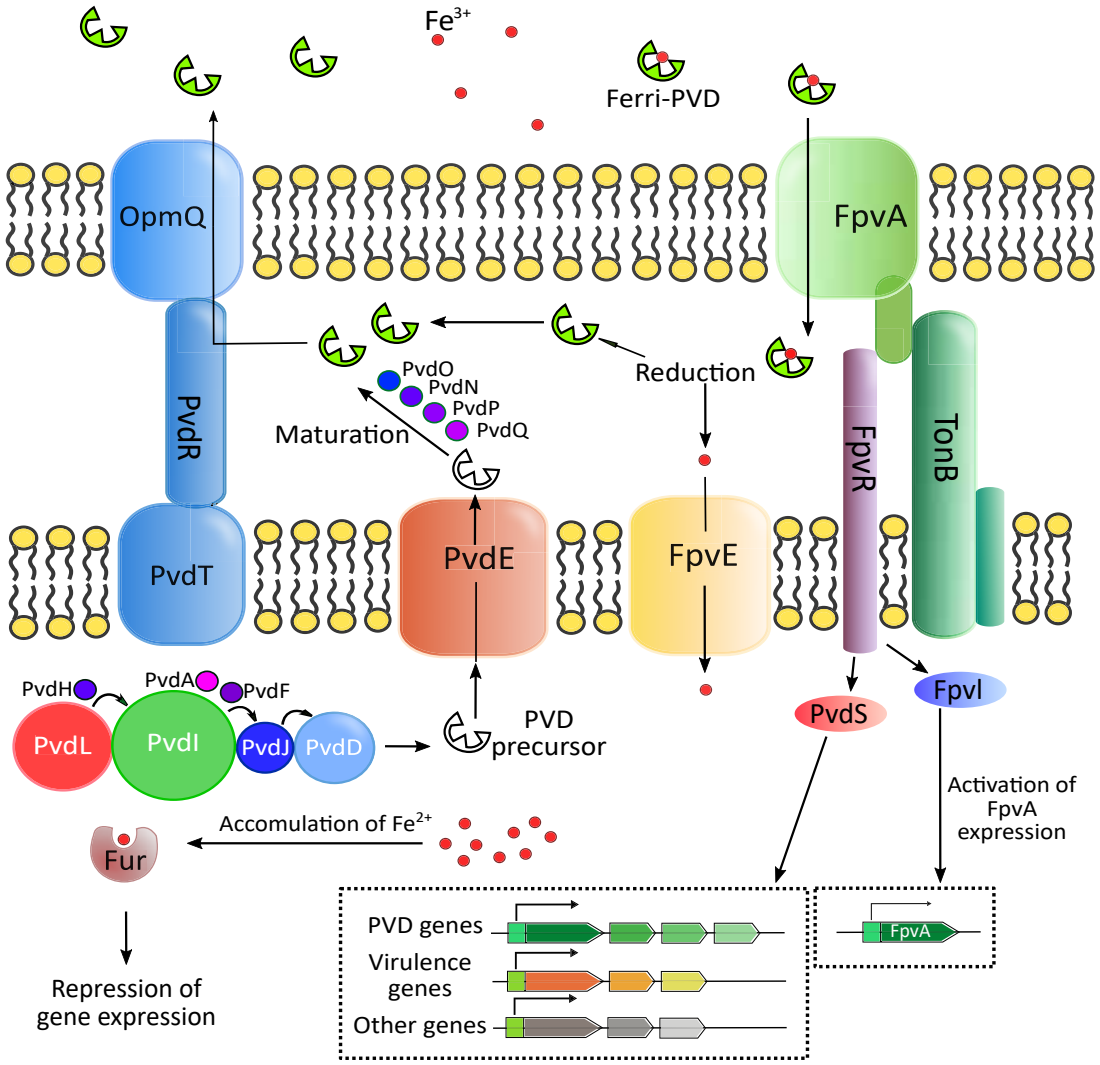

Figure 1.2.7 – Steps of pyoverdine expression and uptake. PVD precursor is synthesized by four NRPS and transported to periplasm by PvdE. In the periplasm it undergoes maturation and fluorophore is formed. Next PVD is exported by PvdRT-OmpQ system where it can chelate iron. Ferri-PVD complex can be recognized by FpvA and transported into periplasm which involves TonB activity and leads to release from FpvR two sigma factors which induce PVD, virulence and FpvA genes transcription. In the periplasm the iron is released from PVD and the molecule can be secreted again.

Expression and Regulation

Most of the genes involved in the PVD pathway are clustered in a BGC (Figure 1.2.8). Then most of these genes are sharing similar promoters, transcription factors or repressor and are

likely expressed or repressed quite similarly. Such BGC makes it the possible for the bacteria to switch on or off all the machinery from the PVD pathway. NRPS expression of the PVD biosynthetic pathway can be finely activated or repressed experimentally - mostly by controlling the concentration of iron in the growing media.

Indeed, the expression of genes encoding most of the proteins of the PVD pathway is under the control of the ferric uptake regulator (Fur). If the intracellular iron concentration is sufficient, free Fe binds to Fur forming a complex. Fur-Fe^{2+} interacts with a conserved sequence in the promoter region repressing gene expression of the cluster of genes. This single repression is able to switch off the complete pathway to prevent its expression in the presence of iron.

In case of decrease of the level of iron, the repression by Fur can be removed - allowing genes to be expressed at basal levels. Interestingly, an activating loop exists which allow achieving high levels of pyoverdine production. This mechanism starts with the binding of ferri-PVD complex to the outer membrane transporter FpvA (Figure 1.2.7). The uptake process which involves TonB activity lead to liberation of two sigma factors - PvdS and FpvI - which are otherwise sequestered by the inner membrane anti-sigma factor, FpvR[93]. FpvI activates FpvA expression, while PvdS activates the transcription of all the other PVD genes. PvdS is also responsible of the activation of the expression of virulence-related genes such as the protease PrpL and the exotoxin A[109]. If PVD is unable to chelate iron in the outer space and no Fe-PVD complex are sens at the FpvA level, FpvR blocks again almost all PvdS and FpvI, stopping the transcription of all these genes to keep only a basal levels of genes expression.

One unique particularity of this regulation loop is the extracellular step of PVD excretion/uptake, adding a spatial input into the model. Outside the cell, PVD is behaving as a public good able to diffuse in the vicinity of the producing cell and can benefit to other cells including non-producing ones. The concentration of Ferri-PVD can thus be seen as a proxy for sensing iron in the environment but also for remotely sensing neighboring producing bacteria density and/or to sense for environmental conditions like diffusion or flow, allowing cells to avoid the secretion of costly molecules under conditions where they would quickly diffuse away [110]- ultimately leading to fitness cost minimization. The information provided by the extracellular concentration of Ferri-PVD molecules is responsible for large-scale changes in NRPS gene expression and is a critical part of the mechanistic understanding of NRPS expression collective regulation.

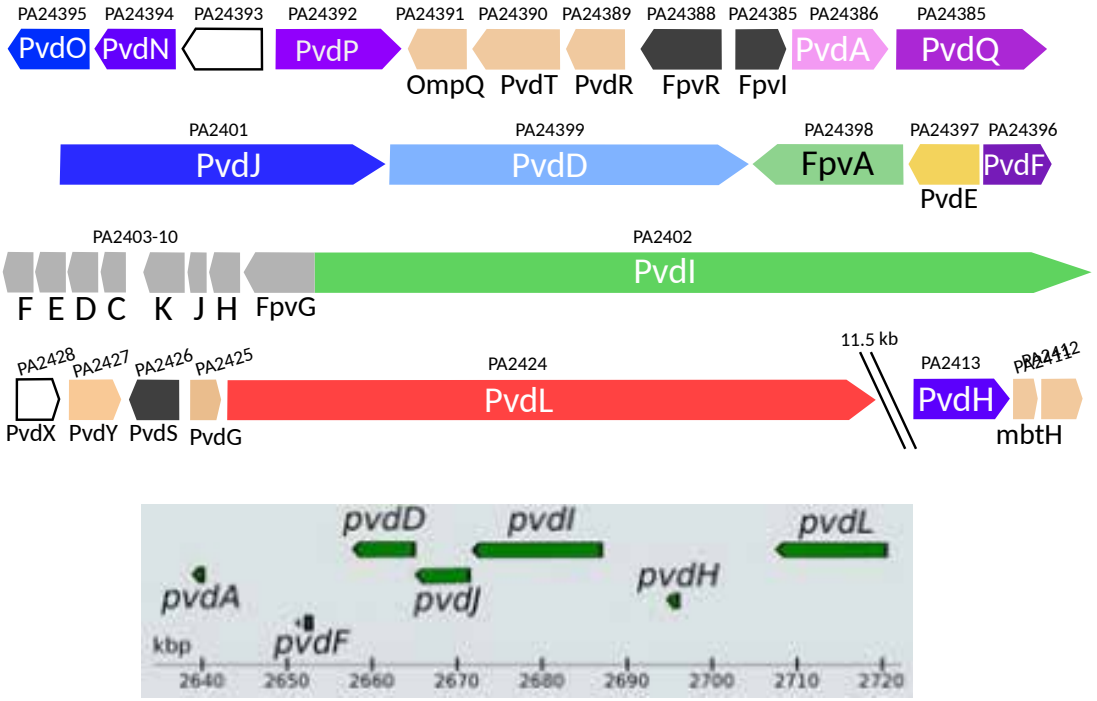

Figure 1.2.8 – Organization of PVDI genes in *P.aeruginosa* PaO1 genome and focus on the NRPS genes (see section 1.2.4 for more details). The genes coding for enzymes involved in pyoverdine biosynthesis and transport are represented in color boxes.

Space and time organization

The pyoverdine production and the expression of the proteins of the PVD pathway is highly demanding in term of metabolism - so that the expression levels and activity of all the enzymes involve have to be precisely regulated to optimize fitness.

Synthesis of the precursor of the PVD requires the coordinated action of seven specific cytoplasmic enzymes - including four NRPS (PvdL, PvdI, PvdJ, PvdD) expected to act in a time-line manner. It has been proposed that all the enzymes involved in synthesis of PVD cytoplasmic precursor may form so called siderosomes[111, 112] , a multi-enzyme complexes in which the organization depends on interaction between the proteins[93]. Such complex, that may form when all the genes are simultaneously expressed, might gather all the necessary enzymatic properties for an efficient synthesis of the PVD precursor in the cytoplasm. But so far existence of siderosome has not been directly demonstrated in cells, likely because the study at the molecular-level of protein-protein interactions dynamic in living cells is challenging and because siderosomes might be transient.

It has been shown that PvdA physically interacts with M2 module of PvdJ by two-hybrid and pull-down assays. Moreover, pull-down assay showed weak affinity of PvdA for M4 module of

PvdL[112]. The dynamic and transient interaction of PvdA with PvdL and PvdJ enzymes was suggested based on a small fraction of these proteins trapped by PvdA proteins used as a bait. The interactions of PvdA with four NRPS were also investigated by FLIM-FRET. This work showed that PvdA interacts not only with PvdI and PvdJ, the enzymes which use modified amino acids produced by PvdA, but with all the four enzymes in PVDI pathway[113].

One of the attempts to confirm the presence of siderosomes was performed by confocal microscopy. The protein complexes are mostly detected at the cell poles (Figure 1.2.9) in early exponential phase but appeared more homogeneously distributed during late exponential and stationary phases. It was suggested that the enzymes of the PVD pathway are spatially organized while clusters of PvdA are colocalized with PvdL, PvdJ and PvdD [112]. However, the limited resolution in classical fluorescence microscopy does not allow to obtain accurate localization information leading to inability to correctly interpret colocalization experiments.

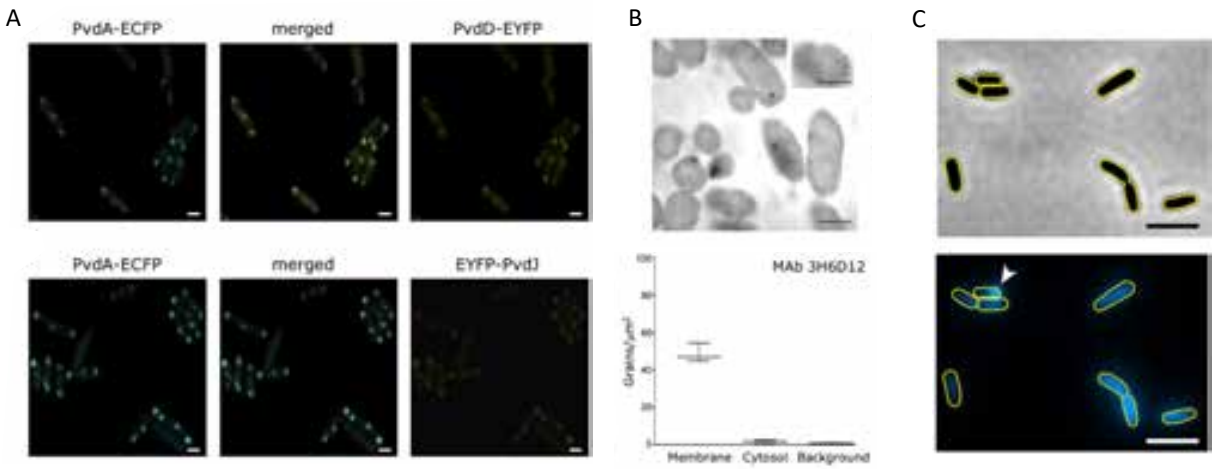

Figure 1.2.9 – **A**. Images obtained by confocal microscopy showing that enzymes are mostly located near the cell pole where PvdA colocalizes with PvdD (upper images) and PvdJ (lower images) [112]. **B**. Immunoelectron microscopy images showing membrane localization of PvdA [112]. **C**. Phase contrast (upper) and fluorescence microscopy images showing that PvdA is homogeneoustly distributed in the cytoplasm and only some bacteria present the fluorescent spots on the pole [113].

The diffusion properties of the protein in live cell can provide the information about interactions due to lower diffusion coefficients for complexes of proteins. The dynamics of PvdA was investigated by FRAP and sptPALM. FRAP, a technique that allows to retrieve diffusion coefficients by photobleaching the region and measuring the rate of fluorescence recovery. The diffusion rate of PvdA was found to be lower than predicted suggesting that PvdA in cytoplasm is bound to the complexes[111]. This was confirmed by sptPALM experiments but the results also showed that diffusion of PvdA can be better described by two diffusive populations, trapped (∼15%) and diffusing that is in line with nature of siderosomes which can associate and dissociate in vivo[113, 93].

Immunoelectron microscopy experiments showed that PvdA was mostly detected close to the membrane (Figure 1.2.9). Besides, PvdA can be associated with the inner membrane due to hydrophobic, inner-membrane-anchoring domain at the N terminus[112]. Together with myristic acid chain introduced at the first step by M1 module of PvdL this led to suggestion that PVDI is synthesized by siderosomes associated with the inner membrane. In addition it has been reported that ∼50% of PvdL and PvdI and ∼20% of PvdD and PvdJ were associated with *P. aeruginosa* membrane[112].

Although, the PvdA diffusion and its interactions with four NRPSs were investigated, the clear characterization of NRPSs complexes is still missing. The proposed siderosome organization probably results in highly dynamic or transient formation imposing difficulties in capturing its sub-cellular organization. Thus methods with high spatial and temporal resolutions are required in order to capture NRPSs in cells.

The siderosome concept, proposing a sub cellular compartmentalization of secondary metabolic pathway in prokaryotes is a new view of the cellular organization of Gram-negative bacteria. Multi-enzyme organization is certainly not specific to siderosomes but a general mechanism in bacterial cells producing toxins or any substance potentially poisonous. This project is thus expected to provide exciting opportunities regarding the characterization of other non ribosomal bacterial metabolite pathways, including those leading to other antibiotic - of which some could be of interest like new antibiotics.

1.3 Deep Learning techniques in microscopy

There are many microscopy images processing methods such as feature extraction, classification, segmentation etc. which may include specific analysis and sophisticated calculations. In classical programming every step has to be defined by human, which means that the analysis process, error checking and consideration of all the possible decisions needs to be done to anticipate any problem. Subsequently, the data is processed according to the rules defined by the programmer in order to obtain the desired results. Therefore, conventional methods require significant amount of time or involvement of computational experts.

The rise of machine learning methods allowed to change the programming paradigm so that it became possible to obtain the rules at the output by providing the input data and the expected results [114] (Figure 1.3.1).

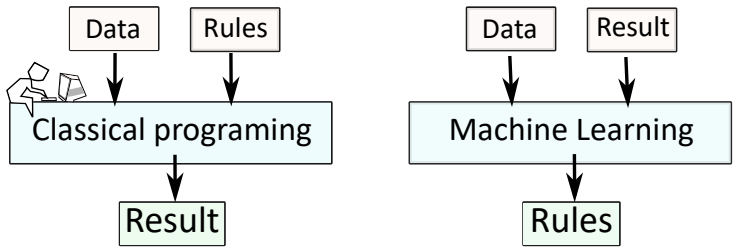

Figure 1.3.1 – The difference between classical programming and machine learning

Deep learning methods are a part of a broader category of machine learning. The main difference between these methods lies in the number of layers of representation in the deep learning models. The 'depth' of the model represents the number of layers which contribute to the model training.

These last years, machine learning and deep learning have found increasing applications in microscopy [115].

1.3.1 Machine Learning

Machine learning in general includes algorithms and computational models developed to allow computers to work on specific tasks based on previous experience and example data. The algorithms are 'learned' to make predictions without being explicitly programmed for this[116].

Machine learning basic principle

The most common tasks in machine learning are classification and regression. In Classification, the algorithm is learning to specify to which of categories the input belongs to. The common

example of classification problem is object recognition such as a classical exercise of dogs and cats discrimination in input images (Figure 1.3.2).

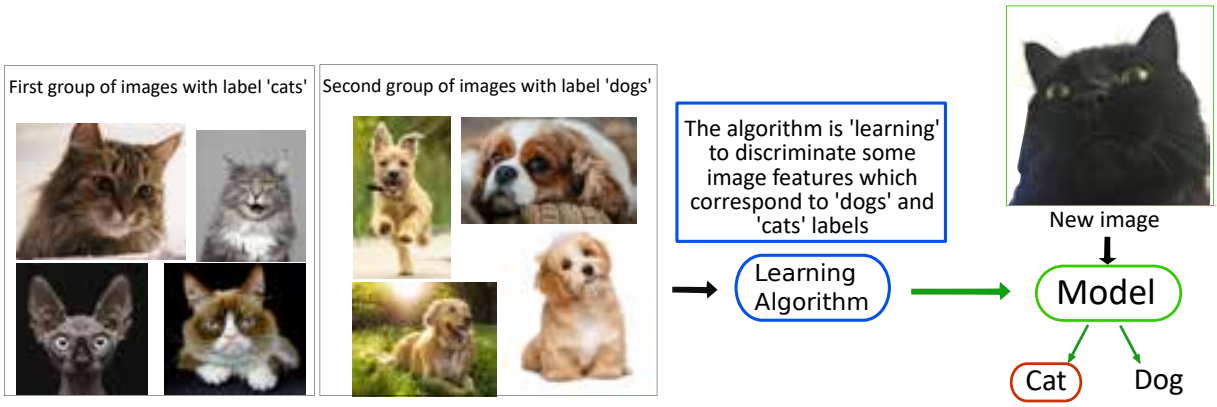

Figure 1.3.2 – The working principle of machine learning application for the classification task. Two groups of labeled images containing cats and dogs are used as an example (training) set. The term 'labeled' means that for each image there is a corresponding value indicating the group to which this image belongs to. The algorithm is 'learning' the statistical rules to associate the specific image to specific label with minimal error. Afterwards the trained model can be used to specify to which group a new input image belongs.

In regression tasks the algorithm is predicting a numerical value as an output. The classical examples of regression task are prediction of house prices depending on some features, or understanding relationship between drug dosage and effect on the patient etc.

In machine learning , a training data set is required in order to train the algorithm. This set contains the example data composed of input values and required output, also called the ground truth values. The training set is used to fit the parameters of the model. At the output this model provides a so called hypothesis containing the trained parameters which then can be used to predict values or categories for new data.

For example, let's consider x-y plane which contains some dot values. (Figure 1.3.3, A). To be able to predict an $\hat{y}$-values for any new x-values we need to train an algorithm.

The hypothesis produced at the output of the algorithm contains the parameters θ_0 and θ_1 of the model (equation 1.4).

$$function \quad h : x \rightarrow y \qquad \mathbf{h}(x) = \theta_0 + \theta_1 x \tag{1.4}$$

The model training is the process during which the model parameters are optimised to get the best fit to the training data. The optimisation is done by minimising a so called loss function (Figure 1.3.3, B) which basically represents the difference between the obtained hypothesis and the input data, measuring how well the model is able to predict the required values (equation 1.5).

$$J(\theta) = \frac{1}{m} * \sum (h(x) - y)^2, \qquad m - number\ of\ samples \tag{1.5}$$

Thus, the closer to the minimum J(θ), the more precisely the hypothesis describes the data. During an optimization process the loss function should decrease with every iteration. The model training eventually stops at the moment when the minimum of the loss function for all the parameters is reached. The final obtained hypothesis (Figure 1.3.3, C red line) then can be used to predict an $\hat{y}$ value for a new input x (a green dot which corresponds to value x=6 on the Figure 1.3.3, C).

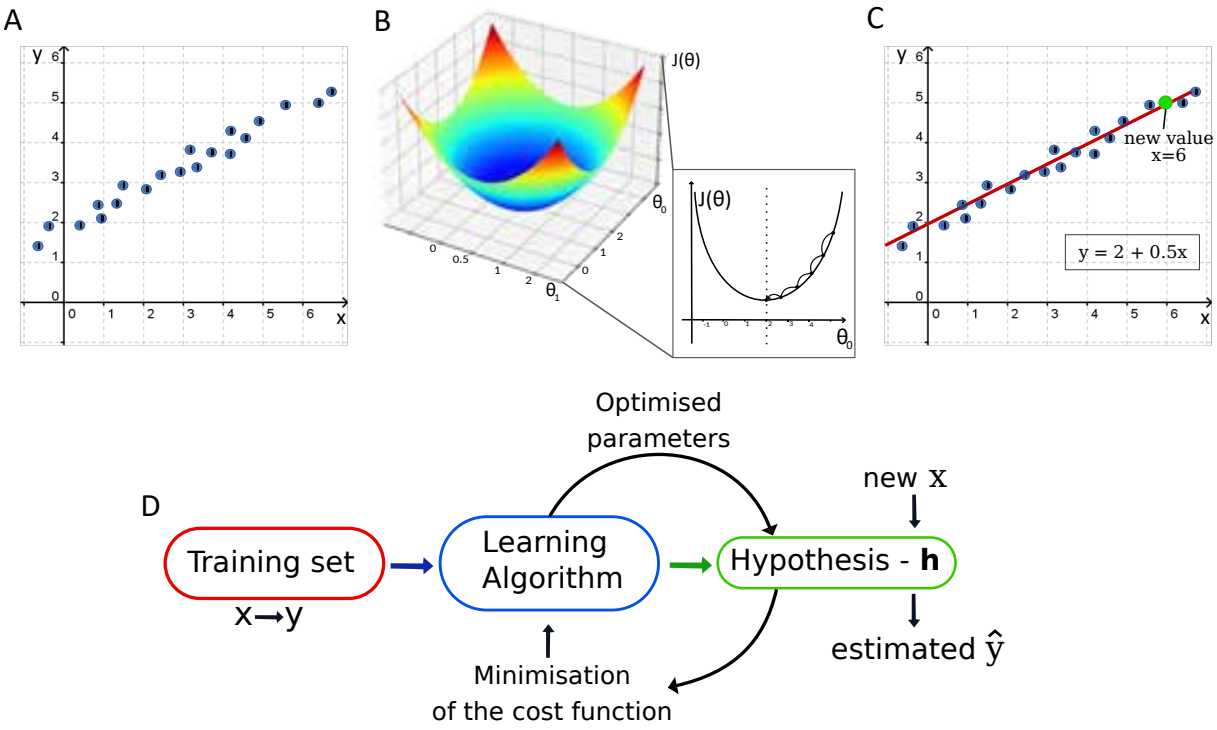

Figure 1.3.3 – **A**. The data set containing x and y values is used as an example to train the algorithm. **B**. The loss function minimization. In our example the loss function is optimized for two parameters θ_0 and θ_1. It can be represented as a 2D surface featuring a minimum, which corresponds to the combination of optimal values for the two parameters. **C**. The linear hypothesis (red line) is fitted to the data set. The y value can be predicted for a previously unseen x = 6 value (green dot). **D**. The scheme representing the process of machine learning. A training set is provided to the algorithm, the algorithm provides at the output the function called a hypothesis. The parameters contained in the hypothesis are optimized by minimizing the loss function until the minimum of the loss function is reached. Then the hypothesis can be used to estimate/predict the new values.

In the basic example above the data can be described by a linear function making it similar to simple linear regression task. Usually machine learning algorithms are not used for these kind of tasks because the rules can be easily defined by human. In reality, the hypothesis may take

various complex forms (that could for example be better described by a polynomial model like in 1.6).

$$\mathbf{h}(x) = \theta_0 + \theta_1 x_1 + \theta_2 x_2^2 + \theta_3 x_3^3 + ... + \theta_m x_m^m \tag{1.6}$$

In general, steps involved in classification and regression tasks in machine learning are quite close except the produced output which can take discrete (0, 1 or intermediate values indicating the probability of belonging to one of the classes) for classification task or continuous values in regression task (it has also implications on the loss function to minimize).

Despite their name, machine learning methods are not entirely autonomous and limited in their ability to process raw natural data. Machine learning methods are limited in the operations which they can be applied to transform the data by the predefined set. These techniques actually require human intervention on the step of feature extraction and data preparation, for example giving the labels in the task of dogs and cats discrimination and transforming the data into suitable representation [117].

1.3.2 Neural networks and deep learning

Neural networks (NN) have emerged as a more sophisticated group of methods aimed at solving more complex tasks. Inspired by biological neural networks artificial NN were developed in order to achieve more autonomous 'learning' [117] and to be independent of a predefined set of available data transformations.

Similarly to machine learning, the input data (x) and the corresponding ground true values (y) are required for the neural network to learn. However, in the NN a so called 'hidden layer' is present between the input and the output layers. This hidden layer can not be directly observed from the inputs and outputs of the system but it pays the central role by allowing the network to learn complex non-linear problems.

Let's consider the simplest neural network comprising an input layer which contains x_1, x_2 values, one hidden layer with only one unit and the output layer (Figure 1.3.4, A). In the hidden layer the a_1 is calculated by summing biases and the weighted values of x_1 and x_2 and calculating an activation function (f_a) of this sum (equation 1.7). The activation function transforms the values at the unit output into values of some range : $[0, 1]$, (sigmoid), $[-1, 1]$ (tanh), $[0, \infty]$ (relu), etc. The choice of activation function has a large impact on the capability and performance of the neural network. This function is used to introduce a non-linearity into network which is required to learn from the data more complex patterns because otherwise each unit would introduce only linear transformations on the input data using weights and biases [118].

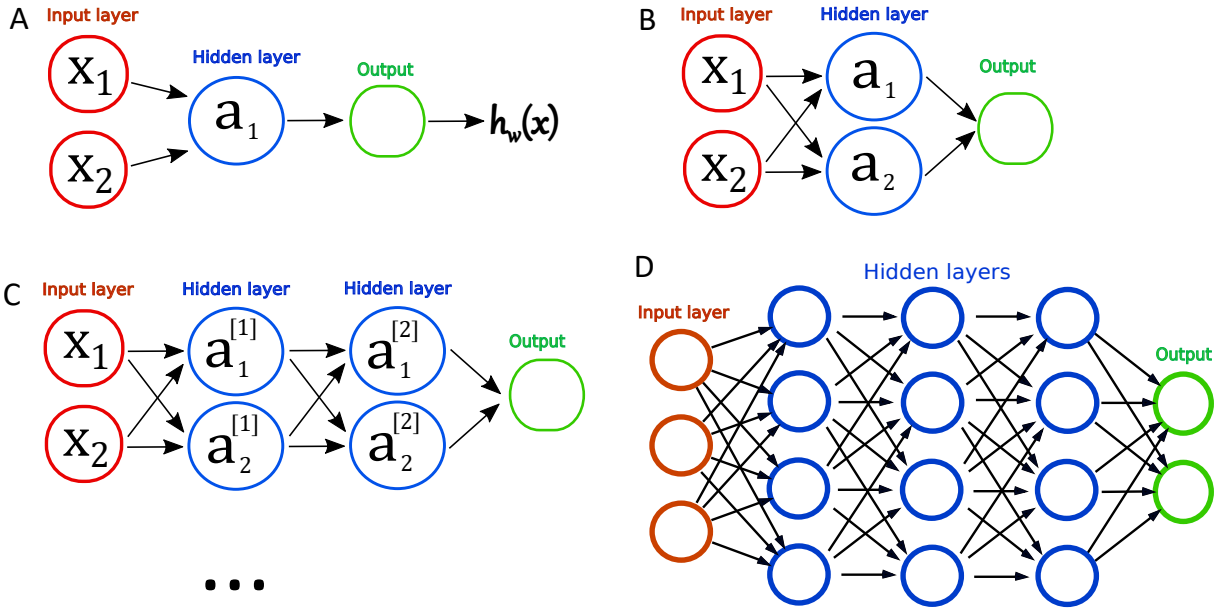

Figure 1.3.4 – **A**. The simplest example of neural network is the one layer NN with one unit in hidden layer. **B**. One layer NN with two units in hidden layer. **C**. Two layers NN with two units in each hidden layer. **D**. An example of a more complex NN architecture.

$$\begin{matrix} x_1 \rightarrow w_1 x_1 + b_1 \\ x_2 \rightarrow w_2 x_2 + b_2 \end{matrix} \implies a_1 = f_a(w_1 x_1 + b_1 + w_2 x_2 + b_2) \implies h = a_1 \implies \textit{Loss f.} \quad (1.7)$$

In the equation 1.7 the output h is equal to a_1 and the loss function can be calculated similarly to 1.5. The process of direct calculation of the output and loss function is also called a *'forward propagation'*.

In order to use the network for solving more complex task, an additional unit can be added to the hidden layer (Figure 1.3.4, B). Thus in the hidden layer two a-values need to be calculated for each unit. Then the equation will take the form of 1.8 (starting for here the biases - b are dropped). For each of two units a separate set of weight is utilised and the output is obtained by calculation of activation function of the weighted sum of a_1 and a_2 values.

$$\begin{matrix} a_1 = f_a(w_{11} x_1 + w_{12} x_2) \\ a_2 = f_a(w_{21} x_1 + w_{22} x_2) \end{matrix} \implies h = f_a(w_1 a_1 + w_2 a_2) \implies \textit{Loss f.} \quad (1.8)$$

Single-layer NN can be used to treat the data which is linearly separable [119]. Theoretically, the network with one hidden layer which contains sufficient number of units for the prediction of any function [120, 121]. Nevertheless, the number of units in this layer may become enormously large resulting in an inability of the network to represent this function and learn. The number

of units in one layer can be reduced by adding more layers to the network, or in other words by creating a deeper model [122].

To make the previous network (Figure 1.3.4, B) deeper a second hidden layer with two units can be added. In this case a_{11}, a_{12}, a_{21}, a_{22} need to be calculated (equation 1.9)

$$\begin{matrix} a_{11} = f_a(w_{11}^{[1]}x_1 + w_{21}^{[1]}x_2) \\ a_{12} = f_a(w_{21}^{[1]}x_1 + w_{22}^{[1]}x_2) \end{matrix} \Longrightarrow \begin{matrix} a_{21} = f_a(w_{11}^{[2]}x_1 + w_{21}^{[2]}x_2) \\ a_{22} = f_a(w_{21}^{[2]}x_1 + w_{22}^{[2]}x_2) \end{matrix} \Longrightarrow h = f_a(w_1a_1 + w_2a_2) \Longrightarrow Loss\ f. \tag{1.9}$$

The size of input and output layers depends on the entry data and the required output, respectively. The numbers of required hidden layers and units are chosen depending on the task and can take a variety of shapes (as an example Figure 1.3.4, D). Despite the different methods used there is no exact rule how to create an optimal network architecture [123]. Thereby, frequently an architecture is chosen by the previous experience (the networks which were already used for similar kind of tasks).

The model is 'trained' when the parameters are adjusted so that the loss function (the difference between the output and the true target) is minimal. In order to train the network all the weights are adjusted by a little bit at each *training loop* (Figure 1.3.5) so that the new values lower the loss function. This process is performed by an 'optimizer' and is called the 'backpropagation'.

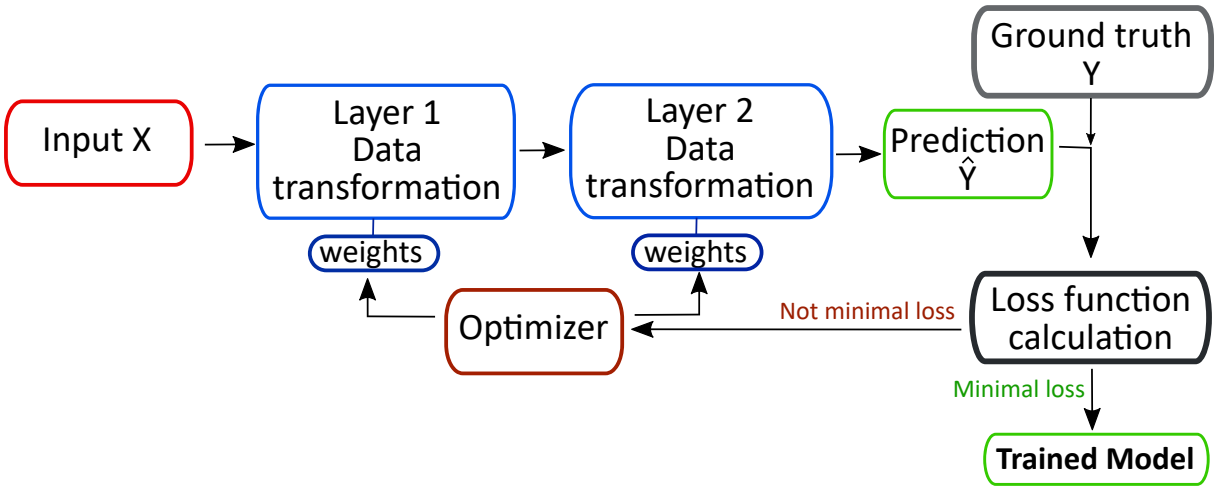

Figure 1.3.5 – The scheme of network training. The input data is given to the hidden layers of the network. At the output the network produces a prediction, which is then used to calculate the loss function. The loss function represents how close is the prediction to the target ground true value. If the loss function is not minimal the optimizer is used to slightly adjust the weights in the direction of loss function decrease. When the loss function acquires its minimal value the model is considered trained and can be used to make predictions.

During the backpropagation procedure the gradients of a loss function are computed with respect

to the weights (and biases). Thus for each single input-output example the weights are slightly updated with the step which can be optimized by the learning rate (equation 1.10).

$$w \leftarrow \quad w - \alpha \frac{d(Loss(w))}{dw}, \qquad \alpha \text{ - } learning\ rate \tag{1.10}$$

1.3.3 Convolutional neural networks

The convolutional neural networks (CNN) were mostly applied for array data. This may include 2D arrays as images, 1D arrays (signals, text, ...) or 3D arrays as video or volumetric images [124].

The main component in CNN are convolutional layers which contain a filter or kernel, an array of weights applied to an area on the input array calculating a single product value. Then the kernel shifts step by step across the entire image producing the output array (Figure 1.3.6, A). Thus each unit in the next layer receives only a section of the previous layer. This allows the network to learn local features of the data and to give equivarient response regardless of some variations such as translation. Using multiple different filters is the mean to learn different features in the data.

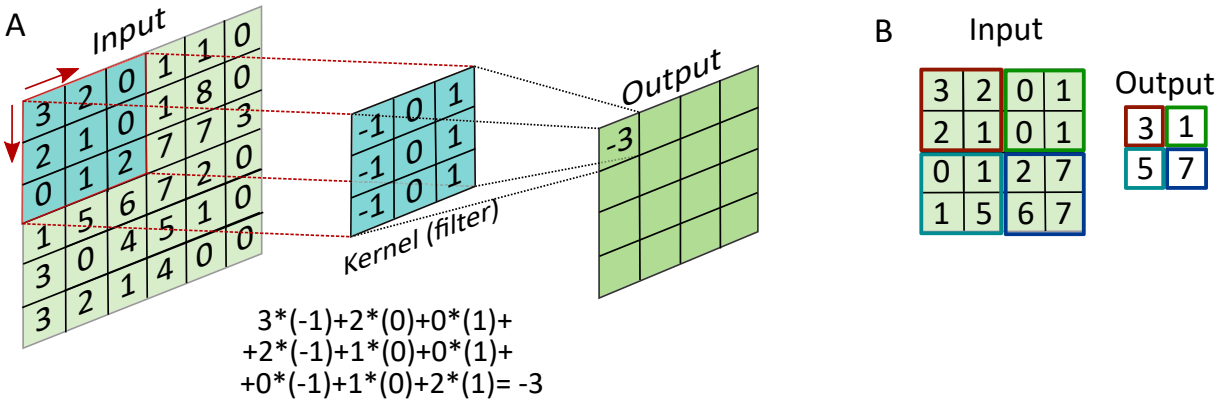

Figure 1.3.6 – A. Convolution example on 6 × 6 array input. The kernel is applied to the image area forming a product value in the output array. By moving across the entire image the output feature map is formed. **B**. Max pooling example. The 2×2 kernel is applied to an array extracting maximal value.

Typical CNN contains several layers. These are the convolutional layer followed by layer which consist of activation function to introduce non-linearity and the pooling layer [125, 126, 127]. The pooling layers such max or average pooling return the maximum or average value of the part of image which depends on the kernel size (Figure 1.3.6, B). This layer is used as the way

to avoid overfitting and learning the location-dependent features which may come up as a result of convolution layer []. Nevertheless, it was shown that the pooling layer can be effectively replaced with just convolutional layers with a stride of two [128]. The stride parameter can be used to modify the step of kernel movement over the image (for example in the figure 1.3.6, A the kernel is moving with a step of 1 pixel, so the stride is equal to 1). After a set of convolutional and pooling layers such network contains several fully-connected layers to perform classification (Figure 1.3.7, A).

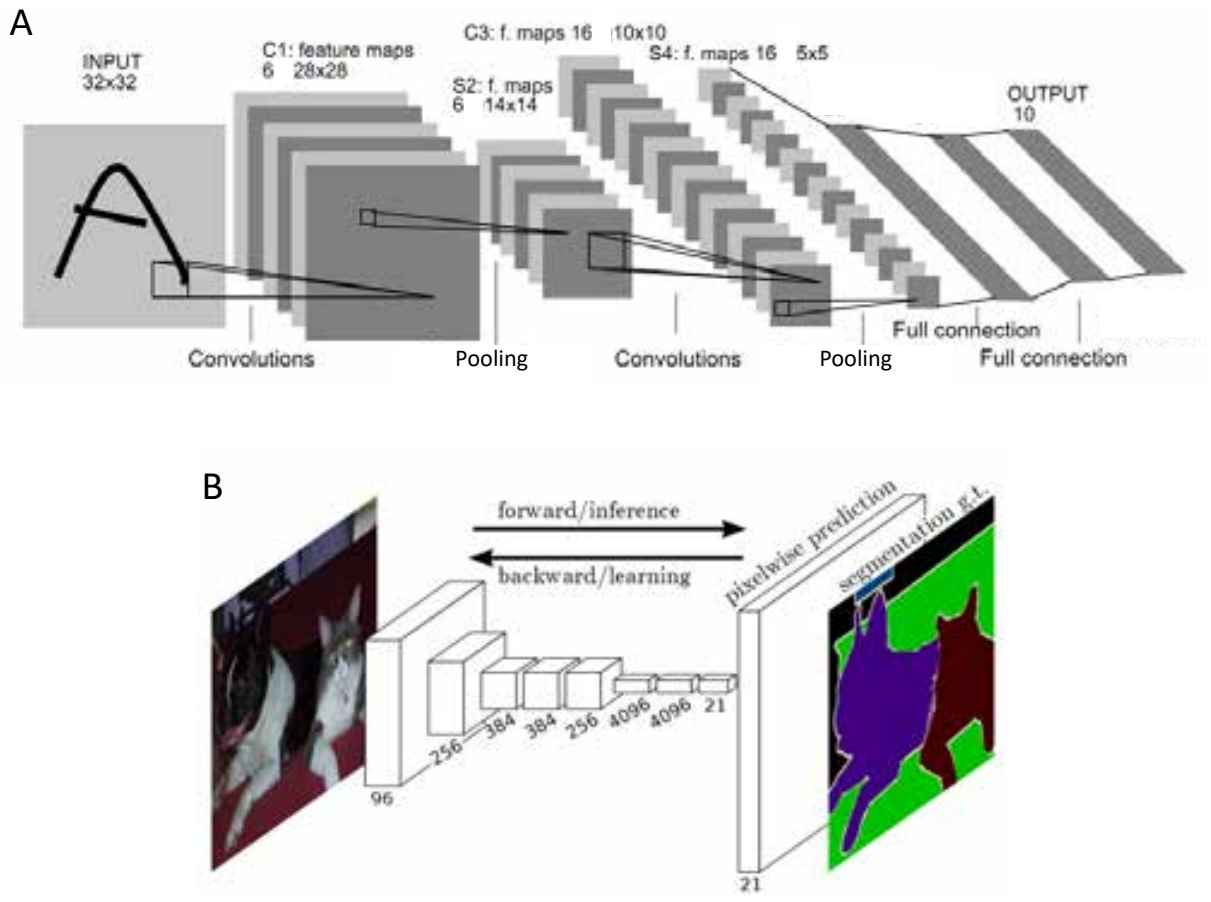

Figure 1.3.7 – **A**. Architecture of the CNN used for digits recognition (adapted from [124]). **B**. An example of fully convolutional network used to make predictions for such task like semantic segmentation [129]

CNNs were used in classification, object recognition, speech recognition etc. In CNN the input data is downsized at each step allowing to efficiently predict a single output label. However, in many visual tasks the desired output requires that each pixel of the image is marked with a label as in semantic segmentation. For this task fully convolutional networks were used, where the image is upsampled to produces pixelwise output [129] (Figure 1.3.7, B).

1.3.4 U-net architecture

The U-net architecture was initially developed for biomedical image segmentation [130]. This architecture is based on fully convolutional networks but complemented with successive upsampling layers to increase the resolution of the output. This network contains downsampling (similar to typical convolutional network) and upsampling paths which are more or lees symmetric creating a u-shaped architecture (Figure 1.3.8). To not loose the information from the pixels in the border regions after every convolution the feature maps of both paths are concatenated (the grey arrow on Figure 1.3.8).

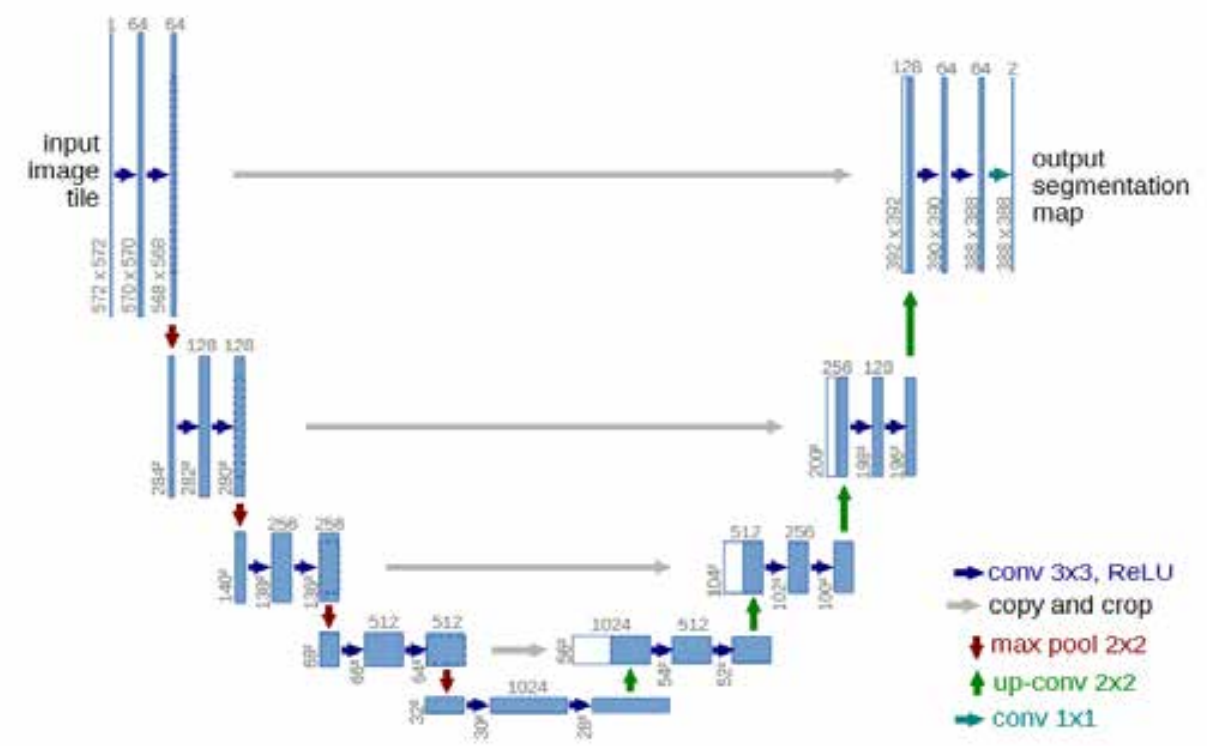

Figure 1.3.8 – The U-net architecture. The network contains convolutional, ReLU (activation) and max pooling layers in the downsampling path. In the upsampling path the pooling layer is changed for the up-convolution. The white boxes represent copied feature maps [130].

In the segmentation task the U-net was shown to provide more precise segmentations while exhibiting faster learning and requiring less number of images for training [130].

1.3.5 Use in microscopy

The development of deep learning techniques had a significant impact on the image processing and analysis fields. In recent years these techniques found various applications in the field of microscopy imaging in particular in super-resolution fluorescence microscopy. The application of DL methods allowed to overcome some constraints in SR microscopy such as long time required for the acquisition of sufficient number of localizations in DNA-PAINT technique due to low rate, limited temporal resolution in STORM and PALM due to photobleaching and photodamage, low SNR, segmentation and classification problems etc.

Several models were implemented to facilitate faster image acquisition in SMLM. This include ANNA-PALM which allows to predict the super-resolved image from one with incomplete structure obtained from smaller number of input frames [131]. DECODE method permits to simultaneously perform detection and localization of the emitters in 3D improving localization error and detection accuracy of dense data [132] (Figure 1.3.9, A). The DeepSTORM network is able to predict the emitter positions form high-density data to obtain super-resolved mages from shorter acquisitions [133, 134]. DeepSTORM was used for STORM, PALM and DNA-PAINT [135] (Figure 1.3.9, C) techniques.

Deep models were also used to improve spatial resolution [136] or increase SNR [137] (Figure 1.3.9, B). In most cases the implementation of deep learning algorithms to super-resolution microscopy includes several steps : the preparation of training data and model training. The training data may contain for example pairs of corresponding low and high resolution images. The training set containing too small number of images may result in overfitting and lack of generalization. Various technique were developed to reduce the amount of overfitting [138, 139, 140]. The amount of data can be increased by creating synthetic data [141] or using data augmentation [142, 143]. In this approach more data is added by generating transformed versions of the original data.

Despite an already huge impact of the deep learning techniques on different fields of science it is still a developing technology, so numerous new applications, architectures and different ways of data preparation are expected to come in the coming years.

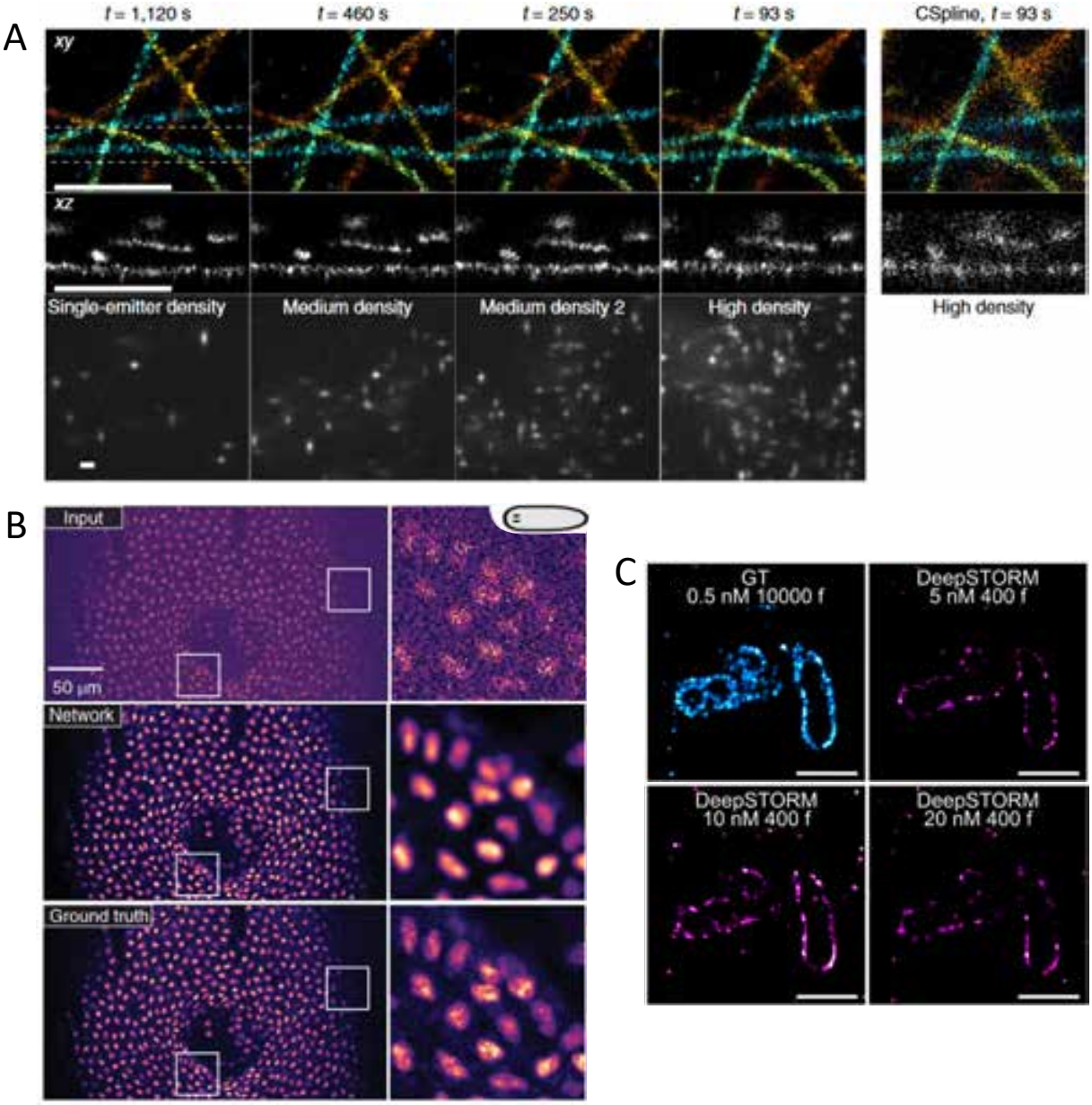

Figure 1.3.9 – **A**.DECODE method applied to reduce the acquisition time of α-tubulin labeled with AF657. The comparison with CSpline (Cubic Spline method) shown for high density activation [132]. **B**. CARE network used to improve SNR on the images of nucleus of flatworm (S. mediterranea) stained with RedDot1. The raw input image is shown on the top, the network prediction is in the middle and the ground truth image in the lower row. [137]. **C**. GT (Ground Truth) and DeepSTORM predicted images of a TOM20 structure recorded at different imager strand concentrations [135].

1.4 Objectives of this thesis

Production of pyoverdine in *Pseudomonas* presents an important mechanism for the virulence of these bacteria, however, the biosynthesis details are not sufficiently studied.

The objectives of the research works presented in this thesis are double :

— **first to investigate the dynamics and organization of the four NRPSs involved in pyoverdine biosynthesis in *P. aeruginosa* with available technologies**. Using super-resolution microscopy techniques, such as sptPALM, single-color DNA-PAINT, two-color DNA-PAINT and FLIM-FRET, we aim to elucidate further the details of NRPS machinery. Very few works have focused on the bacterial metabolic pathways at the single cell resolution.

— **second - to enhance the performance of SMLM techniques to make them more suitable for mulitplexed multi-colour dynamic imaging**. srSMLM is a powerful microscopy technique, which could be potentially useful for tracking or imaging several enzymes of a single pathway at the same time. We aimed to advance the srSMLM technique using deep learning and advanced signal analysis to overcome some of current limitations of the technique with in mind the idea that new methods enable new science.

These topics are developed in the next sections of this document

Publication I

Recent Developments in Spectrally-Resolved Single Molecule Super-Resolution Microscopy

Recent Developments in Spectrally-Resolved Single Molecule Super-Resolution Microscopy

Hanna Manko[1], **Yves Mély**[2], **and Julien Godet**[1,3,4,✉]

[1]Laboratoire de BioImagerie et Pathologies, UMR CNRS 7021, ITI InnoVec, Université de Strasbourg, Illkirch, France
[2]Laboratoire de BioImagerie et Pathologies, UMR CNRS 7021, Université de Strasbourg, Illkirch, France
[3]Groupe Méthodes Recherche Clinique, Hôpitaux Universitaires de Strasbourg, France
[4]Laboratoire iCube, UMR CNRS 7357, Equipe IMAGeS, Université de Strasbourg, Strasbourg, France

Summary

Spectrally-resolved Single-Molecule Localization Microscopy (srSMLM) reveals the spectral dimension of single-molecules while producing nanoscale images. This is made possible by simultaneously estimating the localization and spectrum characteristics of single fluorescent emitters. As a fledging technique, srSMLM continues to be actively developed and many important improvements have been proposed lately. In this short review we overlook the latest hardware and software developments, including deep learning, proposed to advance srSMLM. The innovation momentum in the srSMLM community is very high and the latest developments should make srSMLM as accessible and simple as single molecule localization microscopy can be.

spectrally resolved single molecule localization microscopy, super resolution, imaging, deep learning

Correspondence: ***julien.godet@unistra.fr***

Introduction

The development of Single Molecule Localization Microscopy (SMLM) technique (1–4) allowed to overcome the diffraction limit in microscopy and thus enabled imaging at the sub-cellular levels. These methods are based on imaging of individual fluorophores at different time points. Through determining the true positions of non-overlapping fluorophore emissions it became possible to reconstruct the super-resolved images. Implementation of SMLM techniques allows to achieve spatial resolution of 10-30 nm (5). Nevertheless, the spectral information behind the fluorophore emission remained unexplored.

In order to overcome this limitation, several research teams worked on the development of new technique, named spectrally-resolved super-resolution microscopy. Basing on the working principle of SMLM techniques srSMLM allows to simultaneously acquire single molecule localizations (similarly to conventional SMLM) and the spectral signatures of each individual emitting molecule (Figure 1, A. This technique was widely used to reveal fundamental processes in cell biology, and material sciences (6–10). It also was applied to drastically increase the number of fluorescent species that can be imaged simultaneously in the same sample, theoretically reaching the number of 15-20 fluorophores with the corresponding emission peaks separated by $\sim$ 20 nm (11).

The ability of srSMLM to obtain both spatial and spectral information at the same time is provided by the introduction of additional dispersive element such as prisms (6, 11–14) and diffraction gratings (7, 9, 10, 15, 16). In configurations utilizing prisms the separation of the collected protons into two optical paths is required (Figure 1, B). Typically this can be achieved by introducing the beam splitter with a desired positional-spectral splitting ratio (50:50 (11, 13, 14), 30:70 (17)) or alternatively by using dual objective system (6, 12) which provides higher photon collection efficiency but complicates the setup and poses strong limitations on the samples studied.

In contrast to the refraction prisms, the use of diffraction gratings does not require beam splitting and consequently the additional discrete optical components, thus greatly simplifying the setup (Fig 1, C). Typically, blazed transmission diffraction gratings are used in this type of configurations. Therefore the emission from the sample can be collected in the 0^{th} and the 1^{st} diffraction orders (7, 9, 10, 15, 16) for the spatial and spectral image part, respectively (Figure 1, B).

Despite the great potential of this technique it still has several limitations, most importantly concerning spatial and spectral resolution due to the low photon budget, molecule classification accuracy by the spectral signatures and low useful data ratio. Various methods were applied in order to overcome these constrains and improve the performance of srSMLM. In this review we will discuss the existing problems, improvement and recent developments in the field of spectrally-resolved super-resolution microscopy.

Limits to overcome

The main limitations in spectrally-resolved microscopy are related to the photon budget in both spatial and spectral channels. Despite the highest collection efficiency in dual-objective systems this configuration was not widely used due to high complexity and limited choice of samples. The setup can be simplified by the price of collection efficiency by using beam splitters and further by utilizing dispersive gratings.

In general, both the dispersive elements impose specific limitations on the technique. The refraction prisms are mostly used for the applications requiring low spectral precision due to their relatively low dispersion. Furthermore, addition calibration may be required in order to correct the nonlinear spectral dispersion of prisms. The optical losses in the configuration utilizing prism may occur at the surface of reflective mirrors, the beam splitter and the prism.

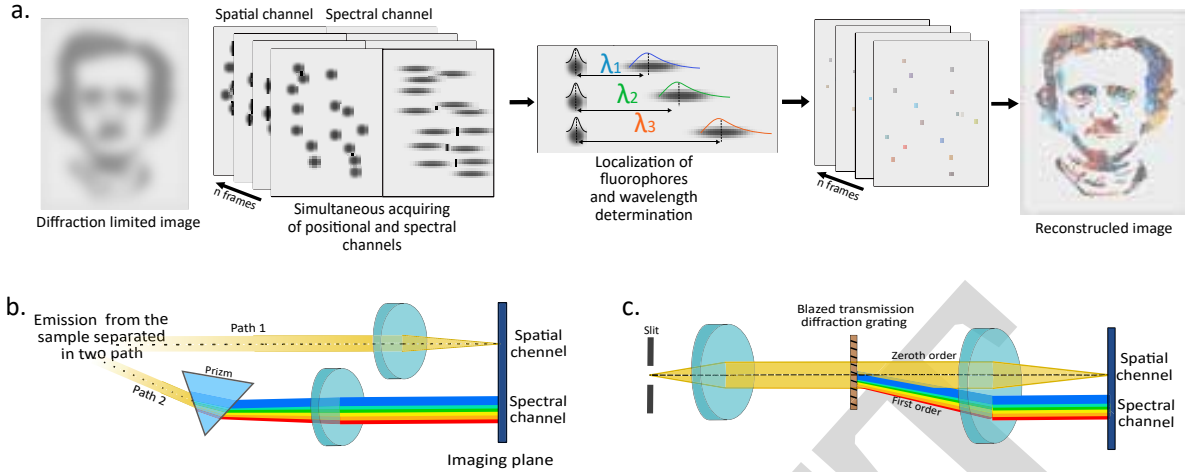

Fig. 1. Principle and main reported optical setups of srSMLM super-resolution microscopy.
a. Principle of srSMLM. srSMLM is based on the working principle of SMLM (spatial channel) and additionnaly record a spectral channel. In srSMLM, PSF of single emitters are recorded together with their corresponding diffracted signals resulting from the use of a dispersive element. Similarly to conventional SMLM techniques, localizations of single emitters are inferred from their PSF. Fluorescence spectra of emitters are encoded by the distances between the PSF in the spatial channel and the spectra signals in the spectral channel. srSMLM allows true color imaging. The spectroscopic information is usually rendered in the reconstructed super-resolution image by extracting a key characteristic of the spectra (e.g. weighted average wavelength)
b. Use of a dispersive prism. The light collected from the sample need to be separated into two paths. One path is used to create the localization image while light is dispersed by the prism in the second path to record the spectral information.
c. Use of a diffraction grating. Typically, blazed transmission diffraction gratings are used allowing to collect the light into zero and first order to create localization and spectral images respectively.

In contrast to prisms, diffraction gratings allow to avoid additional calibration procedure due to their linear dispersion. Moreover, they provide a wider spectral dispersion that can be further adjusted by switching the gratings with various number of lines per millimeter. In the configurations with a grating the intensity loss is determined by wavelength dependent grating efficiency which in turn depends on the characteristics of the diffraction grating itself. In general gratings have higher transmission losses than prisms leading to lower photon numbers (16).

The precision is directly affected by the number of photons and the background level. In all the srSMLM configurations the separation of the sample emission needed to create two corresponding images results in lower number of photons in both parts. Spatial and spectral precision are affected by the corresponding fraction of light resulting in another major trade-off of srSMLM techniques.

Moreover, the signal shape in the spectral part is more spread compared to that in spatial one, resulting in less number of detected photons per pixel. The restricted photon budget may affect the ability to recognise the spectral shape and consequently decreases wavelength allocation probability. This results in lower data ratio which can be used for spectral image reconstruction. Due to this fact the acquisition time in srSMLM is usually much longer than for localization microscopy methods.

Additional error in wavelength determination may be introduced due to spectral calibration procedure leading to subpixel spectral shift. This effect is more significant in the systems performing lower spectral dispersion (18).

Hardware improvements

Multiple techniques aimed to increase the photon budget and consequently improve the precision in one or both channels of srSMLM were developed in resent years. One of the efficient methods is to use grating which allows to symmetrically disperse the light into -1^{st} and 1^{st} orders (22) (Figure 2, a). Then the two spectral images of the same emitting molecule are captured. A spatial information is obtained by calculating the middle points between the two symmetrical spectral images. Thus all the collected photons are shared between spatial and spectral channels allowing to alleviate the problem of reduced photon budget. The achieved improvement is about 42% in spatial precision and 10% in spectral one when compared to the use of grating with 1:3 ratio between spatial and spectral channels (22). Nevertheless, such grating display limited transmission efficiency for the -1^{st} and 1^{st} orders and nonzero efficiency for the 0^{th} order resulting in certain intensity losses. This can be improved by using for example a phase grating.

Another approach to enhance the SNR in the spectral part is directly decrease the the size of spectral spot by using the grating with minimal dispersion of about 0.2 nm/nm(spatial/spectral), thus allowing to maximize the the number of photons per pixel. Such minimal dispersion can be obtained by introducing the transmission grating with 70 grooves/mm very close to the imaging plane (inside the camera housing). This configuration allows to image emitters at around 5 times higher density than in classical srSMLM setups. Despite the low spectral dispersion, this method allows to achieve separation of the emitters with a $\sim$10 nm spectral difference (23).

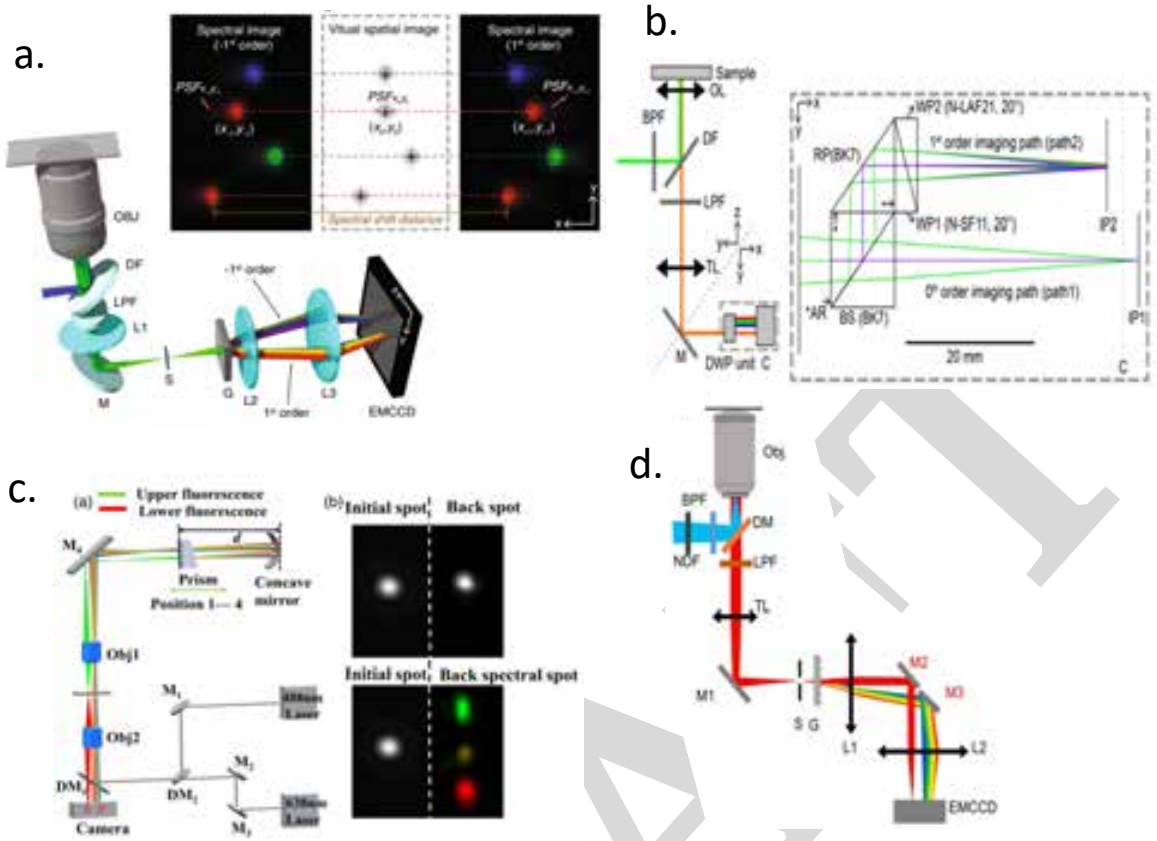

Fig. 2. a. Principle of symmetrically dispersed srSMLM. The light is collected in $1^{s}t$ and -1^{1} orders. In this case the position of the emitter is determined by calculating the middle point between two symmetrical spectral images (18). **b.** Scheme of the system with dual-wedge prism (19). **c.** The scheme of dual-objective system with concave mirror (20). **d.** Schematic of the srSMLM setup utilizing two pickoff mirrors to increase the field of view (21).

Symmetrically dispersed srSMLM can be used together with biplane 3D imaging which have been shown to be the most efficient method to perform 3D spectrally-resolved imaging (9). Herewith, the biplane technique does not suffer from the limited photon number due to light separation required since in SR imaging the light is already separated into two channels. Thus by introducing an axial separation between spatial and spectral images object plane it is possible to achieve an axial localization precision of 50 nm and spectral precision of 4 nm at an average photon count of 1250 (9). However, the detailed spectral analysis may become challenging due to out of focus signal spreading.

In the srSMLM setups utilizing prism the spatial precision can be improved by using dual-wedge prism (DWP) (19) (Figure 2, b). DWP is a monolithic module which consists of cube 50:50 beam splitter, right angle prism and two wedge prisms one with strong chromatic dispersion and the second one with a weak chromatic dispersion. The slight axial shift between spatial and spectral channels enables simultaneous 3D imaging while having the optical configuration which does not require discrete optical components. The estimated improvement in lateral precision provided by DWP is 47% and axial precision by 23% compared to 1:3 ratio grating-based setup (19).

An improved double-objective system was shown by Lui et al (20) (Figure 2, c). In this method two 40× opposing objectives are used. The first objective is used to create a positional image. The path of the other objective, which collects the emission light above the sample, contains a prism and a concave mirror and is used for spectral analysis (Figure). In this configuration the spectral dispersion can be tuned by moving the prism and the position of spectral image can be adjusted by changing the angle of concave mirror. Thus the light splitting is no more required resulting in spatial precision similar to one in conventional SMLM methods. Moreover, typically unused upper fluorescence is used to perform spectral analysis and this methods does not pose limitations on the sample, contrary to conventional dual objective setups.

Several techniques featuring altered field-of-view (FOV) were developed pursuing various goals. One of these methods is addressed to overcome the requirement to restrict the FOV needed to avoid the overlap between spatial and spectral channels. The FOV can be increased by using pick-off mirrors controlling 0^{th} and the 1^{st} orders separately (21) (Figure 2, d). On the other hand, the second approach is using the restricted FOV in order to image dense non-blinking fluorophores (26).

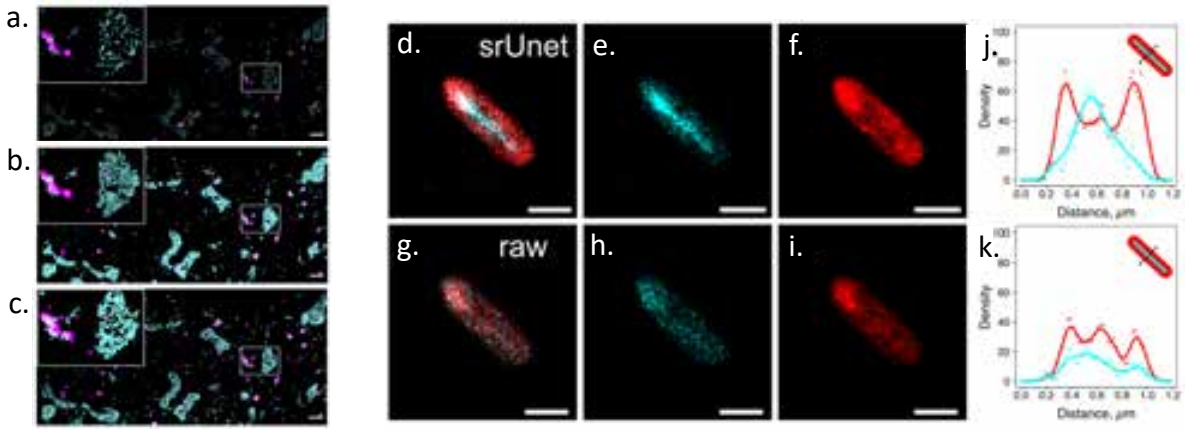

Fig. 3. Use of Deep learning models to enhance srSMLM technique. Two-color images of mitochondria (cyan) and peroxisome (magenta) at **a.** low density with 5000 frames. **b.** Reconstructed image with Deep model. **c.** High density image obtained over 40, 000 frames (scale bar = 1.5μm) (24).
Images of fixed bacteria labeled with POPO-III (cyan) (**e.** and **h.**) and Nile Red (red) (**f.** and **i.**) dyes. The reconstruction of the raw images **e.f.g** and images treated with srUnet. **j.** The intensity profiles of localization density for images treated with srUnet model and **k.** for raw images.(scale bar = 1μm) (25)

Data analysis and recent software developments

Various setup improvements have provided a significant impact on the photon budget and allowed to increase the precision in spatial and spectral channels. Furthermore, the spatial precision in srSMLM can be improved on the data analysis step by combination of localization information from both spatial and spectral orders (21). Thus the position of the emitting molecule is obtained by processing the zero order signals and first order spectral peaks. Then the two sets of obtained localizations are combined, which allows to increase the localization precision. In such a way the precision can be improved by 30% along the x-axis and by 45% along the y-axis. Somewhat lesser improvement on the x-axis is the result of a stronger spreading of the spectral peak along this axis. In addition, the localization precision can be enhanced by accumulating photons from individual molecule using its spectroscopic signatures (27).

However, the rich spectral dimension is still not fully utilized due to restricted number of localizations with corresponding high-quality spectra. Low photon budget and high noise levels may result in an inability to extract the corresponding wavelength information, which results in low classification accuracy and limited useful data ratio. The best spectral precision can be achieved by using the spectral dispersion that matches to a given photon budget (18). The accuracy of wavelength determination can be also affected by the procedure used. In general, two methods to encode spectral information were utilized including spectral centroids which are calculated by averaging spectral mean values (6) and determination of fluorescent wavelength at the emission maximum (7). Despite the intrinsically high spectral precision in srSMLM, in the case of microscopy data with high noise levels both methods may fail to distinguish between two fluorophrores with small peak separation. The classification accuracy can be greatly improved by summarizing the full spectra information. This can be achieved by applying spectral phasor transformation to the fluorescent spectra (Figure??). This approach allows to transform the spectral data into a coordinate defined by its amplitude and phase in a Fourier space. Thus the position of the spectra phasor spot is defined by both its central position and shape. Furthermore, such representation allows to classify single molecules with higher efficiency (28).

Exploiting Deep Learning.

Recent developments of deep learning (DL) methods revealed previously unavailable powerful tools in image processing (29, 30). In the field of SMLM analysis these algorithms allowed to restore the quality of underexposed images (31), to perform fast DNA-PAINT imaging in densely labeled samples (32), to classify the molecules based on the point spread function (PSF) (30) etc. To the date various DL methods application to srSMLM were reported, including fast reconstruction of high-density multicolour images by acquiring fewer frames (24) (Figure 3, abc). Moreover, several DL algorithms were applied in order to increase the classification accuracy and useful data ratio. One of these methods was addressed to classify molecules with higher accuracy by using their full spectral profiles (33). By using two dyes with spectral peak separation of 10 nm (Af647 an CF660) the authors showed that useful data ratio is about 10% from whole data set, while high classification accuracy can reach 99% only by discarding all the single molecule emissions with less that 2000 photon counts. The use of DL method allowed to increase the percentage of useful data to more than 50% and keep the same classification accuracies under 0.7 correlation threshold (33).
Another DL U-net based approach (srUnet) was recently developed in order to enhance the signals in both spatial and spectral channels, thus leading to higher precision and wavelength allocation probability, respectively (Figure 3, d-k). The core of this approach is a newly proposed method of training data set creation, which, in turn, is based on the spatial frequency fusion of the images featuring the same emitter

appearing at several frames. Compared to raw data, a similar probability of wavelength allocation for a given localization can be achieved while having the corresponding number of photons being around 10 times lower (25).

Conclusions

SrSMLM technique revealed the spectral dimension for nanoscale investigations. Various setup improvements allowed to increase photon budget leading to higher precision in spatial and spectral channels. The localization precision can be also improved on the images post processing steps by combining the positional information obtained from both channels. Moreover, several methods were developed to improve molecule classification accuracy and useful data ratio. This includes using of Fourier transformation of the spectral data and implementation of several DL models.

Significant improvements have been achieved in the field of srSMLM in recent years. Nevertheless, the best performance of a srSMLM technique can be achieved only by a combination of the optimal setup, properly chosen dispersive element, which provides optimal spectral dispersion for the specific application, and careful data analysis. Further improvement could be performed with the help of deep learning techniques. The field of deep learning for microscopy applications is actively developing, so new methods are expected to arise in the following years. An alternative approach towards obtaining higher photon budget in srSMLM lies in development of brighter and/or more photostable fluorophores. (34, 35)

References

1. Alexey Sharonov and M. Hochstrasser, Robin. Wide-field subdiffraction imaging by accumulated binding of diffusing probes. *Proc Natl Acad Sci*, 103(50):18911–18916, 2006.
2. J. Rust, Michael, Mark Bates, and Xiaowei Zhuang. Sub-diffraction-limit imaging by stochastic optical reconstruction microscopy (storm). *Nature Methods*, 3(10):793, 2006.
3. Eric Betzig, H. Patterson, George, Rachid Sougrat, Wolf Lindwasser, O., Scott Olenych, S. Bonifacini, Juan, W. Davidson, Michael, Jennifer Lippincott-Schwartz, and F. Hess, Harald. Imaging intracellular fluorescent proteins at nanometer resolution. *Science*, 313(5793): 1642–1645, 2006.
4. ST Hess, T.P. Girirajan, and M.D. Mason. Ultra-high resolution imaging by fluorescence photoactivation localization microscopy. *Biophysical Journal*, 91(11):4258–72, 2006.
5. M. Khater, Ismail, Robert Nabi, Ivan, and Ghassan Hamarneh. A review of super-resolution single-molecule localization microscopy cluster analysis and quantification methods. *Patterns*, 1(3), 2020.
6. Z Zhang, SJ Kenny, M Hauser, W Li, and K Xu. Ultrahigh-troughput single-molecule spectroscopy and spectrally resolved super-resolution microscopy. *Nature Methods*, 12(10): 935–938, 2015.
7. M.N. Bongiovanni, J Godet, M.H. Horrocks, L. Tasatto, A.R. Carr, D.C. Wirthensohn, R.T. Ranasinghe, Ji-Eun Lee, A. Ponjavic, J.V. Fritz, C.M. Dobson, D. Klenerman, and Steven F. Lee. Multi-dimensional super-resolution imaging enables surface hydrophobicity mapping. *Nature Communications*, 7:1–9, 2016.
8. B. Dong, L.M. Almassalha, Y. Stypula-Cyrus, B.E. Urban, J.E. Chandler, C. Nguyen, T.Q. adn Sun, H.F. Zhang, and V. Backman. Superresolution intristic fluorescence imaging of chromatin utilizing native, unmodified nucleic acids for contrast. *Proc Natl Acad Sci USA*, 113(35):9716–9721, 2016.
9. K-H Song, G Zhang, Y adn Wang, C Sun, and HF Zhang. Three-dimentional biplane spectroscopic single-molecule localization microscopy. *Optica*, 6(10):1374, 2019.
10. Ji-Eun Lee, JC Sang, M Rodrigues, AR Carr, MH Horrocks, Suman De, MN Bongiovanni, P Flagmeier, CM Dobson, DJ Wales, Steven F Lee, and D Klenerman. Mapping surface hydrophobicity of a-synuclein oligomers at the nanoscale. *Nano Letters*, 18(12):7494–7501, 2018.
11. MJ Mlodzianoski, NM Curthoys, MS Gunewardene, S Carter, and ST Hess. Super-resolution imaging of molecular emission spectra and signle molecule spectral fluctuations. *PLoS One*, 11(3):1–12, 2016.
12. D Kim, Z Zhang, and K Xu. Spectrally resolved super-resolution microscopy unveils multipath reaction pathways of single spiropyram molecules. *Journal of Americal Chemical Society*, 139(28):9447–9450, 2017.
13. S Moon, R Yan, SJ Kenny, Y Shyu, L Xiang, W Li, and Ke Xu. Spectrally-resolved, functional super-resolution nanoscale compositional heterogeneity in live-cell membranes. *Journal of Americal Chemical Society*, 139(32):10944–10947, 2017.
14. L Xiang, M Wojcik, SJ Kenny, Rui Yan, S Moon, and Ke Xu. Optical characterisation of surface adlayers and their compositional demixing at the nanoscale. *Nature Communications*, 9(1):1–9, 2018.
15. Hannah J Stern, Ruizhi Wang, Ye Fan, Ryo Mizuta, James C Stewart, Lisa-Maria Needham, Trevor D Roberts, Rebecca Wai, Naomi S Ginsberg, David Klenerman, and Steven F Lee. Spectrally resolved photodynamics of individual emitters in large-area monolayers of hexagonal boron nitride. *ACS Nano*, 13(4):4538–4547, 2019.
16. Janel L. Davis, Yang Zhang, Sijia Yi, Fanfan Du, K-H Song, Evan A Scott, Cheng Sun, and Hao F Zhang. Super-resolution imaging of self-assembled nanocarriers using quantitative spectroscopic analysis for cluster extraction. *Langmuir*, 36(9):2291–2299, 2020.
17. T. Huang, C. Phelps, J. Wang, Li-Jubng Lin, A Bittel, Z Scott, S Jacques, SL Gibbs, JW Gray, and Xiaolin Nan. Simultaneous multicolor single-molecule tracking with single-laser excitation via spectral imaging. *Biophysical Journal*, 114(2):301–310, 2018.
18. K-H. Song, B. Dong, C. Sun, and H.F. Zhang. Theoretical analysis of spectral precision in spectroscopic single-molecule localization microscopy. *Review of Scientific instruments*, 89 (12), 2018.
19. K-H. Song, B. Brenner, W-H. Yeo, J. Kweon, Z. Cai, Y. Zhang, Y. Lee, X. Yang, C. Sun, and Hao F. Zhang. Monolithic dual-wedge prism-based spectroscopic single-molecule localization microscopy. *Nanophotonics*, 11(8):1527–1535, 2022.
20. X. Lui, L. Yao, W. Yang, Y. Fei, L. Mi, and J. Ma. Spectroscopic fluorescent tracking of a single molecule in a live cell with a dual-objective fluorescent reflection microscope. *Applied Physics Express*, 12:112007, 2019.
21. B. Brenner, K-H. Song, C. Sun, and H.F. Zhang. Improving spatial precision and field-of-view in wavelength-tagged single-particle tracking using spectroscopic single-molecule localization microscopy. *Applied Optics*, 60:3647–3658, 2021.
22. K-H. Song, Y. Zhang, B. Brenner, C. Sun, and Hao F. Zhang. Symmetrically dispersed spectroscopic single-molecule localization microscopy. *Light: Science & Applications*, 9 (92), 2020.
23. Koen J.A. Martens, Martijn Gobes, Emmanouil Archontakis, Roger R. Brillas, Niels Zijlstra, Lorenzo Albertazzi, and Johannes Hohlbein. Enabling spectrally resolved single-molecule localization microscopy at high emitter densities. *bioRxiv*, 2022. doi: 10.1101/2022.06.29.498127.
24. S.K. Gaire, Y. Zhang, H. Li, R. Yu, H.F. Zhang, and L. Ying. Accelerating multicolor spectroscopic single-molecule localization microscopy using deep learning. *Biomedical Optics Express*, 11(5):2705, 2020.
25. Hanna Manko, Yves Mély, and Julien Godet. Advancing spectrally-resolved single molecule localization microscopy using deep learning. *bioRxiv*, 2022. doi: 10.1101/2022.07.29.502097.
26. Y. Zhang, Yu. Zhang, K-H. Song, W. Li, C. Sun, George C. Schatz, and H.F. Zhang. Investigating single-molecule fluorescence spectral heterogeneity of rhodamines using high-throughput single-molecule spectroscopy. *The Journal of Physical Chemistry Letters*, 12: 3914–3921, 2021.
27. B. Dong, K-H. Song, S.J. Davis, H.F. Zhang, and C. Sun. Sub-10 nm Distance Measurements between Fluorophores using Photon-Accumulation Enhanced Reconstruction. *Advanced Photonics Research*, 1:2000038, 2020.
28. Hanna Manko, Yves Mély, and Julien Godet. Spectral phasor applied to spectrally-resolved super resolution microscopy. *In preparation*.
29. Lucas von Chamier, Romain F. Laine, Johanna Jukkala, Christoph Spahn, Daniel Krentzel, Elias Nehme, Martina Lerche, Sara Hernández-Pérez, Pieta K. Mattila, Eleni Karinou, Séamus Holden, Ahmet Can Solak, Alexander Krull, Tim-Oliver Buchholz, Martin L. Jones, Loïc A. Royer, Christophe Leterrier, Yoav Shechtman, Florian Jug, Mike Heilemann, Guillaume Jacquemet, and Ricardo Henriques. Democratising deep learning for microscopy with zerocostdl4mic. *Nature Communications*, 12(1):2276, 2021. doi: 10.1038/s41467-021-22518-0.
30. P. Zhang, S. Lui, A. Chaurasia, D. Ma, M.J. Mlodzianoski, E. Culurciello, and F Huang. Analyzing complex single-molecule emission patterns with deep learning. *Nature Methods*, 15(11):913–916, 2018.
31. Martin Weigert, Uwe Schmidt, Tobias Boothe, Andreas Müller, Alexandr Dibrov, Akanksha Jain, Benjamin Wilhelm, Deborah Schmidt, Coleman Broaddus, Siân Culley, Mauricio Rocha-Martins, Fabián Segovia-Miranda, Caren Norden, Ricardo Henriques, Marino Zerial, Michele Solimena, Jochen Rink, Pavel Tomancak, Loic Royer, Florian Jug, and Eugene W. Myers. Content-aware image restoration: pushing the limits of fluorescence microscopy. *Nature Methods*, 15(12):1090–1097, 2018. doi: 10.1038/s41592-018-0216-7.
32. Kaarjel K. Narayanasamy, Johanna V. Rahm, Siddharth Tourani, and Mike Heilemann. Fast dna-paint imaging using a deep neural network. *bioRxiv*, 2021. doi: 10.1101/2021.11.20.469366.
33. Z. Zhang, Y. Zhang, L. Ying, C. Sun, and H.F. Zhang. Machine-learning based spectral classification for spectroscopic single-molecule localization microscopy. *Optics Letters*, 44: 5864–5867, 2019.
34. R. Yan, S. Moon, S.J. Kenny, and K. Xu. Spectrally resolved and functional super-resolution microscopy via ultrahigh-throughput single-molecule spectroscopy. *Accounts of Chemical Research*, 51:697–705, 2018.
35. D.I. Danylchuk, S. Moon, K. Xu, and A.C. Klymchenko. Switchable solvatochromic probes for live-cell super-resolution imaging of plasma membrane organization. *Angewandte Chemie*, 58(42):14920–14924, 2019.

Materials and methods

2.1 Cell lines

Most of the work performed on bacteria described in this thesis were done on *Pseudomonas aeruginosa*. PaO1 strain (PAO1 - DSM 22644) and mutants derived from this strain were mostly provided by Isabelle J Schalk lab (CNRS, UMR7242). The last mutants recently used were designed and constructed in our lab by Tania Stefan, following the Schalk lab protocol described in Manko et al [144].

In brief, mutations in the chromosomal genome of *P. aeruginosa* PAO1 were generated by transferring a suicide vector from E. coli TOP10 strain into the PAO1 recipient strain.

DNA fragments from PAO1 used for cloning were amplified from the genomic DNA of the PAO1 strain with Phusion High-Fidelity DNA polymerase (ThermoFisher Scientific). The general procedure for the construction of the suicide plasmid vector involved insertion of the mcherry, egfp or photo-activatable mcherry gene flanked by upstream and downstream regions of 700 bp, corresponding to the insertion site, into a pME3088 or a pEXG2 vector. Mutations in the chromosomal genome of PAO1 were generated by transferring the suicide vector from E. coli TOP10 strain into the PAO1 recipient strain i na step of coculture. PAO1 integrating the plasmid into their chromosome were then selected using tetracycline resistance (for pME3088 (Voisard et al., 1994)) or gentamicin resistance (for pEXG2). A second crossing-over event excising the vector was achieved by enrichment for tetracycline-sensitive cells (pME3088) or sucrose resistant cells selection (pEXG2), to generate the corresponding mutants (Ye et al., 1995). All tag insertion mutants were verified by PCR and sequencing.

Mutants used for experiments are presented in table 2.1.

Strain name	Collection Number	Modification
Localization microscopy		
PAS180	406	PaO1 PvdA-eGFP
PAS214	460	PaO1 eGFP-PvdD
PAS215	461	PaO1 eGFP-PvdL
PAS216	462	PaO1 PvdI-eGFP
PAS471		PaO1 PvdJ-eGFP
Single Molecule tracking		
PAS405	688	PaO1 PvdA PAmCherry
PAS406	689	PaO1 PAmCherry PvdL
PAS407	690	PaO1 PvdI PAmCherry
-	-	PaO1 PvdJ PAmCherry
-	-	PaO1 PAmCherry PvdD
Two color localization microscopy		
PAS554	857	PaO1 eGFP-PvdL / PvdJ-mCherry
PAS555	858	PaO1 PvdJ-eGFP / mCherry-PvdL
PAS556	860	PaO1 eGFP-PvdL / mCherry-PvdD
PAS557	861	PaO1 eGFP-PvdL / PvdI-mCherry
PAS559	863	PaO1 PvdJ-eGFP / mCherry-PvdD

Table 2.1 – *Pseudomonas aeruginosa* mutant strains used in this study

2.2 Bacteria cell culture

The following media were used for bacteria cell culture :
1) LB (Luria-Bertani) Broth (Lennox) (Sigma Aldrich)
2) SM (Succinate Medium) was prepared in a volume of 1.0 L of media in Milli-Q Water and is composed of :

- 5.96 g - Potassium Phosphate Dibasic (K_2HPO_4) -Anhyrous
- 3.0 g - Potassium Phosphate Monobasic (KH_2PO4) Ammonium Sulfate ($(NH_4)_2SO_4$),
- 0.2 g - Magnesium Sulfate Heptahydrate ($MgSO_4$, $7H_2O$)
- 9.15 g - Sodium Succinate (Disodium).

The pH was adjusted to ~ 7.0

1. *Pseudomonas aeruginosa* PaO1 overnight culture and fixation :

Bacteria were grown for 24 hours in LB media at 30°C at 200 rpm orbital shaking (5 ml of media in falcon tube). Then cells in 2 ml tubes were pelleted by centrifugation at 10 k rpm for 3 minutes and washed three times with PBS (Phosphate Buffered Saline, PAN BIOTECH,

sterile filtered for cell culture) before being fixed in 500 μl of 4% formaldehyde in PBS 1X for 15 minutes under gentle agitation at room temperature. The reaction was stopped by washing (3 times) the cells in 500 μl PBS. Cells can then be stored up to a month at 4°C.

2. Bacteria cells expressing NRPSs culture and fixation

Pseudomonas aeruginosa NRPSs mutant cells were grown for 24 hours in LB media at 30°C under 200 rpm orbital shaking. After 3 washings with Succinate Medium (SM) the cells were grown in 10 ml of SM for 24 hours in order to trigger the pyoverdine production. The next day bacteria were diluted 10 times and grown for additional 24 hours. Cell density was controlled by measuring the optical density (OD) at 600 nm. The bacteria were diluted to $OD_{600nm} = 0.2$ and grown for about 2 hours to reach $OD_{600nm} \sim [0.4 - 0.5]$. Finally, cells were washed one time with SM, fixed with 4% formaldehyde (Sigma-Aldrich) in PBS and washed 3 times with PBS.

3. Bacteria cell culture for the experiments with live cells.

The cells were grown in LB over night and then in SM for the next 48h in order to induce NRPSs expression in sufficient quantity. Just before experiments, cells were diluted to $OD_{600nm} = 0.5$ in SM and used directly as is for imaging.

2.3 Labeling

Permeabilization and BSA blocking

Cells were pelleted by centrifugation and incubated in 0.2% Triton X-100 (Merk KGaA) for 20 minutes under gentle agitation at room temperature. Further, the cells were washed three times, incubated in PBS containing 100 μl/ml of lysozyme (Sigma-Aldrich) and 5 mM EDTA (Sigma-Aldrich) for 30 minutes and consequently washed three times again before been incubated in 1% BSA (Bovine Serum Albumin, 3% in PBS) for 20 minutes.

Primary antibody straining

The cells were pelleted by centrifugation, incubated while protecting from light for 1 hour in 200 μl of PBS containing 1/1000 primary antibody with 1 % BSA and 0.05 % Triton X-100. Then cells were washed three times in PBS containing 0.05 % Tween-20 (Sigma-Aldrich). The cells can be used for microscopy after being resuspended in PBS.

Secondary antibody straining

Secondary antibody labelling was performed by using a DNA-PAINT Massive-AB- 2-Plex labelling kit (Massive Photonics). The cells previously labeled with primary antibody were washed

once with a washing buffer and incubated in a secondary antibody solution (dilution 1 :200 in the antibody incubation buffer) for 1 hour at room temperature. In case of double labeling the solution contained two diluted antibodies at the same time. After the incubation the bacteria were washed three times with washing buffer. Before imaging the cells were additionally washed once with imaging buffer.

2.4 Sample preparation

2.4.1 Live cells microscopy

The live bacteria were imaged on an agarose pad. A glass-slide was placed on a horizontal surface and two glass-slides topped with two layers of adhesive tape were arranged on both sides. The droplet of 70μl of 1% melted agarose was poured on the middle slide and covered with a fourth slide to flatten the droplet. After about 1 min the covering slide was taken off and 3 μl of bacteria suspension was pipetted onto the agarose gel. The agarose pad was then covered with a microscopy coverslip (22×22 mm, 1.5 mm thickness, Knitel Glass). After that the coverslip was fixed with melted paraffin to seal the sample from the outside.

2.4.2 Fixed cell microscopy

The glass coverslips (0.15 mm thickness, 20 × 20 mm, Knitel Glass) were cleaned in argon plasma cleaner (PDC-002, Harrick Plasma) for 20 min, then the Frame-seal slide chambers (9 × 9, 25μl, Bio-rad, USA) were fixed on the glass coverslip. The chamber was filled with poly-L-lysine solution (0.01% w/v, P4707 Sigma-Aldrich) and incubated for 10 min. Poly-L-lysine solution was rinced with PBS and the chamber was filled with 100 μl of fixed bacteria suspension (fiducial markers (Gold nanoparticles, 80 nm diameter, Sigma-Aldrich)) were added if required) and washed once with PBS. After that the slide was transferred to the microscope using Attofluor cell chamber (A-7816 Thermofisher).

In DNA-PAINT microscopy the cells were washed once with an imaging buffer before the imaging. After that, the imager strands were directly added after dilution in imaging buffer to nanomolar concentrations.

Microspheres

A glass slide was prepared similar to the procedure described in previous paragraph. After the poly-L-lysine coating 25 μl of a solution of fluorescent orange (540/560 nm) and/or red (580/605 nm) beads (Invitrogen, 5 % of solids in PBS), or four color beads (TetraSpeck, size 0.1μm) in PBS was put on top of a 20 mm glass coverslip. After that, a second glass coverslip was attached on top in order to ensure long-term storage and utilization for calibration during microscopy

imaging.

DNA origami nanorulers

Commercially available GATTA-PAINT green (ATTO 542) nanorulers with mark-to-mark distance of 80 nm (GATTAquant GmbH, Germany) were purchased and used as is.

2.5 Microscopy and analysis

2.5.1 Microscopy setup

SMLM and srSMLM imaging experiments were performed on a home-built setup based on Olympus IX-81 inverted optical microscope equipped with 100X 1.4 NA oil-immersion objective (Olympus-Japan) and z-drift control and auto-focus system (ZDC Olympus) (Fig 2.5.1). The microscope was controlled with Micro-Manager software. The excitation was performed using a 405 nm diode laser (Oxxius), 488 nm solid state laser (Spectral-Physics) or 532 nm continuous wavelength diode-pumped solid-state laser (Coherent Sapphire SF), 561nm CW diode laser (Oxxius) and 638 nm diode pumped laser (Cobolt 08-01 series). The fluorescence emission was collected through the same objective using a dichroic mirror (Di01-R488 / Di02-R532 / Di03-R561-t1 / Di650-Di01- Semrock) and filtered by a corresponding longpass filter (BLP01-488R-25 / 532 LP EdgeBasic / LP02-568RU-25 / 645LP Edge Basic, Semrock). The signal was detected by a 512 $\times$ 512 pixels electron multiplayed charged coupled device (EMCCD) camera (ImageEM - Hamamatsu Photonics - Japan).

3D imaging

3D imaging was performed using an astigmatic lens inserted before the camera. The calibration was done by recording the fluorescent beads on the glass coveslip with 25 nm z-axis steps and consequently analyzed by ThunderSTORM plugin in Fiji.

srSMLM

A physical aperture (VA100/M, Thorlabs) and a transmission diffraction grating (300 Grooves/mm, 8.6° Blaze Angle - GT13-03, Thorlabs) were mounted into the light pass before the camera in order to create the spatial and spectral channel, respectively (Figure 2.5.1). The spectral calibration was performed using four color beads excited with 488 nm laser allowing to simultaneously obtain three spectral peaks with maximum emission wavelength at 512 nm, 581.5 nm and 676.5 nm corresponding each to a single fluorophore in the bead. In order to obtain the calibration curve (λ(pixels)) the distance in pixels between the bead localizations and each of spectral peaks was calculated.

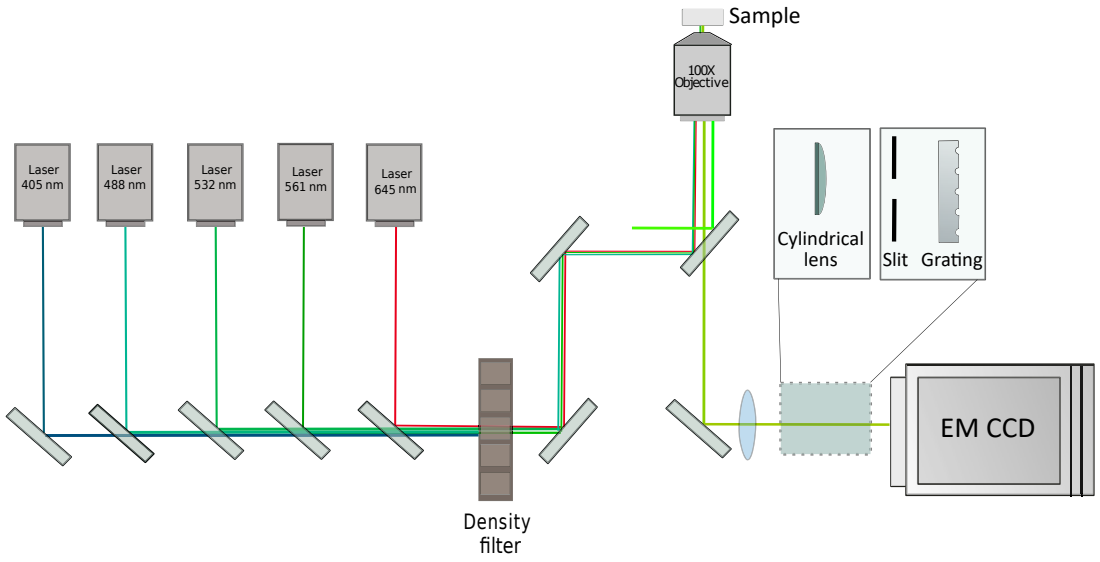

Figure 2.5.1 – The scheme of the setup

2.5.2 Single molecule tracking microscopy

PvdA - PAmCherry fused enzyme was used as a control for single molecule tracking experiments. The data was obtained in three independent experiments each including 4-5 different fields of view. The obtained data was analyzed utilizing a TrackMate plugin in Fiji developed by the group of Jean-Yves Tinevez [145] in order to retrieve the track information. A 0.5 μm linking distance was used.

The obtained data was further processed using a TrackR package in R [113] in order to obtain the jump distances and reconstruct the diffusion maps. The diffusion coefficients and the corresponding amplitudes were calculated for the two component model which considers a coexistence of restrained and mobile complexes (equation 1.3).

2.5.3 DNA-PAINT microscopy

Single-color

A 561 nm laser was used as a light source. For 3D imaging, image stacks of 60000 frames were acquired with an exposure time of 80 ms per frame.

The stack of images were processed in ThunderSTORM - an open source Fiji plugin [146] in order to obtain the molecule localizations.

Two-color

The double mutant bacteria cells were labeled with sets of corresponding primary and secondary antibodies. 561 nm and 645 nm lasers were used for excitation. The image stacks of 60000 frames with exposure time 80 ms per frame were acquired in two separate channels while changing the

illumination laser and the corresponding filter cube every 20000 frames. 3-4 different fields of view were recorded for each sample. The imaging was performed in 3D.

The localizations of the molecules were retrieved using the ThunderSTORM plugin. Then the localisation files were additionally filtered in SMAP [147]. The groups of localizations featuring less then 10 events were discarded and the localizations located only within the 100 nm z-slice in the middle part of bacteria were kept. The further analysis was performed on a z-projection of the filtered data. Next, the data was analysed in Coloc-Tesseler [148] in order to retrieve the tesselation-based Mander's overlap coefficients (Figure 2.5.2).

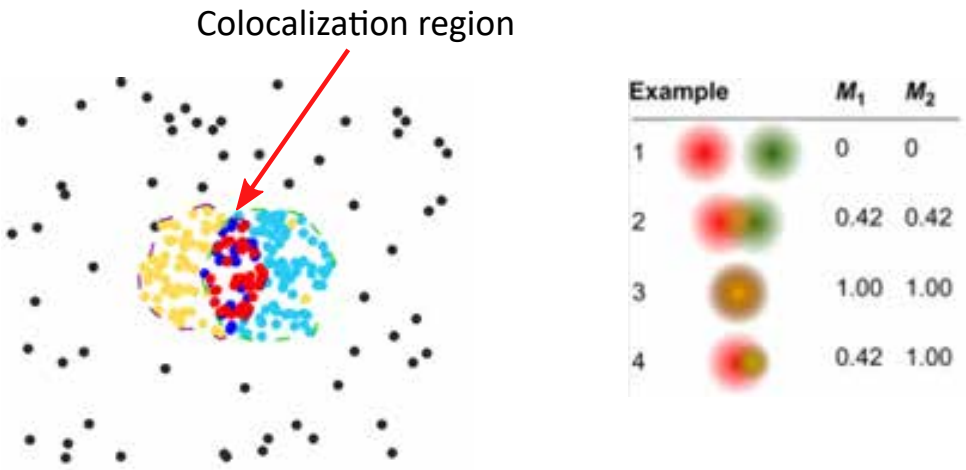

Figure 2.5.2 – The calculation of Mander's overlap coefficients for super-resolution images.

Mander's Overlap coefficients were calculated for every single bacteria in the field of view both for the green/red and red/green channels.

2.6 FLIM-FRET

FLIM measurements were performed on a home-made scanning microscope based on an Olympus IX70 inverted microscope with 60× 1.2NA water immersion objective (Olympus). The Ti :Sapphire oscillator (Insight DeepSee, Spectra Physics - 80MHz repetition rate) was used for two-photon illumination at 930 nm. The detailed protocol of the FLIM-FRET experiments and some experimental examples are presented in the protocol article we have published in JoVE in 2020 (publication 2.6).

Publication II

FLIM-FRET Measurements of Protein-Protein Interactions in Live Bacteria

Published at jove.com doi: 10.3791/61602

TITLE:

FLIM-FRET Measurements of Protein-Protein Interactions in Live Bacteria

AUTHORS AND AFFILIATIONS:

Hanna Manko[1], Vincent Normant[2,3], Quentin Perraud[2,3], Tania Steffan[1], Véronique Gasser[2,3], Emmanuel Boutant[1], Éléonore Réal[1], Isabelle J. Schalk[2,3], Yves Mély[1] and Julien Godet[1, 4, *]

[1]Université de Strasbourg, Laboratoire de Bioimagerie et Pathologies, UMR CNRS 7021, Illkirch, Strasbourg, France
[2]Université de Strasbourg, UMR 7242, ESBS, Bld Sébastien Brand, Illkirch, Strasbourg, France
[3]CNRS, UMR 7242, ESBS, Bld Sébastien Brand, Illkirch, Strasbourg, France
[4]Groupe Méthode Recherche Clinique, Hôpitaux Universitaires de Strasbourg, France

Email Addresses of Co-authors:
Hanna Manko (hanna.manko@etu.unistra.fr)
Vincent Normant (normant@unistra.fr)
Quentin Perraud (q.perraud@unistra.fr)
Tania Steffan (tania.steffan@unistra.fr)
Véronique Gasser (veronique.gasser@unistra.fr)
Emmanuel Boutant (emmanuel.boutant@unistra.fr)
Éléonore Réal (eleonore.real@unistra.fr)
Isabelle J. Schalk (isabelle.schalk@unistra.fr)
Yves Mély (yves.mely@unistra.fr)

Corresponding author:
Julien Godet (julien.godet@unistra.fr)

KEYWORDS:

FRET-FLIM, protein-protein interactions, *Pseudomonas aeruginosa*, bacteria, imaging, fluorescence

SUMMARY:

We describe here a protocol to characterize protein-protein interactions between two highly-differently expressed proteins in live *Pseudomonas aeruginosa* using FLIM-FRET measurements. The protocol includes bacteria strain constructions, bacteria immobilization, imaging and post-imaging data analysis routines.

ABSTRACT:

Protein-protein interactions (PPIs) control various key processes in cells. Fluorescence lifetime imaging microscopy (FLIM) combined with Förster resonance energy transfer (FRET) provide accurate information about PPIs in live cells. FLIM-FRET relies on measuring the fluorescence lifetime decay of a FRET donor at each pixel of the FLIM image, providing quantitative and accurate information about PPIs and their spatial cellular organizations. We propose here a detailed protocol for FLIM-FRET measurements that we applied to monitor PPIs in live

Published at jove.com doi: 10.3791/61602

Pseudomonas aeruginosa in the particular case of two interacting proteins expressed with highly different copy numbers to demonstrate the quality and robustness of the technique at revealing critical features of PPIs. This protocol describes in detail all the necessary steps for PPI characterization - starting from bacterial mutant constructions up to the final analysis using recently developed tools providing advanced visualization possibilities for a straightforward interpretation of complex FLIM-FRET data.

INTRODUCTION:

Protein-protein interactions (PPIs) control various key processes in cells[1]. The roles of PPIs differ based on protein composition, affinities functions and locations in cells[2]. PPIs can be investigated via different techniques[3]. For example, co-immunoprecipitation is a relatively simple, robust, and inexpensive technique commonly used tool to identify or confirm PPIs. However, studying PPIs can be challenging when the interacting proteins have low expression levels or when the interactions are transient or relevant only in specific environments. Studying PPIs occurring between the different enzymes of the pyoverdine pathway in *P. aeruginosa* requires that the repression of the general iron-co-factored repressor Fur is relieved to allow the expression of all the proteins of the pyoverdine pathway to be expressed in the cell[4,5,6]. This common regulation for all the proteins of the pathway results in timely expressions in the cell expected to promote their interactions. The diversity in term of size, nature, expression levels and the number of proteins of this metabolic pathway make it difficult for study in reconstituted systems[6]. Exploring PPIs in their cellular environment is therefore critical to further understand the biological functions of proteins in their native context.

Only few methods including fluorescence allow exploring PPIs in living cells[7]. Amongst the different fluorescence parameters that can be measured, the fluorescence lifetime (i.e., the average time a fluorophore remains in its excited state before emitting a photon) is likely one of the most interesting parameters to explore in living cells. The fluorescence lifetime of a fluorophore is highly sensitive to its environment and FLIM can therefore provide chemical or physical information regarding the fluorophore surroundings[8]. This includes the presence of Förster resonance energy transfer (FRET) that can occur in the presence of an “acceptor” of fluorescence located at a short distance of a fluorescence “donor”. Energy transfer results in significant shortening of the donor fluorescence lifetime (**Figure 1A**), making Fluorescence Lifetime Imaging Microscopy (FLIM) a powerful approach to explore protein-protein interactions directly in live cells. FLIM can additionally provide spatial information about where the interactions take place in cells[7,8]. This approach is extremely powerful for investigating PPIs in situations where the labeling with fluorophores of the two interacting partners is possible.

For FRET to occur - critical conditions on the distance between two fluorophores are required[8,9]. The two fluorophores should not be distant from each other by more than 10 nm. Therefore, cautions must be taken when designing FLIM-FRET experiments to ensure that the donor and the acceptor of fluorescence have a chance to be located close to each other in the interacting complex. While this may seem constraining, it is in fact a true advantage as the distance-dependence of FRET ensures that two labelled proteins undergoing FRET have to physically interact (**Figure 1A**). The difficulties at getting clear answers about PPI in colocalization

Published at jove.com doi: 10.3791/61602

experiments (two colocalized proteins may not necessarily interact) are therefore not an issue using FLIM-FRET.

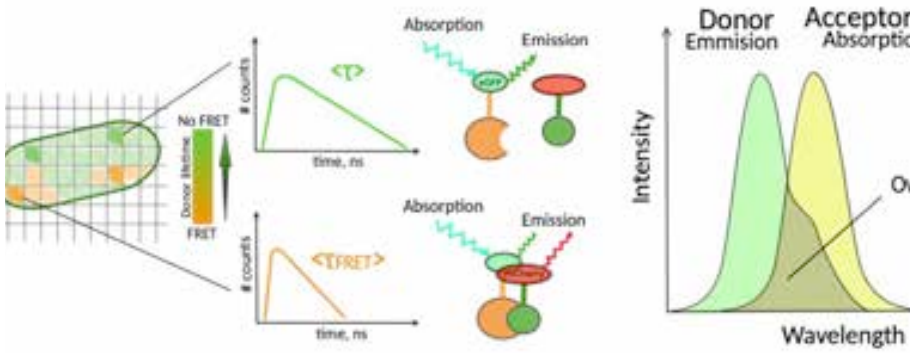

Figure 1: FLIM-FRET analysis principle. Each pixel of the FLIM-FRET multidimensional image contains information about the fluorescence decay recorded at this particular location (#counts = number of detected photons in the channel t). (**A**) The classical representation of the FLIM image is usually a false-color lifetime encoded 2D image (left). A decrease in the mean fluorescence lifetime of the donor - as seen by a change in the color scale - can be observed in the presence of FRET and is informative about the presence of PPIs in this spatial area. (**B**) Overlap between the donor emission spectrum and the acceptor absorption spectrum is necessary for FRET to occur.

A second requirement for FRET is that the emission spectrum of the donor and the absorption spectra of the acceptor should overlap[8] (**Figure 1B**). The fluorescence excitation of the donor should be at wavelengths that contribute very little to the direct fluorescence excitation of the acceptor. Not all combinations of fluorophores are possible and we additionally recommend to preferentially use donors with monoexponential fluorescence decays to facilitate FLIM-FRET interpretations[10]. Several couples of fluorescence proteins meet these requirements, including the popular eGFP-mCherry couple[11] (for a review on the palette of available fluorescent protein FRET pairs see[12,13]).

FLIM-FRET allows measuring the fluorescence lifetime decay of a FRET donor at every pixel of a FLIM image (**Figure 1A**). There are two major techniques to determine fluorescence lifetime that differ in acquisition and analysis: frequency-domain (FD)[14] and time-domain (TD). TD FLIM is more widespread and is performed using a pulsed illumination combined with different possible detection configurations including gating methods[15], streak camera[16] or time-correlated single photon counting (TCSPC) techniques[8]. For both FD and TD techniques, fluorescence lifetime is not directly measured but requires an analysis of the measured data to estimate the lifetime(s) or the presence of interactions. For TCSPC techniques, the most widely used analysis relies on fitting the decays with single or multi exponential functions using least square iterative re-convolutions that minimize the weighted sum of the residuals.

Finally, FLIM-FRET can be performed both by using single photon or multiphoton excitations. The latest have several advantages like reducing autofluorescence and photodamage out of the focal plane. Multiphoton excitations allow also a longer excitation depth if working in thick 3D samples[8]. On the contrary, single photon excitation is usually more efficient as the two-photon

Published at jove.com doi: 10.3791/61602

absorption cross sections of fluorescent proteins are limited[17].

Here, we propose a protocol for FLIM-FRET measurements of PPIs in live *P. aeruginosa* in the particular case of two interacting proteins (PvdA and PvdL) expressed with highly different numbers of copies to demonstrate the quality and robustness of the technique at revealing critical features of PPIs. PvdA and PvdL proteins are involved in pyoverdine biosynthesis. PvdA is a L-ornithine N5-oxygenase and synthesizes the L-N5-formyl-N5-hydroxyornithine from L-ornithine by hydroxylation (PvdA) and formylation (PvdF)[18]. PvdL is a non-ribosomal peptide synthesis (NRPS) enzyme composed of four modules. The first module catalyzes the acylation of myristic acid. The second module catalyzes the activation of L-Glu and its condensation to the myristic-coA. Then, the third module condenses a L-Tyr amino acid that is then isomerized in D-Tyr. Finally, the fourth module binds a L-Dab (Diaminobutyric acid) amino acid to form the acylated tripeptide L-Glu/D-Tyr/L-Dab[6]. PvdL is thus responsible for the synthesis of the three first amino acids of the pyoverdine precursor. The interaction of PvdA protein with PvdL is surprising as PvdL, on the contrary to PvdI and PvdJ, does not carry a module specific for the L-N5-formyl-N5-hydroxyornithine. This interaction suggest that all the enzymes responsible for the pyoverdine precursor biosynthesis are arranged in large transient and dynamic multi-enzymatic complexes[19,20].

In this report we explain in detail how to construct the bacterial strains expressing natively the two interacting eGFP and mCherry labelled proteins. We also describe sample preparation and conditions for efficient FLIM-FRET cell imaging. Finally, we propose a step-by-step tutorial for image analysis including a recently developed tool providing advanced visualization possibilities for straightforward interpretation of complex FLIM-FRET data. With this report, we would like to convince not only adventurous but most biologists that FRET-FLIM is an accessible and powerful technique able to address their questions about PPIs directly in the native cellular environment.

PROTOCOL:

1. Plasmid construction

1.1 Amplify by two PCR (PCR1 and 3) the DNA sequences (use genomic DNA of *P. aeruginosa* PAO1) of the 700 base pairs upstream and downstream of the regions corresponding to the insertion site in *P. aeruginosa* genome with high-fidelity DNA polymerase. Add restriction sites to primers in blue and green and add an overlapping sequence with mCherry to primers in red (**Figure 2**).

1.1.1 For PvdA labelled at the C-terminus with eGFP, amplify the 700 bp region upstream relative to the stop codon by the primers in blue, and amplify the 700 bp downstream region containing the stop codon with the primers in green.

1.1.2 For PvdL labelled at the N-terminus with mCherry, amplify the 700 bp region upstream to the PvdL gene, including the start codon, by the primers in blue, and amplify the 700 bp downstream region with the primers in green.

Published at jove.com doi: 10.3791/61602

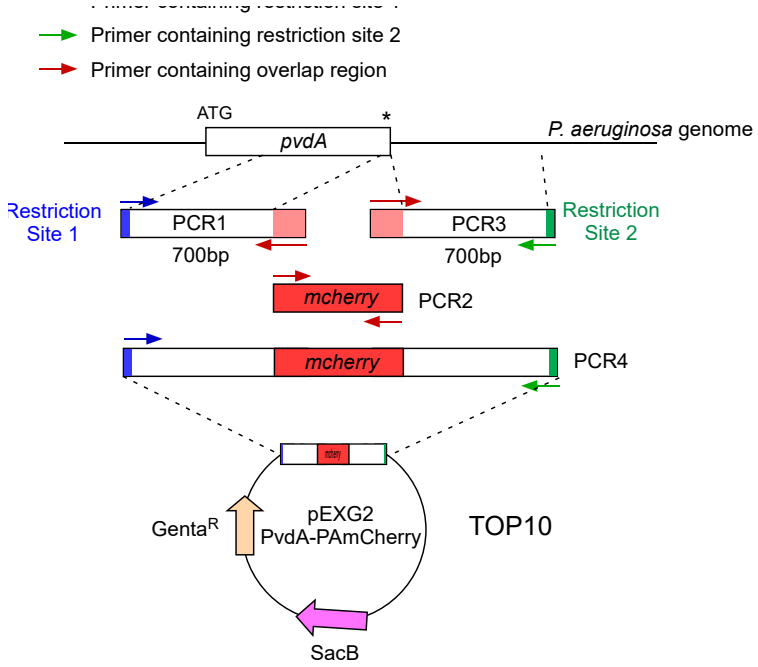

Figure 2: Overview of PCR strategy and plasmids construction used for the construction of PvdA-mCherry. See text for details - pvdA encodes an enzyme involved in the biosynthesis of the siderophore pyoverdine, a secondary metabolite involved in iron acquisition.

1.2 Amplify the eGFP encoding DNA (without the start and stop codons) with primers in red with High-Fidelity DNA polymerase.

1.3 Purify the PCR products on a PCR clean up column (**Table of Materials**).

1.4 Mix overlapping PCR products in equimolar ratio and perform a second PCR using primers with restriction site used for PCR 1 and 3 (green and blue in **Figure 2**).

1.5 Migrate the PCR product in agarose-1x TAE (Tris-Base Acetate EDTA pH 8.0) gel, cut the corresponding band and extract the amplicon with a PCR clean up kit (**Table of Materials**).

NOTE: The protocol can be paused here.

1.6 Digest PCR amplicon and pEXG2 plasmid using the corresponding restriction enzymes[21].

1.7 Ligate plasmid and insert with T4 DNA ligase using 90 ng of plasmid and molecular ratio 1:1 (plasmid:insert).

Published at jove.com doi: 10.3791/61602

1.8 Transform plasmids construction in chemically competent cells *E. coli* TOP10 cells by mixing ligation product and 100 µL of TOP10. Incubate the competent bacteria/plasmid mixture on ice for 30 min before proceeding with a 42 °C heat shock for 60 s. Then, put the tube on ice for 10 min.

1.9 Add 1 mL of lysogeny broth (LB) to the bacteria and incubate at 37 °C for 1 h.

1.10 Plate 100 µL bacteria on LB agar containing 15 µg/mL gentamicin.

1.11 Incubate overnight at 37 °C.

1.12 Screen the presence of the insert by colony PCR: from one isolated transformant colony, pick up a minute amount of bacteria to be added to a PCR mix containing primers hybridizing on the plasmid in such a way that the presence of the amplicon could be detected by running the product on an agarose gel (DNA polymerase). From the same colony used for PCR, transfer a small amount of bacteria on a fresh plate containing 15 µg/mL gentamicin to be isolated and used for plasmid extraction. Finally, isolate and purify the plasmid (**Table of Materials**) and verify the insert by sequencing.

1.13 Store TOP10 bacteria containing the plasmid in LB with 20 % glycerol in 1.5 mL microtube at -80 °C and the purified plasmid at -20 °C in 1.5 mL tube.

NOTE: The protocol can be paused here

2 Fluorescent tag insertion into the chromosomal genome of P. aeruginosa (Figure 3)

2.1 Grow *P. aeruginosa*, TOP10 and *E. coli* helper bacteria, each one in 5 mL of LB without antibiotic at 30 °C under orbital shaking overnight[22]. Generate fluorescent tag insertion in the genome of *P. aeruginosa* by transferring the plasmid from E. coli TOP10 into the PAO1 strain and integrating the plasmid into the genome by homologous recombination. A second crossing-over event excising the vector generate the corresponding mutant.

2.2 Measure the optical density at 600 nm ($OD_{600\ nm}$) of the bacterial culture and mix an equal quantity of *P. aeruginosa* (500 µL, $OD_{600\ nm}$ = 1.0) with *E. coli* TOP10 pEXG2 (500 µL, $OD_{600\ nm}$ = 1.0) and *E. coli* HB101 pRK600 helper (500 µL, $OD_{600\ nm}$ = 1.0) in 1.5 mL microtube.

2.3 Centrifuge 5 min at 9,300 x *g* to pellet the bacteria.

NOTE: Online tools can be used to convert centrifugal g-force to rotation per minute (rpm) to adjust the centrifuge speed.

2.4 Keep the bacterial pellet and discard the supernatant.

2.5 Resuspend the pellet containing bacteria in 50 µL of LB.

Published at jove.com doi: 10.3791/61602

2.6 Plate a spot (~50 µL) of the mixture on the middle of LB agar (preheat at 37 °C) and incubate 5 h at 37 °C.

2.7 Scrap the spot with a sterile inoculation loop and resuspend in 1 mL of LB.

2.8 Plate 100 µL of this bacterial suspension on LB agar containing 10 µg/mL chloramphenicol to eliminate *E. coli* (*E. coli* TOP10 pEXG2 and *E. coli* HB101 pRK600 helper are sensitive to chloramphenicol but *P. aeruginosa* is naturally resistant) and 30 µg/mL gentamicin and incubate 2 days at 37 °C.

2.9 Resuspend one colony in 1 mL LB and incubate at 37 °C under orbital shaking 4h.

2.10 Centrifuge 3 min at 9,300 x *g* and discard 950 µL of supernatant. Resuspend the pellet in 50 µL of LB and isolate the mixture on LB agar containing sucrose and without NaCl.

2.11 Incubate overnight at 30 °C.

2.12 Spot isolated colonies on LB agar and LB agar containing 15 mg/mL gentamicin in order to check the gentamicin sensitivity.

2.13 Verify the eGFP or mCherry insertion by PCR colonies (DNA polymerase) and sequencing using specific primers.

Published at jove.com doi: 10.3791/61602

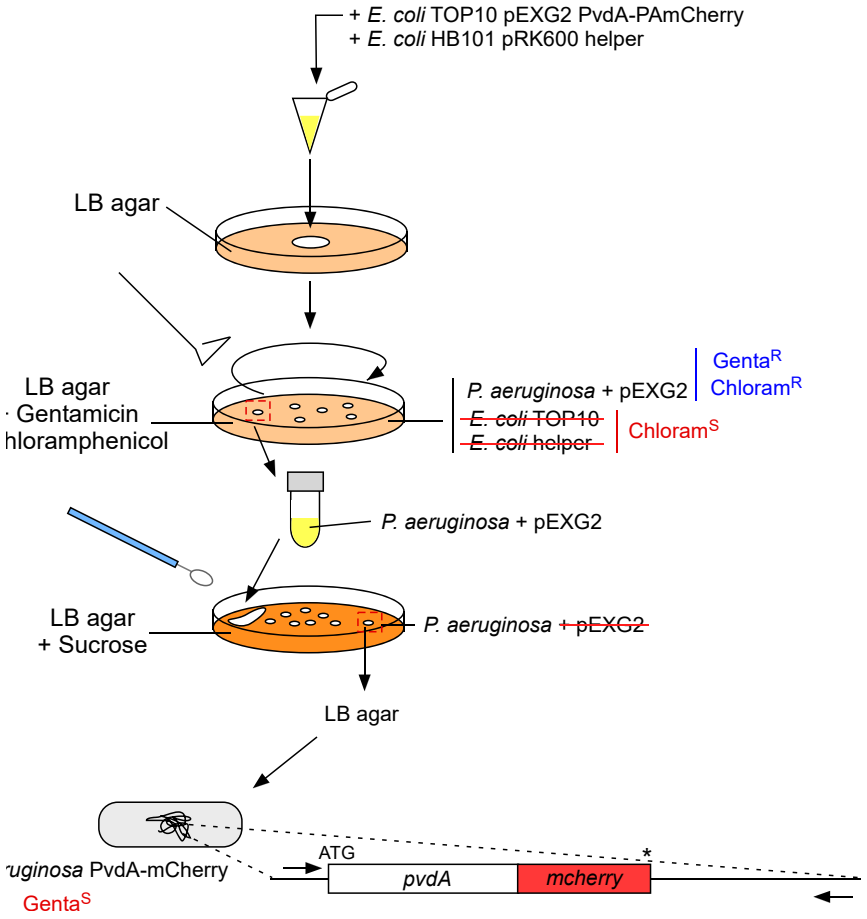

Figure 3: Protocol of construction of *P. aeruginosa* strains by fluorescent tag insertion. See text for details.

3 Pyoverdine measurement

3.1 Grow bacteria in 5 mL of LB at 30 °C under orbital shaking overnight.

3.2 Pellet bacteria by centrifugation, wash and grow them in 5 mL of SM (Succinate Medium, composition: 6 $g \cdot L^{-1}$ K_2HPO_4, 3 $g \cdot L^{-1}$ KH_2PO_4, 1 $g \cdot L^{-1}$ $(NH_4)_2 SO_4$, 0.2 $g \cdot L^{-1}$ $MgSO_4$, 7 H_2O and 4 $g \cdot L^{-1}$ sodium succinate with the pH adjusted to 7.0 by adding NaOH) at 30 °C under orbital shaking overnight. SM is an iron-deprived medium - the absence of iron will activate the expression of the proteins of the pyoverdine pathway normally repressed in the presence of iron.

3.3 Measure $OD_{600\,nm}$ and dilute bacteria again in fresh SM medium at $OD_{600\,nm} = 0.1$ and grow

Published at jove.com doi: 10.3791/61602

them at 30 °C under orbital shaking overnight.

3.4 Measure $OD_{600\ nm}$ to determine the quantity of bacteria in each sample.

3.5 Prepare a quartz cuvette containing 100 µL of *P. aeruginosa* culture and complete to 1 mL of SM (900 µL). Prepare a quartz cuvette containing 1 mL of SM medium (blank).

3.6 Using a UV-visible spectrophotometer, measure the absorbance at the maximum of the absorption peak. At pH 7.0, the maximum of absorption of pyoverdine will occur at ~400 nm. Determine the pyoverdine (apo form) concentration in sample using the Beer-Lambert law using a molar extinction coefficient at 400 nm of ε = 19 000 $M^{-1} \cdot cm^{-1}$.

NOTE: Pyoverdine can be quantified in the range of absorbance from ~0.1 to ~1 (depending on UV-Visible spectrophotometer) in which the absorbance linearly increases with concentration.

4 Bacteria culture and conditions for cells to express PvdA, PvdL and PvdJ

4.1 On day 1, inoculate a tube with 5 mL of LB from the appropriate glycerol stock of bacteria and grow bacteria over night at 30 °C at 200 rpm in an orbital shaker incubator.

4.2 On day 2, pellet cells by centrifugation at 3,000 x *g* for 3 min and discard the supernatant.

4.3 Resuspend the cells in 10 mL of SM.

4.4 Repeat steps 4.2-4.3 once and grow bacteria in SM overnight at 30 °C 200 rpm.

4.5 On day 3, dilute 1/10 the bacteria culture in fresh SM.

4.6 Grow diluted bacteria again overnight at the same conditions.

NOTE: The presence of pyoverdine can be detected visually as it colors in yellow-green the growing media. It shows that the expression of the proteins of the pyoverdine pathway have been activated and that enzymes of interest are being expressed in the cells.

5 Preparation of agarose pad (Figure 4)

5.1 Place a microscope glass-slide on a flat horizontal surface. Arrange two glass-slides topped with two layers of adhesive tape on each side of the initial slide.

NOTE: Keep a 1-2 mm space between the three aligned slides to prevent the meleted agarose to eventually spread on the slides with adhesive tape.

5.2 Pipette and pour a droplet of 70 µL of 1% melted agarose on the glass-slide. Add a fourth slide on the top to flatten the agarose droplet and press down gently. Wait about a minute.

Published at jove.com doi: 10.3791/61602

5.3 Take off the upper slide and drop with a pipette about 3 µL of bacteria into 3 to 4 spots at different locations onto the agarose pad.

5.4 Cover with a microscopy glass coverslip (for example a 22x22 mm #1.5 thickness).

NOTE: Flatness and thickness of the coverslips are important for working with two-photon excitations. Precision coverslips with controlled uniform flatness and low autofluorescence are usually a good choice.

5.5 Fix the coverslip with melted paraffin to seal the coverslip onto the glass slide. Start by fixing the four corners of the coverslip.

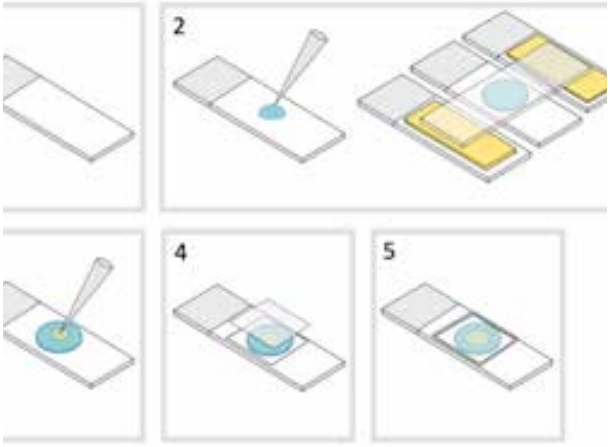

Figure 4: Agarose pad preparation.

6 Imaging with a two-photon microscopy setup

NOTE: We are using a home-made two-photon excitation scanning inverted microscope with a 60x 1.2NA water immersion objective operating in de-scanned fluorescence collection mode. Two-photon excitation wavelength is set at 930 nm. It is provided by a Ti:Sapphire laser (80 MHz repetition rate, ≈ 70 fs pulse width) working at 10-20 mW. Fluorescence photons were collected through a 680 nm short pass filter and a 525/50 nm band-pass filter before being directed to a fiber-coupled avalanche photo-diode connected to a time-correlated single photon counting (TCSPC) module. The microscope is also equipped with a transmission fluorescence lamp. Several FLIM-FRET microscopes are now commercially available and many imaging facilities are equipped with setups able to perform FLIM-FRET measurements.

6.1 Use the fluorescence lamp to focus the objective on the monolayer of bacteria in the sample and select regions of interest.

Published at jove.com doi: 10.3791/61602

6.2 Check that the excitation laser shutter is closed and that the infrared light coming from the laser is blocked and do not enter the microscope.

Caution: Careful attention and constant vigilance should be given working with IR pulsed lasers as the laser light cannot be seen by eyes but any and even transient direct exposition or laser reflection can be extremely harmful and create irreversible eye damages. Please refer to the local laser safety procedures and training before using microscopy setups.

6.3 Place the microscopy slide on the stage with the coverslips facing the objective.

6.4 Check that the fluorescence lamp is ON.

6.5 Turn the filter cube turret to select the eGFP cube and open the fluorescence lamp shutter.

6.6 Send the fluorescence light towards the eyepiece of the microscope.

Caution: Ensure appropriate filters are disposed in the light path to discard direct excitation light coming from the fluorescence lamp that can damage eyes.

6.7 Focus the objective on bacteria using the microscope knob.

6.8 Select a region of interest in the sample by translating it using the joystick controlling the motorized stage

NOTE: Focusing is easier with highly fluorescent sample allowing the fluorescence to be seen directly with eyes.

6.9 Switch the excitation for the 2PE laser for FLIM-FRET measurements.

6.10 Send the fluorescence emission path back towards the detector.

6.11 Turn back the filter cube turret to select for the dichroic cube for the 930 nm laser.

6.12 Set the laser power to 20 mW.

6.13 Set the size of the region of interest to 30 µm. This operation adjusts the voltage operating the galvo-mirrors and defines the range of their movements (**Figure 5**).

6.14 Turn on detector and start scanning the sample - the start and stop buttons controlling the scanning also control the opening and closing of the laser shutter both for safety reasons and to limit the photobleaching of the sample (**Figure 5**).

Published at jove.com doi: 10.3791/61602

Figure 5: Schematic representation of the interface of microscope control software.

6.15 If necessary, adjust the focus by slightly moving the microscope fine focus knob.

6.16 Choose the field of view for imaging by moving finely the stage from the computer interface. This can be done on the setup by moving the cross on the image in the microscope control software (**Figure 5**) that will define the new center of the image and pressing **Move Stage**. A good field of view for acquisition corresponds to an image with 10-30 immobile bacteria, all correctly focused (all bacteria are on the same plane). If interested in extracting single cells FLIM-FRET data, ensure that bacteria are well individualized (image segmentation will be much easier).

6.17 Open the SPCM software (commercial software for data acquisition) and check that the photons count rate is not too high to avoid pile-up effect that can affect lifetime measurements. If necessary, lower down the laser intensity to keep the photon count rate low (around 1% of the laser repetition rate).

NOTE: Pile-Up effect describes the effects of photons lost at high photon count rates due to the dead time of the Time Correlated Single Photon Counting (TCSPC) devices. If Pile-Up occurs, the measured average lifetime becomes artificially shorter with possibly an additional shorter component that can appear in the decay due to the oversampling the fast-emitting photons.

6.18 Adjust acquisition parameters including the acquisition collection time (typically 60 s to 180 s are required to collect enough photons).

6.19 Press the **Start** button and wait for the acquisition to complete.

6.20 Save the data.

6.21 Stop scanning the sample and turn off the detector.

6.22 Select another field of view in sample and repeat steps 6.14-6.22 or image a new microscopy slide by repeating steps 6.1-6.22.

NOTE: *P. aeruginosa* can live and divide for up to 6-8 hours at room temperature on the agarose

Published at jove.com doi: 10.3791/61602

pad (corresponding to at last ~4 doubling time at 20°C). Ideally, do not wait too long to perform FLIM-FRET measurement to avoid observing a pad completely covered with bacteria.

7 Data analysis

7.1. Basic analysis

7.1.1 Run the SPCImage software.

7.1.2 Import the saved SPCM file. The intensity image is displayed on the left upper panel of the software (**Figure 6** blue box).

7.1.3 Examine the decay curve window (**Figure 6** green box) which displays the decay data corresponding to the pixel selected in the intensity image (**Figure 6** blue box). The photon numbers of each time channel are shown as blue dots and the fit of the decay is drawn as a red line. Note that after loading the data the software displays the brightest pixel of the image. Move the blue cross across the image to examine pixels with lower intensity. The decay window will automatically refresh at each new pixel position.

NOTE: Measuring the Instrumental Response Function (IRF) of a laser scanning system is very difficult. An IRF calculated from the rising edge of the fluorescence decay curves in the FLIM data can be used for decay deconvolution. This is the option done by default in SPCimage (**Figure 6** green curve).

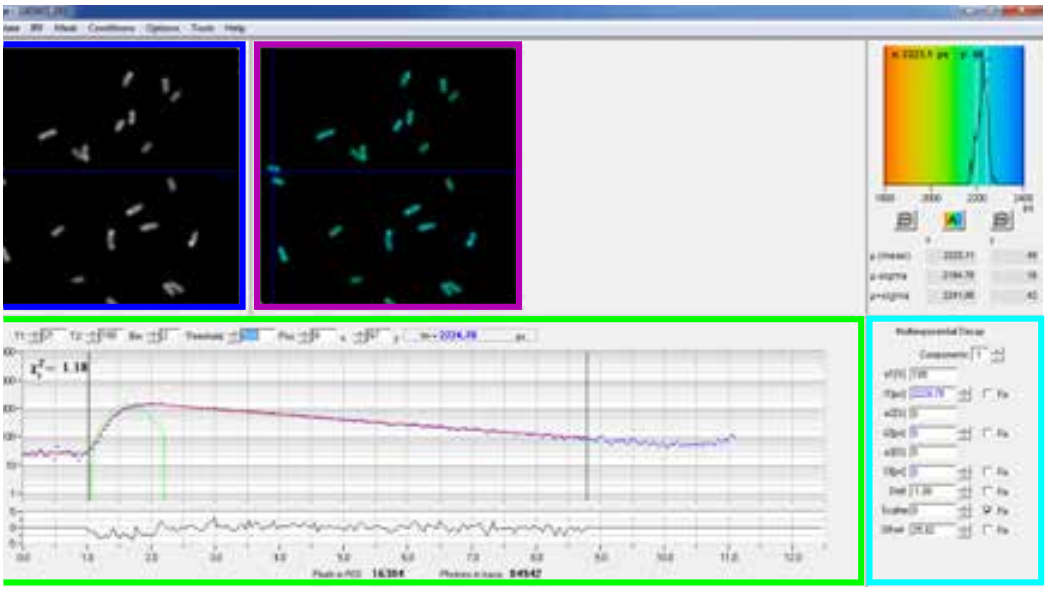

Figure 6: Main panel of the data analysis window of SPCImage software. Intensity image (blue box), lifetime image (purple box), lifetime histogram (upper right), decay curve at selected position (green box), and decay parameters

Published at jove.com doi: 10.3791/61602

at selected position (cyan box) of a representative PvdA-eGFP decay recorded in live *P. aeruginosa* using a bh SPC830 acquisition card on a home-made Two-Photon Excitation-FLIM-FRET setup. The experimental decay curve of the pixel pointed in the above image, its mono-exponential fit (red curve) deconvoluting the decay from its calculated instrumental response function (green curve) can be seen in the green panel.

7.1.4 Adjust the fitting range by moving the starting and ending channels of the fitting box (T1 and T2 in the green box). T1 should start at the first few channels of the rising decay and T2 define the last channel at the end of the decay and can be chosen as one of the last channels of the decay with a number of photons above the photons count offset (i.e., the levels of photons counted before the decay rises).

7.1.5 Choose the binning by changing the **Bin** value. The curve decay integrates the photon counting of the selected pixel together with an area of i pixels around the cursor position defined by the bin parameter (increasing the binning will increase the number of photons in the decay and may be helpful to reach the photon counts required for multi-exponential models).

7.1.6 Adjust the **Threshold** value. Pixels that do not have at least one channel with a number of photons higher than the threshold value will not be included in the fitting procedure. Of course the higher the number of pixels to fit, the longer the analysis.

NOTE: FLIM data can contain an enormous number of pixels and time channels. The last versions of the software allow using GPU (Graphics Processor Unit) to process a large number of pixels in parallel, which massively reduces processing times. It can be interesting to adjust the binning and threshold parameters using images corresponding to bacteria constructions exhibiting the lowest fluorescence intensity (e.g., with bacterial strains with the lowest expression levels). This will ensure that the relevant decays observed in these samples will meet the filtering criteria and will be included in the analysis. These parameters can then be used for all images.

7.1.7 Adjust, if necessary, the decay parameters (cyan box). Let the shift vary, most of the time scatter and offset can be fixed to zero if a look at the decay functions show that their contribution is negligible. The offset can be estimated looking at the first channels of the decay - note that imaging for a long time due to low fluorescence in the sample usually results in non-zero offset. Scattering occurs mostly in thick samples and can be considered negligible otherwise.

7.1.8 Before running the fit, select the fitting algorithm. Open the algorithm settings window in **Show/Hide Model Options**. Select maximum likelihood estimation (MLE) algorithm (**Figure 7A**).

Published at jove.com doi: 10.3791/61602

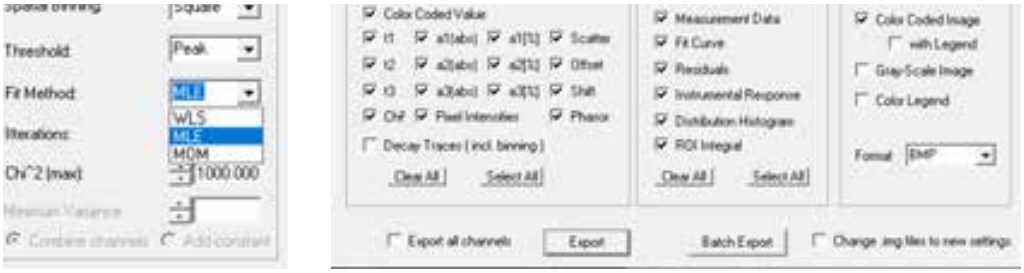

Figure 7: (A) Algorithm settings for fitting the decays with exponential models. Selecting MLE (maximum-likelihood algorithm or maximum-likelihood estimation, MLE) as the fit model, and **(B) export options window**.

7.1.9 Run the fitting of the image by clicking **Calculate | Decay matrix**. Once completed, the lifetime encoded FLIM image appears in the lifetime image panel (**Figure 6** purple box).

NOTE: On the decay curve window (**Figure 6** green box) it is possible to see the lifetime value that corresponds to each pixel of the image by moving the blue cross.

NOTE: to process a large number of similar FLIM data files automatically, a batch processing mode can be used.

7.1.10 Check the quality of the fit looking at the residuals (ideally distributed randomly around 0) and a Chi square value close to 1.

7.1.11 Fitted data can be exported in different formats. To export files in txt files, go to **File | Export**. In the **Export** options window (**Figure 7B**), choose **Select All** and then click **Export**.

7.1.12 Finally save the analysis file. Analysis files are saved as **.img* files and can be reopened directly in SPCImage.

NOTE: In particular cases of unbalanced donor/acceptor quantities, FLIM-FRET can reveal sub-populations in a mixture of interacting protein complexes - in particular when the concentrations of the two partners are very different, thus resulting in mixtures of complex and free species. Non-interacting species (characterized by a decay very similar to the donor only decay) can be discriminated from interacting ones assuming a spatial invariance of the donor lifetime components across the data set. Similarly, non-stoichiometric interacting complexes with either more donors or more acceptor of fluorescence may form. The fluorescence decays of such complexes are usually difficult to interpret. A FLIM diagram plot can be used to provide critical information about stoichiometry and binding mode of PPIs[20,23]. The FLIM diagram plot is a graphical representation of the shortest lifetime component as a function of its amplitude. It can be used to visualize pixels with similar decay signatures. To draw such representations,

Published at jove.com doi: 10.3791/61602

experimental fluorescence decays have to be fitted with a two exponential model. The following steps can be a guide through this process.

7.1.13 Start by analyzing the data of the donor only construction. It will allow determining the lifetime value of the donor. Ideally, measure this value over several images recorded in the same conditions as the donor/acceptor constructions to retrieve a robust lifetime value for the donor.

7.1.14 Once determined, fit the fluorescence decays of donor/acceptor constructions with a two-exponential model. In the cyan decay parameter box (**Figure 6**), set the number of components to 2. Fix t2(ps) parameter to the robust lifetime value of the donor determined in step 1 and check the box to fix this parameter.

NOTE: It is important to fix the long-lived lifetime τ2 in order to limit over-fitting, to improve fitting convergence, and to obtain more reliable two-exponential fit parameters[24,25,26].

7.1.15 Save the **img* file and export data as **.asc* files as in step 7.1.11.

7.2. Advanced analysis of the FLIM images in R

7.2.1 Install R (https://cran.r-project.org) and RStudio (https://rstudio.com) if necessary.

7.2.2 Open RStudio and create a new project.

7.2.3 Move all analysis **.asc* file in a folder called “data” in the project main folder.

7.2.4 Open a new script file (or open the supplementary script FLIM_analysis.R).

7.2.5 Install the dedicated flimDiagRam package for flim data analysis https://github.com/jgodet/flimDiagRam. Call the package in the workspace. (See the notice HowTo_FlimDiagRam)

NOTE: Installation of packages have to be done only once. Once installed, packages can be called from any new R session. Downloading R packages from github requires installing ‘devtools’ package. The installation of ‘devtools’ can take several minutes. The *flimDiagRam* package can be used to represent the parameters and distributions of the FLIM data, to extract FLIM data at the level of single individualized cells, to compare FLIM results across conditions or strains and to explore FLIM data using advanced visualization tools like the FLIM diagram plot.

7.2.6 Use the step-by-step commented code and the data are made available to independently reproduce all the sub-figures presented in the Representative Results section below. This tutorial can be found in the notice HowTo_FlimDiagRam at https://github.com/jgodet/flimDiagRam/blob/master/HowTo.pdf. The code can be easily transposed to analyze the data.

Published at jove.com doi: 10.3791/61602

REPRESENTATIVE RESULTS:

Empirical cumulative distribution functions (ecdf) of the fluorescence lifetimes measured for the different bacterial strains are shown in **Figure 8**. If FRET occurs, the ecdfs are shifted towards the shorter-lived lifetimes (**Figure 8A,8B**). Note that when the interaction of the two proteins results in a long distance between the two fluorophores, no FRET can occur (**Figure 8C**). This situation cannot be distinguished from the absence of interaction between the two partners in FLIM. It is therefore important, when inter-dye distance cannot be predicted from molecular models or known architectures of the complex, to consider labelling the proteins at different positions to maximize chances to probe the interaction. Similarly, due to the large difference in protein expressions between PvdA (highly expressed) and the non-ribosomal peptide synthetase PvdL (few copies per cells), the same PvdA/PvdL complex does not result in similar FLIM-FRET data. In fact, unbalanced stoichiometries can complicate the interpretation of FLIM-FRET data. Depending on which protein is labelled with the donor, unbalanced stoichiometries lead to differences in the contribution of the free as compared to the bound donor-labelled proteins in the recorded fluorescence lifetime distribution (**Figure 8A,8B**).

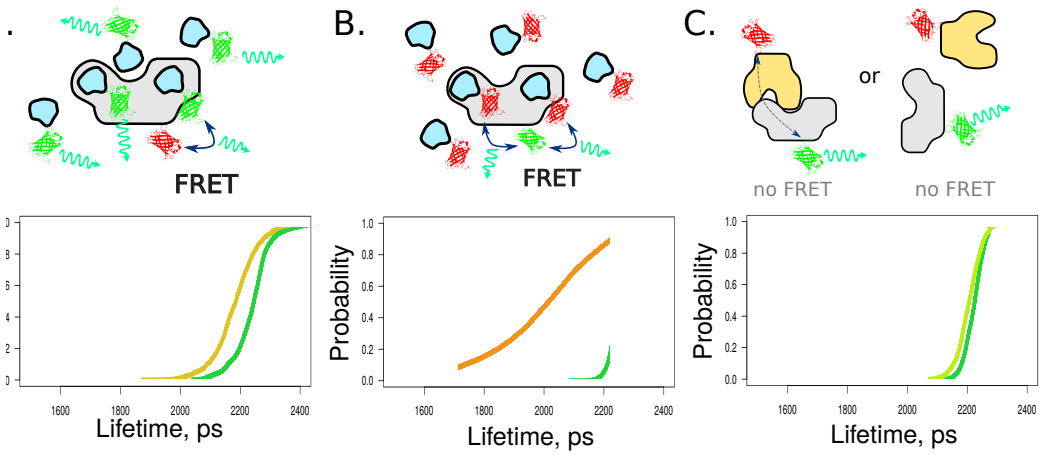

Figure 8: Illustration of changes occurring in the donor mean fluorescence lifetime distribution in response to FRET (single exponential model). Representation of the interactions of PvdL (grey form) with PvdA (blue form) (**A and B**) or PvdJ (yellow form) (**C**) proteins labeled with eGFP (green) or mCherry (red) fluorescent proteins. The empirical cumulative distribution functions (lower graphs) can clearly highlight the differences between the fluorescence lifetime distributions. (**A**) In the presence of an excess of PvdA labeled with the donor of fluorescence, the mean lifetime distribution of eGFP donors is dominated by donors that do not undergo FRET but also integrate the lifetime of the few donors undergoing FRET with mCherry-PvdL. In this situation, the lifetime distribution of the mixture (green-orange curve) is close to the lifetime distribution of the same mixture formed with unlabeled PvdL only (green curve). (**B**) If the order of labelling is changed and an excess of PvdA labeled with acceptors is present, the mean lifetime distribution is governed by the transferring species, including possibly donors that undergo FRET with multiple acceptors (orange curve). This distribution is therefore very different from the same complex formed with unlabeled PvdA (green curve). (**C**) If no FRET occurs because proteins do not interact or because the inter-dye distance is too large in the complex, changes in the lifetime distribution is almost superimposable to that of the donor only (compare the light green curve corresponding to the fluorescence lifetime distribution of the PvdJ-eGFP/mCherry-PvdL to the green curve corresponding to PvdJ-eGFP).

Published at jove.com doi: 10.3791/61602

The diagram plot can be used to provide critical information about the stoichiometry as seen in **Figure 9**. In the PvdA-eGFP/mCherry PvdL mutant, the quantity of donor-labelled PvdA is much higher than the quantity of mCherry PvdL. Amongst all donors present in the sample, only a few of them are interacting with PvdL. Contrary to the average FLIM value distribution, the FLIM diagram plot gives only the specific information contained in the decay component of the donors undergoing FRET. In **Figure 9A**, a single tau1 value centered at ~2.3 ns can be observed, representing about 30-40% of the species in the mixture. The single tau1 value suggests that each PvdA-eGFP donor can only transfer with one mCherry PvdL acceptor.

From the reverse labelling (PvdA-mCherry/eGFP PvdL), most of the eGFP PvdL proteins are expected to interact with PvdA-mCherry, due to the low number of PvdL as compared to PvdA. This is confirmed by the alpha1 values that are shifted towards higher values. Moreover, the tau1 values became much more distributed (**Figure 9B**) with the apparition of short-lived species with lifetimes as low as ~1.5 ns. This suggests that additional transfers occur as compared to the situation in **Figure 9A** and thus, that multiple PvdA proteins may bind to a single PvdL protein. As a result, for each complex, the eGFP lifetime will depend on the number and distribution of mCherry proteins with which eGFP is transferring energy. Taken together, the data suggest that each PvdL protein can interact with multiple PvdA proteins

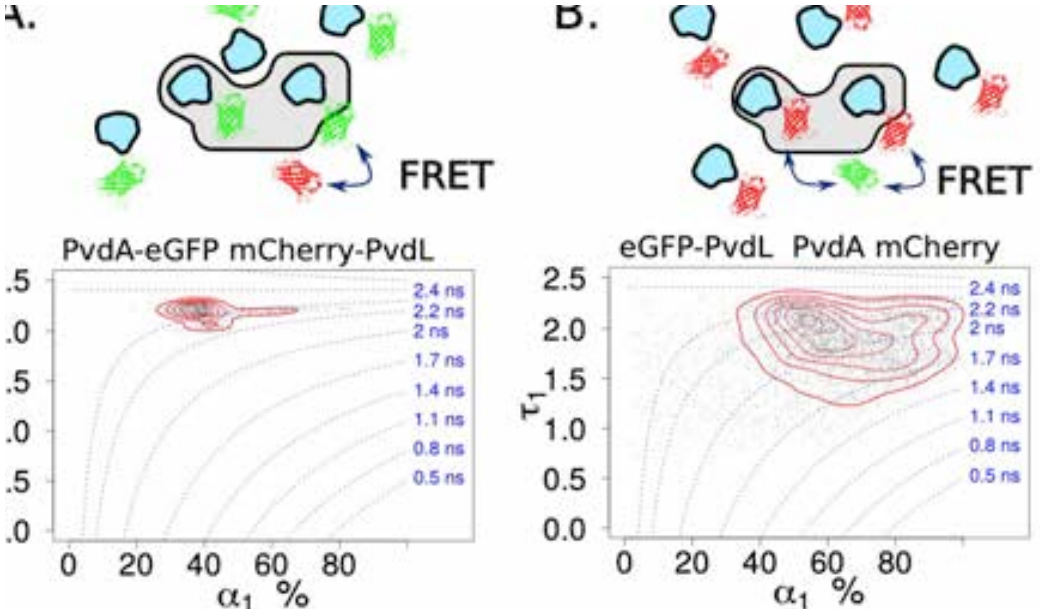

Figure 9: FLIM diagram plots in case of excess of donors (A) or acceptors (B) and multiple binding sites. The FLIM diagram plot gives the specific information contained in the decay component of the donor undergoing FRET retrieved using a two-exponential fit. In the PvdA-eGFP/mCherry-PvdL mutant (**A**), a single tau1 value is observed and its amplitude given by the scattered position of the data points on the horizontal axis is informative about the population of donors engaged in FRET. In the PvdA-mCherry/eGFP-PvdL system (**B**), the tau1 values are much more distributed, indicating that one PvdL (grey form) protein may interact with multiple PvdA (blue form) proteins.

Published at jove.com doi: 10.3791/61602

DISCUSSION:

FLIM-FRET offers some key advantages over intensity-based FRET imaging. Fluorescence lifetime is an intrinsic parameter of the fluorophore. As a consequence, it is not dependent on local concentrations of fluorophores neither on the intensity of the light excitation. The fluorescence lifetime is additionally also poorly affected by photo-bleaching. It is particularly interesting to evidence PPIs in cells where local proteins concentrations can be highly heterogeneous throughout the subcellular compartments or regions. FLIM-FRET is also interesting in all situations where the concentration of complex is low because the expression levels of both proteins or of one of the proteins are low.

In the context of PPIs, the FRET mechanisms responsible for the shortening of the lifetime and therefore information about the nature of the interactions are hard to infer considering only the average lifetime. Indeed, a shortening of the average lifetime can be due to a high proportion of species interacting with moderate FRET, or on the opposite to a low proportion of donors interacting at a short distance with the acceptor. This situation is even more complicated when complexes with unbalanced stoichiometries form. Graphical visualization tools allowing the representation of several dimensions (in the case of the diagram plot tau1, alpha and <tau>) can be useful to provide critical information on the nature of the complexes that form. Alternative graphical representations of the data, like the phasor based analysis[27,28] proposing a graphical representation of the raw FLIM data in a vector space, are also interesting in this context.

Choosing how to tag the proteins of interest is a key point for successful FLIM-FRET experiments. Most critically, tags should not modify or alter the interaction of proteins. Unfortunately, except in rare cases where the structures of the proteins are known or can be predicted, in most cases one is compelled to trial-and-error approaches. Interpretations of FLIM-FRET in the absence of energy transfer have therefore always to consider the possibility that labels can alter the interaction. For this reason, FLIM-FRET can be seen as a confirmatory technique in the sense that if an interaction is observed, it should exist in the absence of label. Disposing of an external functional readout - like checking that the production of pyoverdine by the mutated strains expressing doubly labelled proteins is similar to wild type strains - is particularly useful to interpret FLIM-FRET results.

Imaging is not a high-throughput method for detecting PPIs and has been so far exploited to confirm suspected or predicted PPIs. In this confirmatory context, pushing the analysis to extract from the data as much information as possible makes sense to gain deeper understandings of the mechanisms involved in the PPI. Some attempts are being performed[29,30,31] to turn FLIM-FRET setups adapted to screening strategies. Developing advanced easily available and automated analysis will ensure the possibility to process the large amount of data produced by high-throughput screening methods. In this context, fitting procedures using least square methods that require high count statistics might be poorly adapted to estimate FRET. A variety of alternative methods have been developed[16,32], including non-fitting methods (reviewed in Padilla-Parra et al. 2011 [33]). These methods differ in calculation speed, minimal number of photons required for proper analysis, accuracy, complexity and type of data that can be efficiently processed. Techniques like the minimal fraction of interacting donor[34] or phasor

approach[35,36,37] have the potential to perform high speed acquisitions in FRET–FLIM and still be quantitative to process large amount of data or even to reach video-rate speeds.

The requirement of constructing fluorescently labelled protein that do not perturb the native functions of the proteins in cells is a major concern for scaling up the speed and the number of PPI explored. Alternative new labelling strategies, based for example on small-molecule fluorogenic probes[38,39] may be a way to circumvent this critical limitation. Disposing of fluorescent probes compatible with FLIM-FRET and able to label other cell components (like nucleic acids or membrane) will also broaden the nature of the interactions FLIM-FRET can characterize.

In a close future, we believe the greatest breakthrough in the FLIM-FRET field will result from innovation in data processing. Methods like compressed sensing[40] should enable efficient and accurate reconstruction of FLIM image from sparse decay data - possibly speeding up further the acquisition rate that would allow to perform real time FLIM-FRET on fast changing process. Similarly, machine learning applied to FLIM data regarding pixel classification or regression, denoising or signal restoration will allow outstanding image reconstruction and analysis that will further increase the interest of FRET-FLIM methods[41,42].

ACKNOWLEDGMENTS:
We acknowledge Dr Ludovic Richert for his valuable assistance on FLIM data acquisition and for the technical maintenance and development of the FLIM setup. This work was funded by grants from Fondation pour la Recherche en Chimie (https://icfrc.fr/). VN is funded by the Fondation pour la Recherche Médicale (FRM-SPF201809006906). YM is grateful to the Institut Universitaire de France (IUF) for support and providing additional time to be dedicated to research. IJS and JG acknowledge the Institute on Drug Delivery of Strasbourg for its financial support.

DISCLOSURES:
The authors have nothing to disclose.

REFERENCES:
1. Braun, P., Gingras, A. C. History of protein-protein interactions: From egg-white to complex networks. *Proteomics*. **12**, 1478–1498 (2012).
2. Nooren, I. M. A., Thornton, J. M. Structural characterisation and functional significance of transient protein-protein interactions. *Journal of Molecular Biology*. **325**, 991–1018 (2003).
3. Hayes, S., Malacrida, B., Kiely, M., Kiely, P. A. Studying protein-protein interactions: Progress, pitfalls and solutions. *Biochemical Society Transactions*. **44**, 994–1004 (2016).
4. Guillon, L., Altenburger, S., Graumann, P. L., Schalk, I. J. Deciphering protein dynamics of the siderophore pyoverdine pathway in Pseudomonas aeruginosa. *PLoS ONE* **8**, 1–9 (2013).
5. Ringel, M. T., Brüser, T. The biosynthesis of pyoverdines. *Microbial Cell*. **5**, 424–437 (2018).
6. Schalk, I. J., Rigouin, C., Godet, J. An overview of siderophore biosynthesis among fluorescent Pseudomonads and new insights into their complex cellular organization. *Environmental Microbiology*. **22**, 1447–1466 (2020).
7. Cui, Y. et al. Techniques for detecting protein-protein interactions in living cells: principles, limitations, and recent progress. *Science China Life Sciences*. (2019)
8. Day, R. N., Mazumder, N., Sun, Y., Christopher, K. G. FRET microscopy: Basics, issues and advantages of

FLIM-FRET imaging. *Springer Series in Chemical Physics*. **111**, 249–276 (2015).
9. Bastiaens, P. I. H., Squire, A. Fluorescence lifetime imaging microscopy: Spatial resolution of biochemical processes in the cell. *Trends in Cell Biology*. **9**, 48–52 (1999).
10. Yasuda, R. Imaging spatiotemporal dynamics of neuronal signaling using fluorescence resonance energy transfer and fluorescence lifetime imaging microscopy. *Current Opinion in Neurobiology*. **16**, 551–561 (2006).
11. Tramier, M., Zahid, M., Mevel, J.-C., Masse, M.-J., Coppey-Moisan, M. Sensitivity of CFP/YFP and GFP/mCherry Pairs to Donor Photobleaching on FRET Determination by Fluorescence Lifetime Imaging Microscopy in Living Cells. *Microscopy Research and Technique*. **71**, 146–157 (2008).
12. Bajar, B. T., Wang, E. S., Zhang, S., Lin, M. Z., Chu, J. A guide to fluorescent protein FRET pairs. *Sensors (Switzerland)* . **16**, 1–24 (2016).
13. Piston, D. W., Kremers, G. J. Fluorescent protein FRET: the good, the bad and the ugly. *Trends in Biochemical Sciences*. **32**, 407–414 (2007).
14. Leray, A. et al. Optimized protocol of a frequency domain fluorescence lifetime imaging microscope for fret measurements. *Microscopy Research and Technique*. **72**, 371–379 (2009).
15. Elson, D. S. et al. Real-time time-domain fluorescence lifetime imaging including single-shot acquisition with a segmented optical image intensifier. *New Journal of Physics*. **6**, 1–13 (2004).
16. Rajoria, S., Zhao, L., Intes, X., Barroso, M. FLIM-FRET for Cancer Applications. *Current Molecular Imaging.* **3**, 144–161 (2014).
17. Drobizhev, M., Makarov, N. S., Tillo, S. E., Hughes, T. E., Rebane, A. Two-photon absorption properties of fluorescent proteins. *Nature Methods*. **8**, 393–399 (2011).
18. Visca, P., Ciervo, A., Orsi, N. Cloning and nucleotide sequence of the pvdA gene encoding the pyoverdin biosynthetic enzyme L-ornithine N5-oxygenase in Pseudomonas aeruginosa. *Journal of Bacteriology*. **176**, 1128–1140 (1994).
19. Imperi, F., Visca, P. Subcellular localization of the pyoverdine biogenesis machinery of Pseudomonas aeruginosa: A membrane-associated 'siderosome'. *FEBS Letters*. **587**, 3387–3391 (2013).
20. Gasser, V. et al. In cellulo FRET-FLIM and single molecule tracking reveal the supra-molecular organization of the pyoverdine bio-synthetic enzymes in Pseudomonas aeruginosa. *Quarterly Reviews of Biophysics*. 1–11 (2019).
21. Rietsch, A., Mekalanos, J. J. Metabolic regulation of type III secretion gene expression in Pseudomonas aeruginosa. *Molecular Microbiology*. **59**, 807–820 (2006).
22. Herrero, M., De Lorenzo, V., Timmis, K. N. Transposon vectors containing non-antibiotic resistance selection markers for cloning and stable chromosomal insertion of foreign genes in gram-negative bacteria. *Journal of Bacteriology*. **172**, 6557–6567 (1990).
23. Godet, J., Mély, Y. Exploring protein-protein interactions with large differences in protein expression levels using FLIM-FRET. *Methods and Applications in Fluorescence*. **8**, 014007 (2019).
24. El Meshri, S. E. et al. Role of the nucleocapsid domain in HIV-1 gag oligomerization and trafficking to the plasma membrane: A fluorescence lifetime imaging microscopy investigation. *Journal of Molecular Biology*. **427**, 1480–1494 (2015).
25. Becker, W. The bh TCSPC Handbook. *Scanning*. 1–566 (2010).
26. Richert, L., Didier, P., de Rocquigny, H., Mély, Y. *Monitoring HIV-1 protein oligomerization by FLIM FRET microscopy*. *Springer Series in Chemical Physics*. **111** (2015).
27. Fereidouni, F., Blab, G. A., Gerritsen, H. C. Phasor based analysis of FRET images recorded using spectrally resolved lifetime imaging. *Methods and Applications in Fluorescence*. **2**, (2014).
28. Fereidouni, F., Gorpas, D., Ma, D., Fatakdawala, H., Marcu, L. Rapid fluorescence lifetime estimation with modified phasor approach and Laguerre deconvolution: a comparative study. *Methods and Applications in Fluorescence*. **5**, 035003 (2017).
29. Margineanu, A. et al. Screening for protein-protein interactions using Förster resonance energy transfer (FRET) and fluorescence lifetime imaging microscopy (FLIM). *Scientific Reports*. **6**, (2016).
30. Guzmán, C., Oetken-Lindholm, C., Abankwa, D. Automated High-Throughput Fluorescence Lifetime Imaging Microscopy to Detect Protein–Protein Interactions. *Journal of Laboratory Automation*. **21**, 238–245 (2016).
31. Liu, W., Cui, Y., Ren, W., Irudayaraj, J. Epigenetic biomarker screening by FLIM-FRET for combination therapy in ER+ breast cancer. *Clinical Epigenetics*. **11**, 1–9 (2019).
32. Liu, X. et al. Fast fluorescence lifetime imaging techniques: A review on challenge and development. *Journal of Innovative Optical Health Sciences*. **12**, 1–27 (2019).

33. Padilla-Parra, S., Auduge, N., Coppey-Moisan, M., Tramier, M. Non fitting based FRET-FLIM analysis approaches applied to quantify protein-protein interactions in live cells. *Biophysical Reviews*. **3**, 63–70 (2011).
34. Padilla-Parra, S., Audugé, N., Coppey-Moisan, M., Tramier, M. Quantitative FRET analysis by fast acquisition time domain FLIM at high spatial resolution in living cells. *Biophysical Journal*. **95**, 2976–2988 (2008).
35. Stringari, C. et al. Phasor approach to fluorescence lifetime microscopy distinguishes different metabolic states of germ cells in a live tissue. *Proceedings of the National Academy of Sciences of the United States of America*. **108**, 13582–13587 (2011).
36. Digman, M. A., Caiolfa, V. R., Zamai, M., Gratton, E. The phasor approach to fluorescence lifetime imaging analysis. *Biophysical Journal*. **94**, L14–L16 (2008).
37. Liang, Z., Lou, J., Scipioni, L., Gratton, E., Hinde, E. Quantifying nuclear wide chromatin compaction by phasor analysis of histone Förster resonance energy transfer (FRET) in frequency domain fluorescence lifetime imaging microscopy (FLIM) data. *Data in Brief*. **30**, 105401 (2020).
38. Grimm, J. B., Heckman, L. M., Lavis, L. D. *The chemistry of small-molecule fluorogenic probes. Progress in Molecular Biology and Translational Science*. **113** (Elsevier Inc., 2013).
39. Li, L., Sun, H. Next Generation of Small-Molecule Fluorogenic Probes for Bioimaging. *Biochemistry*. **59**, 216–217 (2020).
40. Yao, R., Ochoa, M., Yan, P., Intes, X. Net-FLICS: fast quantitative wide-field fluorescence lifetime imaging with compressed sensing – a deep learning approach. *Light: Science and Applications*. **8**, 1–7 (2019).
41. Smith, J. T. et al. Fast fit-free analysis of fluorescence lifetime imaging via deep learning. *Proceedings of the National Academy of Sciences of the United States of America*. **116**, 24019–24030 (2019).
42. Yao, R., Ochoa, M., Intes, X., Yan, P. Deep compressive macroscopic fluorescence lifetime imaging. *Proceedings - International Symposium on Biomedical Imaging*. **2018-April**, 908–911 (2018).

3.1 Organisation of NRPSs involved in pyoverdine synthesis in *Pseudomonas aeruginosa*.

3.1.1 Single-Molecule Tracking

In the first part of the project, single molecule tracking experiments were performed in order to obtain information about the diffusion of proteins of interest inside live bacteria cells (Figure 3.1.1). The purpose of tracking experiments is to decipher the motion modes of NRPSs inside live bacteria. In these experiments PAmCherry fusion enzymes were used. If we observe differences in the diffusion coefficients of the different NRPS, it could imply that they are diffusing independently from each other, notably in case of their diffusion coefficient appeared to be dependant on the size of the protein. On the opposite, if we observe a similar diffusive mode for all the four NRPS, it would corroborate the formation of complexes between different NRPSs. Of course, in case of transient interactions, would correspond in mixture of these two situations.

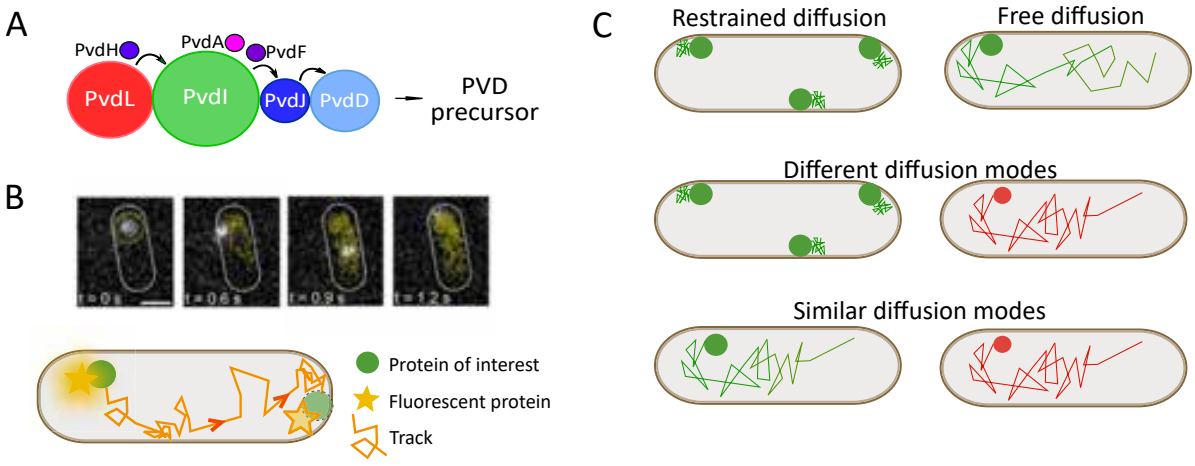

Figure 3.1.1 – **A**. The spatial organization of the proteins of pyoverdine synthesis pathway is still unknown. The NRPSs involved in the process could either form complexes (siderosome), transient or not, or diffuse freely inside the bacteria. **B**. The trajectory of a labeled NRPS molecule can be tracked by linking the positions of the molecule within consecutive microscopy frames. **C**. Expected behaviour of two NRPSs in case of a complex formation vs free diffusion.

Single molecule tracking could then provide interesting information about NRPS organization.

In order to examine the diffusion of single enzyme we reconstructed diffusion maps at the single cell level (Figure 3.1.2, A). The patterns of diffusion of each NRPS visually appear to be similar from cell to cell. PvdA was used as an external control as its diffusion was previously determined [113]. We can observe smaller jumps and more confined tracks near the regions of bacterial membrane (Figure 3.1.2, A). The diffusion of PvdL , the first enzyme involved in the pyoverdine production process - appeared to be more restricted than those of the three other NRPSs resulting in more confined tracks (Figure 3.1.2, A (PvdL)).

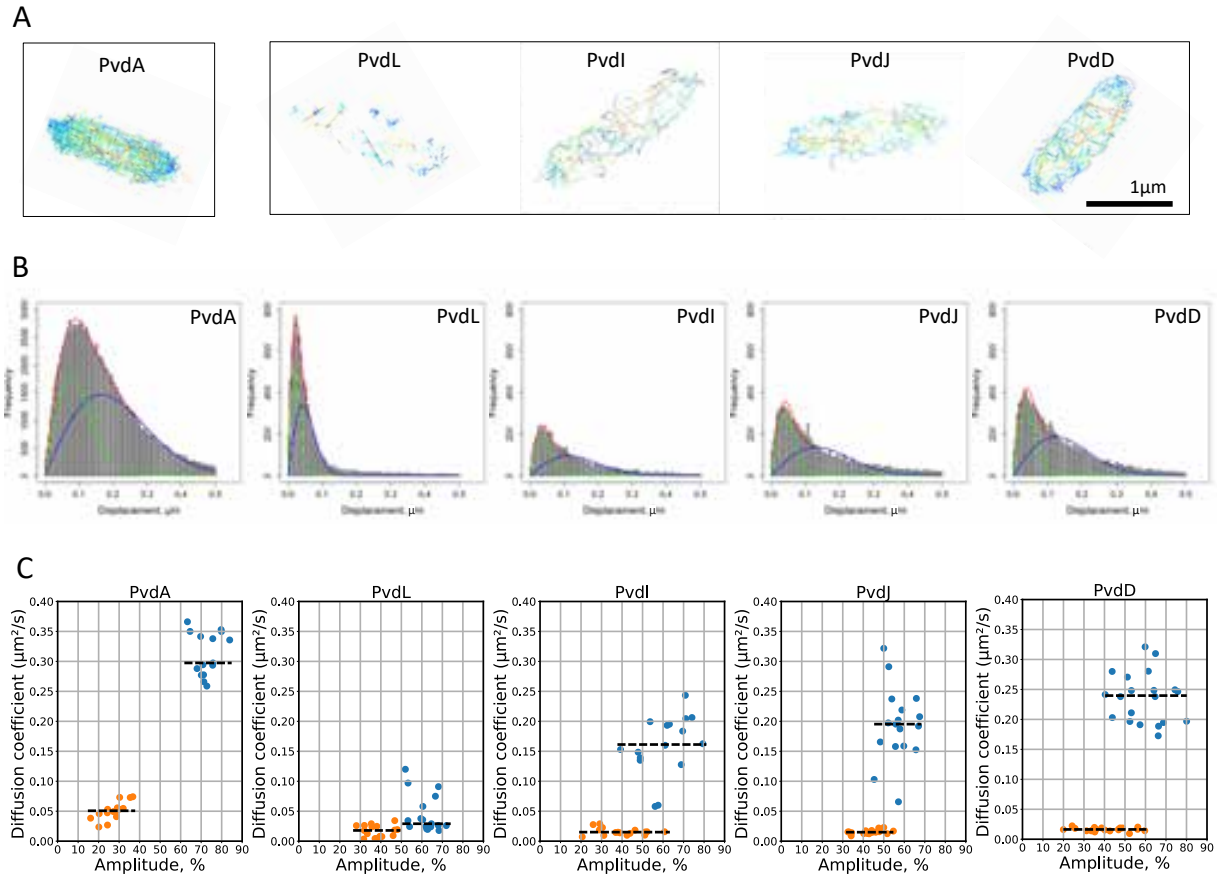

Figure 3.1.2 – **A**. Diffusion maps. **B**. Jump distance distributions builded for all the enzymes of interest. The histograms were fitted with two component model, which consider coexistence of mobile (blue line) and restrained (green line) complexes. **C**. The obtained diffusion coefficients and corresponding amplitudes. The black dashed line corresponds to diffusion coefficient median value.

All the obtained tracks containing more than three spots were used to build a Jump Distance (JD) distribution (Figure 3.1.2, B) from which is is possible to calculate the diffusion coefficients and their corresponding amplitudes (Figure 3.1.2, C). Two populations (or two modes of diffusion) were systematically required to adjust properly the JD distribution (blue and green line on fig 3.1.2, B). We speculated that these two modes corresponded to a mobile diffusion mode

(blue line, blue dots) and to a restrained diffusion mode (green line, yellow dots). Not shown in the figure, but the histograms of jump distances among different experiments for each NRPS appeared very similar - showing that the biological replicates are giving similar results.

For the five proteins measured, the larger difference in the shape of the JD histograms can be observed between the JD distributions of PvdA and those of four NRPSs (Figure 3.1.2, B) which is probably the consequence of smaller size, high mobility and much higher expression levels of this enzyme.

Among the four NRPSs, the JD distributions of PvdL was found to exhibit much higher frequencies at smaller jump distances (Figure 3.1.2, B). In line with this observation, the slowest diffusion rate of mobile diffusion mode was found for PvdL with the diffusion coefficient of 0.049 $[0.045 - 0.052]$ $\mu m^2 s^{-1}$ (median $[IQR]$). This value is close to the diffusion coefficient of the restrained diffusion mode of PvdA : 0.048 $[0.044 - 0.053]$ $\mu m^2 s^{-1}$. All together this suggests that PvdL diffusion is mostly restrained.

Interestingly, the restrained diffusion coefficients of the different NRPS were found to be very similar to each others (Figure 3.1.2, C) whereas the mobile diffusion coefficients were differing between the different NRPSs. This possibly indicates an independent diffusion of the mobile fractions. Nevertheless, we cannot reject that some fraction of enzymes may diffuse in complexes as the changes occurred independently from the protein sizes.

In addition, we can see scattered values of the mobile diffusion coefficients with, for example, partially overlapping values for the mobile diffusion coefficients of PvdI and PvdJ enzyme. This can suggest that the diffusions modes are more complex than a simple two state system. Unfortunately, more than two (close) modes of diffusions cannot be resolved using the approach.

Amplitudes of the species with restrained diffusion were very close (about 40%) for all NRPS, although roughly defined. This is surprising because the level of expression of the different NRPS can be strongly different. Then, we can conclude that NRPS bind to the complex likely with different stoichiometries.

Taken together, these data suggest that NRPSs may form a very dynamic complexes. It strongly suggest that the fraction of proteins which corresponds to restrained complexes may correspond a complex where all NRPS are interacting in the regions near the membrane (where we saw more confined tracks). Each NRPS would nevertheless also coexist in complex of different sizes, possibly with different interacting partners, in and out this large membrane complex.

The study of NRPS diffusion using sptPALM is to a certain degree limited by the fluorophore photostability. After initial photoactivation the fluorescence signal is eventually lost due to photobleaching, which allows to obtain only a part of each track. In addition, the time resolution is limited by the necessary compromise that has to be made in exposure for collecting a sufficient number of photons in each frames. Technical methods with better resolution, like MINFLUX, or

with better fluorophores to lengthen the tracking traced, maybe using organic fluorophores with hallo tags for example, might provide interesting cross-validation data to these observations.

3.1.2 Localization microscopy

In a next step we aimed to explore the subcellular localizations of NRPSs inside the bacteria. The static images of NRPSs positions in fixed cells were obtained for the four NRPSs and for PvdA using 3D DNA-PAINT super-resolution microscopy. In 3D imaging, PvdA appears to be more localized near the membrane area than inside the bacteria (Figure 3.1.3). We can observe partial exclusion zones in the middle part of cell which probably corresponds to the region of the nucleoid (Figure 3.1.3). The tracking experiments and previous 2D experiments [113] were unable to reveal this exclusion area (Figure 3.1.2) because the measurement were done in TIRF where only the cellular part close to the glass slide were observed.

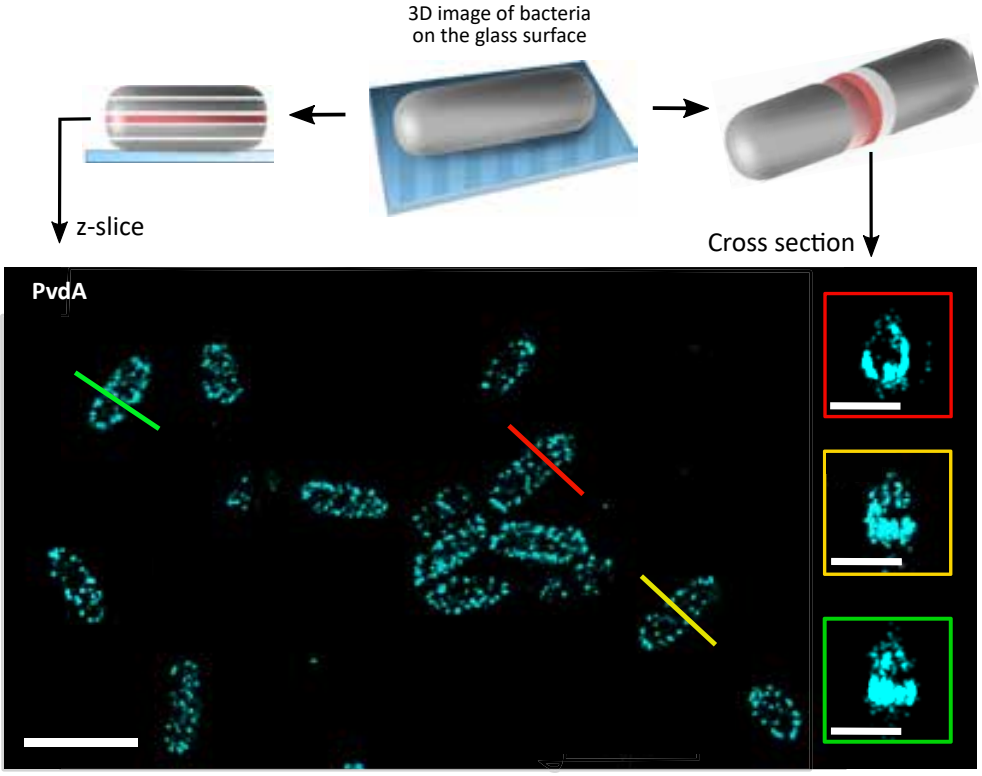

Figure 3.1.3 – z-slice of 3D image of PvdA imaged in fixed bacteria with DNA-PAINT technique (scale bar 2 μm). Cross-sections of three different bacteria in the field of view are presented in the color boxes (scale bar 1 μm) .

Similar distribution patterns were observed for all the four NRPS enzymes (Figure 3.1.4, Figure 3.1.5).

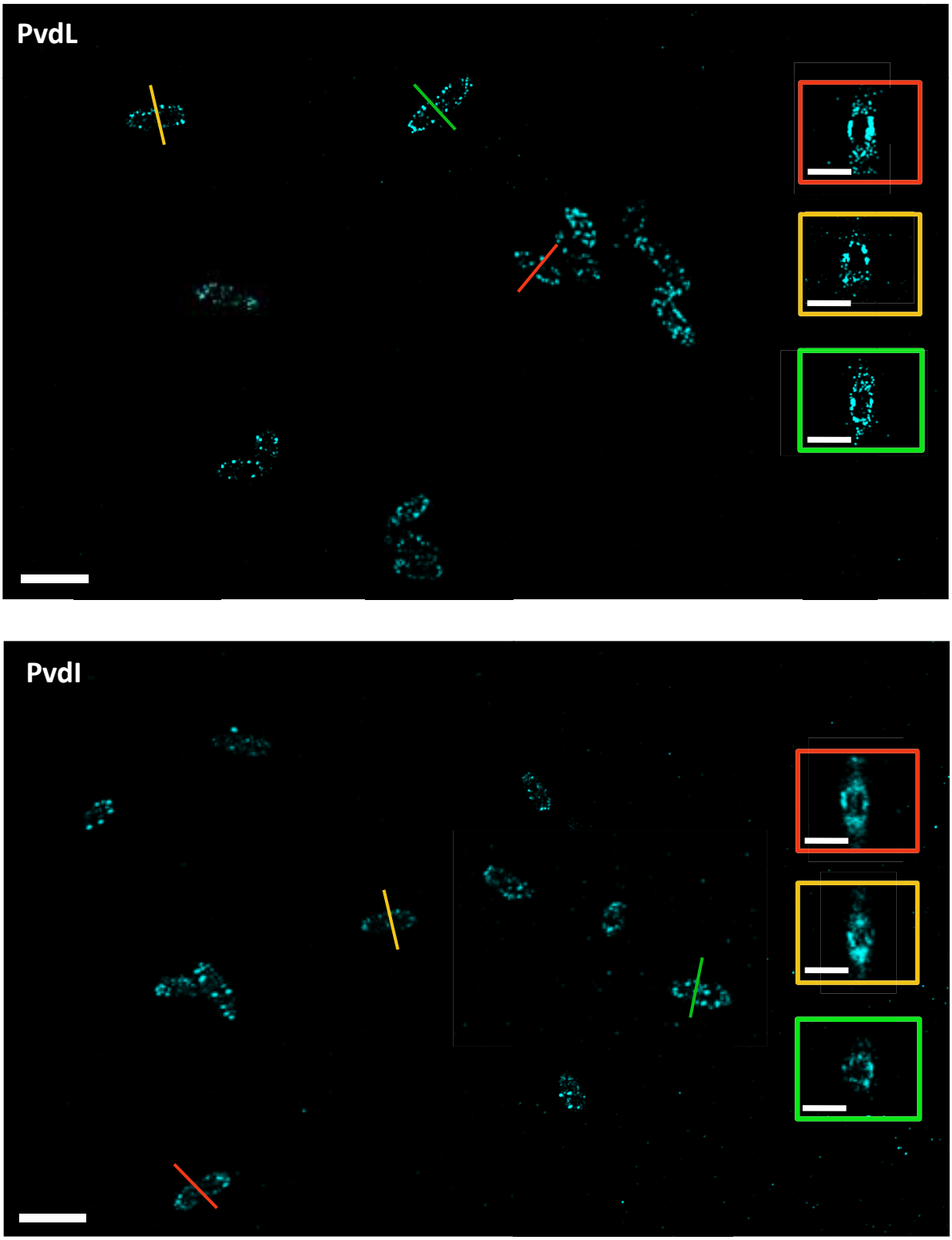

Figure 3.1.4 – z-slice of 3D image of PvdL (top image) and PvdI (lower image) enzymes in fixed bacteria (scale bar 2 μm) and cross-sections in the color boxes (scale bar 1 μm).

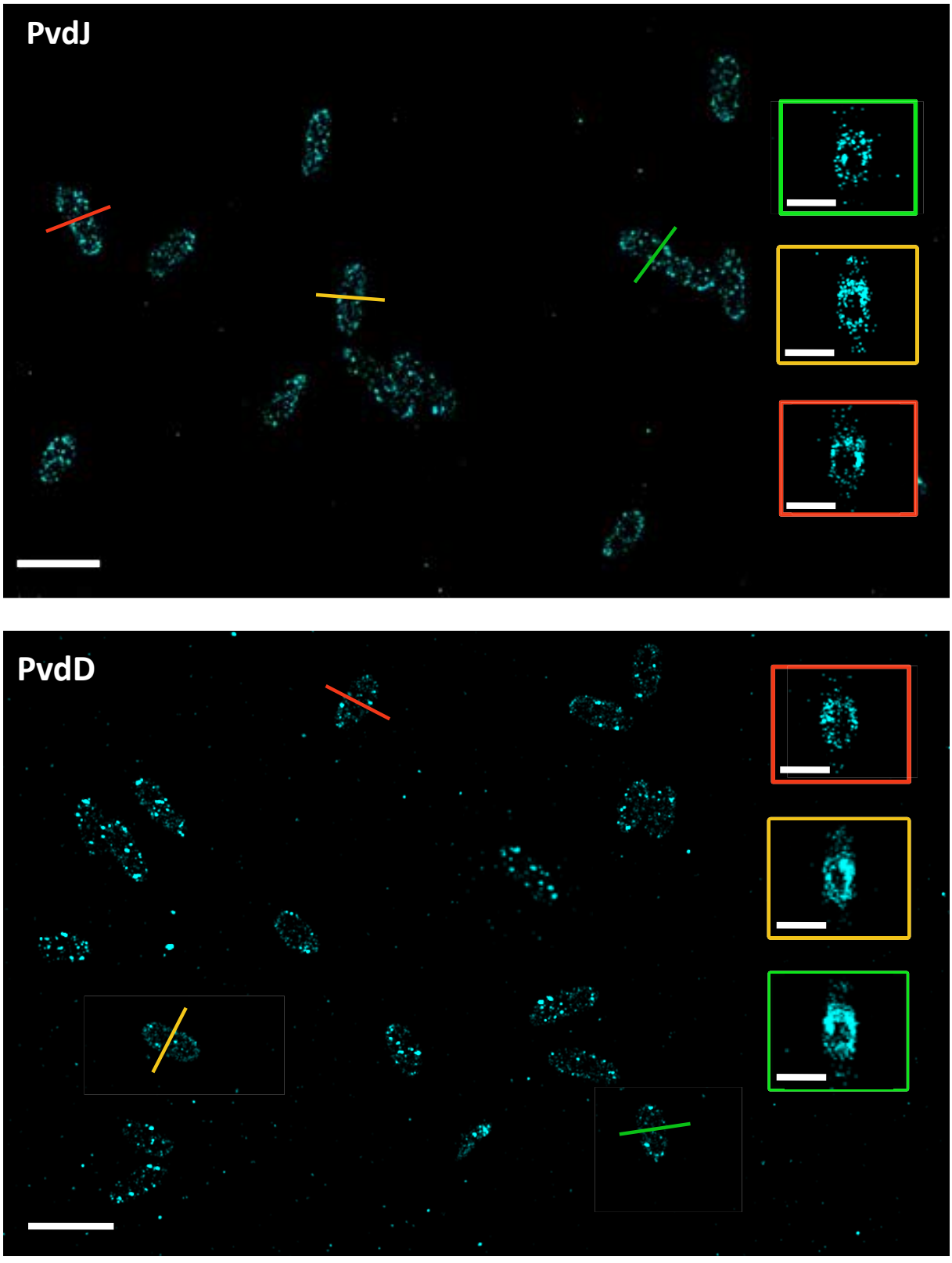

Figure 3.1.5 – z-slice of 3D image of PvdJ (top image) and PvdD (lower image) enzymes in fixed bacteria (scale bar 2 μm) and cross-sections in the color boxes (scale bar 1 μm).

For each NRPS, localizations were mostly found excluded from the center part of the bacterial core. Then these images suggest that NRPSs are preferably localized near the membrane region. The precision of the 3D DNA-PAINT cannot answer to the question of whether the NRPS are bound or not to the memebrane - but this question can partially be answered by the previsouly made tracking experiment showing at least one of the two diffusion modes incompatible with membrane insersion.

In order to check whether the cell fixation and the procedure of antibody labelling may disrupt the enzymes localizations we compared the reconstructed images obtained in two techniques : the enzymes imaged with DNA-PAINT and with PALM (Figure 3.1.6). DNA-PAINT technique allows to acquire the localizations which correspond to the same molecule repeatedly, thus allowing to distinguish true molecular positions by the number of events. The price to pay is to bind a primary and a secondary antibody to the labelled protein. In PALM, direct observations of the labelled protein can be made, but due to a fast photobleaching, localization signals are dimmer and its is harder to separate true localizations from spurious noise emissions.

The harder difficulty in this experiment is the fact that the expression levels of NRPS can be very low - for example, in the case of PvdL and PvdJ enzymes (Figure 3.1.6). This likely correspond to very few hundreds (or less than a hunderd) of proteins in the cell. In this conditions, it is necessary much harder to observe - at least visually - the exclusion area at the central part of cytoplasm.

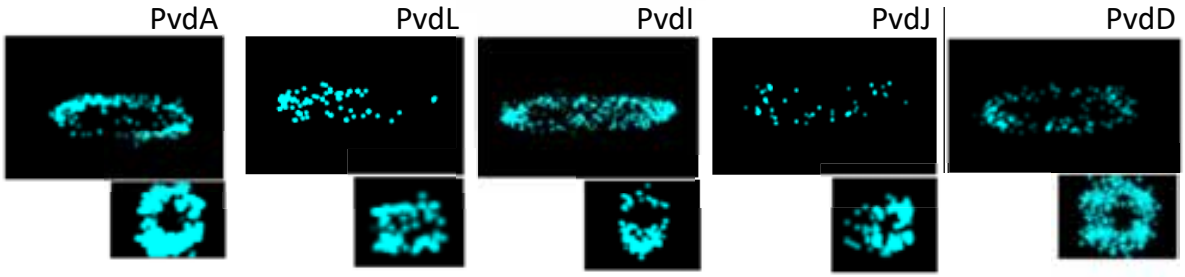

Figure 3.1.6 – Localization images obtained in live using PAmCherry fused proteins. The images were analysed in the same way as DNA-PAINT one.

3.1.3 Colocalization microscopy

Next, we performed two-color DNA-PAINT microscopy to better understand the NRPS organization in cell by measuring protein-protein interactions. In two-color DNA-PAINT experiments we used double mutant bacteria with pairs of enzymes fused to eGFP and mCherry, respectively (Figure 3.1.7).

Colocalization analysis in classical microscopy is not always able to reliably indicate the presence of protein-protein interactions because two proteins colocalizing at the pixel levels with at best a lateral resolution of 200-300 nm can be close in space but without interacting. This limitation make the protein-preotein interaction characterization using colocalization sometimes difficult to anlayse.

Here we propose to work at the single molecule level, measuring the colocalization based on localization coordinates of single molecules. Although the limitations described just before still occur, they are now much more limited by the much better pointing precision of the localization.

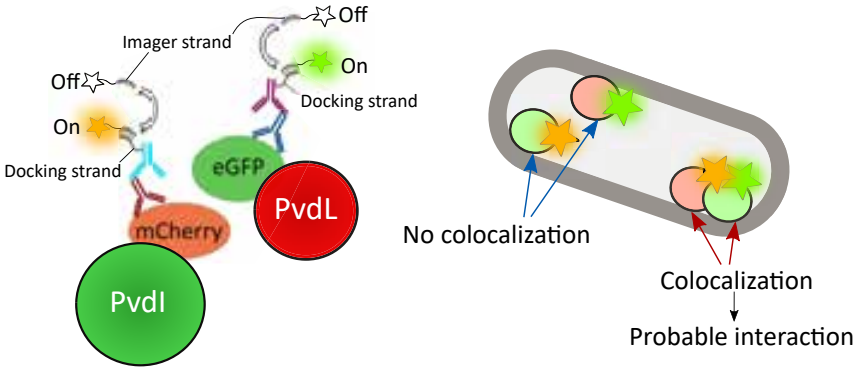

Figure 3.1.7 – The double mutant bacteria with pairs of enzymes fused to mCherry and eGFP fluorescent proteins were labeled with primary and secondary antibodies and imaged with DNA-PAINT technique. The goal of this set of experiments was to get the information about relative organisation of NRPSs and their probable interactions.

First we checked whether the experimental and data post processing protocols are performing well on our system. To to this, we explored of whether we obtained similar results independently of the order of labelling of the pairs of proteins for which we are looking for interaction. This was carried out by imaging the two double mutant bacteria strains : eGFP-PvdL/PvdJ-mCherry and PvdJ-eGFP/mCherry-PvdL. The obtained Mander's overlap coefficients (calculation example in figure 2.5.2) were found to be in a similar range (Figure 3.1.8, B, grey box).

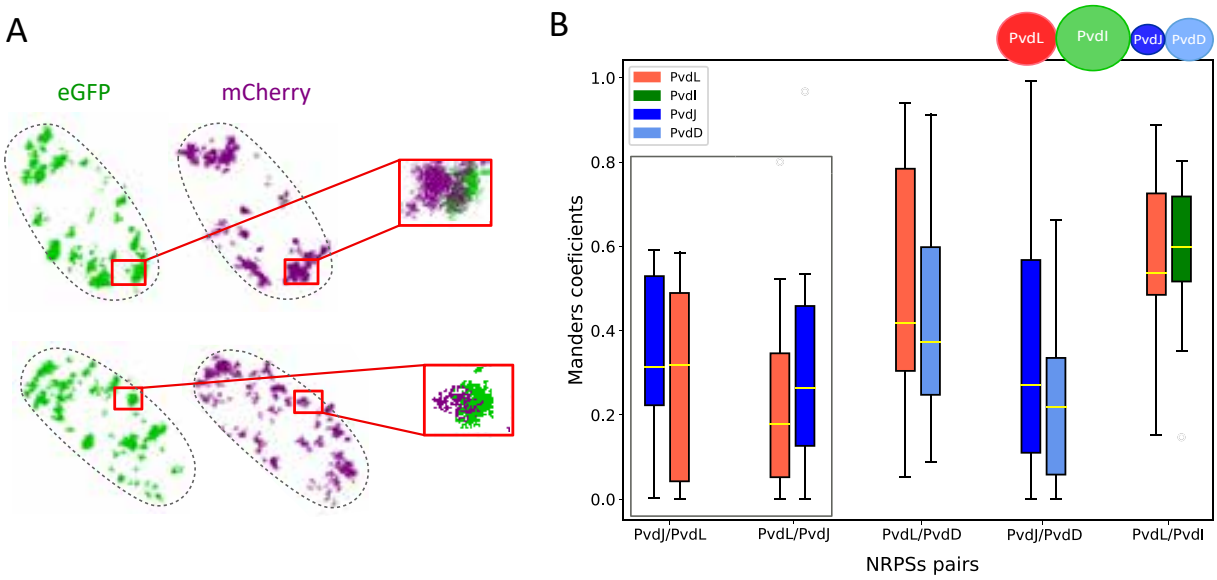

Figure 3.1.8 – A. Reconstructed images of PvdL (eGFP channel) and PvdI (mCherry channel) enzyme pair images with DNA-PAINT technique. **B**. The Mander's overlap coefficients (the higher the more the interaction) was calculated for each pair of proteins in regard to eGFP/mCherry (first of two boxes) and mCherry/eGFP (second box) channels.

Further we performed the same experiments on each of the double mutant bacteria. Almost in all cases, the distribution of the Mander's overlap coefficients appeared to be spread over a wide range of values. This fact may indicate that the levels of interaction can be strongly varying from cell to cell. At this point it is not yet fully clear whether the possible reason is the expression level variability of the two proteins in cells, or the cell to cell variability connected to their respective state of PVD production (for example, if the production is pulsatile with production periods separated by non-producting periods). In addition to that, it is also worth to consider the reasons of the distribution, which are related to the technique. Thus, Mander's overlap coefficients could be affected by the uncertainty in the localization coordinates. Moreover, the possible misalignment at the nanometer scale of the eGFP and mCherry channels (a chromatic abberation) is expected to have a varying impact in case of different experiments, different fields of view or even different regions in the image. This point has to be explored further in our data.

Nevertheless, the highest value, corresponding to ∼0.56 (median) was obtained for the pair PvdL/PvdI, which are the two first enzymes in the pyoverdine biosynthesis process. Relatively high values were also observed for the pair of PvdL/PvdD (median ∼0.4), which is rather unexpected given that these are the first and the last enzyme in the production process, respectively. Interestingly, it was reported based on bioinformatic analysis that the first and the last enzymes metabolic pathways in *E.coli* are preferably localized [149]. In this publication, they suggest that such organization could induce pathways optimisation in order to minimize the production cost.

Even if the true quantification of these measurement is difficult, they provide at least some qualitative information about the fact that PvdL and PvdI and to a lesser extent PvdL and PvdD are interacting.

3.1.4 FLIM-FRET to measure the protein-protein interaction between NRPSs

In order to explore the interactions between the NPRSs we used Förster resonance energy transfer measured by fluorescence lifetime imaging (FLIM-FRET) technique. FLIM-FRET is used for the protein pairs labeled with donor and acceptor fluorophores (in our case these are eGFP and mCherry, respectively) and in principle may provide quantitative information about the protein-protein interactions (Figure 3.1.9, A).

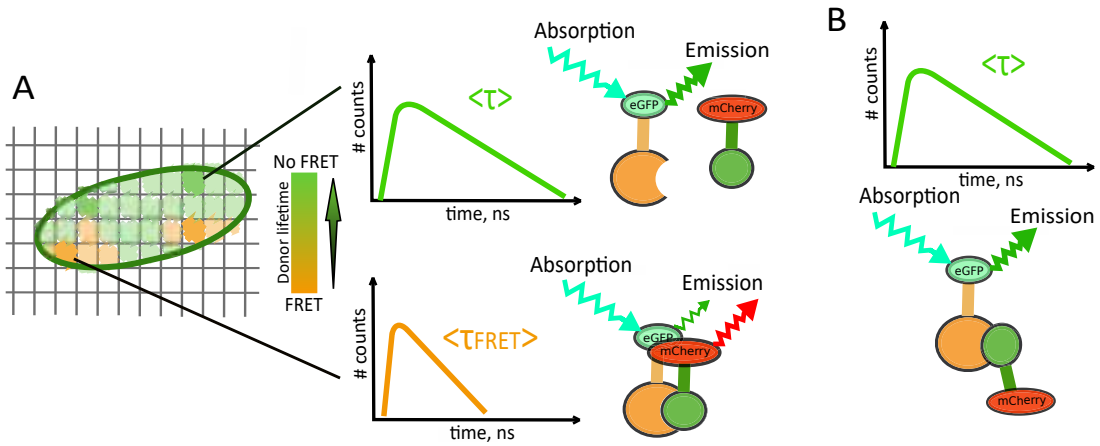

Figure 3.1.9 – FLIM-FRET technique applied to the detection of protein-protein interactions. **A**. The fluorescence lifetime of the donor molecule diminishes in case of an efficient FRET process, which is only possible when the acceptor is located in close proximity - if, for example, protein-protein interaction occurs. **B**. Due to labels position or due to the size of the interacting proteins, dye-to-dye distances can be too long for FRET to occur, even in case of a protein-protein interaction.

The measured experimental values (averaged over several field of view) are presented in table 3.1. The calculated FRET efficiency values appear to be negligible for almost all the investigated pairs except, probably, PvdL / PvdD. We were unable to reliably confirm these findings by using an analysis method described in Publication II. Moreover, it was not possible to detect any signal for PvdJ / PvdD NRPS pair.

There are several possible explanations for incoherent results obtained during FRET experiments. FLIM-FRET technique is strongly dependent on the distance between the donor and acceptor molecules as the FRET efficiency is inversely proportional to the power six of the dye-to-dye distance ($\sim 1/R^6$). In some cases the interaction of proteins can not be clearly distinguished. FRET will not occur when the interaction of the two proteins results in a relatively

Strain name	τ eGFP, ns	τ eGFP - mCherry, ns	E
eGFP-PvdL / PvdJ-mCherry	2.3	2.3	0.0
PvdJ-eGFP / mCherry-PvdL	2.3	2.3	0.0
eGFP-PvdL / mCherry-PvdD	2.3	2.0	0.13
eGFP-PvdL / PvdI-mCherry	2.3	2.2	0.04
PvdJ-eGFP / mCherry-PvdD	Na	Na	Na

Table 3.1 – The lifetime values obtained for donor (eGFP) and donor-acceptor (eGFP - mCherry) pair and FRET efficiency (E) in FLIM-FRET experiments

long distance between the two attached fluorophores (Figure 3.1.9, B). The interpretation of the FLIM-FRET data can be further complicated by unbalanced stoichiometry and transient interactions which involve only a fraction of the proteins of interest. The low expression levels of NRPSs involved in PVD biosynthesis resulted in less signal recorded from the sample which made the analysis more complicated.

To analyse these data we used a phasor approach which is able to provide global understanding on heterogeneous lifetime values [150]. In this approach each fluorescence decay which corresponds to one pixel can be transformed into a phasor point. The phasor coordinates are defined by real (g) and imaginary (s) parts of the Fourier transform. The phasor points are mapped to a semicircle which displays the lifetime values which increases conterclockwise (Figure 3.1.10, A). The donor phasor will appear at some place in the semicircle depending on its lifetime (Figure 3.1.10, A, green filled circle). When all the donor molecules undergo FRET the phasor is shifted in the direction of lower lifetimes as showed in the Figure 3.1.10, A (red filled circle). In the case of lower FRET efficiency the fraction of unquenched donor may effect the phasor position so it shifts to the middle part between two possible phasors (corresponding no FRET and maximal FRET phasors) (Figure 3.1.10, A, yellow filled circle).

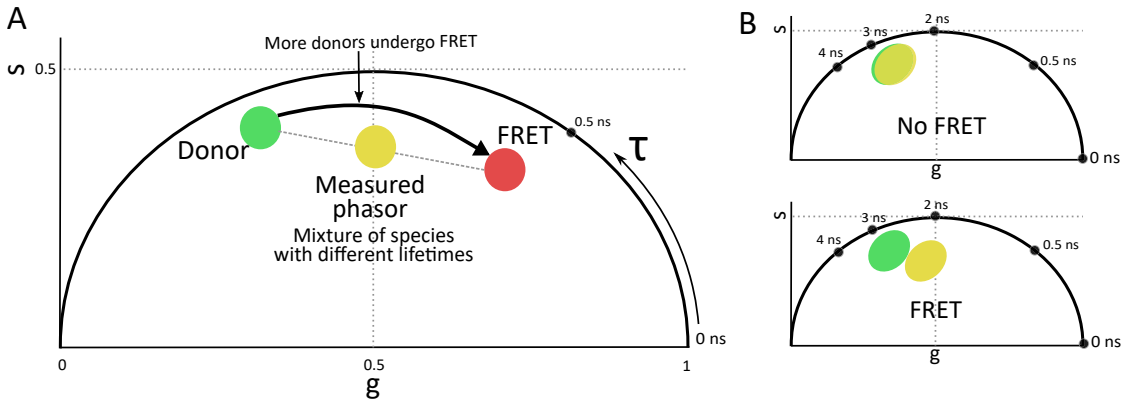

Figure 3.1.10 – **A**. Schematic phasor plot. The position of the donor phasor in the semicircle is shown as green filled circle. The phasor shifts towards the position of the red filled circle if all the donor molecules undergo FRET with high transfer efficiency. The yellow filled circle represents the phasor position in the case of mixture of unquenched (no FRET) and quenched (FRET) species. **B**. Possible positions of the donor and measured phasors in the case of low FRET efficiency.

By using phasor approach it was possible to observe the shift between donor (eGFP-PvdL) and donor-acceptor (eGFP - PvdL/mCherry - PvdD) phasors (Figure 3.1.11). Similar behaviour was observed for different fields of view in the sample. For all the other investigated pair we observed no shift of the donor and donor acceptor phasors.

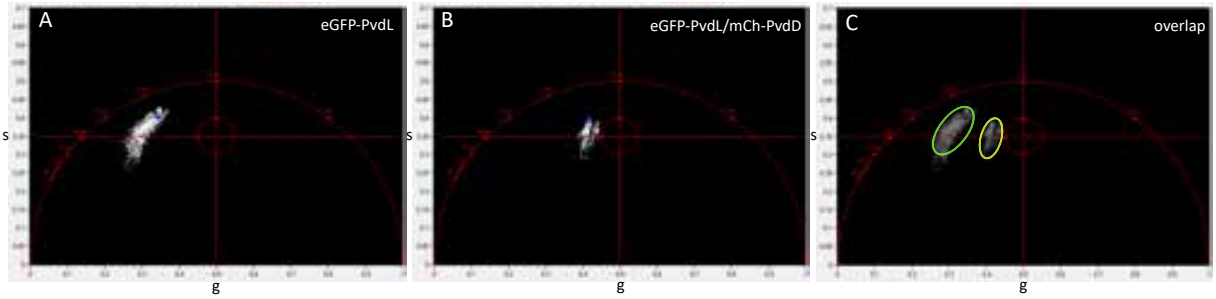

Figure 3.1.11 – The phasor plots of **A** donor - eGFP-PvdL, **B** donor and acceptor - eGFP - PvdL/mCherry - PvdD and **C** their overlap.

This finding allows to confirm the colocalization microscopy results showing PvdL/PvdD colocalization.

Altogether, the large size of the NRPS and the low expression levels were challenging factors to evidence NRPS-NRPS interactions. We nevertheless were able to evidence a protein-protein interaction in PvdL/PvdD (FRET and colocalization).

3.1.5 Speculation on global organization biology of NRPSs

The results of experiments performed during this project allow to suggest that the four large NRPS involved in PVD biosynthesis may form a very dynamic complexes near the cell inner membrane in order synthezise the Pyoverdine precursor (Figure 3.1.12). The localization microscopy experiments showed that the NRPS were preferably located near the membrane regions, further corroborating the suggestion that PVD synthesis occurs near the membrane. Our results are in line with a fact that Pyoverdine molecule includes a hydrophobic myristic or myristoleic acid residue, introduced by the first enzyme in the production process - PvdL - and suggesting its membrane anchoring.

Moreover, PvdL was found to exhibit the most restricted diffusion among all the four NRPS studied, performing mostly confined movement near the membrane. Three other enzymes, PvdI, PvdJ and PvdD, exhibited two distinct diffusion modes. The mobile fraction of NRPSs with high diffusion coefficients seems to be diffusing in the bacteria cytoplasm. The values of the diffusion coefficients do not fully correspond to the expected coefficient calculated based on the molecular size of these proteins. Also approximative, this teoretical estimation suggest that NRPS are not

diffusing 'alone' as monomers in the cytoplasm. This conclusion should to be taken cautiously, because we demonstrate in our data that the volume in which the NRPS are allowed to diffuse is strongly limited in the cell. Indeed, we observed the partial exclusion zones in the middle part of the bacterial cytoplasm which could not be seen previously nor in FRAP [111] neither in 2D sptPALM experiments [113]. This exclusion from the large bacteria nucleoid, resulting in a more restricted diffusion volume in the bacteria cell, may induce constrained diffusion (a molecule freely diffusing in a 'too' small volume will exhibit reduced diffusion coefficient) and therefore may also explain why we retrieved lower diffusion values than expected. We probably need to explore mean square displacement (MSD) plot (or change the step time in the JD distribution) to see if we can evidence restricted diffusion in our data.

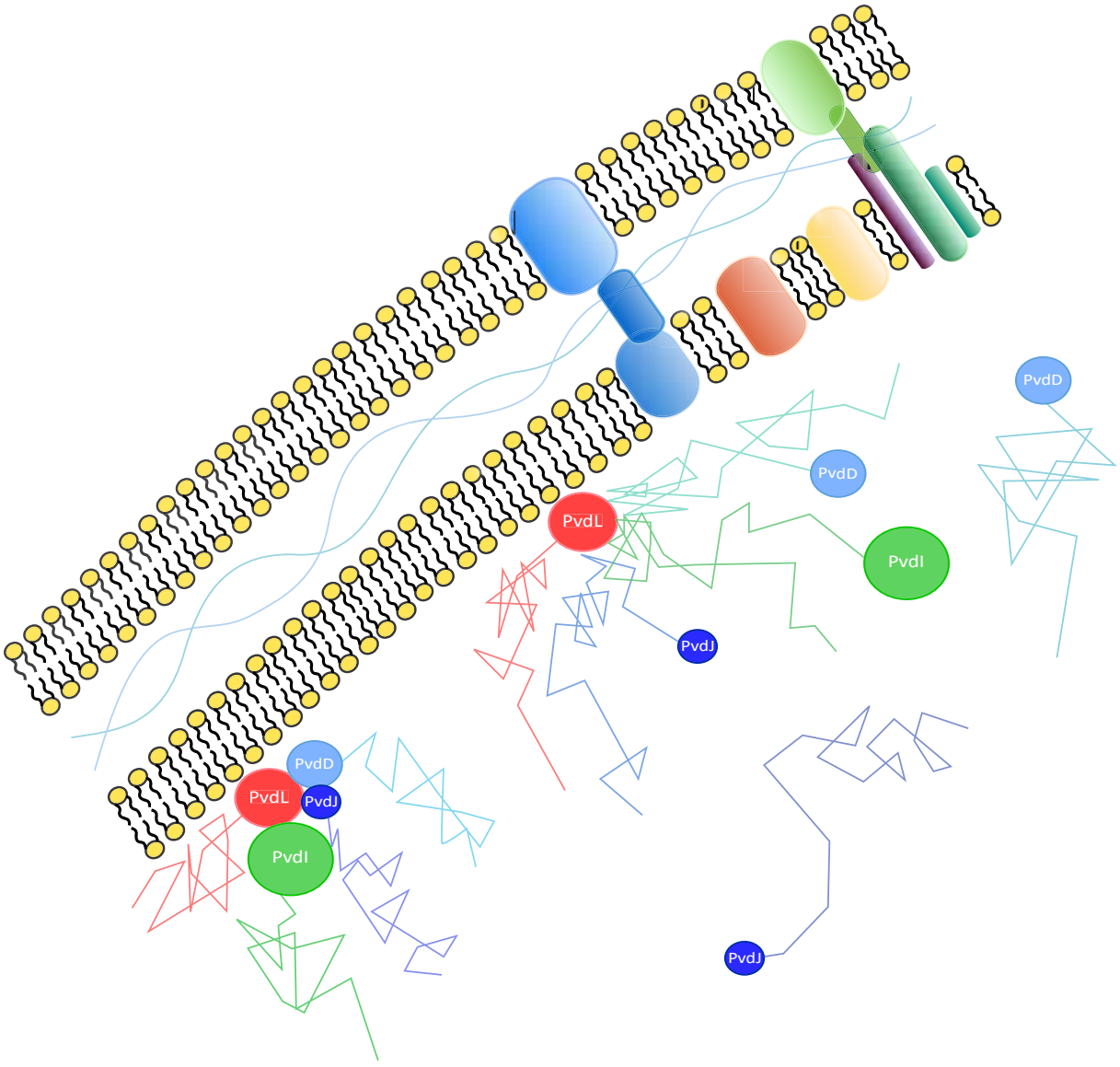

Figure 3.1.12 – Hypothetical NRPS organization in bacteria cell.

The colocalization experiments revealed a preferable colocalization of PvdL with PvdI and PvdD, which are first, second and the last enzymes of the biosynthesis process, respectively. The interaction of PvdL and PvdD pair was confirmed in FLIM-FRET experiments. Such a preferable colocalization could possibly be indicative of an existence of a certain synthetic pathway optimization, however, further experiments are needed in order to confirm this suggestion.

A major limitation impeding the understanding of NRPS organization is related to the fact that the experiments were performed at maximum with two enzymes at the same time - giving only a partial view of the organization of the four NRPS.

Our objective was then to perform multi-species imaging and tracking and to establish an original multi-color tracking procedure to track simultaneously different NRPS in live cells. This will be done using the srSMLM [36] which was recently set-up in our lab. Thanks to a complete spectral decomposition of single-emitters, strongly overlapping spectra can be discriminated, making it possible to excite with a single laser and track simultaneously up to four fluorescent proteins differing only by slightly shifted emission spectra. Tracking traces will be calculated on multidimensional data (space, time and spectra) to improve traces assignment.

But to make srSMLM sufficiently efficient to work with multiple colours, we worked on advancing srSMLM using deep learning.

3.2 Deep Learning to enhance the performance of srSMLM

Basically, there are three major parameters to trade-off for fluorescence imaging : spatial and temporal resolutions and multiplexity.

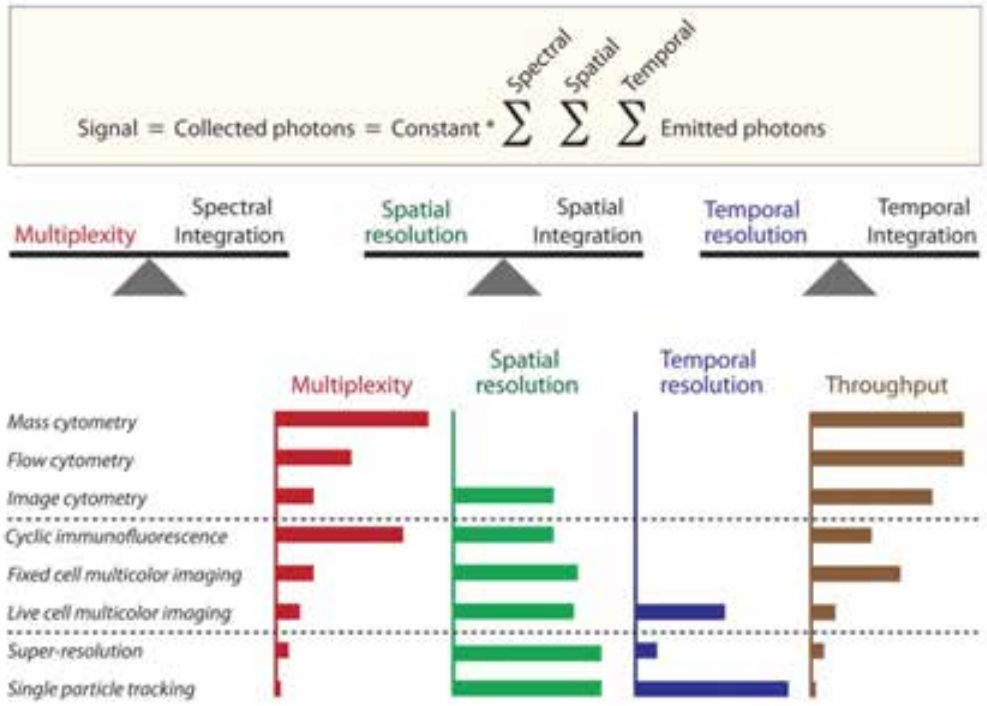

Figure 3.2.1 – Main parameters to trade-off in fluorescence imaging and cytometry [151]

SMLM is at the moment the technique achieving the highest spatial resolution in optical imaging routine experiments. The spatial resolution that can be achieved is dependent on both the pointing precision (defined by the number of photons collected from a single emitter) and on the localisations spatial density (often referred as molecular density). The minimal number of molecules required within an area (sampling size) has to be of at least (2/resolution)D (D = spatial dimensionality) to capture all the information of the structure to be imaged (Nyquist criterion) [152]. For example, to achieve 20 nm resolution in two dimensions, 10,000 localizations/μm^2 are required - and $\sim 10^6$ per μm3 for a 3D image. These numbers apply for each of the co-imaged components. Sequential imaging of two colors requires an acquisition time which is at least twice longer compared to a single-colour SMLM (given that a single-colour image with $\sim$ 30 nm resolution typically requires few minutes of acquisition to accumulate enough localizations). On a practical point of view, imaging different channels at the nm-scale faces additional challenges like a higher sensitivity to chromatic aberrations (the more separated the colors the higher the

aberrations), instrumental drifting over time or finding compatible imaging buffers for the different organic fluorophores to be combined – making SMLM not easily scalable to multi-colours. The price to pay for the improved resolution is therefore to sacrifice the temporal resolution – this price is even higher if multiple targets of interest are planned to be localised in images. In single molecule tracking (smTracking), localizations of a given single molecule are linked to reconstitute a trace (positions (x, y, (z)) as a function of time) from which velocities (distance / time) or diffusions (area / time) can be derived. Low fluorophore density is required to isolate single emitters in space. smTracking is not limited by the requirement of accumulating high localisation densities. smTracking is then able to reach fast temporal resolution while keeping high pointing precision. The temporal limit – typically in the ms range - is driven by the exposure time required to capture enough signal from single emitters to properly localize them in frames and by the risk of imaging motion-blurred localisations due to the diffusion of molecules during the exposure time if it is too long.

For revealing how proteins relate to each other over time at the nanoscale, sequential acquisition are poorly efficient and multi-colour tracking is required to capture simultaneous positions and movements of different partners. With increasing the number of simultaneous components to be co-imaged, the spectral overlap between the fluorophores labelling them inevitably increases imposing to narrow-down the spectral detection range for each fluorophore. The spectral selection is then associated to a reduction in the amount of collected photons, and therefore signal-to-noise ratio. The limited number of separable channels in multi-colour tracking narrows the boundaries of achievable multicolour multiplexed imaging.

For all these reasons, progress in multicolour SMLM and smTracking has not yet really moved beyond the stage of sequential observation of few proteins within complex multi-protein architectures.

The technical challenge is now therefore to develop approaches able to combine the information obtained simultaneously on different molecules and to combine at the same time high spatial resolution, high temporal resolution and multiplexity.

SrSMLM (Figure 3.2.2, A) has the potential to reach these requirements that would allow to track simultaneously up to four non-ribosomal peptide synthetases (NRPS) of the pyoverdine pathway in live P. aeruginosa

But despite various recent setup and analysis improvements in the field of srSMLM, this technique still suffers from low SNR particularly in the spectral part.

We then aimed to develop the deep learning model able to increase the SNR of the images and useful data ratio for the srSMLM technique. The main challenge in application of deep learning to improve SNR in the spectrally-resolved technique is that it is not possible to acquire the corresponding low and high SNR images due to stochastic nature of the emission. In order to circumvent this issue we decided to create the high SNR images by imaging a DNA-PAINT

origami nanoruler, which allows to obtain multiple emitting events for the same position in the sample. After that we clustered the images which corresponded to repeated measurements of the same position and were observed at a minimum of 8 frames. We worked on 64×16 image patches (concatenated 16×16 container centered around the emitter position and 48×16 container which contained the corresponding spectra). For the cluster of n frames we kept one image as low SNR to use in the training set (x_train). To create the corresponding high SNR image (y_train) we fused (n-1) images using Spatial Frequency weighting averaging [153] followed by white top-hat transformation (Figure 3.2.2, B). Thus we obtained n corresponding pairs of low and high SNR images per cluster. In addition, we introduced random shift to the spectral container along the x-axis to simulate the spectral shift of the emission and we generated about 15% of noisy images (without any localization present on the image). This process was repeated for the images obtained at different laser intensities allowing to create a training set of ∼265,000 image pairs without using data augmentation. The 10% of the images were used as a test set.

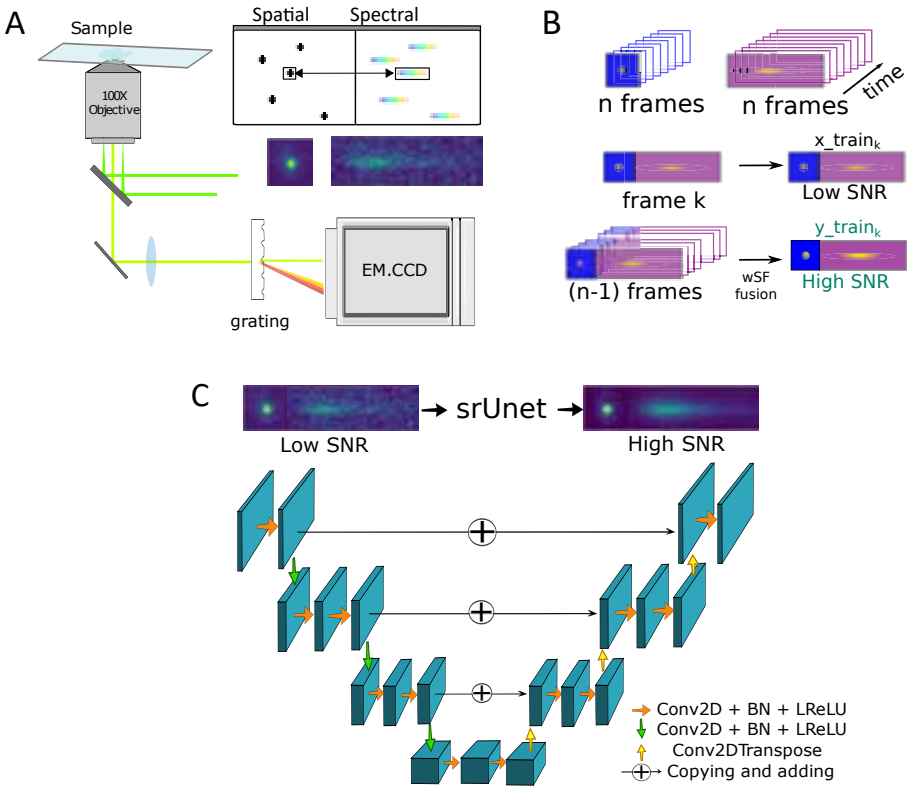

Figure 3.2.2 – A. In srSMLM the emitter position and its corresponding spectra are acquired at the same time by introducing the dispersive element into the light path before the camera. **B**. The spectral and spatial information of single emitting molecule can be recorded in different frames. Such image stacks can be used to create the training set for the srUnet by keeping one image as a low SNR (x_train) and by fusing other (n-1) using weighted spatial frequency calculations in order to create the corresponding high SNR image (y_train). **C**. Unet-based network architecture which contains contracting path (including convolution (Conv2D), batch normalization (BN) and uses Leaky Rectified Linear Activation (LReLU) as activation function) and symmetric expanding path (including Transposed convolution (Conv2DTranspose) layers) and cross connections between some same-sized parts.

The network architecture was optimized for our task. The network is composed of 6×6 convolutional layers with Exponential Linear Unit (ELU) activation function followed by Batch normalization and Leaky Rectified Unit (Leacky ReLU) (Figure 3.2.2, C). Furthermore, the trained model was tested using previously unseen nanoruler images. We showed that the network allows to increase spatial and spectral precision especially for the localizations with a low photon bunget and strongly improve the probability to allocate the wavelength. In addition, we demonstrated the ability of the model to reconstruct the images in the presence of spectral shift while preserving the linearity of the response. Moreover, the model was tested for multicolor imaging of bacteria cells labeled by two dyes with overlapping spectra.

The results are presented in the following article.

Publication III

Advancing Spectrally-Resolved Single Molecule Localization Microscopy using Deep Learning

Advancing Spectrally-Resolved Single Molecule Localization Microscopy using Deep Learning

Hanna Manko[1], Yves Mély[2], and Julien Godet[1,3,4,✉]

[1]Laboratoire de BioImagerie et Pathologies, UMR CNRS 7021, ITI InnoVec, Université de Strasbourg, Illkirch, France
[2]Laboratoire de BioImagerie et Pathologies, UMR CNRS 7021, Université de Strasbourg, Illkirch, France
[3]Groupe Méthodes Recherche Clinique, Hôpitaux Universitaires de Strasbourg, France
[4]Laboratoire iCube, UMR CNRS 7357, Equipe IMAGeS, Université de Strasbourg, Strasbourg, France

Spectrally-Resolved Single Molecule Localization Microscopy (srSMLM) is a recent multidimensional technique enriching single molecule localization imaging by the simultaneous recording of single emitters spectra. As for SMLM, the localization precision is fundamentally limited by the number of photons collected per emitters . But srSMLM is more impacted because splitting the emission light from single emitters into a spatial and a spectral channel further reduces the number of photons available for each channel and impairs both spatial and spectral precision - or forces the sacrifice of one or the other. Here, we explored the potential of deep learning to overcome this limitation. We report srUnet - a Unet-based image processing that enhances the spectral and spatial signals and compensates for the signal loss inherent in recording the spectral component. We showed that localization and spectral precision of low-emitting species remain as good as those obtained with a high photons budget together with improving the fraction of localizations whose signal is both spatially and spectrally interpretable. srUnet is able to deal with spectral shift and its application to multicolour imaging in biological sample is straightforward.

srUnet advances spectrally resolved single molecule localization microscopy to achieve performance close to conventional SMLM without complicating its use.

spectrally resolved single molecule localization microscopy | deep learning | U-net|super-resolution microscopy

Correspondence: ***julien.godet@unistra.fr***

Introduction

Super-resolution microscopy has opened exciting new opportunities in life science to study biological processes at the nanometer scale. Among the super-resolution imaging methods, single molecule localization microscopy (SMLM) (1–3) is widely used - presumably because it builds on conventional wide-field imaging and is relatively easy to implement (4). SMLM is based on the principle that the localization of a molecule can be determined with high accuracy from its PSF if the latter corresponds to a single molecule emitter. The elegant idea behind SMLM is to achieve the spatial isolation of single emitters by repeatedly recording sparse subsets of individual fluorophores stochastically-activated over time. Isolated emitters are then pinpointed and their localizations accumulated to reconstruct a SMLM image. The routine lateral resolution of SMLM is in the range of 10-50 nm - an order of magnitude improvement over conventional diffraction-limited microscopy resolutions.

SMLM has recently been extended beyond the spatial positions of single emitters to explore additional dimensions of their emission signals. In Spectrally-resolved SMLM (srSMLM), both the full emission spectra and the localizations of single emitters are simultaneously recorded (5–8). The additional characterization of the spectral component is a breakthrough and srSMLM has rapidly found successful applications in multicolour imaging (5, 8–10) or tracking (9, 11–13), single molecule conformational changes (14–17), or single-molecule polarity sensing (6, 18–20).

Different technical approaches have been reported to capture the spectral decomposition of light (21). A dual-objective configuration was initially described (5) where one objective lens is dedicated to localization measurements and the second - combined with a prism - is used for collecting spectral-measurements of the same single molecules. While this design achieved excellent light collection efficiency, more recent works reported the use of a single-objective combined either with a transmission grating (Fig. 1 a.) or with the association of a beam splitter and a prism. These setups are simpler in design and impose fewer constraints on sample mounting as compared to a dual-objective setup. But splitting the signal into two paths reduces the number of photons available for each path. Additionally, strong spectral dispersion reduces the signal-to-noise ratio in the spatial domain, so that parameters of the emission spectra cannot always be recovered or properly characterized for all detected molecules - particularly for the lowest emissive ones. These are limiting srSMLM because the final image resolution depends on the accuracy of each individual localization measurement (the higher the number of emitted photons, the better the pointing precision) and on the spatial density of emitters localized in the final image (Nyquist sampling theory). Some recent attempts have been made for improving srSMLM resolutions - either by improving the photon detection efficiency (9), proposing new fluorophores (20) or by enabling higher emitter densities (22, 23) - but the improvements remain modest.

In this work, we aimed to advance srSMLM through data post-processing. Recent developments in deep learning methods now offer powerful analysis tools that have the potential to outperform conventional image processing (24, 25). For example, content-aware image restoration (CARE) (26) can improve and restore the quality of under-exposed or under-sampled images and makes it possible to recover important biological information from noisy images. CARE

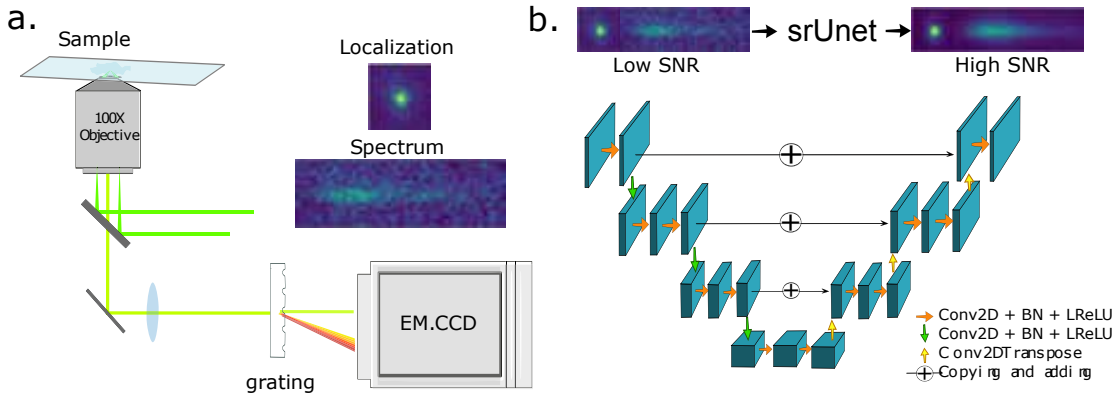

Fig. 1. srSMLM and srUnet principles.
a. Schematic representation of srSMLM. In srSMLM, the diffraction-limited image (PSF) of a single emitter is recorded in a spatial space - allowing its localization to be estimated with high accuracy. Simultaneously, part of the emission light is diffracted and the emission spectrum is recorded in a spectral space on the same detector - giving access to spectroscopic information on the emitter.
b. srUnet architecture. srUnet is based on a Unet architecture. A Unet is a convolutional neural network made of a contracting path (left part of the U - operating 2D convolutions (Conv2D), batch normalization (BN) and using Leaky Rectified Linear Activation (LReLU) as activation function) and a symmetric expanding path (right part of the U: based on Transposed convolution (Conv2DTranspose) layers also called deconvolution layers) with cross connections between some same-sized parts of the down-sampling and of the up-sampling paths (horizontal arrows). srUnet can be trained end-to-end to restore high signal-to-noise ratio (SNR) from low-SNR image.

network architectures are based on convolutional U-nets (27). These deep artificial convolutional network architectures can be trained end-to-end with relatively few images and with relative quick training time to denoise and restore images.
We presented here srUnet, a U-net-based image processing for srSMLM that enhances the spectral and spatial signals and compensates for the photon loss inherent in recording the spectral component.

Results

Convolutional network.

Convolutional neural networks are very efficient at semantic segmentation, classification, image denoising, domain translation, or reconstruction (28, 29). U-net are particular convolutional networks made of a contracting path (left hand side of the U) and a symmetric expanding path (right hand part.) (Fig. 1 b.) with cross connections between same sized parts of the down-sampling and the up-sampling paths (27, 30). In image denoising, U-nets can efficiently restore high signal to noise ratio (SNR) images from low SNR images. The model has first to be trained with pairs of images, using the low SNR images as inputs and their corresponding high SNR images as targets. Once trained, the network can be used to predict high SNR images from any new low SNR images with good generalizing properties for images unseen during the training.

Generating a training data set.

We first built a training data set made of noisy low-SNR images (x_train) paired with their corresponding high-SNR images (y_train).
Because of the stochastic nature of the emissions in SMLM it is improbable to match low and high SNR acquisition sequences composed of exactly similar localizations in space and time at the scale of a field of view. To circumvent this, we worked on 64x16 pixels image patches - themselves a concatenation of a 16x16 pixels container centered around the PSF in the spatial channel and a 48x16 pixels container collecting the corresponding spectra in the spectral channel (Fig. 2 a. and b.). At the localization scale, collecting the same single molecule several time with different SNR is possible.
We imaged the ATTO 542 dye of a DNA-PAINT origami nanoruler (GATTA-PAINT 80RG with , GattaQuant GmbH) immobilized on a microscope glass slide. Each DNA-PAINT origami nanoruler has three docking sites for labelled imaging DNA strands (imagers), creating three aligned localization sites with robust and reproducible mark-to-mark distances of 80 nm (31). To fully control the matching between high and low SNR localizations, we took advantage of the fact that the signal from an emitter can be observed on several consecutive frames during the acquisition - in particular at low laser illumination intensity - generating repeated measurements of the same emitter at a given position (Fig. 2 b.). These repeated measurements can be clustered in space and time and clusters with at least three localizations observed in a radius of less than 10 nm were kept. Within a cluster c composed of n frames, a random frame k was selected to append the training set (x_train_c) while the $(n-1)$ left images of the cluster were fused using Spatial Frequency weighted averaging (wSF fusion) (32) followed by a white top-hat transformation to create the corresponding high SNR image (y_train_c). (Fig. 2 c.). This original approach allowed us to build a training data set made of pairs of low SNR / high SNR images of the same PSF. The training set was composed of pairs of images acquired at different laser intensities to collect different levels of signal and/or noise. We also augmented the training set with images in which the spectral container box was randomly shifted along the spectra axis - mimicking a shift of the emission spectra of the emitter. Finally we introduced about 15% of images without

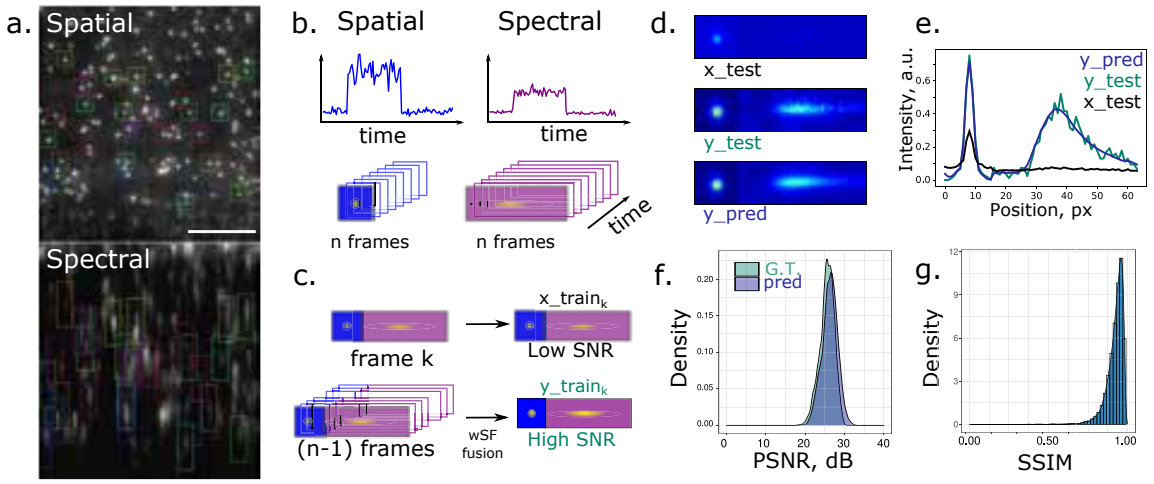

Fig. 2. Training data set and performance of the srUnet to learn to predict ground-truth images.
a. Raw srSMLM image (scale bar 10 µm). The PSF of a single emitter in the spatial channel can be associated to its spectral decomposition in the spectral channel. The total signal of a single emitter is detected in two distinct domains.
b. Cluster of "mergeable" frames of a single molecule. In single molecule microscopy, fluorescent molecules can be detected in their 'on' state for more than one frame. Molecules appearing on several consecutive frames are usually merged as a single localization.
c. Building srUnet training data-set. Here we used signal appearing on consecutive frames to generate the srUnet training data-set. All but one image of a cluster were fused using a weighting based on their spatial frequencies to generate a reference image with higher signal to noise ratio (ground truth image or y_train). The image left is used as a train low SNR image (x_train). The training set was composed of $k \approx 265,000$ pairs of images and split in a train and a test data-set.
d. Representative images and e. signal profiles of the test data set and of their srUnet predictions. The y_pred image predicted by the srUnet for the x_test image appears very similar to the y_test reference image used as a target.
f. Peak signal-to-noise ratio (PSNR) and g. structural similarity index (SSIM). The restored images predicted by the network (pred) exhibited an average improvement of $\sim$ 26 dB, a value very similar to the improvement between the raw images and their corresponding ground truth (G.T.). Similarly, the SSIM values between predicted images and their ground-truth target were very close to one, showing that srUnet was able to predict ground truth quality images from raw noisy data

any localization in the training data set to force the network to make parsimonious predictions. Taken together, we generated a training matrix of dimensions (265000, 16, 64, 2) (Fig. 2 c.) that we split in a train (90%) and a test (10%) data set.

Training the network.

The srUnet was trained on the $\sim$ 240,000 pairs of images of the training set. The training time was about 60 min (200 epochs of 15-20 seconds each) on a GPU (Nvidia GTX 1080 Ti) using keras data generator (33). The $\sim 25,000$ pairs of images of the test data set were used to evaluate the quality of the training. Restored images (y_pred) were generated from the x_test images and compared to the y_test images used as a ground truth (G.T.) (Fig. 2 d. and e.). Visually, predicted images were very similar to the targeted G.T. images. As compared to the raw images, the restored images predicted by the network ($\hat{Y}$ or y_pred) exhibited an average improvement of 26 [22-29] dB (mean [CI$_{95\%}$]) measured by peak signal-to-noise ratio (PSNR) (Fig. 2 f.). The corresponding value between raw images and their corresponding ground truth was 25.5 [21-29] dB (mean [CI$_{95\%}$]). As expected from these very similar PSNR and from the visual impression, the structural similarity index (SSIM), a perceptual metric used to quantify the difference between the y_pred images and their corresponding ground truth images, was 0.93 [0.90-0.96] (median [IQR]) (Fig. 2 g.). These high SSIM values clearly demonstrate that the network was able to predict ground truth quality images from raw noisy data.

Exploring the reconstruction performance of the srUnet.

To evaluate further the reconstruction performance of the trained network (SSIM evaluated differences at the pixel level), we applied it to the previously unseen images of a validation set built independently from the testing set. We first explored the ability of the srUnet to reconstruct properly images from raw noisy images. We explored whether we could fit a PSF in the reconstructed image if a localization was initially truly present in the G.T. image. From the confusion matrix (Fig. 3 a.) we calculated a sensitivity of 99.5%. The specificity was also very good (Sp= 0.988%). Together, the accuracy reached 99.4%, showing that discrepancies relative to the G.T. data was minimal. To explore the properties of the reconstructed PSF, we fitted the G.T. PSF and the reconstructed PSF of the validation data set using the same software (Peakfit) with same setup parameters. Compared to the G.T. PSF, we observed a small systematic bias both on the center position of the 2D-Gaussian fits, with about 4 nm and about 2 nm on the X and Y axes, respectively (Fig. 3 b.), The standard deviation (SD) distributions of the circular 2D-Gaussian fits were very similar (Fig. 3 c.). The presence of the limited spatial bias is hard to interpret because of the unknown true position of the emitting molecules in the sample. This systematic bias is not critical as it only results in a translation of a few nanometers of the reconstructed image. The number of detected photons by emitters calculated as the integral of the 2D-Gaussian fits were greatly increased in the reconstructed srUnet image as compared to the the original

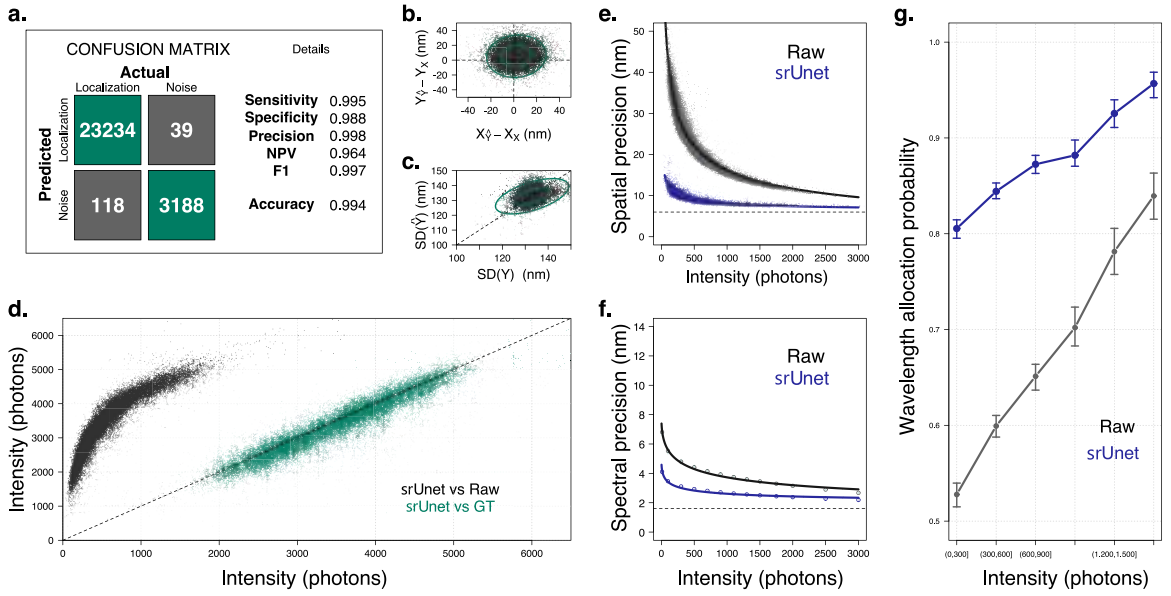

Fig. 3. U-net performance evaluated on a validation set.
a. Confusion matrix and localization detection performance metrics. The localizations retrieved on srUnet restored images were compared to the actual localizations.
b. Center position bias (in nm) and c. standard deviation change of the 2-D Gaussian fits of the PSF. A few nanometer systematic bias was found in the localization coordinates of the srUnet images using the raw data as a reference, but was not observed in the standard deviation of the 2D Gaussian fits.
d. Comparison of the number of collected photons between the srUnet and (black) raw images or (green) ground truth images. Interestingly, the improvement factor provided by the srUnet was increasing with the decrease of the raw signals.
e. Spatial and f. spectral precision as a function of the number of collected photons. We found an ultimate spatial precision of about 6 nm and an ultimate spectral precision of about 1.9 nm. The use of srUnet resulted in great improvement in both spatial and spectral precision.
g. Wavelength allocation probability as a function of the collected intensity signals. The fraction of localization for which a wavelength can be assigned increases with the signal intensity of single molecules. The fraction retrieved using srUnet was largely increased as compared to raw data and was at least as good as the one obtained for the highest signals in the raw data.

raw image. The number of photons increased by a factor of 4 to 15, with a clear tendency for the least emissive emitters to be more improved than the most emissive ones (Fig. 3 d. - black dots). Interestingly, the number of photons in the reconstructed images were very similar the the number of photons retrieved in the G.T. ones, showing that the srUnet was able to learn to reconstruct images with G.T. qualities (Fig. 3 d. - green dots).

Then we explored comparatively the spatial and spectral precisions achievable as a function of the number of photons. In the spatial domain, typical photons values obtained during srSMLM (400-1,500 photons) led to a spatial pointing precision of 25 nm to 13 nm in the raw images (Fig. 3 e.) . The ultimate spatial precision of the instrument (that is with an infinite photon number) was 6 ± 0.5 nm. In line with the enhanced signal in the reconstructed images, the precision calculated from the reconstruction of the same images with the srUnet was much better and in the range of 9 nm to 7nm. For the intensity signals ranging from 400 to 1,500 photons, the spatial precision remained close to the ultimate achievable value of about 6 nm. Interestingly, the spatial precision of the srUnet images was improved over the entire intensity range. The precisions of lowest emitting molecules with the srUnet were at least as good as those obtained for the most emissive molecules in the raw data. A similar trend was observed for the spectral precision. In Fig. 3 f., the conditional standard deviation of the retrieved wavelengths were calculated as the root square of the squared distance from the mean distance (the residuals) of a regression modeling the wavelength as a function of the signal intensity. The ultimate spectral precision was found to be about 1.9 ± 0.3 nm. At the typical intensity of 1,000 photons, the spatial precision was 2.6 ± 0.1 nm for the srUnet images as compared to 3.9 ± 0.2 nm for the raw data.

Finally, we quantified the fraction of localizations for which the spectral parameters were retrieved as a function of their intensityies In the raw data, and as expected, the wavelength allocation probability increased with the intensity, reaching about 80% for the highest emissive molecules and only about 50% for the lowest intense signals. Compared to the raw data, the srUnet wavelength allocation probability was largely improved with a minimal value of about 80% at the lowest intensity to nearly 95% for the highest intensities.

All these results showed that the localization and the spectral precisions of low-emitting species were greatly improved by the srUnet. Their precisions remained as good as those obtained with a high photons budget in the raw data, even for emitting species whose fluorescence intensity was reduced up to 10 times as compared to the best acquisition conditions. The fraction of localizations whose signal is both spatially and spectrally interpretable was also significantly improved and was well above the usual fraction retrieved in the ab-

sence of srUnet. Taken together, the use of srUnet resulted in improved pointing precisions and increased the density of spots characterized both spatially and spectrally. As these two parameters define the quality of super-resolution images, srUnet advances Spectrally-Resolved Single Molecule Localization Microscopy to reach performances close to classical SMLM.

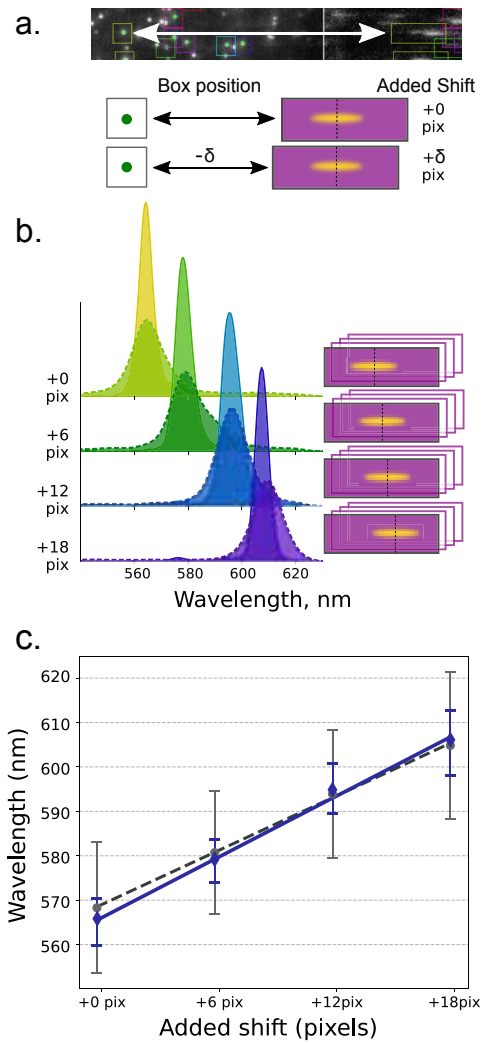

Fig. 4. Image reconstruction in the presence of a spectral shift.
a. Synthetic spectral shift. An artificial shift in the emission spectra is added by shifting the position of the container in the spectral domain relative to the position of the localization container.
b. Retrieved distributions of the wavelength at the maximum of the emission spectra. Distributions measured in raw data (dashed lines) were systematically wider as compared to those measured in srUnet images (continuous lines).
c. Mean wavelength at the maximum of emission as a function of the added shift. srUnet preserves the linearity of the response (r^2 = 0.993).

Effect of spectral shift on the srUnet images.

srSMLM has been elegantly used for single-molecule polarity detection (6, 18–20) where local hydrophobicity is probed by slight spectral shifts of spectrally responsive (solvatochromic) fluorophores. It was therefore important to explore the ability of the network to reconstruct images in the presence of spectral shifts of the emission signals. To do so, we artificially added a defined spectral shift to the validation images by shifting the position of the container in the spectral domain relative to the position of the localization container (Fig. 4 a.). We randomly reduce the distance between the containers to induce spectral shifts of 6, 12 or 18 pixels (Fig. 4 b.). The wavelengths at the maximum of the emission spectra were then determined in the raw and in the srUnet images. The distributions of wavelengths at the maximum of the emission spectra are shown in Fig. 4 b. . As expected, the centers of the distributions were shifted to the red with the increase of the added shifts, both in the raw images and in the srUnet images. Distributions retrieved in the raw images appeared wider than the ones of the srUnet images - in line with the fact that uncertainty on the spectra positions are reduced with srUnet. Plotting the mean retrieved wavelengths at the maximum of emission as a function of the added shift (Fig 4 c.) showed that the srUnet preserves the linearity of the response as demonstrated by r^2 values of 0.993 for the srUnet and r^2 = 0.978 for the raw images. In full line with the calibration curve used to characterize the spectral component of srSMLM data (6), we found a slope of 2.1 ± 0.1 nm per pixels for the spectral resolution of the setup.
These data clearly demonstrate that srUnet can be applied for single-molecule polarity sensing experiments as srUnet preserves the linearity of the experimental response (when using a transmission grating for light dispersion). This property is also important for multicolour experiments.

Multicolour imaging with single laser excitation and fluorophores with overlapping spectra.

Successful applications of srSMLM in multicolour imaging largely rely on its ability to achieve true color imaging (5, 8, 9) - offering the potential to clearly outperform multicolour measurements based on the detection of signals in spectrally separated channels. The ability to record the full emission spectra makes srSMLM suitable for multicolour imaging with closely emitting fluorophores, limiting chromatic aberrations and allowing single laser excitation. Even though the complete spectra fluorophores are captured in srSMLM, the fluorophores distinctions are generally made on the basis of their spectral weighted means or positions of their emission maximum - exposing to misidentifications. Improving spectral signals and precision is expected to result in more easily identifiable spectra.
We imaged small fixed and permeabilized Gram negative rod-shaped bacteria with two fluorophores in PAINT mode (3). We used Nile-Red, a solvatochromic dye labelling preferentially lipid membranes and emitting in this sample in the range of 590-620 nm based on local hydrophobicity (34) , and POPO-III iodide - a symmetric cyanine dye dimer with high affinity for DNA, poorly emitting in water but showing strong signal when bound to DNA. POPO-III is emitting at its maximum at ∼575 nm. This is to our knowledge the first reported use of POPO-III as a PAINT probe. Both dyes are excited by

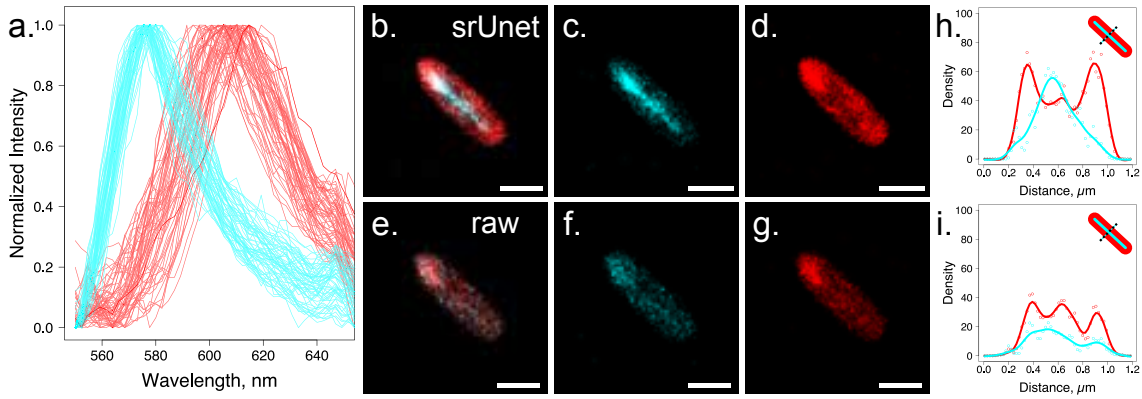

Fig. 5. Multicolour srSMLM in bacteria with Nile Red and POPO-III fluorophores.
a. srUnet augmented experimental spectra. About 200 experimental normalized spectra of single molecules of POPO-III (cyan) and Nile Red (red) are represented to illustrate the spectral overlap between the two fluorophores.
b.-g. srSMLM images of fixed *Pseudomonas aeruginosa*. (scale bar 1 μm) (b. and e.) For visualization, true colours where changed for cyan ($\lambda \leq 580$ nm) or red ($\lambda > 585$ nm). Reconstruction are represented using (b.) or not (e.) srUnet. The localizations were also split to represent the reconstruction of the spatial positions of POPO-III (c. and f.) and Nile Red (d. and g.)
h.and i. Transverse intensity profiles of the localizations density in the image in b. (h.) or e. (i.), showing better contrasts between the Nile Red stained membranes and the POPO-III labelled DNA-rich nucleoid using srUnet.

a solid state 532 nm laser source and imaged in TIRF mode, limiting the excitation in the sample to the bacterial membrane and nucleoid close to the glass-slide surface. As seen in Fig. 5 a., the experimental emission spectra of POPO-III and Nile Red were largely overlapping. The effect of srUnet on improving the quality of the two-color srSMLM images is double. First, the number of localizations with characterized wavelength information is largely increased, resulting in higher localization densities in the super-resolution images (Fig. 5 b,c,d *vs* e,f,g). Then, the improved precision of the spectral dimension resulted in easier fluorophore determination. In this sample, spatial cross-talk between the two fluorophores is expected because in TIRF mode the Nile Red signals localized in the membrane are projected partially in the same areas as the POPO-III signals staining the DNA rich nucleoid of the bacteria. As a result, the two fluorophores are not spatially separated, challenging fluorophore identification. A better fluorophore discrimination is obtained using U-net. This was easily observed on the transverse section showing better contrasts between the expected Nile Red stained membrane and the POPO-III labelled nucleoid (DNA rich area) (Fig. 5 h-i). Additionally, the distribution of the wavelengths at the maximum of emission of the Nile Red was very similar if the dye was present alone or in mixture with POPO-III - whatever the order of addition of the two fluorophores in the sample. (Supplementary fig Sx)
Together, we demonstrate that srUnet improves multicolour imaging in a demanding small sample where the labelled components are not spatially exclusive - even using fluorophores with overlapping spectra and excited by a single laser.

Conclusions

In this work, we trained a deep convolutional U-net (srUnet) to restore in post-processing high signal-to-noise (SNR) images from srSMLM acquisitions. This was made possible by building an original training data set based on spatial-frequency weighted image fusion of the same PSF recorded over several frames. We showed that localization and spectral precision of low-emitting species remain as good as those obtained with a high photons budget, even for emitting species whose fluorescence intensity is reduced up to 10 times. The spatial precision of srSMLM localizations obtained with srUnet are very similar to those obtained in classical SMLM. The use of srUnet therefore almost fully compensates the photon loss inherent to the recording of the spectral information. As a consequence of the signal restoration, the fraction of localizations whose signal is both spatially and spectrally interpretable was largely improved and well above 80% under all tested conditions. srUnet was also able to reconstruct properly images in the presence of spectral shifts. Finally, we demonstrated that srUnet is easily applicable to real data collected in biological samples and greatly facilitates multicolour imaging with single laser excitation - even for fluorophores with overlapping emission. spectra As the trained srUnet showed good generalization properties for Nile Red and POPO-III dyes, our approach is expected to work for many other fluorophores and other technical setups designed for srSMLM.

If the contributions of the network are extremely interesting as is, it could be envisioned to further advance the approach. This might include coupling the inference on the localization coordinates and spectral wavelengths directly within the deep learning network. A deep network could also be built to directly learn image reconstruction from raw data and derived versions could also be created for multicolour spectrally-resolved single molecule tracking experiments.

srSMLM can greatly benefit from the latest improvements in deep learning. Coupling srSMLM with deep learning could overcome the potential actual limitations of srSMLM and

make its use as broad and easy as SMLM.

Material and Methods

Spectrally-resolved Single molecule localization microscopy
SMLM imaging was performed on a home-built bespoke Micro-Manager controlled Olympus IX-81 inverted optical microscope equipped with a 100X 1.4 NA oil-immersion objective (Olympus - Japan) and a z-drift control and auto-focus system (ZDC Olympus). A 532 nm continuous wavelength diode-pumped solid-state laser (Coherent Sapphire SF) was used as a light source. The fluorescent emission was collected through the same objective using a 532 nm dichroic mirror (Di02-R532 - Semrock) and filtered by a longpass filter (532 LP Edge Basic, Semrock). A physical aperture (VA100/M, Thorlabs) and a transmission diffraction grating (300 Grooves/mm 8.6° Blaze Angle - GT13-03 Thorlabs) were mounted before the detector to create the spatial and spectral channels on a 512×512 pixels electron multiplied charged coupled device (EMCCD) camera (ImagEM - Hamamatsu Photonics - Japan).
Typical image stacks ranging from 10,000 to 15,000 frames with exposure time 40 ms were recorded. Image were processed by PeakFit (part of GDSC SMLM2 plugin) and/or ThunderSTORM an open source software packages for Fiji in order to retrieve molecules localization coordinates. The procedure described in Bongiovanni et al. (6) was used for spectral calibration. All subsequent and additional image processing were performed using self-written scripts in Python (version 3.8).

DNA origami nanorulers
Green (ATTO 542) nanorulers with mark-to-mark distances in the sizes 80 nm (Gatta-Paint) were available commercially (GATTAquant GmbH, Germany) and used according to the manufacturer recommendations.

Culture and sample preparation of bacteria
Briefly, *Pseudomonas aeruginosa* (PAO1 - DSM 22644) were grown overnight in 5 mL lysogeny broth (LB) (L3152, Sigma Aldrich) at 30 °C under 220 rpm orbital shaking. Cells were then diluted at OD_{600nm} = 0.1 and grown for an additional 2 to 3 hours. Cell cultures were pelleted by centrifugation, washed three times with Phosphate Buffered Saline (PBS) before being fixed using para-formaldehyde (PFA 4%) for 15 minutes at room temperature under gentle agitation. Cells were finally washed three times with PBS, permeabilized with lysosyme and stored at +4 °C. The detailed protocol can be found elsewhere (35).

Preparation of the coverslips for PAO1 imaging
Glass coverslips (0.13 mm thickness, 20×20 mm)(Knittel Glass) were cleaned using an argon plasma cleaner (PDC-002, Harrick Plasma) for 20 min. Frame-seal slide chambers (9×9 mm, Bio-rad, USA) were affixed to the glass coverslips. The chamber was filled with poly-L-lysine solution (0.01% w/v, P4707 Sigma Aldrich) to fully coat the coverglass surface, incubated for at least 10 min and then washed ones with PBS buffer. Fifty µL of fixed PAO1 cell solution were allowed to settle on PLL treated coverslips for 10 min before being washed ones with PBS buffer. The slide was transferred to the microscope stage using an Attofluor cell chamber (A-7816 Thermofisher) and optically coupled to the objective lens through index-matching immersion oil (n=1.518, Olympus, Japan). Diluted solution of Nile Red (Invitrogen) or POPO-III-iodide (Invitrogen) dyes were added directly on the sample on the microscope stage.

srUnet
The srUnet was adapted from the princeps Unet paper (27) and built using Keras library package (2.4.0) running on Tensorflow backend (2.5.0). The model was composed of 6×6 convolutions with Exponential Linear Unit (ELU) activation function followed by batch normalization and a Leaky Rectified Linear Unit (Leaky ReLU) (Fig. 1, b). The model had about $1.3 \cdot 10^6$ trainable parameters. The root mean squared error loss function was minimized using RMSprop optimizer. The model was trained using batch size of 70 over about 200 epochs. The training time was fast and the algorithm converged smoothly.

Weighted image fusion
Image fusion was used to gather all the important information from multiple images. We used spatial frequency (SF) measures to weight the different images as SF measures the overall information level in an image. SF was defined as

$$SF = \sqrt{(RF)^2 + (CF)^2}$$

where RF and CF are respectively the row frequency

$$RF = \sqrt{\frac{1}{MN} \sum_{m=1}^{M} \sum_{n=2}^{N} [I(m,n) - I(m,n-1)]^2}$$

and column frequency

$$CF = \sqrt{\frac{1}{MN} \sum_{n=1}^{N} \sum_{m=2}^{M} [I(m,n) - I(m-1,n)]^2}$$

in which M and N are the number of pixels of the (MxN) grey image and I(m,n) is the intensity of the pixel of coordinates (m,n).

Metrics for classification performance and Image quality assessment
We used Accuracy ($Acc = (tp + tn)/N$, Specificity ($Sp = tn/(tn + fp)$), Sensitivity or Recall ($Se = tp/(tp + fn)$, Positive Predictive Value or Precision ($Precision = tp/(tp + fp)$, Negative Predictive Value ($NPV = tn/(fn + tn)$) and F_1 ($F_1 = 2.(precision.recall)/(precision + recall)$ metrics for performance evaluation. All these measurements were expressed in terms of tp = true positive, tn = true negative, fp = false positive and fn = false negative.
Image quality assessment were reported using classical MSE, PSNB and SSIM metrics (36) defined as:

Mean Squared Error (MSE)

$$MSE = \frac{1}{m\,n}\sum_{i=0}^{m-1}\sum_{j=0}^{n-1}[I(i,j) - K(i,j)]^2$$

Peak signal-to-noise ratio (PSNR) in dB

$$PSNR = 20 \cdot \log_{10}\left(\frac{MAX_I}{\sqrt{MSE}}\right)$$

with $MAX_I = 2^{16}$

Structural similarity index measure (SSIM)

$$\mathrm{SSIM}(x,y) = \frac{(2\mu_x\mu_y + c_1)(2\sigma_{xy} + c_2)}{(\mu_x^2 + \mu_y^2 + c_1)(\sigma_x^2 + \sigma_y^2 + c_2)}$$

Software and Hardware Availability. The code used for the training set generation and training the network is available on https://github.com/hmanko/srSMLM_DeepL.
Most figures of this article can be reproduced independently using the code found on this repository.

ACKNOWLEDGEMENTS

We thank Dr Isablle Schalk for providing PAO1 bacteria strain.
This research was supported by the ITI Innovec (IdEx (ANR-10-IDEX-0002) and SFRI (ANR-20-SFRI-0012)). HM was funded by a 3-years contract (Contrat doctoral) from Ministère de la Recherche, France. YM is grateful to the Institut Universitaire de France (IUF) for support and providing additional time to be dedicated to research.

AUTHOR CONTRIBUTIONS

These contributions follow the Contributor Roles Taxonomy guidelines: https://casrai.org/credit/. Conceptualization: H.M., J.G; Data acquisition and curation: H.M., J.G.; Formal analysis: H.M.,J.G.; Funding acquisition: J.G., Y.M.; Investigation: H.M., J.G.; Methodology: H.M., J.G.; Project administration: J.G.; Resources: J.G., Y.M.; Software: H.M., J.G.; Supervision: J.G.; Validation: J.G.; Visualization: H.M., J.G.; Writing of original draft: H.M., J.G.; Writing review & editing: all authors.

COMPETING FINANCIAL INTERESTS

The funders had no role in study design, data collection and interpretation, or the decision to submit the work for publication. The authors declare no other competing financial interests.

Bibliography

1. Eric Betzig, George H. Patterson, Rachid Sougrat, O. Wolf Lindwasser, Scott Olenych, Juan S. Bonifacino, Michael W. Davidson, Jennifer Lippincott-Schwartz, and Harald F. Hess. Imaging intracellular fluorescent proteins at nanometer resolution. *Science*, 313(5793): 1642–1645, sep 2006. ISSN 00368075. doi: 10.1126/science.1127344.
2. Michael J. Rust, Mark Bates, and Xiaowei Zhuang. Sub-diffraction-limit imaging by stochastic optical reconstruction microscopy (STORM). *Nature Methods*, 3(10):793–795, oct 2006. ISSN 15487091. doi: 10.1038/nmeth929.
3. Alexey Sharonov and Robin M. Hochstrasser. Wide-field subdiffraction imaging by accumulated binding of diffusing probes. *Proceedings of the National Academy of Sciences of the United States of America*, 103(50):18911–18916, dec 2006. ISSN 00278424. doi: 10.1073/pnas.0609643104.
4. Suliana Manley, Julia Gunzenhäuser, and Nicolas Olivier. A starter kit for point-localization super-resolution imaging. *Current Opinion in Chemical Biology*, 15(6):813–821, 2011. ISSN 18790402. doi: 10.1016/j.cbpa.2011.10.009.
5. Zhengyang Zhang, Samuel J. Kenny, Margaret Hauser, Wan Li, and Ke Xu. Ultrahigh-throughput single-molecule spectroscopy and spectrally resolved super-resolution microscopy. *Nature Methods*, 12(10):935–938, oct 2015. ISSN 15487105. doi: 10.1038/nmeth.3528.
6. Marie N. Bongiovanni, Julien Godet, Mathew H. Horrocks, Laura Tosatto, Alexander R. Carr, David C. Wirthensohn, Rohan T. Ranasinghe, Ji Eun Lee, Aleks Ponjavic, Joelle V. Fritz, Christopher M. Dobson, David Klenerman, and Steven F. Lee. Multi-dimensional super-resolution imaging enables surface hydrophobicity mapping. *Nature Communications*, 7: 13544, dec 2016. ISSN 20411723. doi: 10.1038/ncomms13544.
7. Michael J. Mlodzianoski, Nikki M. Curthoys, Mudalige S. Gunewardene, Sean Carter, and Samuel T. Hess. Super-resolution imaging of molecular emission spectra and single molecule spectral fluctuations. *PLoS ONE*, 11(3):e0147506, 2016. ISSN 19326203. doi: 10.1371/journal.pone.0147506.
8. Biqin Dong, Luay Almassalha, Ben E. Urban, The Quyen Nguyen, Satya Khuon, Teng Leong Chew, Vadim Backman, Cheng Sun, and Hao F. Zhang. Super-resolution spectroscopic microscopy via photon localization. *Nature Communications*, 7:12290, 2016. ISSN 20411723. doi: 10.1038/ncomms12290.
9. Ki Hee Song, Yang Zhang, Benjamin Brenner, Cheng Sun, and Hao F. Zhang. Symmetrically dispersed spectroscopic single-molecule localization microscopy. *Light: Science and Applications*, 9(1):1–10, 2020. ISSN 20477538. doi: 10.1038/s41377-020-0333-9.
10. Yang Zhang, Ki-Hee Song, Biqin Dong, Janel L. Davis, Guangbin Shao, Cheng Sun, and Hao F. Zhang. Multicolor super-resolution imaging using spectroscopic single-molecule localization microscopy with optimal spectral dispersion. *Applied Optics*, 58(9):2248, 2019. ISSN 1559-128X. doi: 10.1364/ao.58.002248.
11. Tao Huang, Carey Phelps, Jing Wang, Li Jung Lin, Amy Bittel, Zubenelgenubi Scott, Steven Jacques, Summer L. Gibbs, Joe W. Gray, and Xiaolin Nan. Simultaneous Multicolor Single-Molecule Tracking with Single-Laser Excitation via Spectral Imaging. *Biophysical Journal*, 114(2):301–310, 2018. ISSN 15420086. doi: 10.1016/j.bpj.2017.11.013.
12. Xiaolan Liu, Longfang Yao, Weidong Yang, Yiyan Fei, Lan Mi, and Jiong Ma. Spectroscopic fluorescent tracking of a single molecule in a live cell with a dual-objective fluorescent reflection microscope. *Applied Physics Express*, 12(11):112007, 2019. ISSN 18820786. doi: 10.7567/1882-0786/ab4b16.
13. Benjamin Brenner, Ki-Hee Song, Cheng Sun, and Hao F. Zhang. Improving spatial precision and field-of-view in wavelength-tagged single-particle tracking using spectroscopic single-molecule localization microscopy. *Applied Optics*, 60(13):3647, 2021. ISSN 1559-128X. doi: 10.1364/ao.415275.
14. Doory Kim, Zhengyang Zhang, and Ke Xu. Spectrally Resolved Super-Resolution Microscopy Unveils Multipath Reaction Pathways of Single Spiropyran Molecules. *Journal of the American Chemical Society*, 139(28):9447–9450, jul 2017. ISSN 0002-7863. doi: 10.1021/jacs.7b04602.
15. Lorenzo Sansalone, Yang Zhang, Mercedes M.A. Mazza, Janel L. Davis, Ki Hee Song, Burjor Captain, Hao F. Zhang, and Françisco M. Raymo. High-Throughput Single-Molecule Spectroscopy Resolves the Conformational Isomers of BODIPY Chromophores. *Journal of Physical Chemistry Letters*, 10(21):6807–6812, 2019. ISSN 19487185. doi: 10.1021/acs.jpclett.9b02250.
16. Yang Zhang, Yu Zhang, Ki Hee Song, Wei Lin, Cheng Sun, George C. Schatz, and Hao F. Zhang. Investigating Single-Molecule Fluorescence Spectral Heterogeneity of Rhodamines Using High-Throughput Single-Molecule Spectroscopy. *Journal of Physical Chemistry Letters*, 12(16):3914–3921, 2021. ISSN 19487185. doi: 10.1021/acs.jpclett.1c00192.
17. Hannah L. Stern, Ruizhi Wang, Ye Fan, Ryo Mizuta, James C. Stewart, Lisa-Maria Needham, Trevor D. Roberts, Rebecca Wai, Naomi S. Ginsberg, David Klenerman, Stephan Hofmann, and Steven F. Lee. Spectrally Resolved Photodynamics of Individual Emitters in Large-Area Monolayers of Hexagonal Boron Nitride. *ACS Nano*, 13(4):4538–4547, apr 2019. ISSN 1936-0851. doi: 10.1021/acsnano.9b00274.
18. Seonah Moon, Rui Yan, Samuel J. Kenny, Yennie Shyu, Limin Xiang, Wan Li, and Ke Xu. Spectrally Resolved, Functional Super-Resolution Microscopy Reveals Nanoscale Compositional Heterogeneity in Live-Cell Membranes. *Journal of the American Chemical Society*, 139(32):10944–10947, 2017. ISSN 15205126. doi: 10.1021/jacs.7b03846.
19. Ji Eun Lee, Jason C. Sang, Margarida Rodrigues, Alexander R. Carr, Mathew H. Horrocks, Suman De, Marie N. Bongiovanni, Patrick Flagmeier, Christopher M. Dobson, David J. Wales, Steven F. Lee, and David Klenerman. Mapping Surface Hydrophobicity of α-Synuclein Oligomers at the Nanoscale. *Nano Letters*, 18(12):7494–7501, 2018. ISSN 15306992. doi: 10.1021/acs.nanolett.8b02916.
20. Dmytro I. Danylchuk, Seonah Moon, Ke Xu, and Andrey S. Klymchenko. Switchable Solvatochromic Probes for Live-Cell Super-resolution Imaging of Plasma Membrane Organization. *Angewandte Chemie - International Edition*, 58(42):14920–14924, 2019. ISSN 15213773. doi: 10.1002/anie.201907690.
21. Rui Yan, Seonah Moon, Samuel J. Kenny, and Ke Xu. Spectrally Resolved and Functional Super-resolution Microscopy via Ultrahigh-Throughput Single-Molecule Spectroscopy. *Accounts of Chemical Research*, 51(3):697–705, 2018. ISSN 15204898. doi: 10.1021/acs.accounts.7b00545.
22. Sunil Kumar Gaire, Yang Zhang, Hongyu Li, Ray Yu, Hao F. Zhang, and Leslie Ying. Accelerating multicolor spectroscopic single-molecule localization microscopy using deep learning. *Biomedical Optics Express*, 11(5):2705, 2020. ISSN 2156-7085. doi: 10.1364/boe.391806.
23. Koen JA Martens, Martijn Gobes, Emmanouil Archontakis, Roger R Brillas, Niels Zijlstra, Lorenzo Albertazzi, and Johannes Hohlbein. Enabling spectrally resolved single-molecule localization microscopy at high emitter densities. *bioRxiv*, 2022.
24. Lucas von Chamier, Romain F. Laine, Johanna Jukkala, Christoph Spahn, Daniel Krentzel, Elias Nehme, Martina Lerche, Sara Hernández-Pérez, Pieta K. Mattila, Eleni Karinou, Séamus Holden, Ahmet Can Solak, Alexander Krull, Tim Oliver Buchholz, Martin L. Jones, Loïc A. Royer, Christophe Leterrier, Yoav Shechtman, Florian Jug, Mike Heilemann, Guillaume Jacquemet, and Ricardo Henriques. Democratising deep learning for microscopy with ZeroCostDL4Mic. *Nature Communications*, 12(1):1–18, 2021. ISSN 20411723. doi: 10.1038/s41467-021-22518-0.
25. Peiyi Zhang, Sheng Liu, Abhishek Chaurasia, Donghan Ma, Michael J. Mlodzianoski, Eugenio Culurciello, and Fang Huang. Analyzing complex single-molecule emission patterns with deep learning. *Nature Methods*, 15(11):913–916, 2018. ISSN 15487105. doi: 10.1038/s41592-018-0153-5.
26. Martin Weigert, Uwe Schmidt, Tobias Boothe, Andreas Müller, Alexandr Dibrov, Akanksha Jain, Benjamin Wilhelm, Deborah Schmidt, Coleman Broaddus, Siân Culley, Mauricio Rocha-Martins, Fabián Segovia-Miranda, Caren Norden, Ricardo Henriques, Marino Zerial, Michele Solimena, Jochen Rink, Pavel Tomancak, Loic Royer, Florian Jug, and Eugene W. Myers. Content-aware image restoration: pushing the limits of fluorescence microscopy. *Nature Methods*, 15(12):1090–1097, 2018. ISSN 15487105. doi: 10.1038/s41592-018-0216-7.
27. O. Ronneberg, P. Fisher, and T. Brox. U-net: Convolutional networks for biomedical image segmentation. *MICCAI*, 2015.
28. Y LeCun and Y Bengio. Convolutional networks for images, speech, and time series. *The handbook of brain theory and neural networks*, 3361(10):255–258, 1995.
29. Yann LeCun, Yoshua Bengio, and Geoffrey Hinton. Deep learning. *Nature*, 521(7553): 436–444, may 2015. ISSN 0028-0836. doi: 10.1038/nature14539.
30. J. Akeret, C. Chang, A. Lucchi, and A. Refregier. Radio frequency interference mitigation using deep convolutional neural networks. *Astronomy and Computing*, 18:35–39, 2017. ISSN 22131337. doi: 10.1016/j.ascom.2017.01.002.

31. Jürgen J. Schmied, Mario Raab, Carsten Forthmann, Enrico Pibiri, Bettina Wünsch, Thorben Dammeyer, and Philip Tinnefeld. DNA origami-based standards for quantitative fluorescence microscopy. *Nature Protocols*, 9(6):1367–1391, 2014. ISSN 17502799. doi: 10.1038/nprot.2014.079.
32. Shutao Li, James T. Kwok, and Yaonan Wang. Combination of images with diverse focuses using the spatial frequency. *Information Fusion*, 2(3):169–176, sep 2001. ISSN 15662535. doi: 10.1016/S1566-2535(01)00038-0.
33. Francois Chollet et al. Keras, 2015.
34. Oleksandr A Kucherak, Sule Oncul, Zeinab Darwich, Dmytro A Yushchenko, Youri Arntz, Pascal Didier, Yves Mély, and Andrey S Klymchenko. Switchable nile red-based probe for cholesterol and lipid order at the outer leaflet of biomembranes. *Journal of the American Chemical Society*, 132(13):4907–4916, 2010.
35. Hanna Manko, Vincent Normant, Quentin Perraud, Tania Steffan, Véronique Gasser, Emmanuel Boutant, Éléonore Réal, Isabelle J Schalk, Yves Mély, and Julien Godet. Flim-fret measurements of protein-protein interactions in live bacteria. *JoVE (Journal of Visualized Experiments)*, (162):e61602, 2020.
36. Zhou Wang, Alan C Bovik, Hamid R Sheikh, and Eero P Simoncelli. Image quality assessment: from error visibility to structural similarity. *IEEE transactions on image processing*, 13 (4):600–612, 2004.

3.3 Spectral phasor applied to enhance srSMLM analysis

In srSMLM the spectral information can be encoded in several ways including weighted average emission wavelength or fluorescent wavelength at the emission maximum. Nevertheless, theses two methods may pose difficulties in determination of true wavelength and in distinguishing the close emission peaks, which results in a decrease of useful data ratio. Therefore, an alternative method is required that would allow obtaining the information which is contained in a full emission spectrum of the fluorophore. This can be achieved by applying a so called spectral phasor, which can be plotted using the transformation of spectra data into Fourier space coordinates defined by amplitude and phase. In such representation the emission wavelength is encoded in the position on the circle or semicircle, while the spectral width can be described by the distance from the circle centre (Figure 3.3.1).

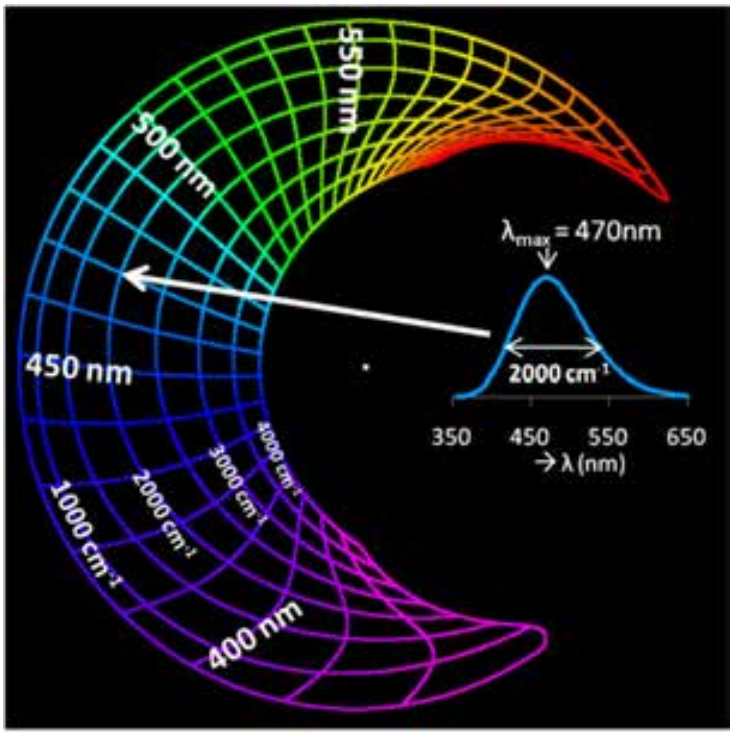

Figure 3.3.1 – An example of spectral phasor representation for Gaussian spectra [154]

The spectral information is transformed by calculating the Fourier sine and cosine according to :

$$g = \frac{\sum_\lambda I(\lambda)\cos(2\pi n\lambda/L)}{\sum_\lambda I(\lambda)} \tag{3.1}$$

$$s = \frac{\sum_\lambda I(\lambda)\sin(2\pi n\lambda/L)}{\sum_\lambda I(\lambda)}, \tag{3.2}$$

where L is the range of observations of the spectra, I(λ) is the fluorescence intensity at a given wavelength λ and n is the number of harmonic, which is set to 1.

Spectral phasor was applied for spectral unmixing in classical multicolor fluoresnece microscopy [154] and in FLIM-FRET [155] techniques. Nevertheless, the application of spectral phasor to srSMLM can be challenging due to high noise levels in the spectral part.

To explore the performance of this method it was first tested on the images of different fluorescent beads with emission peaks at 512, 560, 605 and 676 nm, respectively. The srSMLM setup displayed linear response over 500 - 700 nm spectral range. The emission wavelengths at the emission maxima were in good agreement with the experimental spectroscopy data. Next, spectral phasor method was tested on the synthetic data in order to explore the effect of noise in spectra (Figure 3.3.2). An addition of noise causes a shift of the phasor position towards the centre, while maintaining the same wavelength.

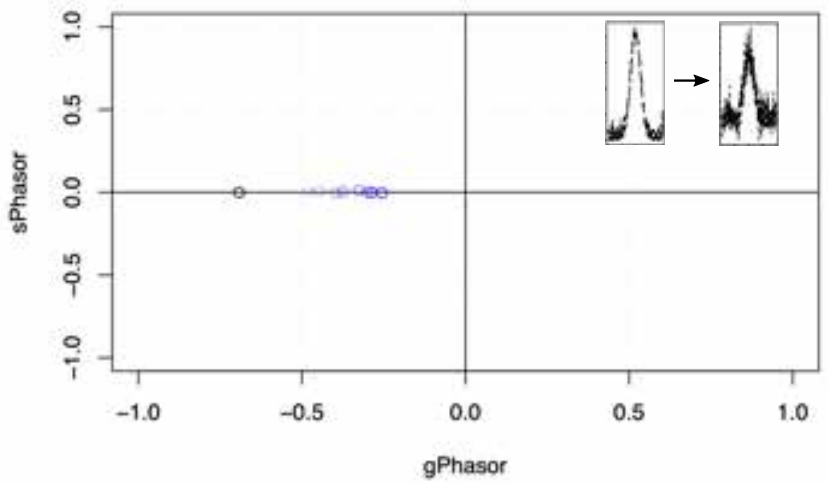

Figure 3.3.2 – The effect of spectra noise on the position of phasor. The low-noise signal (black circle) is shifted towards the centre (blue circles) upon addition of noise.

On the next step, the method was tested on mixed spectra of yellow-green and orange beads imaged at low laser intensities in order to observe the effect of spectral mixing. The effect of spectra intensity was, in turn, monitored using green fluorescence bead imaged at different laser intensities. Moreover, the method was applied to two-color images of *P.aeruginosa* membrane stained with POPO-3 and Nile Red dyes. the spectral phasor properties were further tested using srSMLM and FLIM images of *Enterococcus hirae* membrane stained with Nile Red under antibiotic(gramicidine) exposure (the obtained data in in course of analysis).

In the following section we present the article draft describing this work. Currently this draft is in progress.

Publication IV

Spectral phasor applied to spectrally-resolved super resolution microscopy

Spectral phasor applied to spectrally-resolved super resolution microscopy

Hanna Manko[1], Matthew G Burton[1], Isabelle J Schalk[2,3], Yves Mély[1], and Julien Godet[1,4]

[1]Laboratoire de BioImagerie et Pathologies, UMR CNRS 7021, ITI InnoVec, Université de Strasbourg, Illkirch, France
[2]CNRS, UMR 7242, ITI InnoVec, ESBS, Illkirch, Strasbourg, France
[3]Université de Strasbourg, UMR 7242, ESBS, Illkirch, Strasbourg, France
[4]Groupe Méthodes Recherche Clinique, Hôpitaux Universitaires de Strasbourg, France

Spectrally-resolved super resolution microscopy (srSMLM) has recently emerged as an elegant way to explore fluorescence emission properties of single emitters in localization microscopy. By pairing simultaneously the spatial locations and the spectroscopic signatures of single emitters, sr-SMLM enables exploring an additional dimension in super-resolution imaging. Investigating the spectral dimension requires appropriate and dedicated tools.

Here we propose to apply spectral phasor to summarize the spectral information of srSMLM. The spectral phasor resumes the complete spectra into a two dimension space and shows nice properties for single molecule spectra exploration. We demonstrate here that the spectral phasor can be used to efficiently classify single Nile Red fluorescence emissions from largely overlapping cyanine fluorescence signals in two colour PAINT experiments. We also used spectral phasor to evidence minute changes occurring in the membrane of Gram-positive *Enterococcus hirae* in response to gramicidin exposure - a membrane disturbing antibiotic treatment.

Spectral phasor provides a robust model-free analytic tool for the detailed analysis of the spectral component of srSMLM and enhances capabilities for multi-colour spectrally-resolved single molecule imaging.

spectrally resolved single molecule localization microscopy | spectral phasor | PAINT

Correspondence: ***julien.godet@unistra.fr***

Introduction

Single molecule super resolution microscopy (SMLM) is a generic term for all optical microscopy techniques achieving super-resolution by isolating emitters and fitting their point spread functions (PSF) to determine their localization (1, 2). The elegant idea behind SMLM is that the localization (x- y- (and z-) coordinates) of an isolated emitter can be estimated from its PSF with great accuracy provided the fitted PSF corresponds to a single emitter (3). The sequential activation of photo-switchable, photo-activatable or fluorogenic fluorophores is operated to pinpoint - frame-by-frame - spatially distinct molecules' positions - thus solving the problem of PSF emission that would otherwise spatially overlap. The subsequent accumulation of localizations results in an image with about an order of magnitude improved resolution as compared to conventional microscopy. SMLM is at the moment one of the optical imaging techniques achieving the best spatial resolution in routine optical imaging.

A new class of super resolution imaging has recently emerged based on the working principle of SMLM but that additionally records simultaneously the spectral signatures of the single emitters (4–10). Spectrally-resolved SMLM (or srSMLM) aims to collect spectral decomposition of single emitter together with their localization coordinates to build spectrally-enriched super-resolution image. srSMLM incorporates an additional dispersive element (prism, transmission grating, ...) in the detection path of classical single-molecule microscopes to capture hyperspectral information of emitters (Figure 1a). By pairing both the spatial localizations and the spectroscopic signatures of single emitters, srSMLM offers a new rich dimension to explore with evident applications for probing biological and chemical systems at the nanoscale levels (11). Previous works have encoded spectral information as a single parameter resuming the complete spectral decomposition, either by reporting the weighted averaged emission wavelength (4) or by determining the fluorescence wavelength at the maximum of the emission spectra (7).

As an emerging imaging technology, srSMLM must be advanced to fully capitalize on the multi-dimensional localization data generated. In particular, scrutinizing the spectral dimension necessitates appropriate and dedicated tools (12). Here, we propose to apply spectral phasor to srSMLM to summarize the whole information contained in the spectrum of an emitter.

A phasor is a model-free transformation of a signal into a coordinate pair defined by its amplitude and phase (g,s) in a Fourier space. The phasor approach has proven to be very valuable for frequency and time domain lifetime imaging data analysis (13–16). Phasor has also been applied to spectral imaging as a simple graphical method for spectral un-mixing (17) or to detect subtle shifts in solvatochromic dye emissions due to micro-environment heterogeneity in cell membranes (18, 19). Converting observation signals into a Fourier space has also been applied to localize the center and depth of single fluorescent emitters with very high speed and low-demanding computational resources in single molecule experiments (20). Applied to fluorescence spectra, the phasor transformation not only defines the spectra by their central positions but also summarizes its complete shape. Information about the spectra widths are then taken integrated to define coordinates in the phasor space. Therefore, in case of two different spectra with similar maximum emission wavelengths that would appear hardly distinguishable using currently reported analysis, differences in the spectrum widths

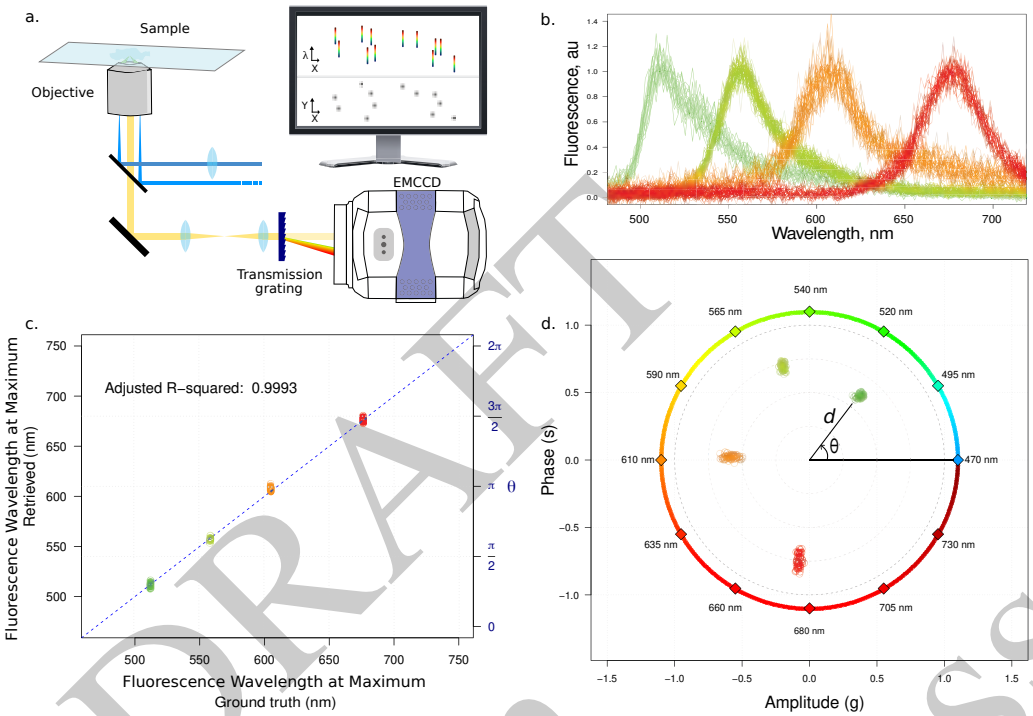

Fig. 1. srSMLM and spectral phasor principles.
a. In srSMLM, the fluorescence of single emitters is passed through a blazed transmission grating splitting the signal into an non-diffracted- (0th diffraction order) and a diffracted-beam (1st diffraction order) forming a spatial (x,y) and a spectral (x, λ) area in the image plane of the microscope recorded simultaneously with an EMCCD camera.
b. Superposition of multiple normalized spectra retrieved from four different fluorescent microspheres (0.04 µm). Microspheres were stained with fluorescent dyes that display either green (512 nm), green/yellow (560 nm), orange (605 nm) or dark red (676 nm) emission peaks.
c. Concordance of the retrieved wavelengths at the maximum of emission with the true wavelengths at the maximum of emission of the different beads. After correction, the system displays a clear linear response on the green-to-red spectral range
d. Phasor plot representation of the different spectra shown in b. In the phasor plot, the longer the emission wavelength, the larger the angle ϕ. The width of the emission spectra defines the distance from the center of the phasor plot (the narrower the spectrum, the longer the distance m).

or shapes can make the discrimination possible using phasor. In this work we explored the new opportunities spectral phasor can provide to enhance srSMLM analysis. The successful application of spectral phasor to srSMLM data was not obvious as single molecule spectra are much noisier that that of ensemble measurements. We demonstrate here that the spectral phasor can be used to efficiently discriminate single-molecule Nile Red fluorescence emissions from the largely overlapping POPO-III fluorescence emissions in single-laser excitation two colors PAINT experiments. Finally, we attempted to exploit the spectral phasor properties to evidence minute changes occurring in the membrane of the Gram-positive *Enterococcus hirae* in response to exposure to a membrane disturbing antibiotic treatment.

Results

Spectral phasor of fluorescent beads with different colours. To illustrate the principle of the spectral phasor, we imaged four different microspheres loaded with different fluorophores. We recorded the spectra of each individual fluorescent beads using srSMLM (Figure 1b). For each individual spectrum, we determined the wavelengths at the maximum of emission and compared it to the experimentally determined wavelengths recorded using ensemble fluorescence spectroscopy and used as a reference (Figure 1c). The agreement between the retrieved and the ground truth wavelengths was very good (all $CV_{RMSE} \leq 0.003$) showing that srSMLM can be used as a single particle spectroscope that displays a clear linear response on the green-to-red spectral range ($r^2 > 0.999$). All the recorded spectra were then transformed into phasor.s The spectral phasor transformation calculates the Fourier sine and cosine transforms of a given spectrum according to:

$$g = \frac{\sum_\lambda I(\lambda) \cos\left(\frac{2\pi n\lambda}{\lambda_{max}-\lambda_{min}}\right)}{\sum_\lambda I(\lambda)} \quad \textbf{(1)}$$

$$s = \frac{\sum_\lambda I(\lambda) \sin\left(\frac{2\pi n\lambda}{\lambda_{max}-\lambda_{min}}\right)}{\sum_\lambda I(\lambda)} \quad \textbf{(2)}$$

where n is the harmonic number (set to 1), λ_{min} and λ_{max} define the range of observations of the spectra and $I(\lambda)$ is the fluorescence intensity at a given wavelength λ (17). g

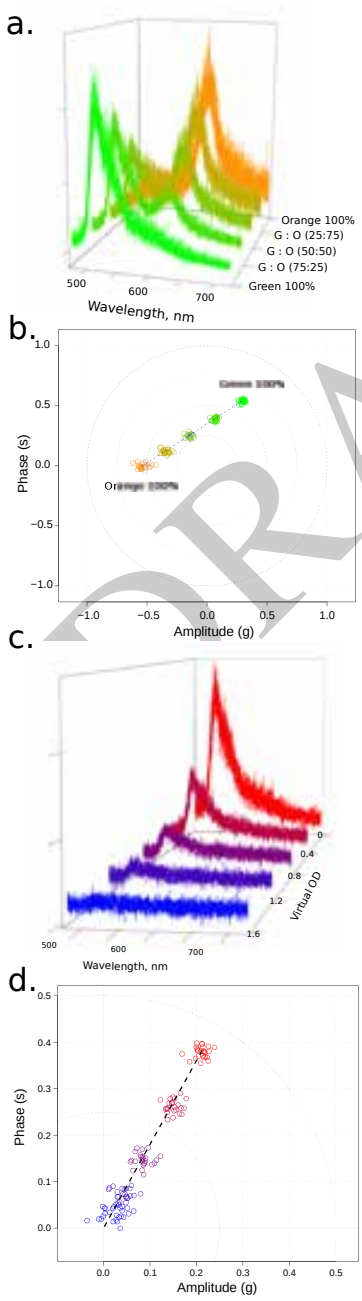

Fig. 2. Phasor linear properties

a. Typical single molecule synthetic spectra built as mixture of experimental green and orange spectra of microsphere beads images at low laser power.

b. Projections of the different mixture spectra showing that mixture spectra are distributed along the segment between the green and the orange coordinates.

c. Single molecule spectra of a microsphere imaged with increasing laser power illumination.

d. The modulation m increases with the spectra intensity and narrowing of its FWHM.

and s correspond to the real and imaginary components of the Fourier decomposition, respectively.

The spectral phasor transformation captures the center of mass (phase, ϕ) and full-width-of-the-half-maximum (FWHM) (Modulation, m) of the spectra. In the polar coordinates of the phasor plot, spectra with increasing emission wavelengths are distributed counterclockwise in the polar plot. The longer the emission wavelength of the spectra, the larger the phase ϕ as ϕ is defined by:

$$\phi = arctan(s/g) \quad \textbf{(3)}$$

As it can be seen Figure 1d, the angular position in the phasor plot is defined by the center of mass of its spectrum. The linearity on the 500 nm-700 nm range is conserved after being transformed into a phasor (Figure 1b - right axis).

The width of the emission of a spectra defines the distance from the center of the phasor plot. The modulation is indeed defined by

$$m = \sqrt{s^2 + g^2} \quad \textbf{(4)}$$

The narrower the spectrum, the longer the distance m, as it can be seen in Figure 1c when looking closely at the spectra of green and green/yellow fluorescent beads for example that exhibit larger spectra width. The distance m reports also somehow the intensity of the spectra (see Figure 2).

Applied to single fluorescent microspheres spectroscopy, the phasor coordinates of the different microspheres were clearly distinct from one to the other. The intra-bead coordinates were highly clustered and exhibited a low spatial distribution in the phasor plot ($\sigma_\phi < 0.03$rad, $\sigma_m < 0.06$).

Taken together and as previously described (17, 21), the spectral phasor reports the rich information on the spectral component of srSMLM by summarizing the complete spectra of single emitters.

Linear properties of the spectral phasor.

One additional advantage of spectral phasor is its capability of unmixing spectra due to its linear combination properties. If a spectra is a linear mixture of two other spectra A and B, its coordinate will be on the line between A and B with relative distances to A and B that correspond to the contribution of each spectra in the mixture. To investigate of whether it is possible for the spectral phasor to unmix spectral data recorded with noisy signal (we choose an intensity signal similar to the typical signal of a single molecule PA-mCherry), we imaged immobilized single fluorescent beads (yellow-green and orange beads from FluoSpheres Fluorescent Colour Kit, 0.04 μm, Invitrogen) at low laser illumination to record their spectral signatures. Green and orange spectra were then combined linearly using know amplitude to generate synthetic mixed spectra. Phasor plot of the different synthetic spectral signatures were computed. As expected, mixture of green and orange spectra gave coordinates that aligned on the segment joining the pure green and the pure orange coordinates. If the spectra of the individual dyes are known, this linear system can be solved and the relative amplitude of the individual components composing the mixture can be obtained as seen Figure 2. This property could

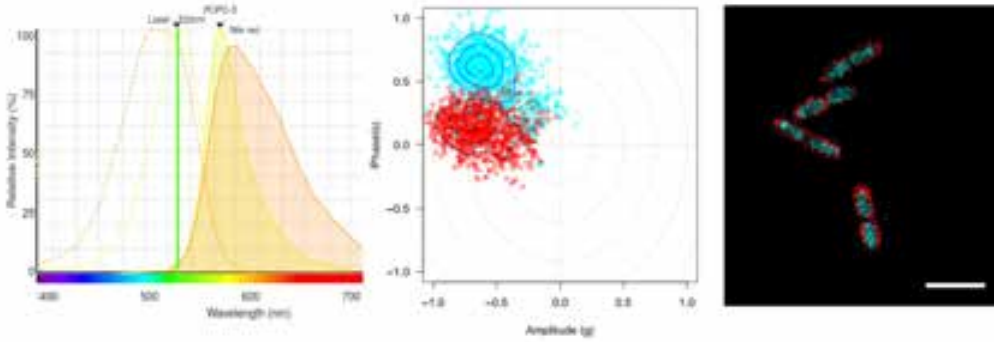

Fig. 3. Mock image to be replaced
a. Normalized single molecule spectra of POPO-III and Nile Red showing large overlap between the two fluorophores
b. Projections of POPO-III (blue n=...) and Nile Red (red n=...) spectra in the phasor space.
c. False color image reconstruction
Colors of the localization are attributed based on the spectral phasor coordinates of the spectra.

be obviously exploited for single molecule FRET filtering as the distribution of FRET energy transfer of pairs of single molecule should lay on a line that pass through the donor only projection points. We also imaged a green bead repeating but with changing step wise the laser intensity used for illumination. Representative spectra are presented Figure 2 c.. The corresponding phasor projections are also aligned along the radius of the phasor plot. The higher the signal to noise ratio (SNR) of the spectra and the further from the center of the phasor plot the spectra is projected in the plot. This property has evident potential for data filtering to discard the spectra with too low amplitude of too wide spectra.

Multicolor sPAINT with single laser excitation.

As demonstrated with fluorescent beads, the spectral phasor projects spectra into a two-dimensional space which offers an opportunity for better spectra discrimination and classification. Correct fluorophore attribution of hardly discernible overlapping spectra might be easier in the 2D space of the phasor plot as compared to the 1D distribution of weighted emission wavelengths. To challenge the spectral phasor's ability to discriminate between fluorophores with overlapping emissions, we imaged fixed and permeabilized *Pseudomonas aeruginosa* PAO1 in sPAINT mode (7) using either POPO-3 Iodide, Nile Red or a combination of both dyes.

In PAINT (22), fluorophores are added directly at low concentration in the sample solution where they are poorly fluorescent and diffuse freely. The binding of the dyes to their targets results in a huge increase of their fluorescence signal - generating a burst of fluorescence from which the position of the fluorophore in the sample can be inferred.

POPO-III Iodide is a symmetric cyanine dimer dye with high-affinity for nucleic acid. POPO-III is poorly fluorescent in water but exhibits strong fluorescence emission bound to nucleic acids with a maxima of emission at around 570 nm. Nile Red is a benzo-phenoxazinone lipophilic stain with very low quantum yield in polar solvent. NR fluoresces intensely once inserted in the hydrophobic environment of the lipid membranes. POPO-III and Nile Red absorption and emission spectra almost completely overlap and cannot be efficiently separated using spectral filters.

To extract quantitative data on the classification performance of the phasor analysis, we recorded localizations and spectral emissions of individual Nile Red or POPO-III fluorophores alone or in mixture in the same sample illuminated with a 532 nm laser. Acquisition sequences were made by adding Nile Red alone first. The same sample was then imaged again after the addition of POPO-III directly in the sample on the microscope. The order of addition was changed for POPO-III first and Nile Red then to check that order of addition had no influence on the data. Localization and spectra were extracted from the concatenated stack corresponding to dye alone and phasor coordinates were calculated and plotted. A simple k-means clustering algorithm was applied on the Cartesian coordinates of the localizations in the phasor plot to partition the observations into two clusters. The performance was surprisingly good with an accuracy of more than 96%.

We then calculated wavelengths and phasor for the acquisitions corresponding to the mixture of dyes. The probability of fluorophores assignation were determined for each coordinates in the phasor plot according to the densities map obtained with single fluorophores. Localizations associated to each fluorophores were rendered as "cyan" (POPO-III attribution) or "red" (NR attribution) in two separated images which were then merged in a composite image. Figure 4 clearly showed that localizations attributed to the red signal were distributed at the membrane whereas the cyan signal was corresponding to the nucleoid of PAO1, in line with the preferential affinities of NR and POPO-III for membranes and DNA, respectively. Images with similar quality were ob-

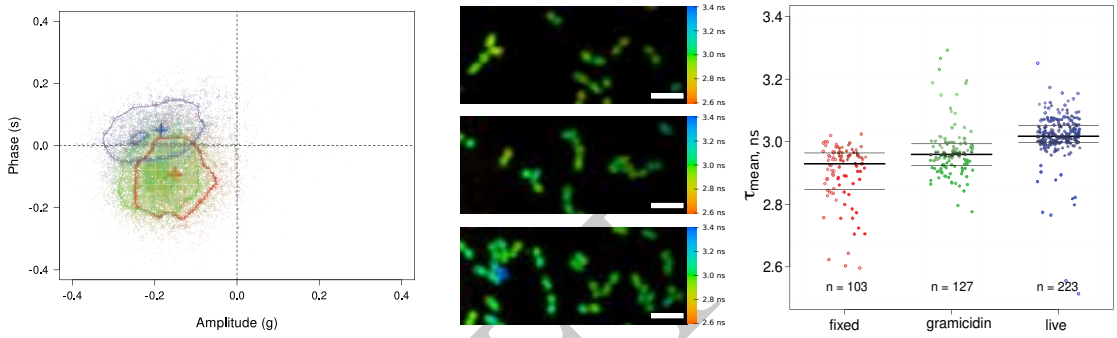

Fig. 4. Phasor plot and fluorescence lifetime imaging of *Enterrococcus hirae* stained with Nile Red
a.
b. Projections of POPO-III (blue n=...) and Nile Red (red n=...) spectra in the phasor space.
c. False color image reconstruction
Colors of the localization are attributed based on the spectral phasor coordinates of the spectra.

served when a combination of both dyes was added tin a different order. Therefore, multicolour imaging can be done just by mixing the two fluorophores in the sample.
These data clearly demonstrate phasor is able to distinguish between individual fluorophores with large overlapping. To our knowledge, this is also the first demonstration of multicolour PAINT using a single laser for excitation where the different fluorophores are acquired simultaneously in wide field imaging. This opens exciting perspectives towards multiplexed PAINT imaging.

Discrete changes of E. hirae membranes upon gramicidin exposure.

srSMLM can exploit dyes that exhibis both an environmentally-specific spectral shift, and can be individually localized at the single-molecule level. Sensing the spectral in molecule like Nile Red allow to sense the local hydrophobicity in the sample. Then it might be possible to sense subtle changes occuring in the lipid membrane of biological membranes perturbated by external agents or mechanical perturbations. Here we attempted to explore if we could sense the minute changes in the membrane organization of *Enterococcus hirae* in response to gramicidine exposure. Gramicidins are linear peptides with 15 amino acids working as antibiotics against gram-positive bacteria. Gramicidins are ionophores forming ion channel-like pores in cell membranes of bacteria, and manipulate the plasma membrane potential (PMP). Gramicidin has also hydrophobic nature and are capable of affecting the organization of membrane lipids. We imaged live *E hirae* either in the presence or absence of 1 MIC of gramicidin. Gramicidin was added in the sample readily on the microscope. We also recorded fixed *E hirae* as a control. Interestingly, the phasor representation of srSMLM spectra improved using srUnet (**?**) exhibited slight differences. Live cells add slightly shorter wavelength and their phasor did not fully overlapped with the one of cells treated with gramicidin or fixed cells.
We also measured FLIM in these conditions. We found that the lifetime of the live cells were slightly longer, in line with the fact that the shorter the wavelength, the longer the lifetime (23). It is hard to figure out if these small changes are due only to change in local hydrophobicity because Nile Red has also been sensitive to membrane potential and depolarization of the cell membrane leads to decreased fluorescence intensity. (24).
Taken together, phasor applied to srSMLM data allowed to evidence minute changes occurring in the membrane of *E hirae* in response to Gramicidin. These change could also be detected in FLIM, even though the mechanism leading to these changes is yet poorly clear.

Discussion

Lorem ipsum dolor sit amet, consectetuer adipiscing elit. Ut purus elit, vestibulum ut, placerat ac, adipiscing vitae, felis. Curabitur dictum gravida mauris. Nam arcu libero, nonummy eget, consectetuer id, vulputate a, magna. Donec vehicula augue eu neque. Pellentesque habitant morbi tristique senectus et netus et malesuada fames ac turpis egestas. Mauris ut leo. Cras viverra metus rhoncus sem. Nulla et lectus vestibulum urna fringilla ultrices. Phasellus eu tellus sit amet tortor gravida placerat. Integer sapien est, iaculis in, pretium quis, viverra ac, nunc. Praesent eget sem vel leo ultrices bibendum. Aenean faucibus. Morbi dolor nulla, malesuada eu, pulvinar at, mollis ac, nulla. Curabitur auctor semper nulla. Donec varius orci eget risus. Duis nibh mi, congue eu, accumsan eleifend, sagittis quis, diam. Duis eget orci sit amet orci dignissim rutrum.
Nam dui ligula, fringilla a, euismod sodales, sollicitudin vel, wisi. Morbi auctor lorem non justo. Nam lacus libero, pretium at, lobortis vitae, ultricies et, tellus. Donec aliquet, tortor sed accumsan bibendum, erat ligula aliquet magna, vitae ornare odio metus a mi. Morbi ac orci et nisl hendrerit mollis. Suspendisse ut massa. Cras nec ante. Pellentesque a nulla. Cum sociis natoque penatibus et magnis dis parturient montes, nascetur ridiculus mus. Aliquam tincidunt urna. Nulla ullamcorper vestibulum turpis. Pellentesque cursus luctus mauris.
Nulla malesuada porttitor diam. Donec felis erat, congue non, volutpat at, tincidunt tristique, libero. Vivamus viverra

fermentum felis. Donec nonummy pellentesque ante. Phasellus adipiscing semper elit. Proin fermentum massa ac quam. Sed diam turpis, molestie vitae, placerat a, molestie nec, leo. Maecenas lacinia. Nam ipsum ligula, eleifend at, accumsan nec, suscipit a, ipsum. Morbi blandit ligula feugiat magna. Nunc eleifend consequat lorem. Sed lacinia nulla vitae enim. Pellentesque tincidunt purus vel magna. Integer non enim. Praesent euismod nunc eu purus. Donec bibendum quam in tellus. Nullam cursus pulvinar lectus. Donec et mi. Nam vulputate metus eu enim. Vestibulum pellentesque felis eu massa.

Material and Methods

Preparation of cells and coverslips for PAO1 imaging
P. aeruginosa (PAO1 - DSM 22644) were grown overnight in 5 mL lysogeny broth (LB) (L3152, Sigma Aldrich) at 30°C under 220 rpm orbital shaking. Cells were then diluted at OD_{600nm} = 0.1 and grown for an additional 2 to 3 hours. Cell cultures were pelleted by centrifugation, washed three times with Phosphate Buffered Saline (PBS) before being fixed using para-formaldehyde (PFA 4%) for 30 minutes at room temperature under gentle agitation. Cells were finally washed three times with PBS and stored at +4 °C. Glass coverslips (0.13 mm thickness, 20×20 mm,(Marque Ref...) were cleaned using an argon plasma cleaner (PDC-002, Harrick Plasma) for 30 min, then Frame-seal slide chambers (9×9 mm, Bio-rad, USA) were affixed to the glass coverslips. The chamber was filled with poly-L-lysine solution (0.01% w/v, P4707 Sigma Aldrich) to fully coat the cover-glass surface, incubated for at least 30 min and then washed three times with PBS buffer. Fifty µL of fixed PAO1 cell solution were allowed to settle on PLL treated coverslips for 10 min before being washed three times with PBS buffer. The slide was transferred to the microscope stage using an Attofluor cell chamber (A-7816 Thermofisher) and optically coupled to the objective lens through index-matching immersion oil (n=1.518, Olympus, Japan).

Sample preparation for E. hirae imaging
Standard overnight culture of *Enterococcus hirae* (DSM 3320) was performed by inoculating a Tryptic Soy Yeast (TSY) media (22092, Sigma Aldrich) from frozen glycerol stock, and grown at 30 °C for at least 8 hours in an orbital shaking incubator at 220 rpm. Prior to experiments, *E. hirae* cultures were diluted based on OD_{600nm} (Eppendorf BioPhotometer) to obtain an OD of 0.1 to 0.2 (approximately 1:20 dilution). Cells were grown for an additional 2-3 hours. Four µL of bacterial culture were then spotted on of a 1% (m/V) agarose (Low EEO Agarose, 9539, Sigma Aldrich) pad. A # 1.5 coverslip was placed ontop and sealed with melted paraffin (Paraplast, P3558 Sigma Aldrich).

Spectrally-resolved Single molecule localisation microscopy
SMLM imaging was performed on a home-built, bespoke Micro-Manager (25) controlled Olympus IX-81 inverted optical microscope equipped with z-drift control and auto-focus system (ZDC Olympus) and coupled to a 512×512 pixels electron multiplied charged coupled device (EMCCD) camera (ImagEM - Hamamatsu Photonics - Japan).
Phase images were generated using a Phase3 100X 1.4NA objective (Olympus) using a 512×512 pixels EM-CCD (ImagEM - Hamamatsu Photonics - Japan). The microscope was configured to operate in objective-type highly inclined and laminated optical sheet (HILO) using a Phase3 100X 1.4NA objective (Olympus - Japan) with a beam of a 150 mW 532 nm continuous wavelength diode-pumped solid-state laser (Spectra physics) or a 561 nm CW diode laser
Epifluorescence excitation was provided by a 488 nm laser diode (spectra physics) using a 488 nm (Di01-R488 - Semrock) dichroic filter. Fluorescence signals were filtered using a 488 nm Long pass filter (BLP01-488R-25 Semrock).
Fixed-PAO1-cells were immobilized on a Poly-lysine coated (26)
1% agarose pad and imaged at 20 °C. Quantitative fluorescence measurements were performed at the cell level using a home-made imageJ plugin for cell segmentation and fluorescence quantification. Initial cell segmentation was based on a Laplacian of Gaussian (LoG) filtering of the phase image and further used to define a rod-shape contour (sphero-cylinder) based on different central moment calculations. Initial rod-shape contours were then refined based on the isotropic 3×3 gradient of the initial image to adjust bacteria contours.

Fluorescence Lifetime Imaging Microscopy (FLIM)
Time-correlated single-photon counting FLIM measurements were performed on a home-made two-photon excitation scanning microscope based on an Olympus IX70 inverted microscope with an Olympus 60x 1.2NA water immersion objective operating in de-scanned fluorescence collection mode (27, 28). Two-photon excitation at 930 nm was provided by a Ti:Sapphire oscillator (Mai Tai DeepSee, Spectra Physics - 80 MHz repetition rate, ≈ 70 fs pulse width) at 10-20mW. Fluorescence photons were collected through a 680 nm short pass filter (F75-680, AHF, Germany) and a 525/50 nm band-pass filter (F37-516, AHF, Germany) and directed to a fibre-coupled avalanche photo-diode (SPCM-AQR-14-FC, Perkin Elmer) connected to a time-correlated single photon counting (TCSPC) module (SPC830, Becker & Hickl, Germany). Cells grown in TSY were immobilized on a 1% agarose pad and rapidly imaged. Typically, area of 50×50 µm in the samples were scanned at 4 µs per pixel (1024×1024 pixels) for 100 s to 600 s to reach the Nyquist-Shannon sampling criteria and to achieve the appropriate photon statistics to investigate the fluorescence decays. Fluorescence decays were processed using a commercial software package (SPCImage V2.8, Becker & Hickl, Germany). A binning of two was applied before processing the fluorescence decays. FLIM data were further analyzed using a homemade ImageJ plugin and R scripts (29).

Software and Hardware Availability. A R package named spectralPhasoR for spectral Phasor representation of spectrally-resolved single molecule localisation microscopy data is available on https://github.com/jgodet/spectralPhasoR.

Most figures of this article can be reproduced independently using the code found on this repository.

ACKNOWLEDGEMENTS
We acknowledge Dr Ludovic Richert for his valuable assistance on FLIM data acquisition and for the technical maintenance and development of the FLIM setup. This research was supported by the ITI Innovec (IdEx (ANR-10-IDEX-0002) and SFRI (ANR-20-SFRI-0012)) and by Fondation pour la Recherche en Chimie (https://icfrc.fr/), ...YM is grateful to the Institut Universitaire de France (IUF) for support and providing additional time to be dedicated to research.

AUTHOR CONTRIBUTIONS
These contributions follow the Contributor Roles Taxonomy guidelines: https://casrai.org/credit/. Conceptualisation: M.B., J.G; Data acquisition and curation: M.B., H.M., J.G.; Formal analysis: J.G.; Funding acquisition: J.G., I.J.S, Y.M.; Investigation: M.B., H.M., J.G.; Methodology: J.G.; Project administration: J.G.; Resources: J.G., I.J.S, Y.M.; Software: J.G.; Supervision: J.G.; Validation: J.G., I.J.S, Y.M.; Visualisation: J.G.; Writing – original draft: M.B., J.G.; Writing – review & editing: all authors.

COMPETING FINANCIAL INTERESTS
MGB was funded by Fondation pour la Recherche en Chimie (https://icfrc.fr/). The funders had no role in study design, data collection and interpretation, or the decision to submit the work for publication. The authors declare no other competing financial interests.

Bibliography

1. Eric Betzig, George H Patterson, Rachid Sougrat, O Wolf Lindwasser, Scott Olenych, Juan S Bonifacino, Michael W Davidson, Jennifer Lippincott-Schwartz, and Harald F Hess. Imaging intracellular fluorescent proteins at nanometer resolution. *Science (New York, N.Y.)*, 313(5793):1642–5, sep 2006. ISSN 1095-9203. doi: 10.1126/science.1127344.
2. Michael J Rust, Mark Bates, and Xiaowei Zhuang. Stochastic optical reconstruction microscopy (STORM) provides sub-diffraction-limit image resolution. *Nature methods*, 3(10): 793–795, oct 2006. ISSN 1548-7091. doi: 10.1038/nmeth929.
3. Antony Lee, Konstantinos Tsekouras, Christopher Calderon, Carlos Bustamante, and Steve Pressé. Unraveling the thousand word picture: An introduction to super-resolution data analysis. *Chemical Reviews*, 117(11):7276–7330, apr 2017. doi: 10.1021/acs.chemrev.6b00729.
4. Zhengyang Zhang, Samuel J Kenny, Margaret Hauser, Wan Li, and Ke Xu. Ultrahigh-throughput single-molecule spectroscopy and spectrally resolved super-resolution microscopy. *Nature methods*, 12(10):935–8, oct 2015. ISSN 1548-7105. doi: 10.1038/nmeth.3528.
5. Biqin Dong, Luay Almassalha, Ben E Urban, The-Quyen Nguyen, Satya Khuon, Teng-Leong Chew, Vadim Backman, Cheng Sun, and Hao F Zhang. Super-resolution spectroscopic microscopy via photon localization. *Nature communications*, 7:12290, 2016. ISSN 2041-1723. doi: 10.1038/ncomms12290.
6. Michael J Mlodzianoski, Nikki M Curthoys, Mudalige S Gunewardene, Sean Carter, and Samuel T Hess. Super-Resolution Imaging of Molecular Emission Spectra and Single Molecule Spectral Fluctuations. *PloS one*, 11(3):e0147506, 2016. ISSN 1932-6203. doi: 10.1371/journal.pone.0147506.
7. Marie N Bongiovanni, Julien Godet, Mathew H Horrocks, Laura Tosatto, Alexander R Carr, David C Wirthensohn, Rohan T Ranasinghe, Ji-Eun Lee, Aleks Ponjavic, Joelle V Fritz, Christopher M Dobson, David Klenerman, and Steven F Lee. Multi-dimensional super-resolution imaging enables surface hydrophobicity mapping. *Nature communications*, 7: 13544, dec 2016. ISSN 2041-1723. doi: 10.1038/ncomms13544.
8. Tao Huang, Carey Phelps, Jing Wang, Li-Jung Lin, Amy Bittel, Zubenelgenubi Scott, Steven Jacques, Summer L Gibbs, Joe W Gray, and Xiaolin Nan. Simultaneous Multicolor Single-Molecule Tracking with Single-Laser Excitation via Spectral Imaging. *Biophysical journal*, 114(June):519–538, 2018. ISSN 1542-0086. doi: 10.1016/j.bpj.2017.11.013.
9. Biqin Dong, Janel L Davis, Cheng Sun, and Hao F Zhang. Spectroscopic analysis beyond the diffraction limit. *The international journal of biochemistry & cell biology*, 101:113–117, 2018. ISSN 1878-5875. doi: 10.1016/j.biocel.2018.06.002.
10. Rui Yan, Seonah Moon, Samuel J Kenny, and Ke Xu. Spectrally Resolved and Functional Super-resolution Microscopy via Ultrahigh-Throughput Single-Molecule Spectroscopy. *Accounts of chemical research*, 51(3):697–705, 2018. ISSN 1520-4898. doi: 10.1021/acs.accounts.7b00545.
11. Geun-ho Kim, Jinkyoung Chung, Hyunbum Park, and Doory Kim. Single-molecule sensing by grating-based spectrally resolved super-resolution microscopy. *Bulletin of the Korean Chemical Society*, 42(2):270–278, 2021.
12. A Ki-Hee Song, B. Biqin Dong, C. Cheng Sun, and D. Hao F. Zhang. Theoretical analysis of spectral precision in spectroscopic single-molecule localization microscopy. *The Review of scientific instruments*, 89(12):123703, dec 2018. ISSN 1089-7623. doi: 10.1063/1.5054144.
13. David M. Jameson, Enrico Gratton, and Robert D. Hall. The measurement and analysis of heterogeneous emissions by multifrequency phase and modulation fluorometry. *Applied Spectroscopy Reviews*, 20(1):55–106, jan 1984. doi: 10.1080/05704928408081716.
14. A. H. A. Clayton, Q. S. Hanley, and P. J. Verveer. Graphical representation and multicomponent analysis of single-frequency fluorescence lifetime imaging microscopy data. *Journal of Microscopy*, 213(1):1–5, jan 2004. doi: 10.1111/j.1365-2818.2004.01265.x.
15. Michelle A. Digman, Valeria R. Caiolfa, Moreno Zamai, and Enrico Gratton. The phasor approach to fluorescence lifetime imaging analysis. *Biophysical Journal*, 94(2):L14–L16, jan 2008. doi: 10.1529/biophysj.107.120154.
16. Suman Ranjit, Leonel Malacrida, David M. Jameson, and Enrico Gratton. Fit-free analysis of fluorescence lifetime imaging data using the phasor approach. *Nature Protocols*, 13(9): 1979–2004, sep 2018. doi: 10.1038/s41596-018-0026-5.
17. Farzad Fereidouni, Arjen N. Bader, and Hans C. Gerritsen. Spectral phasor analysis allows rapid and reliable unmixing of fluorescence microscopy spectral images. *Optics Express*, 20(12):12729, may 2012. doi: 10.1364/oe.20.012729.
18. Ottavia Golfetto, Elizabeth Hinde, and Enrico Gratton. The laurdan spectral phasor method to explore membrane micro-heterogeneity and lipid domains in live cells. In *Methods in Molecular Biology*, pages 273–290. Springer New York, sep 2014. doi: 10.1007/978-1-4939-1752-5_19.
19. Sara Sameni, Leonel Malacrida, Zhiqun Tan, and Michelle A. Digman. Alteration in fluidity of cell plasma membrane in huntington disease revealed by spectral phasor analysis. *Scientific Reports*, 8(1), jan 2018. doi: 10.1038/s41598-018-19160-0.
20. Koen J. A. Martens, Arjen N. Bader, Sander Baas, Bernd Rieger, and Johannes Hohlbein. Phasor based single-molecule localization microscopy in 3d (pSMLM-3d): An algorithm for MHz localization rates using standard CPUs. *The Journal of Chemical Physics*, 148(12): 123311, mar 2018. doi: 10.1063/1.5005899.
21. Belén Torrado, Leonel Malacrida, and Suman Ranjit. Linear combination properties of the phasor space in fluorescence imaging. *Sensors*, 22(3):999, 2022.
22. A. Sharonov and R. M. Hochstrasser. Wide-field subdiffraction imaging by accumulated binding of diffusing probes. *Proceedings of the National Academy of Sciences*, 103(50): 18911–18916, dec 2006. doi: 10.1073/pnas.0609643104.
23. James A Levitt, Pei-Hua Chung, and Klaus Suhling. Spectrally resolved fluorescence lifetime imaging of nile red for measurements of intracellular polarity. *Journal of biomedical optics*, 20(9):096002, 2015.
24. Mayya Sundukova, Efthymia Prifti, Annalisa Bucci, Kseniia Kirillova, Joana Serrao, Luc Reymond, Miwa Umebayashi, Ruud Hovius, Howard Riezman, Kai Johnsson, et al. A chemogenetic approach for the optical monitoring of voltage in neurons. *Angewandte Chemie International Edition*, 58(8):2341–2344, 2019.
25. Arthur D Edelstein, Mark A Tsuchida, Nenad Amodaj, Henry Pinkard, Ronald D Vale, and Nico Stuurman. Advanced methods of microscope control using μmanager software. *Journal of biological methods*, 1(2), 2014.
26. Hanna Manko, Vincent Normant, Quentin Perraud, Tania Steffan, Véronique Gasser, Emmanuel Boutant, Éléonore Réal, Isabelle J Schalk, Yves Mély, and Julien Godet. Flim-fret measurements of protein-protein interactions in live bacteria. *JoVE (Journal of Visualized Experiments)*, (162):e61602, 2020.
27. Salah Edin El Meshri, Denis Dujardin, Julien Godet, Ludovic Richert, Christian Boudier, Jean Luc Darlix, Pascal Didier, Yves Mély, and Hugues de Rocquigny. Role of the nucleocapsid domain in hiv-1 gag oligomerization and trafficking to the plasma membrane: a fluorescence lifetime imaging microscopy investigation. *Journal of molecular biology*, 427 (6):1480–1494, 2015.
28. Julien Batisse, Santiago Xavier Guerrero, Serena Bernacchi, Ludovic Richert, Julien Godet, Valérie Goldschmidt, Yves Mély, Roland Marquet, Hugues de Rocquigny, and Jean-Christophe Paillart. Apobec3g impairs the multimerization of the hiv-1 vif protein in living cells. *Journal of virology*, 87(11):6492–6506, 2013.
29. Julien Godet and Yves Mély. Exploring protein–protein interactions with large differences in protein expression levels using flim-fret. *Methods and Applications in Fluorescence*, 8(1): 014007, 2019.

3.4 Investigation of mechanisms of *P.aeruginosa* tolerance to carbapenems

In this part we aimed to explore the effect of carbapenems (meropenem) on *P.aeruginosa* and the mechanism that allows to tolerate this antibiotics (ATB), as well as the mechanism of recovery from the ATB exposure.

Meropenem belongs to the β-lactams, which comprise a class of broad-spectrum antibiotics that are able to inhibit the cell wall biosynthesis. This occurs by binding to the Penicilin-binding proteins (PBPs) which are required at the final step of the peptidoglycan synthesis in the periplasm. Gram-negative bacteria may form so called spheroplasts [156] under exposure of β-lactams. In this case the synthesis of cell wall is disrupted, consequently the cell takes the shape of a sphere due to the membrane tension, also becoming very fragile. Nevertheless, some bacteria developed a resistance to these ATB. The resistance to β-lactams can occur through the rapid production of beta-lactamase, which are able to hydrolyse the β-lactam ring and thus turn the ATB inactive.

Bacterial tolerance to β-lactams can occur through an adaptive response by transition to a cell wall-deficient morphology, which is the case for *P.aeruginosa*.

In order to investigate the effect of meropenem (Mem) and its removal on *P.aeruginosa* we used a time-lapse microscopy. To enable this type of experiments on our setup (section 2.5.1) and to provide the constant supply of fresh media into the microscope chamber we decided to built a syringe pump using 3D printed details (the models of details were created by Ameloot group on May 10, 2015). Further, we modified the code previously published by Henriques lab [157] to operate with stepper motors (Figure 3.4.1).

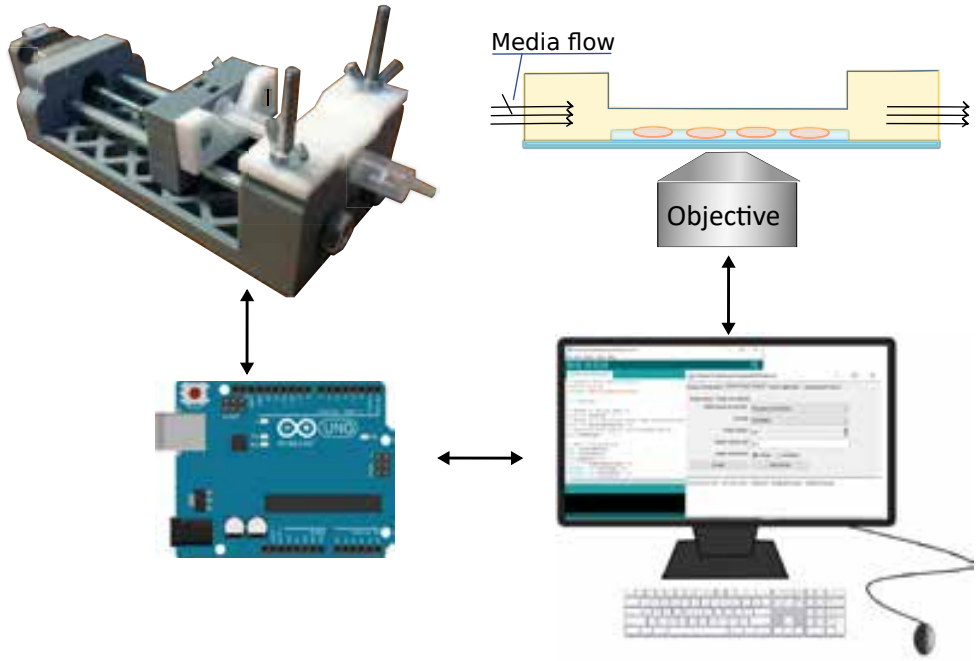

Figure 3.4.1 – The custom syringe pump equipped by a stepper motor was controlled by an Arduino, which was connected to the Micro-Manager in order to synchronise the media flow and image acquisition.

First we tested out this setup on the *P.aeruginosa* , which were cultured under normal conditions (Figure 3.4.2, A). The images were segmented and the percentage of the area occupied by the bacteria was calculated (Figure 3.4.2, B). The doubling time calculated for the exponential phase during the time-lapse experiment was about 125 minutes.

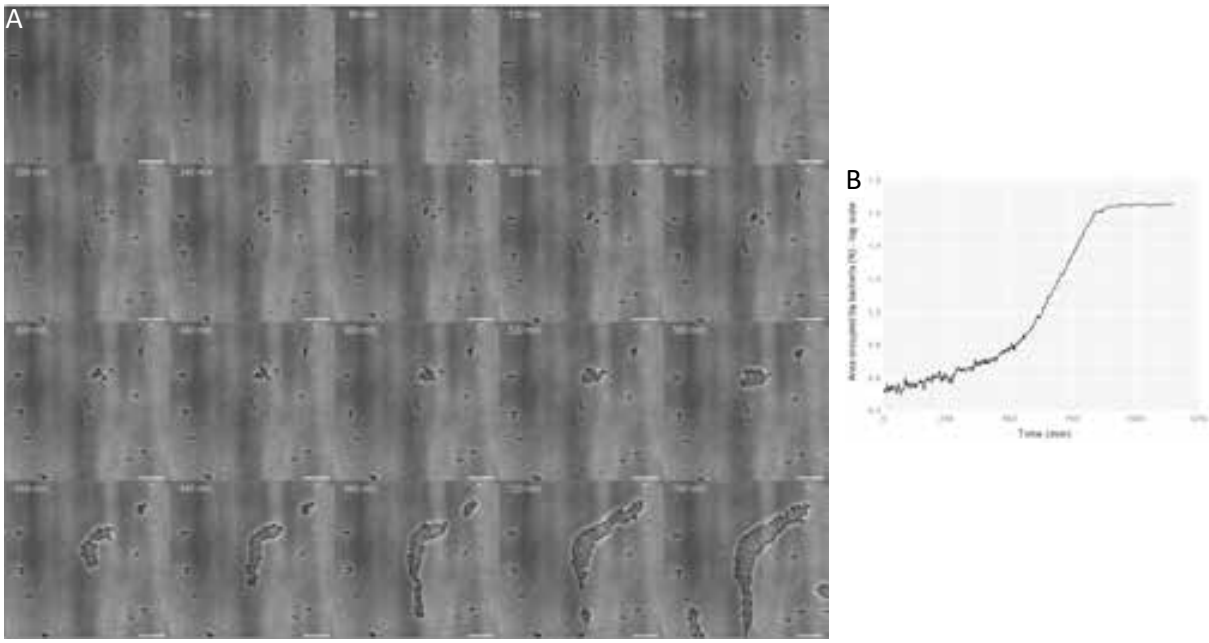

Figure 3.4.2 – **A**. The time-lapse image of PaO1 cells growth. The images were taken every 2 minutes. **B**. Relative area occupied by bacteria during the growth time.

The observed effect of Mem on the bacteria shape over time is in line with the literature data [158]. Under the Mem exposure the *P.aeruginosa* PaO1 cells stop dividing and start growing filamentous (Figure 3.4.3, C). The appearance of localized swelling (also called bulge) in the bacteria middle part was found to occur rather rapidly (1-2 hours) (Figure 3.4.3). The percentage of bulged bacteria increased strongly upon an increase in the time of exposure and Mem concentration (0.5 - 2×MIC (MIC(Mem) = 1 mg/L)) (Figure 3.4.3, D).

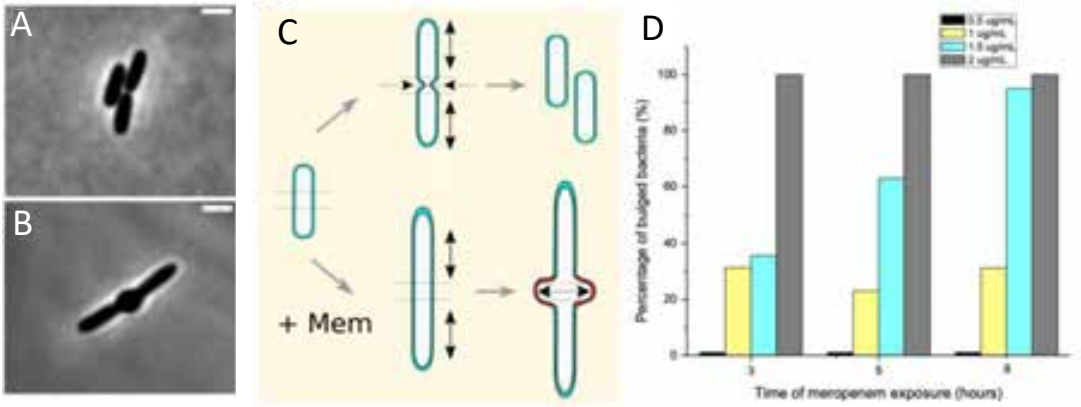

Figure 3.4.3 – Phase contrast **A, B** images of PaO1 cells. Classical morphology **A** and the morphology under meropenem exposure **B** (scale bars 1μm). **C**. Scheme illustrating changes in bacteria morphology under Mem exposure. **D**. Dose response effect over time (expressed in percentage of bacteria featuring a central bulge).

Further, we observed that it becomes possible to stain the plasma membrane in the bulge region with Nile Red dye, which could be possibly attributed to a lipid bilayer exposure caused by the disruption of the cell wall biosynthesis (Figure 3.4.4).

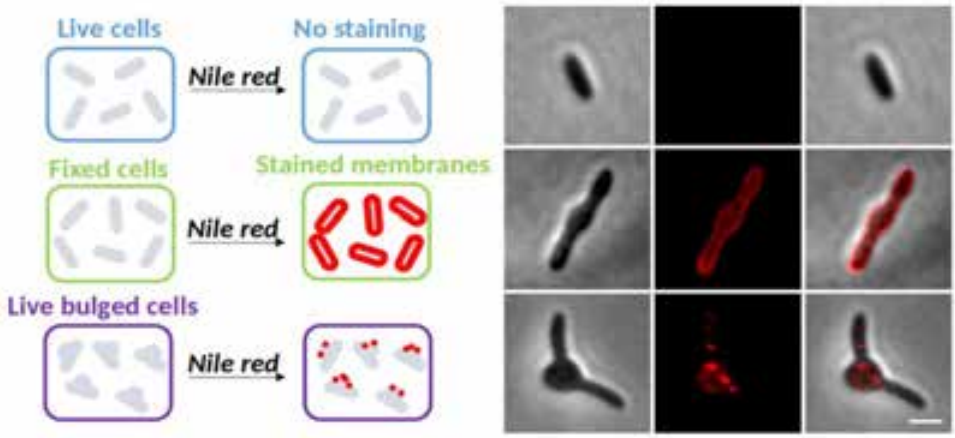

Figure 3.4.4 – Phase contrast and SMLM images of live, fixed and bulged *P.aeruginosa* cells stained with Nile Red (scale bar = 2μm). The live cells can not be stained by NR due to a lipopolysaccharide layer which prevents the diffusion of hydrophobic molecules near the outer membrane. In case of the fixed cells the membrane is readily accessible. The disruption of cell wall biosynthesis with meropenem results in localized changes in the bacteria protecting barrier.

Finally, we observed the recovery of *P.aeruginosa* cells to the initial morphology after the Mem removal. The recovery occurs not only from unaffected cells but also from bulged cells, with the latter exhibiting a separation of distal rode-shaped regions. This allows to suggest that new division cites can be potentially formed at some distance from bulge region in the middle of the cell (Figure 3.4.5, thick arrows). On the contrary, the morphologically changed parts, such as the bulge in the middle or the limited membrane perturbations (Figure 3.4.5, thin arrows), remain unrecovered.

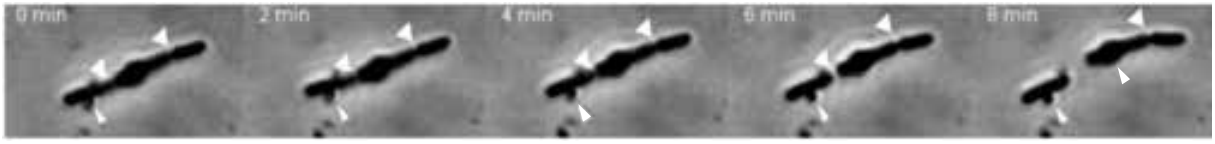

Figure 3.4.5 – Time-lapse phase contrast microscopy showing recovery from meropenem exposure.

In this project the next questions that need to be answered are :

1) how the bacteria membrane properties are impacted by Mem ;

2) why the cell wall synthesis is affected mostly in the middle part of the cell, resulting in bulged morphology.

The first question could possibly be addressed by using srSMLM, such as srPAINT with environment-sensitive Nile Red dye, in order to perform the studies on membrane disruption. This approach is expected to be able to map the local hydrophobicity and lipid order. The second question could possibly be answered by tracking and localizing the proteins involved in the division machinery by multicolor microscopy.

Conclusions and perspectives

Conclusions

This PhD project was divided into several parts. The main objective of the work was to investigate the organization of four large NRPSs involved in pyoverdine biosynthesis in *Pseudomonas aeruginosa* in live and fixed bacteria.

To this aim, we used different advanced microscopy techniques. First, sptPALM technique was applied in order to understand the diffusion properties of the enzymes of interest. As a result of these experiments we were able to observe two distinct diffusion modes which were dedicated to so called restrained and mobile fractions. The diffusion rate of the restrained fraction was found to be similar between different NRPSs while the diffusion rate of mobile fraction was distinctive and increasing with every next enzyme in biosynthesis process. This data allowed to suggest that the pyoverdine biosynthesis occurs via very dynamic complexes of NRPSs formed probably near the membrane. This suggestion was further confirmed by single-color DNA-PAINT super-resolution microscopy in fixed cells. In these experiments we saw the preferable localization of four NRPSs near the bacteria inner membrane and partial exclusion zones in the central part of the cell.

Next, we performed two-color DNA-PAINT microscopy by imaging pairs of NRPSs in order to obtain the information about probable interactions of the enzymes. This technique allowed to reveal the more preferable colocalization of two enzyme pairs : PvdL/PvdI and PvdL/PvdD. The interaction of fraction of PvdL and PvdD enzymes was further confirmed in FLIM-FRET experiments.

In the second part of the project we aimed to enhance the performance of srSMLM techniques which further can be used for tracking and imaging more than two enzymes at the same time. For this aim, we applied the deep learning technique for advanced signal analysis. We trained the convolutional U-net-based network (srUnet) using an originally built training data set. The obtained localization and spectral precision for low-emitting species was showed to remain the same as one obtained for emitting species with 10 times higher intensity. As a consequence the useful data ratio and wavelength allocation probability were strongly enhanced. The method was tested on the bacteria images labeled by two dyes with overlapping spectra.

Further we worked on the enhancing the spectral part analysis in srSMLM technique. For this we applied spectral phasor method which allows to summarize the whole spectra information contained in the emitter spectrum.

Moreover the set of preliminary experiments was performed to investigate the effect of carbapenems (Meropenem) on *P. aeruginosa* and to understand the mechanism of tolerance to this antibiotics. We performed time lapse experiments using the home built syringe pump system. Further, we obtained the data showing that under the Mem exposure the cell membrane can be labeled with Nile Red dye due to the membrane disruption.

Perspectives

Technical developments enable new opportunities in science. In particular here, imaging and tracking multiple targets of a particular metabolic pathway - simultaneously and directly in bacterial cells - can be a game changer.

For example experiments involving simultaneous tracking and localization of all four NRPS have the potential to provide a complete overview of the pyoverdin NRPSs organization in the bacterial cell. We do believe that this is achievable using srSMLM - in localization or in tracking mode of acquisition.

But this demonstration has still to be done in localization. It would be exciting for the community to dispose a technique that could image simultaneously at least 4 targets in the same sample. Coupling this approach with (micro)fuidics, as NanoJ-Fluidics, to make repeated measurement of different combination of dyes in the sample will multiply the number of molecules that can be imaged in a single sample. Possibly, this should also lead to new challenge, like finding appropriate combination of fluorophores to make this to work. This can probably be accompanied by further development in srSMLM. For example, srUnet could be trained to not only increase the SNR of the images but to directly provide the localizations with the corresponding spectra information and reconstruct true color image. Possibly, some developments can also be envisioned to integrate directly the spectral phasor in the neural network to fully capitalize on the full spectra information.

The demonstration of simultaneous multicolor imaging has also to be done in tracking. It is clear that adding a spectral dimension to the tracking data should facilitate the reconstruction of tracks. It would be great to be able to couple both tracking and interaction detection in a four-part system. For a system with transient interactions as the one we studied, many kinetics and interaction parameters could probably be retrieved from such experiments.

On a biological point of view, it would be interesting to collect information on several proteins of

a single pathway during the different growth phases, or in response to change in the environment of the cells, to understand how and if there is dependence of the enzymes organization on the metabolic stage. This might help to better understand the onset of cheater in cell cultures (cells that do benefit from pyoverdine production from neighbouring cells but do not express themselves). This can also be the basis for a better understanding of collective behaviour occurring in culture like the collective and coordinated production of PVD in response to iron depletion in the culture media.

Pyoverdine pathway was used here simply as a model to make a proof of principle. But what has been done and can be done in the context of the metabolic pathway of pyoverdine can be widely generalized to many other cases - we are thinking in particular of the mechanisms of resistance to antibiotics for example.

Finally, the preliminary experiments on the effect of Mem on the bacteria membrane and the mechanism of tolerance to this antibiotic allowed to define the experiments which can be carried out. Exploring further this thematic with srPAINT microscopy will be interesting to investigate the membrane disruption with Nile Red dye. Further experiments can be performed for the proteins involved in the division machinery including single molecule tracking and SMLM. For this aim, significant efforts will have to be done to construct the collection of bacteria mutants expressing the proteins of interest labeled with fluorescent proteins.

Much more needs to be done and discovered, that's what makes this work so exciting...

Bibliographie

1 Joseph R. Lacowicz. *Principles of Fluorescence Spectroscopy*. Springer, 3rd edition, 2006.

2 Fernando D. Stefani, Jacob P. Hoogenboom, and Eli Barkai. Beyond quantum jumps : Blinking nanoscale light emitters. *Physics today*, 62(2) :34, February 2009.

3 Akihiko Nakano. Spinning-disk confocal microscopy - a cutting-edge tool for imaging of membrane traffic. *Cell Structure and Function*, 27(5) :349–355, 2002.

4 E. Abbe. Beiträge zur theorie des mikroskops und der mikroskopischen wahrnehmung. *Archiv für Mikroskopische Anatomie,*, 9 :413–468, 1873.

5 Stefan W. Hell and Jan Wichmann. Breacking the diffraction resolution limit by stimulated emissio : stimulated-emission depletion fluorescence microscopy. *Optics Letters*, 19(11) :780, 1994.

6 M. and Hhofmann. Breaking the diffraction barier in fluoresccence microscopy at low light intensities by using reversibly photoswitchable proteins. *Proc Natl Acad Sci USA*, 102(49) :17565–9, 2005.

7 R. Heintzmann and M.G.L. Gustafsson. Subdiffraction resolution in continuous samples. *Nature Photonics*, 2(7) :362–264, 2009.

8 Mats Gustafsson. Nonlinear structured-illumination microscopy : Wide-field fluorescence imaging with theoretically unlimited resolution. *Proceedings of the National Academy of Sciences of the United States of America*, 102 :13081–6, 10 2005.

9 A. Klar, Thomas, Stefan Jakobs, Marcus Dyba, Alexander Egnet, and W. Hell, Stefan. Fluorescence microscopy with diffraction resolution barrier broken by stimulated emission. *Proc Natl Acad Sci*, 97(15) :8206–8210, 2000.

10 J. Rust, Michael, Mark Bates, and Xiaowei Zhuang. Sub-diffraction-limit imaging by stochastic optical reconstruction microscopy (storm). *Nature Methods*, 3(10) :793, 2006.

11 Mike Heillemann, Sebastian van de Linde, Mark Schuttpelz, Robert Kasper, Britta Seefeldt, Anindita Mukherjee, Philip Tinnefeld, and Markus Sauer. Subdiffraction-resolution fluorescence imaging with conventional fluorescent probes. *Angewandte Chemie*, 47 :6172–6176, 2008.

12 Eric Betzig, H. Patterson, George, Rachid Sougrat, Wolf Lindwasser, O., Scott Olenych, S. Bonifacini, Juan, W. Davidson, Michael, Jennifer Lippincott-Schwartz, and F. Hess, Harald. Imaging intracellular fluorescent proteins at nanometer resolution. *Science*, 313(5793) :1642–1645, 2006.

13 Alexey Sharonov and Robin M. Hochstrasser. Wide-field subdiffraction imaging by accumulated binding of diffusing probes. *Proceedings of the National Academy of Sciences*, 103(50) :18911–18916, 2006.

14 G. Giannone, E. Hosy, J.B. Sibarita, and L. Choquet, D.and Cognet. High-content super-resolution imaging of live cell by upaint. *Methods Mol Biol.*, 950 :95–110, 2013.

15 Ralf Jungmann, Christian Steinhauer, Max Scheible, Anton Kuzyk, Philip Tinnefeld, and Friedrich C. Simmel. Single-molecule kinetics and super-resolution microscopy by fluorescence imaging of transient binding on dna origami. *Nano Letters*, 10(11) :4756–4761, 11 2010.

16 M. Khater, Ismail, Robert Nabi, Ivan, and Ghassan Hamarneh. A review of super-resolution single-molecule localization microscopy cluster analysis and quantification methods. *Patterns*, 1(3), 2020.

17 F. Balzarotti, Y. Eilers, K.C. Gwosch, A.H. Gynna, V. Westphal, F.D. Stefani, J. Elf, and Stefan W. Hell.

Nanometer resolution imaging and tracking of fluorescent molecules with minimal photon fluxes. *Science*, 255 :606–612, 2017.

18 Y. Eilers, H. Ta, K.C. Gwosch, F. Balzarotti, and Stefan W. Hell. Minflux monitors rapid molecular jumps with superior spatiotemporal resolution. *Proc Natl Acad Sci*, 115 :6117–6122, 2018.

19 K.C. Gwosch, J.K. Pape, F. Balzarotti, P. Hoess, J. Ellenberg, J. Ries, and Stefan W. Hell. Minflux nanoscopy delivers 3d multicolor nanometer resolution in cells. *Nature Methods*, 17 :217–224, 2020.

20 S. A. Huang, B. Jones, B. Brandenburg, and X. Zhang. Whole-cell 3d storm reveals interactions between cellular structures with nanometer-scale resolution. *Nature Methods*, 5 :1047–1052, 2008.

21 M.F. Juette, T.J. Could, M.D. Lessard, M.J. Mlodzianoski, B.S. Nagpure, B. T. Bennett, S.T. Hess, and J. Bewersdorf. 3d super-resolution microscopy performance and quantitative analysis assessment using dna-paint and dna origami test samples. *Nature Methods*, 5 :527–529, 2008.

22 S. R. Pavani, M.A. Thompson, J.S. Bitten, S.J. Lord, N. Liu, R.J. Twieg, R. Piestun, and W.E. Moener. Tree-dimentional, single-molecule fluorescence imaging beyond the diffraction limit by using a double-helix posint spread function. *Proc Natl Acad Sci USA*, 106 :2995–2999, 2009.

23 Sri Rama Prasanna Pavani and Rafael Piestun. Three dimensional tracking of fluorescent microparticles using a photon-limited double-helix response system. *Opt. Express*, 16(26) :22048–22057, Dec 2008.

24 M. Tokunaga, N. Imamoto, and K Sakata-Sogawa. Highly inclined thin illumination enables clear single-molecule imaging in cells. *Nature Methods*, 5 :159–161, 2008.

25 L. Gao, L. Shao, B-C. Chen, and Eric Betzig. 3d live fluorescence imaging of cellular dynamics using bessel beam plane illumination microscopy. *Nature Protocols*, 9 :1083–1101, 2014.

26 Suliana Manley, Jennifer M Gillette, George H Patterson, Hari Shroff, Harald F Hess, Eric Betzig, and Jennifer Lippincott-Schwartz. High-density mapping of single-molecule trajectories with photoactivated localization microscopy. *Nature Methods*, 5(2) :155–157, 2008.

27 J.C. Crocker and D.G. Grier. Methods of digital video microscopy for colloidal studies. *Colloid Interface Sci.*, 179(1) :298–310, 1996.

28 D. Reid. An algorythm for tracking multiple targets. *IEEE trans. Autom. Control*, 24(6) :843–857, 1979.

29 K. Jaqaman, D. Loerke, M. Mettlen, H. Kuwata, S. Grinstein, S. L. Schmid, and G. Danuser. Robust single-particle tracking in live-cell time-lapse sequences. *Nature Methods*, 5(8) :695–702, 2008.

30 I.F. Sbalzarini and P. Koumoutsakos. Feature point tracking and trajectory analysis for video imaging in cell biology. *Journal of Structual Biology*, 151(2) :182–195, 2005.

31 C.M. Anderson, G.V. Georgiou, I.E. adn Morrison, and R.J. Cherry. Tracking of cell surface receptors by fluorescence digital imaging microscopy using a charge-coupled device camera. low-density lipoprotein and influenza virus receptor mobility at 4 degrees c. *Journal of cell science*, 101(2) :415–425, 1992.

32 David Grünwald, Robert M. Martin, Volker Buschmann, David P. Bazett-Jones, Heinrich Leonhardt, Ulrich Kubitscheck, and M. Cristina Cardoso. Probing intranuclear environments at the single-molecule level. *Biophysical Journal*, 94(7) :2847–2858, 2022/07/12 2008.

33 J. Crank. *The mathematics of diffusion.* Oxford University Press 1975, 1979.

34 L. Weimann, K.A. Ganzinger, J. McColl, K.L. Irvine, S.J. Davis, N.J. Gay, C.E. Bryant, and D. Klenerman. A quantitative comparison of single-dye tracking analysis tools using monte carlo simulations. *PLoS One*, 8(5) :e64287, 2013.

35 Z Zhang, SJ Kenny, M Hauser, W Li, and K Xu. Ultrahigh-troughput single-molecule spectroscopy and spectrally resolved super-resolution microscopy. *Nature Methods*, 12(10) :935–938, 2015.

36 M.N. Bongiovanni, J Godet, M.H. Horrocks, L. Tasatto, A.R. Carr, D.C. Wirthensohn, R.T. Ranasinghe, Ji-Eun Lee, A. Ponjavic, J.V. Fritz, C.M. Dobson, D. Klenerman, and Steven F. Lee. Multi-dimensional super-resolution imaging enables surface hydrophobicity mapping. *Nature Communications*, 7 :1–9, 2016.

37 MJ Mlodzianoski, NM Curthoys, MS Gunewardene, S Carter, and ST Hess. Super-resolution imaging of molecular emission spectra and signle molecule spectral fluctuations. *PLoS One*, 11(3) :1–12, 2016.

38 B. Dong, L.M. Almassalha, Y. Stypula-Cyrus, B.E. Urban, J.E. Chandler, C. Nguyen, T.Q. adn Sun, H.F.

Zhang, and V. Backman. Superresolution intristic fluorescence imaging of chromatin utilizing native, unmodified nucleic acids for contrast. *Proc Natl Acad Sci USA*, 113(35) :9716–9721, 2016.

39 D Kim, Z Zhang, and K Xu. Spectrally resolved super-resolution microscopy unveils multipath reaction pathways of single spiropyram molecules. *Journal of Americal Chemical Society*, 139(28) :9447–9450, 2017.

40 S Moon, R Yan, SJ Kenny, Y Shyu, L Xiang, W Li, and Ke Xu. Spectrally-resolved, functional super-resolution nanoscale compositional heterogeneity in live-cell membranes. *Journal of Americal Chemical Society*, 139(32) :10944–10947, 2017.

41 L Xiang, M Wojcik, SJ Kenny, Rui Yan, S Moon, and Ke Xu. Optical characterisation of surface adlayers and their compositional demixing at the nanoscale. *Nature Communications*, 9(1) :1–9, 2018.

42 T. Huang, C. Phelps, J. Wang, Li-Jubng Lin, A Bittel, Z Scott, S Jacques, SL Gibbs, JW Gray, and Xiaolin Nan. Simultaneous multicolor single-molecule tracking with single-laser excitation via spectral imaging. *Biophysical Journal*, 114(2) :301–310, 2018.

43 Ji-Eun Lee, JC Sang, M Rodrigues, AR Carr, MH Horrocks, Suman De, MN Bongiovanni, P Flagmeier, CM Dobson, DJ Wales, Steven F Lee, and D Klenerman. Mapping surface hydrophobicity of a-synuclein oligomers at the nanoscale. *Nano Letters*, 18(12) :7494–7501, 2018.

44 K-H Song, G Zhang, Y adn Wang, C Sun, and HF Zhang. Three-dimentional biplane spectroscopic single-molecule localization microscopy. *Optica*, 6(10) :1374, 2019.

45 Hannah J Stern, Ruizhi Wang, Ye Fan, Ryo Mizuta, James C Stewart, Lisa-Maria Needham, Trevor D Roberts, Rebecca Wai, Naomi S Ginsberg, David Klenerman, and Steven F Lee. Spectrally resolved photodynamics of individual emitters in large-area monolayers of hexagonal boron nitride. *ACS Nano*, 13(4) :4538–4547, 2019.

46 Janel L. Davis, Yang Zhang, Sijia Yi, Fanfan Du, K-H Song, Evan A Scott, Cheng Sun, and Hao F Zhang. Super-resolution imaging of self-assembled nanocarriers using quantitative spectroscopic analysis for cluster extraction. *Langmuir*, 36(9) :2291–2299, 2020.

47 A.C. Klymchenko. Solvatochromic and fluorogenic dyes as environment-sensitive probes : Design and biological applications. *Accounts of Chemical Research*, 50(2) :366–375, 2017.

48 L. Sansalone, Y. Zhang, M.M.A. Mazza, H. Davis, J. Song, B. Captain, H.F. Zhang, and F.M. Raymo. High-throughput single-molecule spectroscopy resolves the conformational isomers of bodipy chromophores. *The journal of Physical Chemistry Letters*, 10(12) :6807–6812, 2019.

49 Robert Finking and Mohamed A. Marahiel. Biosynthesis of nonribosomal peptides. *Anual Review of Microbiology*, 58 :453–88, June 10 2004.

50 R.D Süssmuth and A. Mainz. Nonribosomal peptyde synthesis - principles and pprospects. *Angewandte Chemie*, 56 :3770–3821, 2017.

51 Christopher T. Walsh. Insights into the chemical logic and enzymatic machinery of nrps assembly lines. *Nat. Prod. Rep.*, 33 :127–135, 2016.

52 A. M. Gulick. Nonribosomal peptyde synthetase biosynthetic clusters of eskape pathogens. *Natural Product Reports*, 34 :981–1009, 2017.

53 B.K. Scholz-Schroeder, J.D. Soule, and D.C. Gross. The sypa, syps, and sypc synthetase genes encode twenty-two modules involved in the nonribosomal peptide synthesis of syringopeptin by pseudomonas syringae pv. syringae b301d. *Mol Plant Microbe Interact.*, 16(4) :271–80, 2003.

54 Tiia Kittilä, Aurelio Mollo, Louise K. Charkoudian, and Max J. Cryle. New structural data reveal the motion of carrier proteins in nonribosomal peptide synthesis. *Angewandte Chemie International Edition*, 55(34) :9834–9840, 2016.

55 Thomas Weber, Roland Baumgartner, Christian Renner, Mohamed A Marahiel, and Tad A Holak. Solution structure of pcp, a prototype for the peptidyl carrier domains of modular peptide synthetases. *Structure*, 8(4) :407–418, 2000.

56 T. A. Keating, C. G. Marshall, C. T. Walsh, and A. E. Keating. The structure of vibh represents nonribosomal peptide synthetase condensation, cyclization and epimerization domains. *Nature structural biology*,

9(7) :522–526, 2002.

57 M. A. Marahiel, T. Stachelhaus, and H. D. Mootz. Modular peptide synthetases involved in nonribosomal peptide synthesis. *Chemical reviews*, 97(7) :2651–2674, 1997.

58 A. Tanovic, S. A. Samel, L. O. Essen, and M. A. Marahiel. Crystal structure of the termination module of a nonribosomal peptide synthetase. *Science (New York, N.Y.)*, 321(5889) :659–663, 2008.

59 E. J. Drake, B. R. Miller, C. Shi, J. T. Tarrasch, J. A. Sundlov, C. L. Allen, G. Skiniotis, C. C. Aldrich, and A. M. Gulick. Structures of two distinct conformations of holo-non-ribosomal peptide synthetases. *Nature*, 529(7585) :235–238, 2016.

60 S. A. Samel, G. Schoenafinger, T. A. Knappe, M. A. Marahiel, and L. O. Essen. Structural and functional insights into a peptide bond-forming bidomain from a nonribosomal peptide synthetase. *Structure (London, England : 1993)*, 15(7) :781–792, 2007.

61 K. Bloudoff, D. Rodionov, and T. M. Schmeing. Crystal structures of the first condensation domain of cda synthetase suggest conformational changes during the synthetic cycle of nonribosomal peptide synthetases. *Journal of molecular biology*, 425(17) :3137–3150, 2013.

62 S. A. Samel, P. Czodrowski, and L. O. Essen. Structure of the epimerization domain of tyrocidine synthetase a. *Acta crystallographica. Section D, Biological crystallography*, 70(5) :1442–1452, 2014.

63 D. P. Dowling, Y. Kung, A. K. Croft, K. Taghizadeh, W. L. Kelly, C. T. Walsh, and C. L. Drennan. Structural elements of an nrps cyclization domain and its intermodule docking domain. *Proceedings of the National Academy of Sciences of the United States of America*, 113(44) :12432–12437, 2016.

64 K. Haslinger, M. Peschke, C. Brieke, E. Maximowitsch, and M. J. Cryle. X-domain of peptide synthetases recruits oxygenases crucial for glycopeptide biosynthesis. *Nature*, 521(7550) :105–109, 2015.

65 B. Bister, D. Bischoff, G.J. Nicholson, S. Stockert, J. Wink, C. Brunati, S. Donadio, S. Pelzer, W. Wohlleben, and R.D. Süssmuth. Bromobalhimycin and chlorobromobalhimycins–illuminating the potential of halogenases in glycopeptide antibiotic biosyntheses. *Chembiochem*, 4(7) :658–62, 2003.

66 G.H. Hur, C.R. Vickery, and Burkart M.D. Explorations of catalytic domains in non-ribosomal peptide synthetase enzymology. *Nat Prod Rep.*, 29(10) :1074–98, 2012.

67 Smith G. H. Oral cephalosporins in perspective. *DICP : the annals of pharmacotherapy*, 24(1) :45–51, 1990.

68 F. Peypoux, J. M. Bonmatin, and J. Wallach. Recent trends in the biochemistry of surfactin. *Applied microbiology and biotechnology*, 51(5) :553–563, 1999.

69 R. M. Kohli, J. W. Trauger, D. Schwarzer, and C. T. Marahiel, M. A. andWalsh. Generality of peptide cyclization catalyzed by isolated thioesterase domains of nonribosomal peptide synthetases. *Biochemistry*, 40(24) :7099–7108, 2001.

70 A. M. Gehring, I. Mori, and C. T. Walsh. Reconstitution and characterization of the escherichia coli enterobactin synthetase from entb, ente, and entf. *Biochemistry*, 37(8) :648–2659, 1998.

71 Henning D. Mootz, Dirk Schwarzer, and Mohamed A. Marahiel. Ways of assembling complex natural products on modular nonribosomal peptide synthetases. *ChemBioChem*, 3(6) :490–504, 2002.

72 T. A. Keating, C. G. Marshall, and C. T. Walsh. Reconstitution and characterization of the vibrio cholerae vibriobactin synthetase from vibb, vibe, vibf, and vibh. *Biochemistry*, 39(50) :15522–15530, 2000.

73 Wang H., Fewer D.P., Holm L., Rouhiainen L., and Sivonen K. Atlas of nonribosomal peptide and polyketide biosynthetic pathways reveals common occurrence of nonmodular enzymes. *Proceedings of the National Academy of Sciences of the United States of America*, 111(25) :9259–64, 2014.

74 A. Richardt, T. Kemme, S. Wagner, D. Schwarzer, M. A. Marahiel, and B. T. Hovemann. Ebony, a novel nonribosomal peptide synthetase for beta-alanine conjugation with biogenic amines in drosophila. *The Journal of biological chemistry*, 278(42) :41160–41166, 2003.

75 S. Hartwig, C. Dovengerds, C. Herrmann, and B. T. Hovemann. Drosophila ebony : a novel type of nonribosomal peptide synthetase related enzyme with unusually fast peptide bond formation kinetics. *The FEBS journal*, 281(22) :5147–5158, 2014.

76 Marnix Medema, Kai Blin, Peter Cimermancic, Victor Jager, Piotr Zakrzewski, Michael Fischbach, Tilmann

Weber, Eriko Takano, and Rainer Breitling. antismash : rapid identification, annotation and analysis of secondary metabolite biosynthesis gene clusters in bacterial and fungal genome sequences. *Nucleic acids research*, 39 :W339–46, 06 2011.

77 M. Röttig, M. H. Medema, K. Blin, T. Weber, C. Rausch, and O. Kohlbacher. Nrpspredictor2–a web server for predicting nrps adenylation domain specificity. *Nucleic acids research*, 39(Web Server issue) :W362–W367, 2011.

78 Mindong Liang, Leshi Liu, Fei Xu, Xiaoqian Zeng, Runjun Wang, Jinling Yang, Wang Weishan, Karthik Loganathan, Jiakun Liu, Zhiheng Yang, Guoliang Zhu, Shuliu Wang, Linquan Bai, Yaojun Tong, Xueting Liu, Min Wu, Li-Xin Zhang, and Gao-Yi Tan. Activating cryptic biosynthetic gene cluster through a crispr–cas12a-mediated direct cloning approach. *Nucleic Acids Research*, 50, 03 2022.

79 Bahar Behsaz, Edna Bode, Alexey Gurevich, Yan-Ni Shi, Florian Grundmann, Deepa Acharya, Andrés Mauricio Caraballo-Rodríguez, Amina Bouslimani, Morgan Panitchpakdi, Annabell Linck, Changhui Guan, Julia Oh, Pieter C. Dorrestein, Helge B. Bode, Pavel A. Pevzner, and Hosein Mohimani. Integrating genomics and metabolomics for scalable non-ribosomal peptide discovery. *Nature Communications*, 12(1) :3225, 2021.

80 Yi-Ming Chiang, Shu-Lin Chang, Berl Oakley, and Clay Wang. Recent advances in awakening silent biosynthetic gene clusters and linking orphan clusters to natural products in microorganisms. *Current opinion in chemical biology*, 15 :137–43, 02 2011.

81 Marc Chevrette, Fabian Aicheler, Oliver Kohlbacher, Cameron Currie, and Marnix Medema. Sandpuma : Ensemble predictions of nonribosomal peptide chemistry reveals biosynthetic diversity across actinobacteria. *Bioinformatics (Oxford, England)*, 33, 06 2017.

82 Jeffrey Lyczak, B., Carolyn Cannon, L., and Gerald Pier, B. Establishment of pseudomonas aeruginosa infection : lessons from versatile opportunist. *Microbes and Infection*, 2 :1051–1060, 2000.

83 M. Michalska and Wolf P. Pseudomonas exotoxin a : optimized by evolution for effective killing. *Front Microbiol.*, 6 :963, Sep 15 2015.

84 Shira D. P. Rabin and Alan R. Hauser. ¡i¿pseudomonas aeruginosa¡/i¿ exou, a toxin transported by the type iii secretion system, kills ¡i¿saccharomyces cerevisiae¡/i¿. *Infection and Immunity*, 71(7) :4144–4150, 2003.

85 N.V. Kirienko, F.M. Ausubel, and Ruvkun G. Mitophagy confers resistance to siderophore-mediated killing by pseudomonas aeruginosa. *Proc Natl Acad Sci U*, 112(6) :1821–6, 2015.

86 C. K. Stover, X. Q. Pham, A. L. Erwin, S. D. Mizoguchi, P. Warrener, M. J. Hickey, F. S. L. Brinkman, W. O. Hufnagle, D. J. Kowalik, M. Lagrou, R. L. Garber, L. Goltry, E. Tolentino, S. Westbrock-Wadman, Y. Yuan, L. L. Brody, S. N. Coulter, K. R. Folger, A. Kas, K. Larbig, R. Lim, K. Smith, D. Spencer, G. K. S. Wong, Z. Wu, I. T. Paulsen, J. Reizer, M. H. Saier, R. E. W. Hancock, S. Lory, and M. V. Olson. Complete genome sequence of pseudomonas aeruginosa pao1, an opportunistic pathogen. *Nature*, 406(6799) :959–964, 2000.

87 Brittan Scales, Robert Dickson, John Lipuma, and Gary Huffnagle. Microbiology, genomics, and clinical significance of the pseudomonas fluorescens species complex, an unappreciated colonizer of humans. *Clinical microbiology reviews*, 27 :927–948, 10 2014.

88 C. F. Michelsen, J. Watrous, M. A. Glaring, R. Kersten, P. C. Koyama, N.and Dorrestein, and P. Stougaard. Nonribosomal peptides, key biocontrol components for pseudomonas fluorescens in5, isolated from a greenlandic suppressive soil. *mBio*, 6(2) :e00079, 2015.

89 Michael Thomas, Pat Unkefer, Thomas Uchytil, and Richard Durbin. Inhibition of glutamine synthetase from pea by tabtoxinine-beta-lactam. *Plant physiology*, 71 :912–5, 05 1983.

90 Michael Groll, Barbara Schellenberg, Prof. Dr. André Bachmann, Crystal Archer, Robert Huber, Tracy Powell, Steven Lindow, Markus Kaiser, and Robert Dudler. A plant pathogen virulence factor inhibits the eukaryotic proteasome by a novel mechanism. *Nature*, 452 :755–8, 05 2008.

91 Omar González, Randy Ortíz-Castro, César Díaz-Pérez, Alma L Díaz-Pérez, Viridiana Magaña-Dueñas, José López-Bucio, and Jesús Campos-García. Non-ribosomal peptide synthases from pseudomonas aeruginosa play a role in cyclodipeptide biosynthesis, quorum-sensing regulation, and root development in a plant host.

Microbial ecology, 73(3) :616–629, 2017.

92 Nelson Rojas Murcia, Xiaoyun Lee, Patrice Waridel, Alessandro Maspoli, Heidi J. Imker, Tiancong Chai, Christopher T. Walsh, and Cornelia Reimmann. The pseudomonas aeruginosa antimetabolite l -2-amino-4-methoxy-trans-3-butenoic acid (amb) is made from glutamate and two alanine residues via a thiotemplate-linked tripeptide precursor. *Frontiers in Microbiology*, 6, 2015.

93 Isabelle J. Schalk, Coraline Rigoulin, and Julien Godet. An overview of siderophore biosynthesis among fluorescent pseudomonads and new insights into their complex cellular organisation. *Environmental Microbiology*, 22 :1447–1466, 2020.

94 Stephan Kraemer, Alison Butler, Paul Borer, and Javiera Cervini-Silva. 4. siderophores and the dissolution of iron-bearing minerals in marine systems. *Molecular Geomicrobiology*, pages 53–84, 12 2005.

95 Hakim Boukhalfa and Alvin Crumbliss. Chemical aspects of siderophore mediated iron transport. *Biometals : an international journal on the role of metal ions in biology, biochemistry, and medicine*, 15 :325–39, 01 2003.

96 M. L. Guerinot, E. J. Meidl, and O. Plessner. Citrate as a siderophore in bradyrhizobium japonicum. *Journal of bacteriology*, 172(6) :3298–3303, 1990.

97 N. Noinaj, M. Guillier, T. Barnard, and S. K. Buchanan. Tonb-dependent transporters : Regulation, structure, and function. *Anual Review of Microbiology*, 64 :43–60, 2010.

98 J. Greenwald, G. Zeder-Lutz, A. Hagege, H. Celia, and F. Pattus. The metal dependencr of pyoverdine interactions with its outer membrane receptor fpva. *Journal of Bacteriology*, 190 :6548–6558, 2008.

99 I.J. Schalk, G.L. Mislin, and Brillet K. Structure, function and binding selectivity and stereoselectivity of siderophore-iron outer membrane transporters. *Curr Top Membr*, 69 :37–66, 2012.

100 I. J. Schalk and L. Guillon. Pyoverdine biosynthesis and secretion in pseudomonas aeruginosa : Implication for metal homeostasis. *Environmental Microbiology*, 15 :1661 – 1673, 2013.

101 Pierre Cornelis. Iron uptake and metabolism in pseudomonads. *Appl Microbiol Biotechnol*, 86 :1637–1645, 2010.

102 M. Hannauer, A. Braud, F. Hoegy, P. Ronot, A. Boos, P. Gizzi, P. Wehrung, G. L. A. Mislin, H. Budzikiewicz, and Isabelle J. Schalk. Biosynthesis of the pyoverdine siderophore of pseudomonas aeruginosa involves precursors with a myristic or a myristoleic acid chain. *FEBS Letters*, 586 :96–101, 2012.

103 E. Yeterian, L. W. Martin, L. Guillon, L. Journet, I. L. Lamont, and I. J. Schalk. Synthesis of siderophore pyoverdine in prseudomonas aeruginisa involves a periplasmic maturation. *Amino Acids*, 38 :1447–1459, 2010.

104 M. Ringel and T. Bruser. The biosynthesis of pyoverdines. *microbal cell*, 5 :424–437, 2018.

105 J. Poppe, J. Reichelt, and W. Blankenfeldt. Pseudomonas aeruginosa pyoverdine maturation enzyme pvdp has a noncanonical domain architecture and affords insight into a new subclass of tyrosinases. *Journal of Biological Chemistry*, 293 :14926–14936, 2018.

106 M. Hannauer, E. Yeterian, L. W. Martin, I. L. Lamont, and I. J. Schalk. Secretion of newly synthesized pyoverdine by pseudomonas aeruginisa involves an efflux pump. *FEBS lett*, 584 :4751–4755, 2010.

107 P. Visca, F. Imperi, and I. L. Lamont. Pyoverddine siderophores : form biogenesis to biosignificance. *Trends in Microbiology*, 15 :22–30, 2007.

108 Anne Bonneau, Béatrice Roche, and Isabelle J. Schalk. Iron acquisition in pseudomonas aeruginosa by the siderophore pyoverdine : an intricate interacting network including periplasmic and membrane proteins. *Scientific Reports*, 10(1) :120, 2020.

109 F. Minindri, F. Imperi, E. Frangipani, C. Bonchi, M. Visaggio, M. Facchini, P. Pasquali, A. Bragonzi, and P. Visca. Dissecting the role of iron uptacke systems in pseudomonas aeruginosa virulence and airways invection. *Infect Immun*, 84 :2324–2335, 2016.

110 Rosie Redfield. Redfield rj.. is quorum sensing a side effect of diffusion sensing ? trends microbiol 10 : 365-370. *Trends in microbiology*, 10 :365–70, 09 2002.

111 L. Guillon, S. Alternurger, P. L. Graumann, and I. J. Schalk. Deciphering protein dynamics of the siderophore pyoverdine pathway in pseudomonas aeruginisa. *PLoS One*, 8 : e79111, 2012.

112 F. Imperi and P. Visca. Subcellular localisation of pyoverdine biogenesis machinery of pseudomonas aeruginisa : A membrane-associated 'siderosome'. *FEBS Letters*, 587 :3387–3391, 2013.

113 V Gasser, M. Malrieu, A Forster, Y. Mely, I. J. Schalk, and Julien Godet. In cellulo flim-fret and single molecule tracking reveal the supra-molecular organization of the pyoverdine bio-synthetic enzymes in pseudomonas aeruginosa. *Quarterly Reviews of Biophysics*, 53, e1 :1–11, 2020.

114 Francois Chollet. *Deep Learning with Python*. Manning, 2017.

115 Y. Hyun and D. Kim. Development of deep-learning-based single-moolecule localization image analysis. *Internationsl Journal of Molecular Sciences*, 23(6896), 2022.

116 J.R. Koza, F.H Bennet, D. Andre, and M.A. Keane. *Automated Design of Both the Topology and Sizing of Analog Electrical Circuits Using Generic Prigramming*. Springer, Dordrecht, 1996.

117 Y. LeCun, Y. Bengio, and G. Hinton. Deep learning. *Nature*, 521 :436–444, 2015.

118 K.C. Santosh, S. Ghosh, and N. Das. *Deep Learning Models for Medical Imaging*. Academic Press, September 7 2021.

119 Russel Reed and J. Markslls, Robert. *Neural Smithing : Supervised Learning in Feedforward Artificial Neural Networks*. MIT Press, 1999.

120 K. Hornik, M. Stinchcombe, and H.. White. Multilayer feedforward networks are universal approximators. *Natural Networks*, 2 :359–366, 1989.

121 G Cybenko. Approximation by superposition of a sigmoidal function. *Mathemathics of Control, Signals and Systems*, 2 :303–314, 1989.

122 I. Goodfellow, Y. Bengio, and A. Courville. *Deep Learning*. The MIT press, 2016.

123 D. Stathakis. How many hidden layers and nodes ? *Internationsl Journal of Remote Sensing*, 30(8) :2133–2147, 2009.

124 Y LeCun, L. Bottou, Y. Bengio, and P. Haffner. Gradient-based learning applied to document recognition. *Proceedings of the IEEE*, 86(11) :2278–2324, 1998.

125 Ismail Oztel, Gozde Yolcu, Ilker Ersoy, Tommi A. White, and Filiz Bunyak. Mitochondria segmentation in electron microscopy volumes using deep convolutional neural network. *2017 IEEE International Conference on Bioinformatics and Biomedicine (BIBM)*, pages 1195–1200, 2017.

126 Ling Wei and Elijah Roberts. Neural network control of focal position during time-lapse microscopy of cells. *Scientific Reports*, 8, 05 2018.

127 Ari Silburt, Mohamad Ali-Dib, Chenchong Zhu, Alan Jackson, Diana Valencia, Yevgeni Kissin, Daniel Tamayo, and Kristen Menou. Lunar crater identification via deep learning. *Icarus*, 317, 03 2018.

128 J. T. Springenberg, A. Dosovitskiy, T. Brox, and Riedmiller. M. Striving for simplicity : Tha all convolutiona net. 12 2015.

129 E. Shelhamer, J. Long, T. Darrell, and Member IEEE. Fully convolutional neteorks for semantic segmentation. *IEEE trans. Autom. Control*, 39(4) :640–651, 2016.

130 O. Ronneberger and T. Fisher, P. Brox. U-net : Convolutional networks for biomedical image segmentation. *Medical Image Computing and Computer-Assisted Intervention (MICCAI)*, 9351 :34–241, 2015.

131 Wei Ouyang, Andrey Aristov, Mickaël Lelek, Xian Hao, and Christophe Zimmer. Deep learning massively accelerates super-resolution localization microscopy. *Nature Biotechnology*, 36(5) :460–468, 2018.

132 Artur Speiser, Lucas-Raphael Müller, Philipp Hoess, Ulf Matti, Christopher J. Obara, Wesley R. Legant, Anna Kreshuk, Jakob H. Macke, Jonas Ries, and Srinivas C. Turaga. Deep learning enables fast and dense single-molecule localization with high accuracy. *Nature Methods*, 18(9) :1082–1090, 2021.

133 Elias Nehme, Lucien Weiss, Tomer Michaeli, and Yoav Shechtman. Deep-storm : Super resolution single molecule microscopy by deep learning. *Optica*, 5, 01 2018.

134 Elias Nehme, Daniel Freedman, Racheli Gordon, Boris Ferdman, Lucien E. Weiss, Onit Alalouf, Tal Naor, Reut Orange, Tomer Michaeli, and Yoav Shechtman. Deepstorm3d : dense 3d localization microscopy and psf design by deep learning. *Nature Methods*, 17(7) :734–740, 2020.

135 K. Narayanasamy, Kaarjel, Johanna V. Rahm, Siddharth Tourani, and Mike Heilemann. Fast dna-paint

imaging using a deep neural network. *Biorxiv*, 2021.

136 Hongda Wang, Yair Rivenson, Yiyin Jin, Zhensong Wei, Ronald Gao, Harun Günaydın, Laurent A. Bentolila, Comert Kural, and Aydogan Ozcan. Deep learning enables cross-modality super-resolution in fluorescence microscopy. *Nature Methods*, 16(1) :103–110, 2019.

137 Martin Weigert, Uwe Schmidt, Tobias Boothe, Andreas Müller, Alexandr Dibrov, Akanksha Jain, Benjamin Wilhelm, Deborah Schmidt, Coleman Broaddus, Siân Culley, Mauricio Rocha-Martins, Fabián Segovia-Miranda, Caren Norden, Ricardo Henriques, Marino Zerial, Michele Solimena, Jochen Rink, Pavel Tomancak, Loic Royer, Florian Jug, and Eugene W. Myers. Content-aware image restoration : pushing the limits of fluorescence microscopy. *Nature Methods*, 15(12) :1090–1097, 2018.

138 N. Srivastava, G. Hinton, A. Krizhevsky, I. Sutskever, and R. Salakhutdinov. Dropout : A simple way to prevent neural networks from overfitting. *Journal of Machine Learning Research*, 15(56) :1929–1958, 2014.

139 Sergey Ioffe and Christian Szegedy. Batch normalization : Accelerating deep network training by reducing internal covariate shift. In *ICML*, 2015.

140 Anders Krogh and John Hertz. A simple weight decay can improve generalization. In J. Moody, S. Hanson, and R.P. Lippmann, editors, *Advances in Neural Information Processing Systems*, volume 4. Morgan-Kaufmann, 1991.

141 Patrick Trampert, Dmitri Rubinstein, Faysal Boughorbel, Christian Schlinkmann, Maria Luschkova, Philipp Slusallek, Tim Dahmen, and Stefan Sandfeld. Deep neural networks for analysis of microscopy images—synthetic data generation and adaptive sampling. *Crystals*, 11(3), 2021.

142 Sebastien C. Wong, Adam Gatt, Victor Stamatescu, and Mark D. McDonnell. Understanding data augmentation for classification : When to warp ? In *2016 International Conference on Digital Image Computing : Techniques and Applications (DICTA)*, pages 1–6, 2016.

143 Yan Xu, Ran Jia, Lili Mou, Ge Li, Yunchuan Chen, Yangyang Lu, and Zhi Jin. *Improved relation classification by deep recurrent neural networks with data augmentation.* The COLING 2016 Organizing Committee, 2016.

144 H. Manko, V. Normant, Q. Perraud, T. Steffan, V. Gasser, E. Boutant, É. Réal, I.J. Schalk, Y. Mély, and Godet J. Flim-fret measurements of protein-protein interactions in live bacteria. *J Vis Exp*, 162, Aug 25 2020.

145 Jean-Yves Tinevez, Nick Perry, Johannes Schindelin, Genevieve M. Hoopes, Gregory D. Reynolds, Emmanuel Laplantine, Sebastian Y. Bednarek, Spencer L. Shorte, and Kevin W. Eliceiri. Trackmate : An open and extensible platform for single-particle tracking. *Methods*, 115 :80–90, 2017. Image Processing for Biologists.

146 M. Ovesny, P. Krizek, Z. Svindrych, and G. M. Hagen. Thunderstorm : a comprehensive imagej plugin for palm and storm data analysis and super-resolution imaging. *Bioinformatics*, 30(16) :2389–2390, 2014.

147 J. Ries. Smap : a modular super-resolution microscopy analysis platform for smlm data. *Nature Methods*, 17 :870–872, 2020.

148 F. Levet, G. Julien, R Galland, C. Butler, A. Beghin, A. Chazeau, P. Hoess, J. Ries, G. Giannone, and J.B. Sibarita. A tessellation-based colocalization analysis approach for single-molecule localization microscopy. *Nature Communications*, 10(2379), 2019.

149 Pablo Meyer, Guillermo Cecchi, and Gustavo Stolovitzky. Spatial localization of the first and last enzymes effectively connects active metabolic pathways in bacteria. *BMC Systems Biology*, 8(1) :131, 2014.

150 Shiqi Wang, Binglin Shen, Sheng Ren, Yihua Zhao, Silu Zhang, Junle Qu, and Liwei Liu. Implementation and application of fret-flim technology. *Journal of Innovative Optical Health Sciences*, 12, 07 2019.

151 Hernán E. Grecco, Sarah Imtiaz, and Eli Zamir. Multiplexed imaging of intracellular protein networks. *Cytometry Part A*, 89(8) :761–775, 2016.

152 Joel S. Silfies and Stanley A. Schwartz. Molecular density in super-resolution microscopy. nikon instruments, inc.

153 Shutao Li, James T. Kwok, and Yaonan Wang. Combination of images with diverse focuses using the spatial frequency. *Information Fusion*, 2(3) :169–176, 2001.

154 Farzad Fereidouni, Arjen N. Bader, and Hans C. Gerritsen. Spectral phasor analysis allows rapid and reliable

unmixing of fluorescence microscopy spectral images. *Opt. Express*, 20(12) :12729–12741, Jun 2012.

155 Michelle A. Digman, Valeria R. Caiolfa, Moreno Zamai, and Enrico Gratton. The phasor approach to fluorescence lifetime imaging analysis. *Biophysical Journal*, 94(2) :L14–L16, 2008.

156 T. P. Tim Cushnie, Noëlle H. O'Driscoll, and Andrew J. Lamb. Morphological and ultrastructural changes in bacterial cells as an indicator of antibacterial mechanism of action. *Cellular and Molecular Life Sciences*, 73(23) :4471–4492, 2016.

157 Pedro Almada, Pedro M. Pereira, Siân Culley, Ghislaine Caillol, Fanny Boroni-Rueda, Christina L. Dix, Guillaume Charras, Buzz Baum, Romain F. Laine, Christophe Leterrier, and Ricardo Henriques. Automating multimodal microscopy with nanoj-fluidics. *Nature Communications*, 10(1) :1223, 2019.

158 David A. Dik, Chinedu S. Madukoma, Shusuke Tomoshige, Choonkeun Kim, Elena Lastochkin, William C. Boggess, Jed F. Fisher, Joshua D. Shrout, and Shahriar Mobashery. Slt, mltd, and mltg of pseudomonas aeruginosa as targets of bulgecin a in potentiation of beta-lactam antibiotics. *ACS Chemical Biology*, 14(2) :296–303, 02 2019.

List of abbreviations

BODYPY - boron-dipyrromethene
(e)GFP - (enhanced) Green Fluorescent Protein
RFP - Red Fluorescent Protein
TIRF - Total Internal Reflection Fluorescence
PSF - Point Spread Function
NA - Numerical Aperture
SNR - Signal-to-Noise Ratio
(EM)CCD - (Electron Multiplayed) Charge-Coupled Device
CMOS - Complementary Metal-Oxide Semiconductor
STED - Stimulated emission depletion
RESOLFT - REversible Saturable OpticaL Fluorescence Transitions
SIM - Structured Illumination Microscopy
SMLM - Single Molecule Localization Microscopy
(d)STORM - (direct) STochastic Optical Reconstruction Microscopy
PAINT - Points Accumulation for Imaging in NanoscaleTtopography
DNA - Deoxyribonucleic acid
MINFLUX - MINimal emission FLUXes
HILO - Highly Inclined and Laminated Optical sheet
SMT - Single Molecule Tracking
SPT - Single Particle Tracking
MSD - Mean Squared Displacement
JD - Jump Distance
srSMLM - spectrally-resolved Single Molecule Localization Microscopy
RNA - Ribonucleic acid
NRP - Non-Ribosomal Peptide
NRPS -Non-Ribosomal Peptide Synthetases
PCP - Peptidyl Carrier Domain
PVD - Pyoverdine
BGC - Biosynthetic Gene Clusters

FLIM-FRET - Fluorescence Lifetime Imagin by Forster resonance energy transfer
FRAP - Fluorescence Recovery After Photobleaching
sptPALM - Single-Particle Tracking Photoactivated Localization Microscopy
NN - Neural Network
CNN - Convolutional Neural Network
GT Ground Truth
DL - Deep Learning
LB - Luria-Bertrani
SM - Succinate Medium
PBS - Phosphate Buffered Saline
ATP - Adenosine Triphosphate
ATB - Antibody
Mem - Meropenem
NR - Nile Red
smTracking - single-molecule tracking

List of publications

1. Hanna Manko, Vincent Normant, Quentin Perraud, Tania Steffan, Véronique Gasser, et al.. FLIM- FRET Measurements of Protein-Protein Interactions in Live Bacteria. Journal of visualized experiments : JoVE, JoVE, 2020, 10.3791/61602 . hal-03085907

2. Advancing Spectrally-Resolved Single Molecule Localization Microscopy using Deep Learning Hanna Manko, Yves Mély, Julien Godet bioRxiv 2022.07.29.502097 ;
doi : https ://doi.org/10.1101/2022.07.29.502097

Articles in preparation :

3. Hanna Manko, Yves Mély, Julien Godet. Recent developments in Spectrally-Resolved Single Molecule Localization Microscopy.

4. Hanna Manko, Matthew G Burton, Isabelle J Schalk, Yves Mély and Julien Godet. Spectral phasor applied to spectrally-resolved super resolution microscopy.

5. Hanna Manko, Tania Steffan, Véronique Gasser, Yves Mély, Isabelle J Schalk and Julien Godet. Spatio-temporal organization and regulation of Non-Ribosomal Peptide Synthetases involved in the pyoverdine biosynthesis in Pseudomonas aeruginosa.

List of presentations

1. Hanna Manko, Julien Godet (oral presentation). Spatio-temporal organisation and regulation of enzymes involved in siderophore biosynthesis in Pseudomonas. "The Doctoral School Days 2021", Strasbourg
2. Hanna Manko, Tania Steffan, Yves Mély, Julien Godet (poster presentation). Spatio-temporal organisation of enzymes involved in siderophore biosynthesis in Pseudomonas. SMLMs 2021, Lausanne
3. Hanna Manko, Tania Steffan, Isabelle Schalk, Yves Mély, Julien Godet (poster presentation). Super-resolution microscopy techniques to investigate enzymes organization in bacteria. Mifobio 2021
4. Hanna Manko, Tania Steffan, Yves Mély, Julien Godet. (oral presentation). Organization of NRPSs in Pseudomonas aeruginosa pyoverdine pathway. "The Doctoral School Days 2022", Strasbourg

Resumé de thèse long en français

Organisation spatio-temporelle et régulation des enzymes impliquées dans la biosynthèse des sidérophores chez *Pseudomonas aeruginosa*

Les bactéries ont développé des mécanismes sophistiqués leur permettant de survivre dans des conditions environnementales variées. Une large gamme de peptides - appelés peptides non ribosomaux (PNR) - peuvent être produits indépendamment des ribosomes pour procurer un avantage sélectif. Les PNRs sont synthétisés par une famille de grandes enzymes appelées synthétases de peptides non ribosomiques (NRPS en anglais). Au cours de la synthèse des PNRs, des modules spécifiques portés par les NRPS sont responsables de l'addition sélective d'un (et d'un seul) AA ou AA modifié. La synthèse s'effectue par addition, blocs après blocs, d'AA et le produit de synthèse se transloque d'un module à l'autre - ces modules pouvant se trouver ou non sur la même NRPS. Contrairement à la machinerie du ribosome, les peptides synthétisés par les NRPS ne sont pas limités aux AA naturels pour leur synthèse, mais des centaines de composés divers (AA de série D, AA modifiés, ...) peuvent être utilisés. Cela conduit à des peptides complexes ayant de multipless activités biologiques. Parmi les molécules produites par les NRPS, certaines sont par exemple utilisées en clinique comme médicaments imunosuppresseurs, antitumoraux ou antibactériens : [1]

Mais malgré leur caractère unique et leur importance, on sait peu de choses sur l'organisation des NPRS dans l'environnement cellulaire natif. La voie de la pyoverdine de *P. aeruginosa* a été choisie comme modèle.

P. aeruginosa est un pathogène humain opportuniste présentant une résistance élevée aux antibiotiques [2]. Dans des conditions de carence en fer, les *P. aeruginosa* peuvent produire de petites molécules - appelées sidérophores - capables de chélater le fer présent dans l'environnement avec une grande affinité - tout en exprimant des transporteurs spécifiques capables d'importer le complexe sidérophore/Fe. *P. aeruginosa* produit deux principaux sidérophores spécifiques de cette souche : la pyocheline et la pyoverdine.

La biosynthèse de la pyoverdine implique quatre NRPS et plusieurs enzymes accessoires plus petites. Ces quatre NRPS - PvdL, PvdI, PvdJ et PvdD - sont responsables de la synthèse du squelette peptidique du précurseur de la pyoverdine [3] . Une synthèse correcte et efficace nécessite une orchestration dans le temps et l'espace de ces quatre enzymes. Ce mécanisme n'est pas décrit mais il a été proposé que les NRPS forment, avec les enzymes accessoires de la voie de la pyoverdine, un grand complexe actif multimoléculaire, appelé sidérosome, par analogie avec d'autres complexosome.

L'objectif de mon projet de doctorat est d'étudier l'organisation dans l'espace et dans le temps des NRPS impliquées dans la voie de biosynthèse de la pyoverdine chez *Pseudomonas aeruginosa*.

Afin d'obtenir des informations sur la localisation et la dynamique des NRPS, nous nous sommes appuyés sur des techniques de microscopie de localisation de molécules uniques (SMLM). En

particulier, nous avons utilisé le suivi de molécules uniques (single molecule tracking) et la microscopie de localisation monochrome et multicolore. Le but de mon travail était de collecter et d'analyser les données correspondant à des milliers d'enzymes individuelles dans leur environnement cellulaire natif. Les informations sur la localisation (en 2D et 3D), la dynamique et les co-localisations (positions d'une NRPS par rapport à une autre) de ces molécules individuelles permettent de construire une première image claire de leur organisation dans la cellule.

Résultats

Dynamique

Durant la première partie du projet, une série d'expériences a été réalisée afin d'obtenir des informations sur les interactions et les diffusions des enzymes PvdA, PvdL, PvdI, PvdJ et PvdD fusionnées à PAmCherry (une version photoactivable de mCherry). La PvdA, qui n'est pas une NRPS, a été utilisée comme témoin dans ces expériences parce que sa diffusion a été précédemment caractérisée par FRAP [4]. PvdA est une enzyme accessoire responsable avec PvdH de la synthèse d'une hydroxy-ornithine - un AA modifié. Nous avons caractérisé l'interaction de la PvdA avec les différents NRPS en utilisant la méthode FLIM-FRET. Nous avons pu montrer que la PvdA se lie aux quatre NRPS, et pas seulement à celles capables d'intégrer la HO-ornithine dans la séquence de la pyoverdine. Ce travail a conduit à ma première publication dans JOVE [5] - publication dans laquelle nous avons décrit en détail les protocoles et les routines d'analyse.

Pour obtenir des informations sur la diffusion des NRPS, nous avons analysé les données de tracking en utilisant une analyse des distance de déplacement (jump distance analysis). Les résultats ont montré que la diffusion des NRPS est mieux décrite par un modèle à deux composantes qui considère la coexistence des fractions dites mobiles et immobiles (ou peu mobiles). En accord avec les données précédemment rapportées, PvdA possédait le coefficient de diffusion le plus élevé - en accord avec le fait que PvdA est la plus petite protéine parmi celles étudiées. La PvdL, l'enzyme responsable de la synthèse du premier AA dans le précurseur de la pyoverdine, avait une diffusion beucoup plus restreinte. PvdL, PvdI et PvdD possèdent une mobilité plus élevée que celle de PvdL. Leurs coefficients de diffusion ne semblaient pas dépendre de la taille des protéines (Figure 1, B).

Localisations

Pour mieux comprendre la dynamique de ces protéines, nous avons également caractérisé ces protéines en imagerie microscopique de localisation en utilisant la technique du DNA-PAINT. Les enzymes d'intérêt ont été fusionnées à la protéine eGFP qui a été utilisée comme cible pour des anticorps primaires. Ces anticorps primaires ont été marqués avec une séquence d'ancrage d'ADN simple brin (ADNsb) sur laquelle des ADNs marqués (7-mer) libres (brins imageurs) ont pu se lier de manière transitoire. La liaison de ces imageurs à la séquence d'ancrage sur

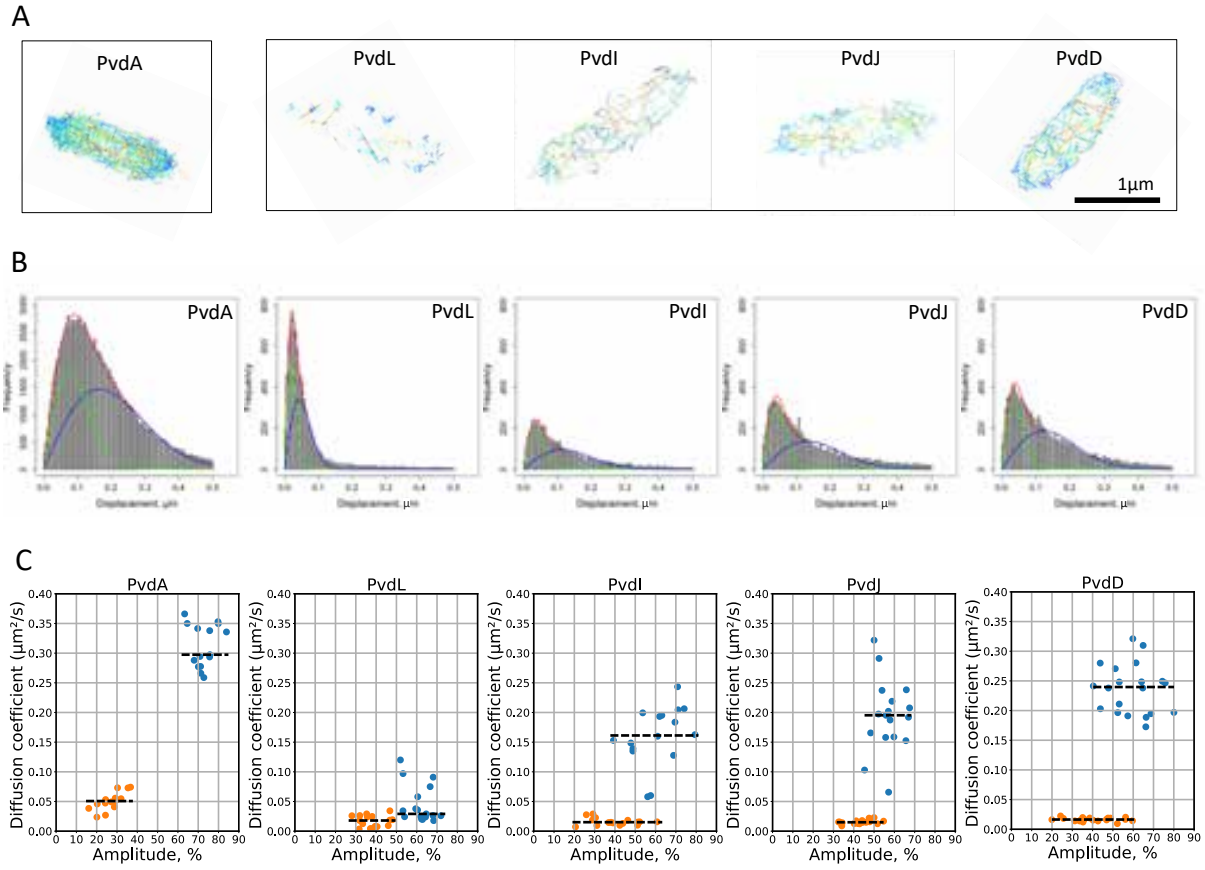

Figure 1 – (A). Cartes de diffusion. **(B)**. Distributions des distance de déplacement (jump distance) construites pour toutes les enzymes d'intérêt. Les histogrammes ont été analysés à l'aide d'un modèle à deux composantes, qui considère la coexistence de complexes mobiles (ligne bleue) et peu mobiles (ligne verte). **(C)**. A partir de ces distributions, on peut estimer les coefficients de diffusion et leurs amplitudes correspondantes. Les lignes noires pointillées correspondent à la valeur médiane du coefficient de diffusion.

l'anticorps primaire génère des signaux répétés à partir desquels la localisation de la protéine peut être caractérisée sans ambiguïté.

Les données de localisation montrent que les quatre NRPS sont principalement exclues de la partie centrale du cytoplasme bactérien (Figure 3, C) - ce qui correspond probablement à une exclusion du nucléoïde. Pour toutes les NRPS, à l'exception de PvdL, ces données ont montré que les NRPS diffusent le long de l'ensemble de la cellule mais surtout à proximité de la membrane interne. La diffusion beaucoup plus faible observée pour PvdL suggère également que PvdL pourrait être en interaction (ou en interaction transitoire) avec la membrane interne. Cette observation est intéressante car le premier module de PvdL, qui est prédit pour fonctionner comme un module de démarrage, couple un coenzyme A avec un acide gras dans une réaction dépendante de l'ATP avant d'adresser ce module au L-glutamate porté par le second module de la PvdL. La présence de cet acide gras suggère que le produit synthétisé pourrait être ancré dans la membrane interne au cours du processus.

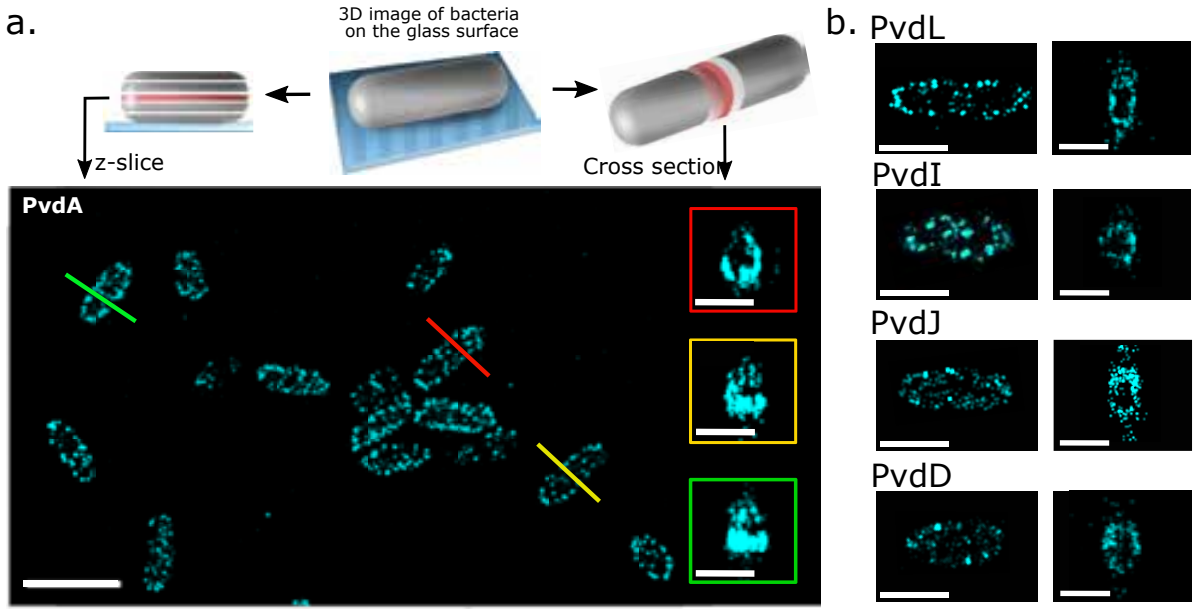

Figure 2 – **(a)**. Images de localisation 3D de la PvdA - et **(b)** des quatre NRPS obtenues par la technique DNA-PAINT

Co-localisation

Les expériences de co-localisation ont été réalisées afin de voir si les différentes NRPS sont situées dans les mêmes zones au sein de la bactérie, ce qui pourrait indiquer une interaction. La microscopie de localisation basée sur du DNA-PAINT à deux couleurs a été réalisée pour cinq doubles mutants, chacun ayant une paire de NRPSs marquée dont l'une est fusionnée à eGFP et l'autre à mCherry : PvdL-PvdJ, PvdJ-PvdL, PvdL-PvdD, PvdL-PvdI, PvdJ-PvdD.

Nous avons d'abord vérifié que les protocoles expérimentaux et d'analyse des données fonctionnaient bien sur notre système. Pour cela, nous avons exploré si nous obtenions des résultats similaires indépendamment de l'ordre de marquage des paires de protéines pour lesquelles nous recherchons une interaction. Ceci a été réalisé en imageant les deux souches de bactéries doubles mutantes : eGFP-PvdL/PvdJ-mCherry et PvdJ-eGFP/mCherry-PvdL. Les coefficients de corrélation de Mander obtenus se sont avérés être dans une plage similaire (Figure 3, B, boîte grise).

Ensuite, nous avons effectué les mêmes expériences sur chacune des bactéries doubles mutantes. Presque dans tous les cas, la distribution des coefficients de corrélation de Mander semble être répartie sur une large gamme de valeurs. La valeur médiane la plus élevée ($\sim$0,56) a été obtenue pour le couple PvdL/PvdI. PvdL et PvdI sont les deux premières enzymes du processus de biosynthèse de la pyoverdine. Des valeurs relativement élevées ont également été observées pour le couple PvdL/PvdD (médiane $\sim$0,4), ce qui est plutôt inattendu étant donné qu'il s'agit respectivement de la première et de la dernière enzyme du processus de production. Enfin, l'interaction de la paire PvdL/PvdD a été confirmée par des expériences FLIM-FRET.

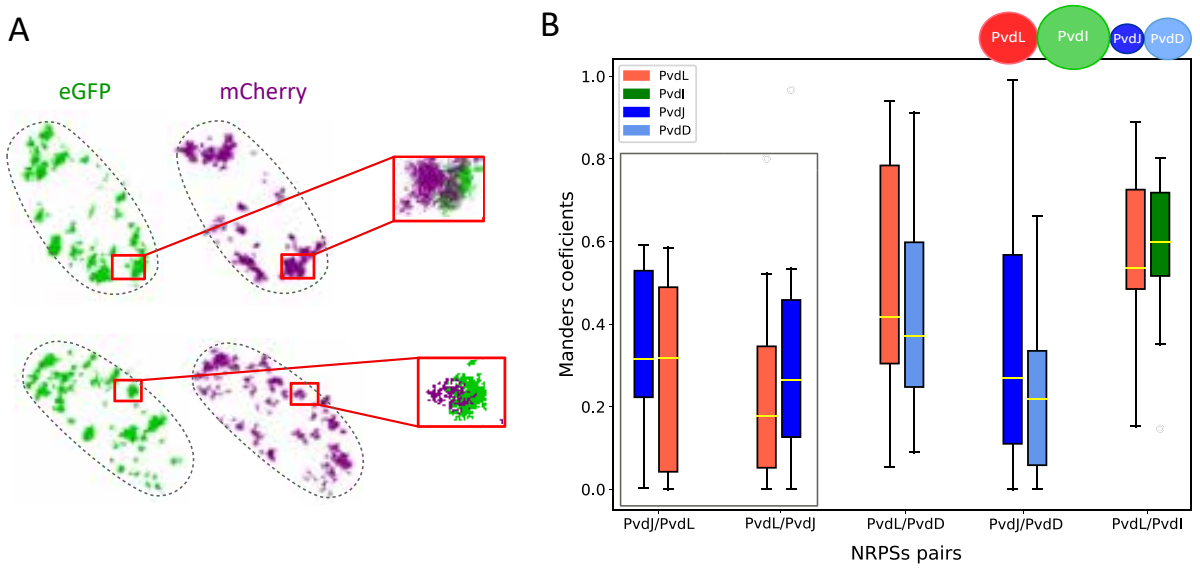

Figure 3 – (A). Expériences de co-localisation des NRPS en cellule. **B**. Les coefficients de corrélation de Mander.

Un objectif ambitieux de mon travail était de réaliser la co-localisation des quatre NRPS en même temps dans des cellules en utilisant une technique récemment développée au laboratoire appelée SMLM à résolution spectrale (SR-SMLM). Pouvoir suivre jusqu'à quatre objets différents dans une cellule au niveau de la molécule unique est extrêmement difficile. Il est très difficile - sinon impossible - de réaliser de la microscopie de localisation à quatre couleurs en utilisant l'approche multicolore classique, car l'utilisation de filtes passe-bandes nécessaires pour enregistrer les différents canaux entraîne une perte importante de photons - un problème crucial dans les expériences en molécules uniques. La SR-SMLM, en enregistrant la décomposition spectrale complète des émetteurs uniques, a le potentiel de surmonter cette limitation. Mais cette technique récente doit encore être améliorée pour atteindre de telles capacités multiplexes.

Pour améliorer le SR-SMLM, j'ai travaillé sur l'application de l'apprentissage profond (deep learning) pour améliorer les performances de la technique SR-SMLM.

Application de l'apprentissage profond pour améliorer la performance de la technique SR-SMLM

J'ai travaillé sur le développement d'une nouvelle méthode d'analyse afin d'améliorer les performances de la technique SR-SMLM. Cette méthode repose sur l'utilisation de méthodes d'apprentissage profond. Ce travail a été initié pendant le confinement, à l'époque où je ne pouvais pas réaliser d'expériences dans le laboratoire. L'idée était d'optimiser la qualité des images de SR-SMLM en utilisant un processus de restauration d'images basé sur l'apprentissage profond pour améliorer à la fois la précision spatiale (précision de localisation) et la précision spectrale (précision dans la détermination de la longueur d'onde). L'amélioration de l'image devrait per-

mettre de discriminer les différents fluorophores, y compris ceux dont les spectres se chevauchent largement.

L'originalité de notre travail a été de pouvoir construire un jeu d'entraînement pertinent pour le réseau d'apprentissage profond. En effet, afin d'entraîner notre réseau de neurones, deux ensembles différents d'images avec des ratios signal/bruit différents étaient nécessaires. Cependant, la nature stochastique de SMLM rend presque impossible l'obtention de deux images localisant les mêmes molécules avec des SNR différents. Nous avons contourné cette limite en imageant une construction en origami d'ADN et en utilisant du DNA-PAINT - ce qui permet d'obtenir le signal du même point sur plusieurs images dans le temps. Le signal des différentes images a été fusionné en utilisant une pondération selon les fréquences spatiales des images. L'image suivie a été filtrée à l'aide d'un filtre white-hat pour obtenir des images cibles à haut rapport signal sur bruit. Une seule image parmi les n images fusionnées a été sauvegardée sans modification pour être utilisée comme image à améliorer avec un faible rapport signal/bruit (Figure 4, A).

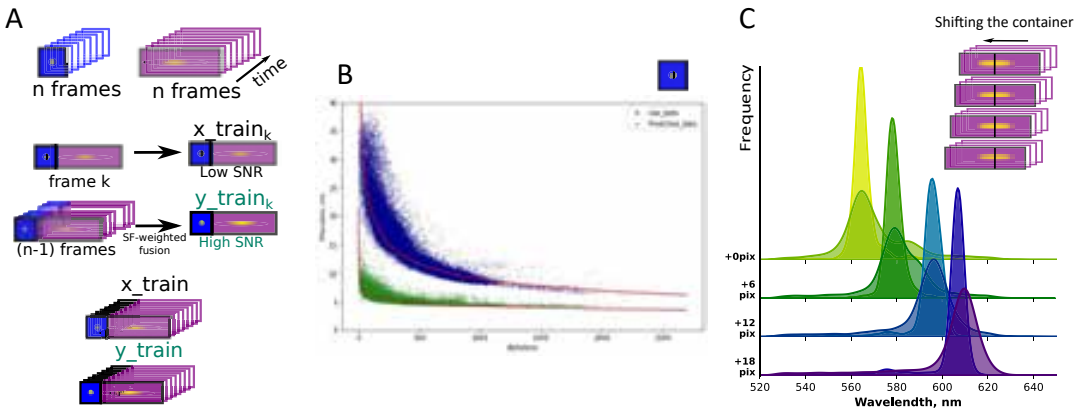

Figure 4 – **(A)**. Préparation du jeu d'entrainement. **(B)**. La précision de pointé des localisations calculée pour les données brutes (bleu) et pour les données améliorées par le réseau profond (vert) montre clairement l'intérêt du réseau de neurone. **(C)**. Réponse au décalage spectral - les distributions plus fines correspondent aux données améliorées par le réseau de neurones.

Un réseau en U (U-net) a été construit et entrainé en utilisant ce jeu d'entrainement. Le réseau a été validé sur des données de test encore non-vues par le réseau. Nous avons montré que le réseau permet d'augmenter la précision de la localisation dans la partie spatiale et spectrale (Figure 4, B). Dans la partie spectrale de l'image, nous avons pu également multiplier par deux le nombre de localisations avec une longueur d'onde précisément déterminée. Afin de vérifier les performances du réseau en cas de changement de la longueur d'onde d'émission des émetteurs, nous avons simulé un décalage spectral en déplaçant aléatoirement le conteneur spectral de 6, 12 et 18 pixels (Figure 4, C) dans nos données. La forme et la largeur du spectre sont restées inchangées, tandis que les nouveaux maximum d'émission correspondaient au déplacement induit, ce qui montre que notre réseau est capable de fonctionner pour divers fluorophores emmettant dans différentes régions spectrales ou dont la longueur d'onde d'émission change (shift spectral).

Les résultats de ces travaux sont actuellement soumis à publication (Manko et al. *en préparation*). En attendant que la publication soit acceptée, nous avions décidé de le déposer en tant que preprint sur bioRxiv pour rendre ce travail accessible à la communauté.

Phasor Spectral

En tant que technologie d'imagerie émergente, la SR-SMLM doit être perfectionnée pour tirer pleinement parti des données multidimensionnelles générées. En particulier, l'analyse de la dimension spectrale nécessite des outils appropriés [6]. Nous avons proposé d'appliquer le phasor spectral à la SR-SMLM pour décrire les informations contenues dans le spectre d'un émetteur unique.

Nous avons démontré que le phasor spectral peut être appliqué avec succès à la SR-SMLM. Nous avons pu l'utiliser pour classer efficacement les émissions de fluorescence du rouge du Nil des signaux de fluorescence d'une cyanine dont les deux spectres se chevauchent largement dans des expériences de PAINT en deux couleurs. Nous avons donc pu démontrer que le phasor spectral fournit un outil analytique robuste pour l'analyse détaillée de la composante spectrale des images de SR-SMLM et améliore ainsi les capacités de cette méthode d'imagerie multidimensionnelle multicolore en molécules uniques.

Le manuscrit décrivant les résultats de ces travaux est prêt. Nous avons fait le choix de le soumettre pour publication une fois que les travaux sur le Unet seront mis à la disposition de la communauté. (Manko H, Burton M et al. *en préparation*)

Conclusions

Au cours de mon projet de thèse, nous avons étudié l'organisation des quatre NRPS impliquées dans la voie de la pyoverdine de *P. aeruginosa* en utilisant plusieurs techniques de microscopie de super-résolution. Les coefficients de diffusion et la localisation des protéines suggèrent une présence prédominante à proximité de la membrane bactérienne. De la microscopie super-résolue à deux couleurs a été réalisée afin d'explorer la localisation de paires d'enzymes.

En parallèle de ce travail, nous avons développé et entraîné un réseau de neurones afin d'améliorer les performances de la technique SR-SMLM. J'ai également participé à une nouvelle méthode d'analyse de la décomposition spectrale de la lumière en SR-SMLM (phasor spectral). Les applications de ces travaux permettent d'améliorer considérablement la qualité des images en microscopie spectralement résolue. L'ensemble de mes travaux de thèse devrait se traduire par 4 publications spécifiques.

Bibliography

[1] R.D Sussmuth and A. Mainz. Nonribosomal peptyde synthesis - principles and pprospects. Angewandte Chemie, 56 :3770–3821, 2017.

[2] Jeffrey Lyczak, B., Carolyn Cannon, L., and Gerald Pier, B. Establishment of pseudomonas aeruginosa infection : lessons from versatile opportunist. Microbes and Infection, 2 :1051–1060, 2000.

[3] Isabelle J. Schalk, Coraline Rigoulin, and Julien Godet. An overview of siderophore biosynthesis among fluorescent pseudomonads and new insights into their complex cellular organisation. Environmental Micro- biology, 22 :1447–1466, 2020.

[4] L. Guillon, S. Alternurger, P. L. Graumann, and I. J. Schalk. Deciphering protein dynamics of the siderophore pyoverdine pathway in pseudomonas aeruginisa. PLoS One, 8 : e79111, 2012.

[5] H. Manko, V. Normant, Q. Perraud, T. Steffan, V. Gasser, E. Boutant, E. Réal, I.J. Schalk, Y. Mély, and Godet J. Flim-fret measurements of protein-protein interactions in live bacteria. J Vis Exp, 162, Aug 25 2020.

[6] K-H. Song, B. Dong, C. Sun, and H.F. Zhang. Theoretical analysis of spectral precision in spectroscopic single-molecule localization microscopy. Review of Scientific instruments, 89(12), 2018.

Hanna MANKO

Organisation spatio-temporelle et régulation des enzymes impliquées dans la biosynthése d'un sidérophore chez *Pseudomonas*

Résumé

Les mécanismes d'adaptation des bactéries peuvent impliquer l'action de synthétases de peptides non ribosomaux (NRPS) permettant de former des molécules peptidiques à large spectre d'activités biologiques. Dans cette thèse nous avons étudié la dynamique et l'organisation de quatre NRPS impliquées dans la biosynthèse de la pyoverdine chez *Pseudomonas aeruginosa*. Nous avons utilisé des approches comme le suivi en molécule unique, la microscopie de super-résolution et de l'imagerie en temps de vie de fluorescence pour montrer que les NRPS sont capables de former des complexes transitoires près de la membrane cellulaire. Afin de dépasser les limites des techniques actuellement disponibles, nous avons développé une méthode d'apprentissage profond permettant d'améliorer les performances de la microscopie de localisation en molécule unique résolue spectralement. Ces développements permettront de progresser plus encore dans la compréhension de l'organisation spatio-temporelle des NRPS.

Mots-clés : microscopie de localisation de molécules uniques, NRPS, *Pseudomonas aeruginosa*, microscopie résolution spectralement, apprentissage profond

Résumé en anglais

Bacteria adaptation mechanisms may involve action of Non-ribosomal peptide synthetases (NRPSs) allowing to synthesize peptide molecules with a broad spectrum of biological activity. Here, the dynamics and organization of four large NRPSs involved in pyoverdine biosynthesis in *P. aeruginosa* were studied using single-molecule tracking, one- and two-color DNA-PAINT microscopy and FLIM-FRET. Our results suggest that NRPSs are able to form transient dynamic complexes near the cell membrane. To overcome the limitations of currently available techniques, we have developed a deep learning method to enhance the performance of spectrally resolved single molecule localization microscopy (srSMLM). These developments will allow to make further progress in the understanding of the spatio-temporal organization of NRPS.

Keywords : Single-Molecule Localization Microscopy, NRPSs, *Pseudomonas aeruginosa*, spectrally-resolved SMLM, Deep Learning